UNIVERSITY OF OKLAHOMA

GRADUATE COLLEGE

ESTABLISHING ELEMENTAL ANALYSIS TO QUANTIFY NANOSCALE INTERACTIONS AT SINGLE NANOPARTICLE AND SINGLE CELL LEVELS

A DISSERTATION

SUBMITTED TO THE GRADUATE FACULTY

in partial fulfillment of the requirements for the

Degree of

DOCTOR OF PHILOSOPHY

By

NATHAN DONAHUE
Norman, Oklahoma
2021

Downloaded from SHAREOK. Persistent Handle URL: https://hdl.handle.net/11244/332401

ESTABLISHING ELEMENTAL ANALYSIS TO QUANTIFY NANOSCALE INTERACTIONS AT SINGLE NANOPARTICLE AND SINGLE CELL LEVELS

A DISSERTATION APPROVED FOR THE
STEPHENSON SCHOOL OF BIOMEDICAL ENGINEERING

BY THE COMMITTEE CONSISTING OF

Dr. Stefan Wilhelm, Chair

Dr. Handan Acar

Dr. Michael Detamore

Dr. Luca Fornelli

© Copyright by NATHAN DONAHUE 2021
All Rights Reserved.

Acknowledgements

I would first like to thank my advisor, Dr. Stefan Wilhelm for his support, mentorship, and reliable responsiveness. Thank you for taking me on as your first Ph.D. student and for providing me with opportunities to become an independent scientist and for showing me how to drive research forward. I appreciated the many helpful brainstorming meetings that taught me how to be adaptable and rational in my scientific approach.

I would further like to thank my committee Dr. Handan Acar, Dr. Michael Detamore, and Dr. Luca Fornelli. I appreciate the insightful input and advice that each of them has provided me. Thank you Dr. Acar for providing me my first research experience at the University of Chicago and for encouraging me to apply to the University of Oklahoma. Thank you to Dr. Detamore for being so positive and knowledgeable about the Ph.D. process. Also thank you Dr. Fornelli for his mass spec expertise and those weekends where he would sneak up on me as I played loud music in the lab.

I would further like to thank Dr. Steven Foster for all the encouragement and assistance he has generously provided. He made my mass spec experience extremely enjoyable with his impeccable taste in music and his colorful stories. I would further like to thank Dee Stone in the chemistry stockroom for providing all the argon that enabled this research. I would also like to thank Dr. Ruth Merrifield at PerkinElmer who taught me everything I needed to know about ICP-MS. I would further like to thank Sandy Kanapilly, Robert Forrester, and Steve Daniels for their continuous technical ICP-MS support.

I further want to thank the Wilhelm lab for their assistance. In particular, Emmy Francek who helped so much with nanoparticle synthesis and characterization. Working with you in the lab was always fun. Also thank you Vinit Sheth for being the de facto lab

manager and an excellent confocal microscopist. I further want to Alyssa Holden, Alex Frickenstein, Wen Yang, and Dr. Lin Wang for your kindness and all the gold nanoparticles I stole from you all. Thank you Majood Haddad for extracting all that ICP-MS data and helping out with TEM image analysis. I would also like to thank former Wilhelm lab members Joanne Lee and Ellen Vance for being so welcoming and helpful when I first joined the lab. Additionally, I want to thank the Detamore lab in particular Drs. Emi Kiyotake and Jakob Townsend for their support and friendship. I also want to thank Peggy Keefe who was so helpful when we shared lab spaces and Emily Thomas for being so passionate and motivated.

I would further like to thank the Sam Noble Microscopy Core Facility for their assistance with TEM. In particular, thank you to Drs. Preston Larson, Julian Sabisch, and Andy Madden for helping me acquire great images of nanoparticles. I also want to thank Drs. Caleb Marlin and Joel Guthridge for their assistance and expertise with mass cytometry. I also would like to thank Drs. Darrell Irvine and Mariane B. Melo at MIT for the many different cell lines that they generously provided me.

Finally, I would like to thank my partner Simon Liang for teaching me how to be devoted to research and for always being there cheering me on. Thank you for being so understanding, our countless scientific discussions, and for reviewing all my data, figures, and equations. I also want to thank my mom, dad, brother, aunts, uncles, cousins, and grandparents for their continued love and support.

Table of Contents

Acknowledgements iv

Table of Contents vi

List of Figures viii

List of Tables xii

Abstract xiv

Chapter 1: Introduction 1

Chapter 2: Concepts of Nanoparticle Cellular Uptake and Corresponding Physicochemical Properties[1] 5

- Abstract 5
- Introduction 6
- Cellular Uptake of Nanoparticles 8
- Mediating nanoparticle cell uptake through material design 20

Nanoparticle Morphology and Cellular Uptake 21

Nanoparticle Surface Charge and Cellular Uptake 25

Nanoparticle Targeting Ligands and Cellular Uptake 28

Nanoparticle Modifications for Intracellular Delivery 33

Discussion 36

Chapter 3: Assessing Nanoparticle Colloidal Stability with Single Particle Inductively Coupled Plasma Mass Spectrometry[2] 38

- Abstract 38
- Introduction 39
- Materials and Methods 42
- Results and Discussion 44

Conclusion 56

Acknowledgements 57

Chapter 4: Quantifying Chemical Composition and Reaction Kinetics of Individual Colloidally Dispersed Nanoparticles[3] 58

- Abstract 58
- Introduction 59
- Methods and Materials 60
- Results and Discussion 65
- Conclusions 75

Acknowledgements 76

Chapter 5: Single Cell Elemental Analysis for Quantification of Nanoparticle Interactions with Individual B Cells[4] 77
Abstract 77
Introduction 78
Materials and Methods 80
Results and Discussion 85
Conclusion 93
Acknowledgements 94
Chapter 6: Conclusion 95
References 106
Appendix A: Figures 136
Appendix B: Tables 187

List of Figures

Chapter 1

No Figures

Chapter 2

Figure 2.1: Overview of nanoparticle uptake pathways via endocytosis.

Figure 2.2: Overview of nanoparticle cytoplasmic delivery pathways and strategies

Figure 2.3: Overview of main nanoparticle intracellular trafficking pathways and mechanisms

Chapter 3

Figure 3.1: Nanoparticle characterization of citrate coated AuNPs

Figure 3.2: Inductively coupled plasma mass spectrometer

Figure 3.3: Nanoparticle characterization using SP-ICP-MS

Figure 3.4: SP-ICP-MS analysis of AuNP mixture

Figure 3.5: Comparing pure nanoparticles sizes and nanoparticle mixtures sizes

Figure 3.6: Single particle analysis of Gold Nanorods

Figure 3.7: SP-ICP-MS to assess AuNPs aggregation

Figure 3.8: Monitoring nanoparticle aggregation kinetics with UV-Vis

Figure 3.9 TEM of aggregated AuNPs

Figure 3.10 Physicochemical characterization of PEGylated AuNPs

Figure 3.11: SP-ICP-MS of PEGylated 16-nm AuNPs in saline solution

Figure 3.12: Comparison of mean nanoparticle masses in saline solution

Chapter 4

Figure 4.1: Overview of dual analyte (isotope) analysis with quadrupole ICP-MS technology in single particle mode

Figure 4.2: Effects of collision cell parameters on transient ion signals

Figure 4.3: Transient ion duration time of lanthanide-ion doped beads

Figure 4.4: Time resolved ion signals for lanthanide beads

Figure 4.5: Dual analyte SP-ICP-MS of lanthanide beads

Figure 4.6: Mass cytometry of lanthanide beads

Figure 4.7: UV-Vis spectrum of AgNPs, AuNPs, and alloy NPs

Figure 4.8: Time resolved ion signals using dual analyte SP-ICP-MS of 100-nm AgNPs

Figure 4.9: TEM analysis of in-house synthesized AuNPs

Figure 4.10: Quantifying paired and unpaired isotope events with dual analyte quadrupole SP-ICP-MS mode for individual nanoparticles.

Figure 4.11: Time resolved ion signals using dual analyte SP-ICP-MS signals of 1:1 mixture of 100-nm AgNPs and AuNPs

Figure 4.12: Transient ion duration time of differently sized AgNPs

Figure 4.13: Dual analyte mass distribution of 30-nm AgNPs

Figure 4.14: Single particle analysis of 50-nm, 70-nm, and 100-nm silver nanoparticles (AgNPs) using dual analyte SP-ICP-MS mode

Figure 4.15: Dual isotope quantification of 70-nm PEGylated AgNPs using SP-ICP-MS

Figure 4.16: Time resolved ion signal using dual analyte SP-ICP-MS of 80-nm gold/silver alloy nanoparticles

Figure 4.17: Compositional analysis of individual 80-nm gold/silver alloy nanoparticles

Figure 4.18: Dual analyte SP-ICP-MS mass distributions and elemental percentages of different gold-silver alloy nanoparticle compositions

Figure 4.19: Quantifying gold etching using KI/I_2 in individual gold/silver alloy nanoparticles *in situ*

Figure 4.20: EDS/STEM line profiles of etched gold-silver alloy nanoparticles

Figure 4.21: Etching of AuNP and AgNP mixture

Figure 4.22: TEM size distribution of 55-nm gold-silver alloy nanoparticle seeds

Figure 4.23: Au/Ag elemental distribution in 55-nm gold-silver alloy nanoparticle seeds

Figure 4.24: Quantifying metal deposition kinetics on individual gold/silver alloy nanoparticles *in situ*

Figure 4.25: Mass distributions of gold and silver deposition on 55-nm gold-silver alloy nanoparticle

Figure 4.26: UV-VIS spectrophotometry of seed-mediated growth of gold-silver alloy nanoparticle

Chapter 5

Figure 5.1: Detecting individual metal-labeled B cells

Figure 5.2: Transmission electron microscopy of streptavidin quantum dots

Figure 5.3: ^{114}Cd signal of streptavidin quantum dots with and without biotinylated antibody

Figure 5.4: Confocal microscopy of quantum dot labeled B cells

Figure 5.5: Hemocytometer image of fixed and stained B cells

Figure 5.6: Epifluorescence microscopy of B cells pre-and post- nebulization

Figure 5.7: Events and transport efficiency of lanthanide doped beads

Figure 5.8: Single particle mass and size distribution of 13-nm AuNPs

Figure 5.9: Transmission electron microscopy of 13-nm AuNPs

Figure 5.10: Schematic representation of maleimide-based nanoparticle surface functionalization

Figure 5.11: Surface modified-AuNP mass distribution under cell culture conditions

Figure 5.12: Quantifying and visualizing nanoparticle-cellular association

Figure 5.13: Effects of K7C AuNPs on B cell viability

Figure 5.14: UV-VIS of etched AuNPs

Figure 5.15: Visualizing and quantifying internalized 13-nm K7C AuNPs

Figure 5.16: ^{197}Au Peak Shapes of B cells exposed to K7C AuNPs

Figure 5.17: Determining AuNP+ B cells

Chapter 6

No figures

List of Tables

Chapter 1

No Tables

Chapter 2

Table 2.1: Examples of different cellular uptake pathways of gold nanoparticles in tissue culture for both cancerous and non-cancerous cells.

Table 2.2: Examples of different types of nanoparticle targeting ligands for enhanced nanoparticle cellular interaction with targeted cell types.

Table 2.3: Examples of surface modifications for intracellular delivery

Chapter 3

Table 3.1 Gold nanoparticle molar decadic extinction coefficients

Table 3.2: SP-ICP-MS conditions

Table 3.3: Determining transport efficiency

Table 3.4: Comparison of nanoparticle measurements

Table 3.5: DLS of AuNPs in saline solution

Chapter 4

Table 4.1: Optimized conditions for SP-ICP-MS

Table 4.2: Transport efficiency in standard and dual analyte mode

Table 4.3: Dual analyte SP-ICP-MS Conditions

Table 4.4: Paired isotope percentages of lanthanide-ion doped beads

Table 4.5: DLS of AgNPs, AuNPs, and gold-silver alloy nanoparticle

Table 4.6: Median masses of AgNPs

Table 4.7: EDS/STEM quantification of gold-silver alloy nanoparticle composition

Chapter 5:

Table 5.1 Optimized conditions for single cell ICP-MS

Table 5.2 DLS of surface engineered 13-nm AuNPs

Table 5.3 Optimized dual analyte single cell ICP-MS conditions

Chapter 6:

No tables

Abstract

For over two decades, nanoscale materials have been utilized as diagnostics and therapeutics. The successful clinical implementation of these platforms depends on well-defined physicochemical properties. However, such nanoparticle characteristics diverge at the single particle level and fluctuate within biological systems. Moreover, single cell diversity often leads to unpredictable and heterogenous biological outcomes upon nanoparticle exposure. Together, these factors complicate and hinder widespread clinical application of nanomaterials. To that end, there exists a need to quantify both the dynamics of individual nanoparticle physicochemical properties and single cell interactions with nanoparticles. Insights from such fundamental studies could guide the design of novel nanomaterials with better controlled physicochemical properties potentially leading to improved clinical performance. To achieve this goal, quantitative analytical methods that capture both dynamic single nanoparticle transformations and single cell heterogeneity are required. Mass spectrometry based on elemental analysis can be applied to investigate such phenomenon. In the current dissertation, single particle inductively coupled plasma mass spectrometry (SP-ICP-MS) was utilized to quantify the mass, colloidal stability, and chemical composition of model nanoparticles *in situ* with high throughput. SP-ICP-MS was further applied to quantify the heterogeneous changes of individual nanoparticle physicochemical properties. With established elemental analysis techniques to track the evolution of single nanoparticle physicochemical properties, the cellular uptake of model nanoparticles was then quantified at the single cell level using human B cells. This elemental analysis approach represents a feasible method for measuring the single cell variety of nanoparticle cellular uptake. Collectively, these results represent a new readily accessible tool for the nanomedicine community that is capable of efficiently quantifying

nanoparticle mass, colloidal stability, chemical composition, and nanoparticle cellular uptake all on the same mass spectrometer. With this elemental analysis approach, future studies can develop strategies to modulate individual nanoparticle physicochemical properties within physiological settings to better control nanoparticle-cell interactions for improved clinical translation.

Chapter 1: Introduction

The long-term goal of this dissertation is the development of safe and effective nanoparticle systems for the treatment and diagnosis of disease guided by single nanoparticle and single cell elemental analysis. Nanoparticles consisting of various materials, sizes, and compositions have been successfully applied in various clinical settings such as cancer treatments, diagnostic imaging agents, immunoassays, and life-saving vaccines. However, the clinical translation of nano-based platforms remains challenging as evidenced by the low number of FDA-approved platforms that utilize nanomaterials. As the biomedical success of these nano-based platforms hinges on well-defined nanoparticle physicochemical characteristics (*i.e.,* size, shape, surface charge, stability, etc.), effective clinical application of nanomaterials necessitates comprehensive characterization. Traditional techniques to probe such physicochemical properties often rely on ensemble measurements that provide average measurements for a population of nanoparticles. However, a given batch of nanoparticles contains a distribution of nanoparticles with varying sizes, composition, and surface chemistries that differ from nanoparticle to nanoparticle. Although ensemble characterization of nanoparticles is commonplace, fast, and cost-effective, data on individual nanoparticle heterogeneity is obscured. Moreover, such nanoparticle properties are dynamic and subject to change upon exposure to biological settings. These fluctuating facets of nanomaterials warrant high throughput methods to reveal and quantify dynamic single particle differences which may offer novel insights on the synthetic and biological identities of individual nanoparticles. Consequently, quantitative *in situ* elemental analysis at the single nanoparticle level has gained traction in the nanotechnology field to provide researchers real-time information on

such crucial phenomena. As opposed to other single particle techniques that require low-throughput image analysis (*i.e.*, electron microscopy) or only measure layers of hydration around single nanoparticles (*i.e.*, nanoparticle tracking analysis), elemental analysis can provide fast and direct mass quantification of anisotropic nanoparticles that consist of transition metals. This type of analysis can enable biomedical researchers to investigate and eventually engineer nanoparticle physicochemical properties at the single nanoparticle level. Additionally, single nanoparticle elemental analysis permits the efficient quantification of changes to nanoparticle size, shape, composition, and surface chemistry without further sample preparation or complex data deconvolution. Single particle elemental analysis can provide better understanding leading to improved control over nanoparticle physicochemical parameters to engender groundbreaking nanotechnology applications.

Like individual nanoparticle heterogeneity, cells possess vast phenotypic differences at the single cell level. Therefore, analytical techniques that also capture this natural biological diversity are essential for detailing how nanoparticles may interact with biological systems. To date, single cell elemental analysis has been applied in multiplexing phenotypic assays of single cells and has the potential to quantify nanoparticle-cell interactions. In tandem, both single nanoparticle and single cell elemental analysis can empower researchers to simultaneously enhance the design of next generation nanotechnologies while also revealing single cell biological outcomes. Currently, there is an unmet need for an economical and commonplace quantitative elemental analysis method that can quantify both single nanoparticle physicochemical properties and how single cells associate with said nanomaterials. Together these powerful techniques are poised to

provide the nanomedicine community a new tool for augmenting the clinical translation of even more nanomaterials in both diagnostic and therapeutic spaces.

In the current dissertation, elemental analysis was applied to quantify different transformations of individual nanoparticles and further applied to measure nanoparticle interactions with single cells in the following three aims. The first aim established single particle inductively coupled plasma mass spectrometry (SP-ICP-MS) as a method for assessing nanoparticle colloidal stability as a function of surface modifications. The second aim was to develop a new SP-ICP-MS method to quantify chemical composition and reactions of bimetallic nanoparticles. The final third aim was to apply these findings to elucidate nanoparticle interactions with single B cells. The subsequent chapters detail these aims in chronological order.

Chapter 2 is a review of the field's current understanding of how nanoparticles interact with cellular systems. First, I provide an overview of nanomedicine and discuss nanomedicine's translational obstacles. Next, I discuss major pathways on how nanoparticles gain access to cells and point to examples in the literature of how these pathways can be leveraged to study nanoparticle-cell interactions. Other pathways that bypass active transport mechanisms are also outlined. I then summarize key nanoparticle physicochemical properties that can be leveraged to favor uptake pathways, alter the intracellular fate of nanomaterials, and review potential biological outcomes. This synopsis provides the foundation that inspired the following experimental chapters.

Chapter 3 addresses aim 1, where I established SP-ICP-MS as a high throughput technique to quantify the size and aggregation behavior of model engineered gold nanoparticles (AuNPs) *in situ*. First, SP-ICP-MS was validated as single particle method

for quantifying AuNPs mass and size by conventional methods like dynamic light scattering and transmission electron microscopy. Upon decorating AuNPs with various densities of polyethylene glycol (PEG), the colloidal stability of these surface-engineered nanoparticles was analyzed *in situ* using SP-ICP-MS.

Chapter 4 addresses aim 2 where I developed an SP-ICP-MS method to quantify two isotopes on individual nanoparticles. Due to the limitations of quadrupole m/z filtering, efficient simultaneous measurement of two isotopes in single particle mode has not been possible. Several key instrument parameters were optimized to permit concurrent dual analyte quantification of model nanoparticles using quadrupole SP-ICP-MS. Dual analyte SP-ICP-MS was validated with mass cytometry and energy dispersive x ray spectroscopy. This new high throughput single particle analysis technique was applied to quantify two different chemical reactions with model bimetallic nanoparticles.

Chapter 5 addresses aim 3 where the concepts of nanoparticle mass quantification and dual analyte detection were applied to measure nanoparticle-B cell interactions. First, B cells were labeled with transition metals to ensure accurate counting and detection of intact single cells. Next, the cellular internalization of AuNPs bearing two different surface charges was assessed using single cell ICP-MS and validated by confocal scanning laser microscopy. Lastly, these two techniques were used in concert to determine the percentage of B cells that had internalized gold nanoparticles.

Chapter 6 summarizes the main findings of this dissertation, discusses the limitations, and provides directions for future work.

Chapter 2: Concepts of Nanoparticle Cellular Uptake and Corresponding Physicochemical Properties[1]

Abstract

Nanoparticle-based therapeutics and diagnostics commonly referred to as nanomedicine have begun to significantly impact healthcare. However, the widespread clinical translation of nano-based platforms remains challenging. One of these challenges is the efficient delivery of nanoparticles to specific cell populations and subcellular targets within the body to elicit desired responses. Therefore, it is critical to understand the fundamental concepts of how nanoparticles interact with cellular systems to predict and control *in vivo* nanoparticle transport for improved clinical benefit. To that end, this chapter summarizes cellular internalization pathways and explores how nanoparticle physicochemical properties affect cellular uptake and intracellular trafficking. This chapter provides an overview of the field's understanding which inspired subsequent studies that focused on characterizing single nanoparticle physicochemical transformations and nanoparticle-cell interactions with the goal to improve clinical translation of nanomedicines.

[1]Published as: Donahue ND, Acar H, Wilhelm S, Concepts of nanoparticle cellular uptake, intracellular trafficking, and kinetics in nanomedicine *Advanced Drug Delivery Reviews* 2019; 143 68-98 doi.org/10.1016/j.addr.2019.04.008

Introduction

The design and medical application of nanoparticles for diagnosis and treatment of diseases represent a flourishing area of current nanotechnology research. This research field has been widely referred to as nanomedicine.[1] In nanomedicine, researchers engineer nanoparticles, for example, as delivery vehicles for therapeutics, vaccines, or imaging agents with the ultimate goal to positively impact people's lives.[2] Achieving this goal necessitates efficient delivery of nanoparticles to specific sites in the body with cellular specificity and oftentimes subcellular precision.[3] To date, the COVID-19 pandemic has spawned the advent of lipid nanoparticle mRNA vaccines and has created a renaissance in the nanomedicine field. Prior to the worldwide administration of hundreds of millions of nanoparticle COVID-19 vaccines, nanotechnology had yet to achieve its breakthrough moment in the clinic. Although the first nanoparticle formulation was FDA approved in 1995 for cancer treatment, nano-based platforms often underperform in clinical trials. The most major setback for nanomedicine's clinical application is the poor delivery efficiency to diseased sites *in vivo* (*i.e.,* tumors).[4] Efficient and effective nanomedicine requires exquisite control over nanoparticle transport in the body. However, this level of control has proved difficult and is one of main reasons so few nanomaterials are used clinically.[5]

To overcome this hurdle, tools that elucidate nanoparticle interactions with biological systems in concert with the rational design of nanomaterials have a dire unmet clinical need.[6] These nanotechnology-biology (*i.e.*, nano-bio) interactions are complex, dynamic, and multiparametric, and pose substantial obstacles for the engineering of more effective nanomedicines.[7] Factors that contribute to this complexity are manifold and include: (i) a nanoparticle's physicochemical properties, including size, shape, surface

chemistry, composition, architecture, density, and modulus; (ii) the biological and biochemical environments, including type of organ/tissue, biomolecular milieu and composition, pH, and other biochemical factors; and (iii) the interplay and interactions between these individual nanoparticle properties and biological/biochemical parameters, including the kinetics of nano-bio interactions.[8]

While researchers are able to synthesize colloidal nanoparticles with precise physicochemical properties and functions, these deliberately designed nanoparticle characteristics oftentimes evolve upon introduction of nanoparticles into a biological environment.[9,10] This phenomenon can be observed, for example, when nanoparticles are administered into the body through intravenous injection. Upon contact with blood, serum proteins adsorb non-specifically onto the nanoparticle surface to form a so-called protein corona.[11,12] This protein corona alters nanoparticles' physicochemical properties by providing them with a new, unintentional biological identity.[13] Ultimately, this biological identity determines a nanoparticle's interactions with biological systems, including organs, tissues, cells, and subcellular organelles.[14–17] Therefore, nanoparticle *in vivo* transport and biodistribution are largely controlled by this biological identity rather than the deliberately engineered synthetic nanoparticle characteristics.[4,18]

The fact that a nanoparticle's physicochemical properties can change significantly upon biological exposure imposes major challenges for the engineering of nanomedicines. To advance our current understanding and to develop fundamental concepts needed for the design of more effective nanomedicines, researchers have started to describe and decipher essential mechanisms of how nanoparticles interact and change within biological systems. These studies can be divided into three categories: (i) nanoparticle interactions at organ

and tissue levels; (ii) nanoparticle interactions at cellular and subcellular levels; and (iii) nanoparticle interactions with biomolecules and biochemical parameters. This chapter focuses on the second category, *i.e.*, cellular interactions of nanoparticles.

To maximize clinical benefits of nanomedicines while minimizing side effects, researchers require profound understanding of nanoparticles' cellular interactions.[19] An intriguing example is the engineering of nanoparticles that are able to distinguish between healthy and diseased cells through the use of precise biomolecular recognition strategies.[20,21] To achieve this level of cellular identification and discrimination, a nanoparticle surface can be decorated with specific biomolecular ligands that can recognize and bind to complementary cell surface receptors on targeted cells.[22] The idea behind this concept is that upon recognition nanoparticles may deliver their payloads (*e.g.*, active pharmaceutical ingredients; nucleic acids; and imaging agents) preferentially to diseased cells while leaving healthy cells mostly unaffected. As some types of nanoparticle payloads require delivery to specific intracellular targets for maximizing efficacy, it is critical for researchers to understand and explore nanoparticles' cellular interactions, intracellular trafficking pathways, and corresponding kinetics to ensure targeted delivery.[23–27] In this introductory chapter, the field's understanding of two distinct aspects of nanoparticle-cell interactions are reviewed: (i) nanoparticle cellular uptake mechanisms; and (ii) physicochemical properties underlying cellular uptake and intracellular trafficking.

Cellular Uptake of Nanoparticles

Cellular uptake of nanoparticles involves highly regulated mechanisms with complex biomolecular interactions to overcome the cell plasma membrane. This biological membrane acts as a barrier and separates a cell's interior from the outside environment.

Structural and biomolecular membrane characteristics (*i.e.*, phospholipid-based bilayer membrane littered with proteins and other biomolecules) result in an overall negative charge of the plasma membrane with few cationic domains and selective permeability to ions, (bio)molecules, and nanoparticles. For nanoparticles to achieve cellular entry, they need to overcome the cell plasma membrane. Knowing how nanoparticles enter cells is important, as the underlying uptake pathways can dictate a nanoparticle's function, intracellular fate, and biological response.[28–30]

Multiple different cellular entry routes are available for nanoparticles to cross a cell's plasma membrane during *in vivo* and *in vitro* cell exposure. These routes can be categorized into two general groups: (i) endocytosis-based uptake pathways (Figure 2.1); and (ii) direct cellular entry of nanoparticles (Figure 2.2). The field's understanding of these nanoparticle cell entry pathways is still evolving, as researchers seek to further elucidate fundamental mechanisms of how nanoparticles gain access into cells. This section summarizes the predominant cellular uptake pathways and provide examples on how nanoparticles enter cells.

Endocytosis is an umbrella term used to describe multiple different pathways and mechanisms of how nanoparticles can enter cells. These pathways can be differentiated into five mechanistically distinct classes: (a) clathrin-dependent endocytosis; (b) caveolin-dependent endocytosis; (c) clathrin- and caveolin-independent endocytosis; (d) phagocytosis; and (e) macropinocytosis (Figure 2.1). From a biomolecular perspective, these uptake pathways are highly regulated and mediated by different types of lipids and transport proteins (*e.g.*, lipid rafts, clathrin, dynamin, caveolin, and pattern recognition receptors). Upon endocytosis, nanoparticles are typically confined within intracellular

vesicles, such as endosomes, phagosomes, or macropinosomes, and therefore do not have direct and immediate access to the cytoplasm or cellular organelles (Figure 2.1). Endosomal vesicles also play critical roles in innate and adaptive immunity as they are important sites for toll-like receptors and major histocompatibility complexes.[31,32]

Clathrin-dependent endocytosis is a major pathway for nanoparticle cellular entry and is initiated by the clustering and binding of nanoparticle surface ligands to corresponding cell membrane receptors (Figure 2.1a). A wide variety of cell membrane receptors are shared across many cell types (*e.g.*, transferrin receptors, low-density lipoprotein receptors, epidermal growth factor receptors, and β2 adrenergic receptors) and are involved in clathrin-dependent endocytosis.[33] Clathrin-dependent endocytosis is a complex multistep process that includes: (i) nucleation of cytosolic proteins involved in endocytosis to form a coated pit; (ii) plasma membrane bending and invagination; (iii) scission (*i.e.*, cutting and separation of the neck of invagination from the plasma membrane to form an intracellular vesicle); and (iv) uncoating and recovery of the endocytotic proteins from intracellular vesicle.[34]

The clathrin-dependent endocytosis pathway results in the entrapment of nanoparticles in intracellular vesicles which exhibit sizes of approximately 100-500 nm.[35] Such vesicles are pinched off the membrane with the help of conformational changes from a GTPase enzyme known as dynamin.[36] Upon scission from the membrane, these vesicles transport typically with the help of intracellular actin filaments to endosomes.[37,38] Endosomes are either recycled or eventually fuse with lysosomes leading to enzymatic breakdown of the engulfed vesicular contents and payloads. Therefore, clathrin-dependent endocytosis provides a pathway for nanoparticles to enter a cell's endolysosomal system.

This pathway can be exploited as reported by Benyettou and coworkers. The researchers modified silver nanoparticles to deliver two anticancer therapeutics, doxorubicin and alendronate drugs, to HeLa cancer cells *in vitro*.[39] Upon cellular uptake and lysosomal entrapment, the nanoparticles released their drug payloads in response to the low pH of lysosomes. The anti-cancer activity exhibited by this nano-based drug combination strategy outperformed the efficacy of both drugs when administered individually. Similar strategies have exploited the low pH and enzymatic activity of late stage endosomes/lysosomes to enhance therapeutic responses of intracellular nanoparticles.

Caveolin-dependent endocytosis is another receptor specific nanoparticle internalization pathway that relies on caveolin-coated plasma membrane invaginations termed caveolae (Figure 2.1b).[40,41] Caveolae are flask-shaped vesicles with diameters of 50-100 nm that are stabilized by a caveolin protein based coat.[42] Upon uptake and activation of a complex signaling cascade, caveolin-coated vesicles are transported through the cytoplasm. Typical intracellular destinations of caveolin-based vesicles include the Golgi apparatus and the endoplasmic reticulum.[43] For this reason, caveolin-dependent nanoparticle endocytosis may be a valuable pathway to explore, if researchers seek to achieve intracellular/organelle targeting. Reports have shown that specific nanoparticle surface engineering strategies favor cellular internalization *via* caveolin-dependent endocytosis and typically use nanoparticle surface ligands such as folic acid, albumin, and cholesterol.[19] Work by Xin *el al.* exploited caveolin-dependent endocytosis for efficient cytosolic delivery of microRNAs. These nucleic acids were able to bypass lysosomal entrapment to enter a cell's cytosol for downstream inhibitory effects and silencing of KRAS.[44]

Caveolin-dependent endocytosis has also been reported to result in transcellular transport of caveolae. This transcellular transport is referred to as transcytosis. Recent studies have focused on exploring caveolin-mediated transcytosis in specific types of cells, including endothelial cells.[45–48] As endothelial cells line the inner surface of blood vessels, these transcytosis-based pathways may allow systemically administered nanoparticles to enter endothelial cells *via* caveolae formation and to cross the endothelium by transcytosis. Such a caveolae-based shuttle mechanism could transport nanoparticles and corresponding payloads actively across the endothelial barrier and may benefit the delivery of therapeutic nanoparticles and their cargoes to diseased tissues in the body for improved efficacy.[49,50]

Virus-like particles and other types of nanoparticles can penetrate the cell plasma membrane and enter cells without relying on clathrin- and caveolin-dependent pathways (Figure 2.1c). One suggested route for such clathrin- and caveolin-independent cellular entry involves lipid rafts, which are cholesterol and sphingolipid-rich domains within the plasma membrane that undergo endocytosis when prompted.[51] Lipid raft-mediated endocytosis is a prevalent pathway in immunological scenarios, where lymphocytes internalize and process interleukins.[42] Additionally, specific ligands, such as cholera toxin B and SIV40 bind to lipid rich areas on the cell plasma membrane that undergo lipid raft-mediated endocytosis.[52] Recent studies have pointed towards a lipid raft-mediated endocytosis pathway for the internalization of nanoparticles modified with particular cell-penetrating peptide (CPPs) and nucleic acids.[53,54] It has been suggested that lipid raft, actin cytoskeleton, and cholera toxin subunit B (CTB) mediated endocytosis may be summarized as actin cytoskeleton and cholera toxin subunit B (CTB) pathways.[55]

Phagocytosis is an uptake process exercised by immune cells, including macrophages, dendritic cells, neutrophils, and B cells. The main role of phagocytosis is to clear pathogens, diseased cells, and synthetic/biological materials that are foreign to the body.[56] Nanoparticle phagocytosis is typically initiated by physical binding to phagocyte cell surface receptors (Figure 2.1d). Examples for these cell surface receptors include: Fc receptors, mannose receptors, scavenger receptors, and complement receptors. Armed with these different types of plasma membrane receptors, phagocytes readily recognize and clear nanoparticles with high efficiency from circulation.[57,58] Recognition and clearance of nanoparticles by phagocytes is mediated by opsonization and adsorption of immunoglobulins, complement proteins and/or other serum proteins onto the nanoparticle surface. Following cellular uptake by phagocytes, nanoparticles are trapped within phagosome vesicles that eventually combine with a lysosome to form a structure known as a phagolysosome. Phagolysosomes are able to enzymatically and biochemically digest foreign "non-self" materials, including nanoparticles.[59,60]

Since phagocytosis is a highly efficient clearance mechanism for opsonized nanoparticles, it represents a significant challenge for effective delivery of nanomedicines to different sites *in vivo*. Intravenously administered nanoparticles typically undergo rapid opsonization upon contact with blood.[61,62] These opsonized nanoparticles are then efficiently and rapidly sequestered by macrophages and other phagocytic cells of the mononuclear phagocyte system (MPS).[63] Up to 99% of a systemically administered nanoparticle bolus dose may be sequestered by the MPS system.[61] Moreover, tissue resident macrophages, such as tumor-associated macrophages, have been shown to uptake cancer cell-targeted nanoparticles to a higher extent than malignant cells.[18]

To reduce nanoparticle MPS sequestration, nanoparticle surface modifications have been developed to minimize nanoparticle opsonization.[17] One of these surface engineering strategies uses poly(ethylene) glycol (PEG) to coat nanoparticle surfaces.[64] The PEG surface density and its degree of polymerization may affect nanoparticle opsonization and blood circulation times.[65] PEGylation of model gold nanoparticles is further explored in chapters 3 and 5. A downside of using polymers, such as PEG, is their potential immunogenicity. Repeated administration of PEGylated nanoparticles may result in accelerated nanoparticle blood clearance due to the formation of PEG-specific antibodies [66,67]. Other recent work has shown that nanoparticles displaying "markers of self" surface ligands (*e.g.*, CD47 peptides) can reduce phagocytotic nanoparticle uptake.[68,69] While these strategies are intriguing approaches to control nanoparticle interactions with phagocytes, there is a need to explore new methods to further minimize immunogenicity and to control unintended phagocytosis of administered nanoparticles.

Macropinocytosis represents a class of non-specific cellular uptake mechanisms that are characterized by engulfment of extracellular fluids and solutes through actin-stabilized plasma membrane extensions (Figure 2.1e).[70] Unlike other endocytotic pathways shown in Figure 2.1, macropinocytosis is initiated *via* actin signaling and subsequent membrane ruffling.[42,71] Through this pathway, nanoparticles and other ingested components become trapped within vesicle structures termed macropinosomes. These vesicles may range in size from approximately 0.5 to 1.5 μm.[72] Macropinosomes have been reported to be leaky intracellular vesicles which may allow entrapped nanoparticles to escape before lysosomal degradation.[73,74]

Macropinocytosis is an important mechanism required for the proper protective functions of the immune system. For instance, immature dendritic cells constitutively macropinocytose extracellular contents for antigen presentation as part of their sentinel function.[75] By virtue of this behavior, immature dendritic cells are excellent candidates for vaccine targets. Hirosue and coworkers engineered a polymer-based nanoparticle vaccine linked to peptide antigens that indirectly targeted immature dendritic cells.[76] The nanoparticle formulation enhanced antigen-cross presentation and boosted vaccine efficacy by relying on immature dendritic cells with strong macropinocytotic activity. Likewise, macrophages are also known to engage in macropinocytosis. Recently, Nab-paclitaxel (a nanoparticle albumin-bound formulation of the cancer drug paclitaxel) was shown to be engulfed by macrophages *via* macropinocytosis.[77] Importantly, this form of uptake was reported to shift tumor-associated macrophage (TAMs) polarization towards the M1 immunostimulatory phenotype. *In vivo* application of this strategy in mouse tumor models showed an increase in M1 phenotype-like TAMs upon administration of Nab-paclitaxel compared to control groups. Such nanoparticle platforms may have promising potential to diminish cancer's ability to evade immune surveillance by intratumoral immunomodulation and leveraging specific cellular uptake pathways.

Typically, direct access of nanoparticles to the cytoplasm is not observed upon endocytosis-based cellular entry. However, such direct access can be achieved by alternative nanoparticle delivery pathways as shown in Figure 2.2. Nanoparticles can cross the cell plasma membrane *via* biochemical or physical means to directly enter the cytoplasm. Nanoparticles that are freely dispersed within the cytoplasm can target and engage subcellular organelles and intracellular structures to elicit deliberate biological

responses and medical functions. These routes avoid endosomal entrapment and energy-dependent transport mechanisms to gain access to the cell's cytoplasm (Figure 2.2a).[78]

Computational models have simulated and elucidated aspects of nanoparticle diffusion through lipid bilayer membranes.[79–82] Based on these studies, researchers have been able to translate *in silico* information and modeling to *in vitro* findings. For example, polymeric nanoparticles with the same surface chemistry and various morphology exhibited different transport paths across the plasma membrane.[83] It was found that both rod and worm-like nanoparticles diffused through the cell plasma membrane more efficiently than spherical micelles.

In that vein, other researchers used semiconductor quantum dot nanoparticles with a size of approximately 8 nm and zwitterionic surface chemistry, and observed direct translocation in red blood cells.[84] This quantum dot internalization process did not lead to visible pore formation within the red blood cell plasma membrane. Surface-enhanced infrared absorption spectroscopy data suggested that zwitterionic quantum dots entered by means of lipid bilayer softening resulting in subsequent flexible membrane confirmations.

Other research relying on zwitterionic ligands used gold nanoparticles with diameters of 2-4 nm to observe direct diffusion through the plasma membrane of HeLa cells *in vitro*. Interestingly, slightly larger zwitterionic gold nanoparticles with diameters of approximately 6 nm were internalized *via* caveolin/lipid-raft endocytosis, indicating a nanoparticle size dependent effect on cellular internalization.[85]

In a different sutdy, Jewell *et al.* sought to understand how the direct entry of monolayer nanoparticles was impacted by cargo size and structure.[86] First, the researchers coated ~5 nm gold nanoparticles with monolayers of a 1:1 mixture of 11-mercapto-1-

undecanesulphonate and 1-octanethiol such that different nanoscale arrangements formed "striped" domains on the nanoparticle surface.[87] Next, double stranded and single stranded DNA of varying lengths were chosen as model payloads that were then affixed to the monolayer gold nanoparticles through thiol linkages. After inhibiting endocytosis, the DNA-striped monolayer nanoparticles were internalized by murine melanoma cells. Ultimately, these nanoparticles were seen to deliver various lengths and types of DNA payloads to cells independent of endocytosis due to their unique surface chemistry.

Another important strategy for direct nanoparticle translocation across the cell plasma membrane relies on the use of cell penetrating peptides (CPPs) as nanoparticle surface ligands. These CPPs ligands are short amino acid sequences (typically less than 40 amino acids) that can traverse cell membranes.[88] Much research has been conducted in recent years to elucidate the specific mechanisms for CPP-mediated nanoparticle entry into cells. Our understanding of these mechanisms is still evolving, but studies have suggested multiple different pathways to be involved in cellular uptake, including endocytosis and direct translocation. Factors that seem to regulate the relevance of these pathways include: (i) the type of nanoparticle that CPPs are attached to; and (ii) local concentrations of lipids and peptides in the plasma membrane.[89–91] Frequently used examples of CPPs for biomedical applications are: TAT, penatratin, arginine-rich sequences, TP10, pVEC, and MPG.[91–94] Upon endocytosis of CPP-decorated nanoparticles, endosomal escape may be achieved *via* CPP-mediated vesicle membrane disruption.[95,96] This provides a pathway for endocytosed nanoparticles to enter a cell's cytoplasm. Endosomal escape of endocytosed nanoparticles is a prerequisite for downstream intracellular targeting of subcellular organelles and other compartments. These examples highlight design parameters that affect

nanoparticle uptake and intracellular trafficking which will be discussed in more detail in the following section.

Lipid fusion is the process by which some types of lipid bilayer coated fuse with a cell's plasma membrane (Figure 2.2b).[97] After membrane fusion, the encapsulated contents within the nanoparticle, for example, proteins, nucleotides, and small molecule payloads, are delivered directly to the cytoplasm.[98,99] One group of researchers exploited this pathway for efficient gene knockdown *via* cytoplasmic siRNA delivery.[100] Lipid fusion was accomplished with silicon nanoparticles that were shrouded in a fusogenic liposomal shell. With their construct, Kim *et al*. saw decreased levels of a proinflammatory marker in macrophages (IRF5) which enabled phagocytic clearance of *Staphylococcus aureus* pneumonia and enhanced survival in mice subjected to infection. Recent work probing the lipid-lipid fusion interface has demonstrated that nanoparticles with an amphiphilic organic shell and gold core exhibit a size-dependent lipid fusion behavior.[101] In the event of endocytosis, Yuba and coworkers delivered immunotherapies to dendritic cells with a liposome antigen delivery system that fused with endosomal membranes for an effective therapy in a murine ovalbumin (OVA)-expressing lymphoma model.[102]

Electroporation strategies physically disrupt a cell's plasma membrane upon application of electrical pulses (Figure 2.2c). This leads to the formation of transient pores within the membrane through which nanoparticles can transport through from the extracellular space into the cytoplasm.[103] Membrane pore formation generated *via* electroporation can be controlled through fine tuning the electrical pulse (*e.g.*, pulse duration and voltage) such that the newly formed pores do not impact cell viability.[104] Electroporation has been shown to successfully deliver nanoparticles with applications in

imaging and genetic engineering. Kim *et al.* used mesoporous silica-coated hollow manganese oxide nanoparticles to label and track adipose derived mesenchymal stem cells.[105] Upon electroporation with an electrical pulse of ~100 V followed by nanoparticle cell entry, the mesenchymal stem cells displayed enhanced contrast in magnetic resonance imaging (MRI) *in vitro* and *in vivo* over the course of 14 days. In a different study, lipid-based nanoparticles efficiently delivered siRNA *via* electroporation (electrical pulse of ~200 V) that silenced PD-L1 and PD-L2 expression on human-monocyte derived dendritic cells.[106] To further demonstrate clinical utility of this method, researchers also reported successful delivery of target antigen mRNA that boosted antigen-specific $CD8^+$ T-cell responses *ex vivo*. Studies have shown that electroporation and subsequent transfection can be performed in a high-throughput manner.[107,108] Such technologies may facilitate experiments that require direct cytoplasmic delivery, including gene regulation studies, to help overcome intracellular delivery barriers, although *in vivo* translation of electroporation remains unfeasible.

Lastly, microinjection strategies are characterized by directly injecting small volumes of nanoparticles into the cytoplasm with the help of specialized microinjectors.[109] With this strategy, cellular and intracellular membrane barriers can be overcome for immediate access of injected nanoparticles to the cytoplasm. As individual cells need to be injected with nanoparticles on a cell-per-cell basis, the throughput of this technique is limited. However, despite being a technically demanding, laborious, and difficult to execute method, microinjection can be a valuable tool to gain nanotoxicology information by excluding extracellular alteration of nanoparticle physicochemical properties (*e.g.,* protein corona formation). This was seen by the microinjection of inorganic nanoparticles

into HeLa cancer cells which was used to evaluate the counteractive measures cells develop in the presence of foreign nanomaterials.[110]

Microinjection was also used as a tool to investigate ligand density effects on organelle targeting, such as targeting of a cell's nucleus with peptide-modified quantum dots.[111] Additional work employing microinjection uncovered that nanoparticle-mediated gene delivery can be inhibited through lysosomal capturing triggered by autophagy.[112]

This overview of major nanoparticle cell uptake pathways demonstrates that there are many different routes available for nanoparticles to enter cells. To further emphasize this point, Table 2.1 shows how model gold nanoparticles can enter cells through different pathways. The relative contribution of these pathways depends on many material designs such as surface chemistry, size, shape, and other biological factors as well. These data highlight the complexity of nano-bio interactions that are involved in cellular entry of nanoparticles. The relative importance and contribution of individual uptake pathways is not always clear and requires supplemental investigation for many studies. The next section of this introductory chapter explores nanoparticle design parameters and how these characteristics affect cellular entry of nanoparticles.

Mediating nanoparticle cell uptake through material design

As shown in Table 2.1 for gold nanoparticles, cells internalize nanoparticles through multiple different uptake routes even when the nanomaterial is kept constant. These findings suggest that material and biological factors play important roles in nanoparticle uptake pathways (Table 2.1).

A study by Saha and coworkers showed that healthy and diseased cells uptake nanoparticles using different pathways. In more detail, healthy mammary epithelium cells

and cancerous HeLa cells were each incubated with four different 10-nm cationic monolayer-modified gold nanoparticles.[113] The researchers demonstrated that HeLa cancer cells and healthy epithelium cells employed different mechanisms for nanoparticle internalization despite identical surface modifications of nanoparticles. Altogether, these data suggest that cancer cells may employ various pathways to internalize nanoparticles in contrast to non-malignant cells. This could potentially provide an avenue for improved nanoparticle-based cancer diagnostics and therapies. Additionally, recent reports indicate that female and male cells from various tissues exhibit different nanoparticle internalization patterns.[114]

To better study and understand which specific pathway is crucial for nanoparticle uptake by cancer cells, researchers can reduce the activity of key proteins involved in endocytosis *via* siRNAs.[115] For example, cancerous HeLa cells with reduced expression of the caveolin-1 protein experienced a ~30% reduction in PEGylated nanoparticle uptake. Meanwhile knocking down CDC42 (a key protein for macropinocytosis) reduced the uptake of PEGylated nanoparticles almost by half.[115]

Considering such complex differences in cellular uptake among various types of cells, nanomedicine researchers focus on manipulating nanoparticles to exhibit deliberate nanoparticle-cell interactions by mediating physicochemical parameters. This section focuses on how nanoparticle physicochemical properties, including size, shape, and surface modifications, affect cellular uptake and intracellular trafficking.

Nanoparticle Morphology and Cellular Uptake

Nanoparticle physicochemical properties, such as size and shape, impact nanoparticle diffusivity, surface-to-cell membrane contact area, membrane adhesion, and strain energy required for membrane movement.[116] In other words, nanoparticle

morphology is a critical physicochemical property that determine the extent and efficiency of initial nanoparticle-cell interactions.

A study by Chithrani *et al.* reported in 2006 that 50-nm spherical gold nanoparticles exhibit highest uptake when exposed to HeLa cells in tissue culture compared to other nanoparticle sizes of 14 nm and 74 nm.[117] While the importance of nanoparticle size for cellular interaction and uptake is well established [118], reported data suggest that there are many more parameters and variables at play that affect cellular entry, such as cell phenotype, nanoparticle rate of sedimentation, nanoparticle density, and protein corona formation.[15,119–122]

To illustrate how multifaceted and complex nanoparticle-cell interactions are, we highlight a study by Albanese and Chan that compared nanoparticle cell uptake of monodispersed gold nanoparticles with hydrodynamic diameters of 30 nm to 170 nm to corresponding nanoparticle aggregates.[123] The researchers reported that HeLa and A549 cells internalized monodisperse gold nanoparticles more than the corresponding gold nanoparticle aggregates. On the other hand, a different cancer cell line (MDA-MB-435 human melanoma cells) showed an increase in nanoparticle accumulation for gold nanoparticle aggregates compared to individual monodisperse nanoparticles. This underlines the importance of cell type on nanoparticle-cell interactions and exemplifies the central role of nanoparticle size and aggregation state on cellular uptake.[123] Motivated by these findings, chapter 3 is dedicated to quantifying gold nanoparticle aggregation as a function of surface chemistry at the single aggregate level.[124]

In addition to inorganic-based nanoparticles, organic nanoparticles have also been reported to exhibit size-dependent cellular uptake patterns. In one study, different sized

polymeric nanoparticles with diameters of 50 nm to 250 nm were used to probe size-dependent trends of internalization pathways in human retinal pigment epithelium (ARPE-19) cells.[125] Suen and coworkers found that smaller nanoparticles (50 nm and 120 nm in size) were internalized through clathrin- and caveolae-dependent endocytosis, while larger nanoparticles (250 nm) were internalized only *via* caveolae-mediated endocytosis. Similarly, distinct uptake patterns were observed when block copolymer nanoparticles were synthesized with different sizes using different hydrophilic chain lengths.[126] These nanoparticles formed micelles (34 nm and 49 nm in diameter) and vesicles (99 nm and 150 nm in diameter) which were incubated with WiDr (human colon carcinoma cells). Upon flow cytometry analysis, smaller micelles were internalized more quickly than the larger vesicles, but after 6 hours the cells had internalized almost equal amounts of nanoparticles for both sizes. These studies suggest that nanoparticle size not only affects the underlying uptake kinetics but also the efficiency of nanoparticle delivery. Similar studies provided the rationale for chapter 4 where the development of an economical high throughput technique is discussed in detail to track individual nanoparticle transformations in response to chemical reactions.

Besides nanoparticle size, both the shape anisotropy and orientation of the nanoparticle relative to the plasma membrane impact cellular uptake.[79,127] For example, when comparing cellular uptake between rod-like shapes and spheres, it was found by Arnida and coworkers that 50-nm spherical gold nanoparticles had higher accumulation inside human prostate cancer cells compared to gold nanorods.[128] Similarly, macropinocytosis-mediated cellular uptake of nanoparticles has been shown to exhibit a geometry-dependent correlation in both cancer and phagocytic cells.

In another study, HeLa cells and A549 cancer cells ingested rod-shaped mesoporous silica nanoparticles with varying aspect ratios *via* macropinocytosis.[129] The rod-like nanoparticles with aspect ratios between 2.1-2.5 were engulfed in higher quantities than the ones with aspect ratios between 1.5-1.7 and 4-4.5. These data suggest that cells possess mechanosensitive processes that sense slight variations in nanoparticle aspect ratio and adapt their cellular uptake response accordingly. Further data on geometry-dependent macropinocytosis concluded that primary human blood phagocytes internalize rod-like stabilized gold nanoparticles (15 nm x 50 nm) more rapidly than stabilized spherical gold nanoparticles with diameters of either 15 nm or 50 nm.[130] Nevertheless, uptake could be decreased through nanoparticle surface functionalization with 3-kDa poly(ethylene oxide). This highlights the importance of how nanoparticle surface modifications can be used as a strategy to avoid phagocytic clearance *in vivo*.

Work by Li and coworkers showed that various shapes of polymeric nanoparticles decorated with mannose surface ligands exhibited different uptake patterns and inflammatory responses in macrophages.[131] The researchers compared the uptake of mannose-decorated spherical and cylindrical micelles using RAW 264.7 macrophages. Spherical micelles were internalized through clathrin- and caveolin-dependent endocytosis and lead to a higher accumulation inside the macrophages when compared to cylindrical micelles. Interestingly, longer cylindrical micelles (215 nm x 47 nm) induced a strong inflammatory response that was linked to an increase in interleukin 6 expression.[131] As pathogenic invaders exhibit many characteristic shapes and sizes on their surfaces, immune cells may be able to recognize a microorganism's conserved topographic features.[132]

In a recent study, Wang *et al.* reported that nanofeatures can participate in the activation of the innate immune system.[133] The group modified inorganic TiO_2 microparticles to bear "nanospikes" which exerted mechanical forces on innate immune cells during phagocytosis. In the presence of either monophosphorylate lipid A or lipopolysaccharide only spiky particles activated K^+ efflux and inflammasomes while the non-spiky rough particles did not. Moreover, the spiky particles along with activation of TLR4 augmented dendritic cell maturation which boosted T-cell and humoral immune responses. These promising effects enhanced the efficacy of dendritic cell-based cancer immunotherapy and influenza vaccination *in vivo*. Ultimately, this work indicates that physical activation of immune responses through material design and particle shape could potentially be translated to other micro/nanomaterials in the future for designing more potent immunotherapies and vaccines. However, more work needs to be done to fully explore the translational potential of these results to different materials, such as polymer-based micro/nanomaterials.

The examples discussed in this section highlight how nanoparticle morphology affect cellular interactions. It is anticipated that nanoparticle physicochemical properties will have significant impact on triggering and controlling robust immune responses in the future. As the field of nano-immunoengineering continues to grow, advanced understanding of how physicochemical properties of nanoparticles affect immune responses may lead to more potent immunotherapies and novel nanoparticle vaccine strategies.

Nanoparticle Surface Charge and Cellular Uptake

Researchers can engineer synthetic nanoparticles with positive, negative, zwitterionic or neutral surface charge. The nanoparticle surface charge is typically

estimated by the so-called zeta potential. The zeta potential corresponds to the electrokinetic potential of a colloidal nanoparticle dispersion.[134] Experimentally, the zeta potential of nanomedicines is quantified by electrophoretic mobility measurements of colloidal dispersions in aqueous media or buffer. Therefore, a nanoparticle's zeta potential indicates the overall nanoparticle surface charge in the corresponding colloidal dispersion.

The nanoparticle zeta potential is dynamic and may change significantly in response to environmental conditions. For example, Walkey *et al.* showed in a systematic study how protein corona formation affects nanoparticle surface charge and zeta potential.[16] A library of gold and silver nanoparticles with positive, negative, and neutral surface charge were exposed to serum samples *in vitro*. Interestingly, regardless of the initial nanoparticle surface charge, the zeta potential was reported to be in the range from approximately -5 mV to -10 mV after incubation with serum proteins. These findings suggest that the formation of a serum protein corona around the nanoparticle surface leads to a "normalization" of the corresponding zeta potential. Normalization means that the adsorption of serum proteins often results in a slight overall negative surface charge of nanoparticles, regardless of their initial surface modification.[16,135–141]

Since the cell plasma membrane is typically overall negatively charged, the nanoparticle zeta potential affects the likelihood of adhesion to the plasma membrane, cellular uptake, and downstream cytotoxicity. Based on Coulomb's law, cationic nanoparticles are more likely to be electrostatically attracted by the negatively charged plasma membrane resulting in increased accumulation inside cells.[85,142–145] However, several reports have demonstrated that nanoparticles with negative surface charges can also efficiently overcome the anionic cell plasma membrane and accumulate within cells.[146–150]

This suggests that nanoparticle surface charge is an important design parameter when engineering nanoparticles for efficient cellular interaction, but the processes involved in nanoparticle cellular uptake are more complicated and go well beyond the simplified notion of Coulomb-driven electrostatic interactions.[15,151]

While both cationic and anionic nanoparticles have been reported to enter mammalian cells, their downstream biological effects may be significantly different. As reported by Lin and coworkers, an increase in cationic charge density on nanoparticle surfaces not only promotes cellular uptake, but also elicits cytotoxic effects.[152] These adverse cytotoxic effects can be attributed to plasma membrane depolarization caused by cationic nanoparticles. This in turn can increase Ca^{2+} influx to inhibit cell proliferation.[153] Furthermore, intracellular accumulation of positively charged nanoparticles in lysosomes may result in lysosome damage, generation of reactive oxygen species (ROS), and damage of cell organelles, such as mitochondria, ultimately leading to apoptosis and cell death.[154]

Other reports have demonstrated that gold nanorods displaying amine-terminated poly(ethylene oxide) promoted anti-inflammatory properties in macrophages, whereas carboxy-terminated poly(ethylene oxide) gold nanorods yielded pro-inflammatory markers.[130] *In vivo* studies have also corroborated the impact of nanoparticle surface charges on biodistribution and toxicity. Mice that were intravenously injected with positively charged lipid nanoparticles experienced severe adverse effects, including hepatotoxicity, weight loss, and a pro-inflammatory response, compared to mice injected with neutral or negatively charged nanoparticles.[155] Further studies are needed to better understand the mechanisms behind these observations and how nanoparticle surface charge affects nano-bio interactions at organ, cellular, and biomolecular levels. To probe how

surface charge affects nanoparticle-cell interactions, our group developed a facile synthesis strategy to reliably produce positively charged peptide-modified gold nanoparticles.[156] We investigated how these cationic gold nanoparticles interacted with triple negative murine breast cancer cells and human umbilical vein endothelial cells *in vitro*. Our results showed that our model positively charged gold nanoparticles had 3 orders of magnitude more uptake compared to neutral gold nanoparticles. Building upon these findings, chapter 5 investigates how these peptide-modified gold nanoparticles interacted with B cells at the single cell level.

When both positive and negative charges are present on a nanoparticle's surface, the resulting surface chemistry can be regarded as a zwitterionic surface modification.[157] The generation of a zwitterionic surface modification can be advantageous and result in significant reduction of protein corona formation. This may alter and affect nanoparticle biodistribution and cellular interactions in comparison to cationic and/or anionic nanoparticle designs.[158]

In summary, surface charge should be considered carefully when designing nanoparticles for biological and medical applications. We emphasize that nanoparticle surface charges are dynamic and may change over time in response to environmental and biological conditions. These changes may affect specific nano-bio interactions resulting in unintentional biological responses of nanoparticles and therapeutic outcomes of nanomedicines.

Nanoparticle Targeting Ligands and Cellular Uptake

The surface of nanoparticles can be modified with so-called targeting ligands to enable specific interaction and binding of nanoparticles to cell surface receptors. This is a

prominent concept in nanomedicine and referred to as "active targeting".[159–162] Targeting ligands that are commonly used in nanomedicine include peptides, small molecules, proteins, antibodies, antibody fragments, and nucleic acids. Table 2.2 summarizes examples of nanoparticle targeting ligands that have been reported for *in vitro* and/or *in vivo* applications in nanomedicine. Many of these ligands recognize and bind cell surface receptors that are overexpressed on malignant cells. The rationale for this surface modification strategy is that targeting ligands may increase a nanoparticle's cellular interaction, activate downstream cell signaling pathways leading to a desired biological response (*e.g.*, cell apoptosis), or enhance cellular uptake of nanoparticles to deliver therapeutic and diagnostic payloads into the cell. To engineer active targeting nanoparticles, a number of design parameters need to be taken into account and optimized for efficient targeting. These parameters include target ligand length, target ligand density, hydrophobicity, and avidity.[163–170]

Nanoparticles that do not exhibit specific surface targeting ligands are referred to as "passive targeting" nanoparticles. Passive targeting indicates that the interactions between nanoparticles and cells are non-specific. These non-specific interactions may facilitate nanoparticle uptake in healthy as well as diseased cells. In contrast to active targeting nanoparticles that have not advanced beyond clinical trial stages yet, passive targeting nanoparticles have been approved by the U.S. Food and Drug Administration (FDA) as cancer nanotherapeutics.[171]

A challenge for passive and active targeting nanoparticles is that their deliberately designed surface chemistry may change upon exposure to a biological environment. For example, nanoparticles that are decorated with targeting ligands may undergo a change in

their targeting abilities upon introduction into a biological milieu, such as the blood stream. One of the reasons for this is the formation of a nanoparticle protein corona due to serum protein surface adsorption. This protein corona formation changes the deliberately designed synthetic identity of nanoparticles to a biological identity which often has significant impact on nanoparticle-cell interactions.[11,172,173] Parameters that can affect formation and composition of nanoparticle protein coronae include incubation temperature, use of different protein/serum sources, human *vs.* animal plasma/serum, local temperature variations for plasmonic nanoparticles, which may facilitate the formation of unique, personalized protein coronae around nanoparticles.[174] In human plasma, nanoparticles are exposed to high amounts of protein, which increases their size and may enhance their subsequent internalization by immune cells.[175] Targeting ligands may be buried within the protein corona resulting in reduction or complete loss of specific targeting capabilities. In a study by Salvati *et al*, 50-nm silicon oxide nanoparticles were coated with transferrin, a popular protein-based ligand for active cancer cell targeting.[176] However, the ability of transferrin moieties to maintain targeting specificity diminished under physiological conditions. This was largely attributed to a shielding effect around the transferrin ligands as a result of nanoparticle protein corona formation.

To address the potential surface shielding effect of the protein corona, Tonigold and coworkers developed a pre-adsorption process to link targeting antibodies (anti-CD63) onto polystyrene carboxy-functionalized nanoparticles.[177] Antibodies that simply adsorbed to the nanoparticle surface were compared with the antibodies that were coupled *via* 1-Ethyl-3-(3-Dimethylaminopropyl) Carbodiimide and N-hydroxysuccinimide (EDC-NHS) chemistry. Regardless of how the antibodies adhered to the nanoparticle surface, the

constructs had maintained similar properties in the absence of serum and were able to bind to CD63 antigen expressed on monocyte-derived dendritic cells. However, under physiological conditions (*e.g.,* in plasma or serum), an impaired targeting efficiency correlated to the method of antibody attachment. The authors observed that in 100% emersion of serum or plasma, the nanoparticles that are covalently bound to the antibodies lost their targeting abilities, whereas the pre-absorbed antibody-nanoparticles were still able to efficiently target the CD63 antigen on monocyte-derived dendritic cells.

A different approach to mitigate the negative impact of the protein corona on nanoparticle cell targeting was reported by Dai *et al.* in 2014 and is referred to as poly(ethylene glycol) (PEG) backfilling.[64] Authors decorated gold nanoparticle surfaces with PEG molecules of different molecular weights and covalently conjugated these PEG molecules with trastuzumab, a monoclonal ErbB2 (HER2) targeting antibody. They concluded that the PEG chain length used to conjugate the targeting antibody affects nanoparticle targeting efficiency. In more detail, the PEG molecules used for surface backfilling need to be of lower molecular weight than the PEG molecules used to conjugate the targeting antibody. This backfilling strategy enabled specific targeting of nanoparticle surface conjugated trastuzumab antibodies to ErbB2 cell surface receptors. In addition, Dai *et al*. demonstrated that surface backfilling with low molecular weight PEG reduced the formation of a serum protein corona. Overall, this design improved targeting specificity of nanoparticles to ErbB2 expressing cells in serum-rich environments in comparison to other surface modification strategies.

While the benefit of active targeting has been demonstrated for *in vitro* tissue culture studies through a large body of publications, it is less clear if the presence of active

targeting ligands on nanoparticle surfaces can result in increased specific cellular interaction *in vivo*. For example, a study by Chan and coworkers published in 2018 demonstrated that there was no statistically significant difference in nanoparticle-cell interaction for 55-nm gold nanoparticles with and without ErbB2 targeting trastuzumab antibody surface modification in preclinical mouse models of human ovarian cancer SKOV-3 xenograft tumors.[18] In addition, this study also demonstrated that intratumoral nanoparticles irrespective of surface modification are more likely to interact with tumor associated macrophages (TAMs) rather than targeted malignant cells. This finding is in line with reports by Weissleder and coworkers, which identified TAMs as major intratumoral biological barriers for targeted nanoparticle delivery to cancer cells.[178–180]

Decorating nanoparticle surfaces with targeting ligands that are specific against cell surface receptors may increase cellular interactions. However, surface modification strategies need to be chosen judiciously and optimized for intended applications. Precise targeting of cell populations *in vitro* and *in vivo* requires that nanoparticle surface modifications can maintain their deliberately designed functions in dynamically changing biological environments. These findings open opportunities for researchers to develop nanoparticle surface designs that can address the above-mentioned challenges to improve specific delivery and interactions between nanoparticles and targeted cells. In this section, a number of nanoparticle physicochemical properties that are critical for enhanced nanoparticle-cell interactions were summarized. Nanoparticle size, shape, surface charge, surface ligands, and ligand density are important design criteria that researchers need to consider when engineering nanomedicines for studying cellular uptake.

Nanoparticle Modifications for Intracellular Delivery

After cellular internalization, nanoparticles undergo transport and trafficking to reach their intracellular destinations. If nanoparticle cellular uptake occurs *via* endocytic pathways, nanoparticles are confined within a membrane-lined vesicle, such as an endosome (Figure 2.1). These vesicles transport throughout the cell in complex trafficking patterns. Currently used methods for probing the intracellular trafficking of nanoparticles include optical- and electron-based microscopy techniques, such as super resolution fluorescence microscopy, confocal laser scanning microscopy, dark-field microscopy, transmission electron microscopy, scanning electron microscopy, atomic force microscopy, flow cytometry, mass cytometry, photoacoustic microscopy, surface-enhanced Raman scattering, laser-ablation inductively-coupled plasma mass spectrometry, and correlative microscopy.[185–187] The later chapters in this dissertation focus on electron microscopy, inductively-coupled plasma mass spectrometry and confocal scanning laser microscopy.

Due to the complexity of nanoparticle intracellular trafficking patterns, it is challenging to paint a complete picture of all intracellular events and processes that take place once nanoparticles enter cells. Hence, in figure 2.3 a simplified overview of intracellular nanoparticle transport processes is presented. Similar to nanoparticle cellular uptake, nanoparticle intracellular trafficking is also dependent upon cell type and a nanoparticle's physicochemical properties, including size, shape, and surface chemistry.

To briefly review the dynamics of intracellular nanoparticle transport, we highlight findings reported by Al-Hajaj and coworkers. Using *in vitro* tissue culture experiments, the researchers compared differences of nanoparticle trafficking in liver cancer cells and non-malignant kidney cells.[184] In this study, researchers modified the surfaces of semiconductor

(quantum dots) nanoparticles made from CdSe@CdZnS with sizes of 8-10 nm and four different surface chemistries: (i) mercaptopropionic acid, (ii) dihydrolipoic acid, (iii) L-cysteine, or (iv) cysteamine ligands. The overall size of quantum dots was not affected by these different surface chemistries. Interestingly, the highest cellular uptake in both liver and kidney cell lines was reported for quantum dots modified with cysteamine, potentially due to their overall cationic surface charge. However, after cellular uptake of these nanoparticles, p-glycoprotein transporters were shown to excrete between 60-70% of the initially accumulated quantum dots with cysteamine surface chemistry in both cell lines over the course of 6 hours. These data demonstrate that intracellular nanoparticles may be excreted from cells over time due to dynamic intracellular transport and trafficking processes. While these data have been obtained in tissue culture experiments, this information is important as liver and kidney cells are involved in degradation, metabolism, and elimination of administered nanoparticles, which are prime aspects of *in vivo* nanotoxicology.[185–188]

Unless interrupted, cells process endocytosed nanoparticles in similar ways as internalized biomolecules (*e.g.,* proteins, carbohydrates, nucleic acids, and lipids). Upon endocytosis, nanoparticles are typically entrapped in vesicular structures, such as endosomes (Figures 2.3a and 2.3b). Endosomes can undergo a variety of processes, such as vesicle aging, that can be briefly characterized by early- to late-stage vesicle transformation (Figures 2.3b-2.3d). These different stages of intracellular vesicle development are typically accompanied by changes in intra-vesicle pH (Figure 2.3ci). Eventually, the acidified endosome may fuse with lysosomal compartments for enzymatic digestion and degradation of vesicle contents (Figure 2.3d). Examples for these pathways

are the formation of phagolysosomes and macropinosomes.[33,189] Endosomes can also be recycled and/or processed at the perinuclear region (Figure 2.3ciii). Viruses often exploit trafficking patterns that lead to the perinuclear region for pathogenesis.[190,191] Endosomes can also be sent to the plasma membrane for downstream exocytosis (Figure 2.3civ). Pridgen *et al*. capitalized on this pathway for the transepithelial transport of nanoparticles.[192] Nanoparticles bearing Fc regions of the IgG antibody were shown to target the neonatal Fc receptor which resulted in enhanced absorption efficiency after oral administration *in vivo*.

More often than not, endosomal entrapment represents a major detriment to nanomedicine efforts. Once confined to intracellular vesicles, nanoparticles may be subjected to lysosomal degradation which can inhibit their intended biological and therapeutic functions. In consequence, some types of nanoparticles need to overcome the endosomal barrier before accessing the cell's cytoplasm, intracellular organelles, and compartments (Figures 2.3e-2.3f). Physicochemical nanoparticle properties, such as surface charge and surface ligand display, can be engineered to facilitate endosomal escape with enhanced efficiency (Figures 2.3cii).[193] Table 2.3 summarizes nanoparticle surface modifications that favor organelle targeting upon endosomal escape.

Therapeutic and diagnostic success of nanomedicines often hinges on efficient intracellular transport of nanoparticles. While organelle targeting is a powerful approach to increase the potency of nanomedicines, further studies to improve endosomal escape and delivery of nanoparticles and their payloads to intracellular targets are needed. Successful organelle targeting *in vivo* proves to be a formidable challenge. First, nanoparticles need to overcome a multitude of biological and physical barriers to reach targeted cell populations

in the body. Second, once nanoparticles reach targeted cells, several cellular barriers need to be overcome before nanoparticles can interact with intracellular proteins and organelles. In addition to these hurdles, nanoparticles and/or their payloads need to accumulate in targeted cellular structures at sufficiently high concentrations to elicit the desired biological and/or therapeutic effect.

In this section, we provided a concise overview of the complex intracellular environment that nanoparticles may experience. Effective strategies to elicit biological and/or therapeutic responses often require that nanoparticles can overcome intracellular barriers efficiently and interact with desired intracellular targets. This requires efficient intracellular transport and trafficking of nanoparticles. In summary, efficient intracellular delivery of nanoparticles and nanoparticle payloads is challenging with multiple different barriers that nanoparticles need to overcome to effectively interact with intracellular targets. Researchers need to consider additional intracellular challenges that are related to nanoparticle trafficking and pharmacokinetics, including rates of nanoparticle endocytosis, endosomal escape, intracellular transport, metabolism/degradation, and exocytosis. Further studies of intracellular nanoparticle PK/PD using *in vivo* systems may provide findings that go beyond tissue culture-based *in vitro* studies to better assess the translational potential of nanomedicines.

Discussion

Nanoparticles can be engineered from inorganic and organic materials with unique physical, chemical, and biological properties for different biomedical applications. Once administered into the body, nanoparticles interact with different tissues and cells. While specific and efficient delivery of nanoparticles to diseased tissue sites and cells in the body is challenging, nanomedicine still offers the potential to transform diagnostic and

therapeutic strategies as demonstrated by the success of the COVID-19 lipid nanoparticle vaccines. With the resurging interest in lipid nanoparticle delivery, more quantitative studies that explore and assess essential mechanisms of nano-bio interactions in great detail are still needed to provide solutions for overcoming biological and physical barriers.

This chapter provided an overview of fundamental interactions between nanoparticles and cells. Such understanding is important for researchers to design nanoparticles for enhanced cellular uptake and intracellular transport with defined pharmacokinetics and therapeutic/biological performance. Since interactions between nanoparticles and cells are complex and multiparametric, including parameters such as nanoparticle size, shape, surface charge, and biological characteristics of cells, better fundamental understanding of these essential nano-bio interactions is required at the single nanoparticle and single cell level. With the development of new analytical techniques in recent years, the dynamics of single nanoparticle transformations in biological settings can be elucidated. These approaches include single-particle and single cell elemental analysis as well as new methods for three-dimensional optical microscopy of intact organs and tissues with subcellular resolution.[194–201] These new analytical methods provide researchers with powerful tools to study the fate of administered nanomedicines *in vitro* and *in vivo* with cellular and subcellular precision. Systematic quantitative studies at the single nanoparticle and single cell level that quantify mechanisms of interactions between individual nanoparticles and cellular systems offer new guiding principles for the design of more effective nanomedicines with the goal to overcome delivery barriers for better control the transport of nanoparticles in the body.

Chapter 3: Assessing Nanoparticle Colloidal Stability with Single Particle Inductively Coupled Plasma Mass Spectrometry[2]

Abstract

Biological interactions, toxicity, and environmental fate of engineered nanoparticles are affected by colloidal stability and aggregation. To assess nanoparticle aggregation, analytical methods are needed that allow quantification of individual nanoparticle aggregates. However, most techniques for nanoparticle aggregation analysis are limited to ensemble measurements or require harsh sample preparation that may introduce artifacts. An ideal method would analyze aggregate size in situ with single nanoparticle resolution. Here, we established and validated single particle inductively coupled plasma mass spectrometry (SP-ICP-MS) as an unbiased high throughout analytical technique to quantify nanoparticle size distributions and aggregation in situ. We induced nanoparticle aggregation by exposure to physiologically relevant saline conditions and applied SP-ICP-MS to quantify aggregate size and aggregation kinetics at the individual aggregate level. In situ SP-ICP-MS analysis revealed rational surface engineering principles for preparation of colloidally stable nanoparticles. Our quantitative SP-ICP-MS technique is a platform technology to evaluate aggregation characteristics of various types of surface engineered nanoparticles under physiologically relevant conditions. Potential widespread applications of this method may include the study of nanoparticle aggregation in environmental samples and the preparation of colloidally stable nanoparticle formulations for bioanalytical assays and nanomedicine.

[2]Published as: Donahue ND, Francek ER, Kiyotake EA, Thomas EE, Yang W, Wang L, Detamore MS, Wilhelm S. Assessing nanoparticle colloidal stability with single-particle inductively coupled plasma mass spectrometry (SP-ICP-MS) *Analytical and Bioanalytical Chemistry* 2020 412 5205-5216. https://doi.org/10.1007/s00216-020-02783-6

Introduction

In contrast to their corresponding bulk materials, nanoparticles exhibit unique size-dependent optical, electric, magnetic, and biological properties that are exploited in various applications, including catalysis, display technology, energy generation and storage, and medicine.[2,202,203] Therefore, the effective application of nanoparticles requires precise and accurate quantification of nanoparticle size, size distributions, colloidal stability and aggregation. Aggregation is a common nanoparticle transformation that changes nanoparticle size and surface chemistry leading to alterations in cellular uptake, biodistribution, pharmacokinetics, toxicity, and overall fate.[204–207] Conventional analytical methods for measuring nanoparticle size and aggregation are often performed in batch mode and only provide population-averaged results.

For a given nanoparticle sample, such averaged results can mask population heterogeneities (e.g., aggregation) that ultimately may affect the performance of nanoparticles in their respective applications. Examples of such batch analytical methods for nanoparticle size characterization include spectroscopy techniques, light scattering, differential centrifugal sedimentation, field flow fractionation, atomic force microscopy, and size exclusion chromatography.[208–210] While batch analytical methods are well-established and widespread, they are unable to measure individual nanoparticle and aggregate sizes. This limitation results in an inability to accurately assess the true size heterogeneity for a given nanoparticle population. An ideal analytical method should rapidly and precisely provide size information at the individual particle level. Several single particle resolution techniques are available and include electron microscopy methods, nanoparticle tracking analysis, and single particle spectroscopy.[211–213] However,

in electron microscopy colloidal nanoparticle samples are typically analyzed after drying on support grids and complex image analysis algorithms are required to pinpoint clusters of nanoparticles over multiple fields of view,[214] Meanwhile, light scattering techniques, such as nanoparticle tracking analysis, could potentially overestimate aggregate size by reporting hydrodynamic diameters and be skewed by changes in a dispersion's viscosity, refractive index, and/or temperature.[215]

One salient example of single particle analytical techniques that is able to detect and quantify individual nanoparticles *via* elemental analysis is single particle inductively coupled plasma mass spectrometry (SP-ICP-MS).[216,217] In a SP-ICP-MS experiment, one nanoparticle at a time is introduced into the ICP-MS instrument *via* a microfluidic system with controlled flow rate. Each individual nanoparticle is then atomized and ionized by an argon plasma, and the resulting ion plume is analyzed by a quadrupole-based mass analyzer to quantify the corresponding nanoparticle mass. This SP-ICP-MS technique has been applied to quantify a variety of nanoparticle types and is being applied to quantify element concentrations inside intact individual cells.[194,217,218]

Our motivation for studying nanoparticle aggregation *via* SP-ICP-MS is driven by the importance of evaluating nanoparticle colloidal stability and how this stability can be affected by nanoparticle surface engineering strategies.[12,219–221] Understanding nanoparticle stability with single particle resolution is critical for determining the environmental and biological impact of nanoparticles.[222–224] Aggregation and colloidal stability are therefore important parameters affecting nanoparticle physicochemical properties that need to be characterized when studying interactions between nanoparticles and ecological and biological systems, including cells, tissues, and organs.[123,225,226]

In the current study, we analyzed the size distributions of various in-house synthesized gold nanoparticles with conventional batch and single particle resolution techniques. We demonstrated and validated SP-ICP-MS to precisely quantify engineered nanoparticles consisting of multiple sizes and shapes. Additionally, we applied SP-ICP-MS to quantify engineered nanoparticle aggregation characteristics with single aggregate resolution *in situ*. These nanoparticle aggregates are clusters of multiple individual nanoparticles and detected by the ICP-MS as a single event exhibiting a mass that corresponds to a single nanoparticle mass multiplied by the number of nanoparticles per aggregate.[227] This approach requires nanoparticles with narrow size distribution, and hence narrow mass distribution, which is typically the case for engineered nanoparticles. Our single particle analytical approach provides a quantitative tool for probing nanoparticle surface chemistries and corresponding colloidal stability *in situ* under physiologically relevant conditions. This reported SP-ICP-MS procedure could be widely applied to study nanoparticle environmental fate and to probe and establish surface engineering approaches leading to nanoparticle formulations with controlled colloidal stability to use in bioanalytical assays and nanomedicine.

Materials and Methods

For all synthesis steps, glass Erlenmeyer flasks were cleaned before synthesis with Aqua Regia, i.e. 3:1 (v/v) mixture of hydrochloric acid (SigmaAldrich, ACS reagent, 37%, St. Louis, MO) and nitric acid (Sigma-Aldrich, ACS reagent, 70%) to remove potential contaminants. AuNPs with a nominal size of 16 nm were synthesized according to a previously published protocol.[219] To synthesize 30- and 55-nm quasi spherical AuNPs, a seed-mediated synthesis protocol developed by Perrault and Chan was adopted using 16-nm AuNPs as seed nanoparticles.[228] Gold nanorods were synthesized according to previously published reports. [229,230]

The ZetaSizer Nano ZS (Malvern, UK) was used to measure the z-average hydrodynamic diameter of nanoparticles based on Dynamic Light Scattering (DLS) and zeta potential based on electrophoretic mobility. Transmission Electron Micrographs (TEM) were taken by a 200-kV field emission JEOL2010F (JEOL, USA) equipped with a Direct Electron DE-12 camera (Direct Electron, USA). ImageJ (NIH) software was used to determine the diameters of AuNPs in the TEM images. Agilent Cary 5000 UV-Vis-NIR spectrophotometer (Agilent, USA) was used to measure the visible spectrum of AuNPs from 400 nm - 700 nm in 1.5-mL PMMA cuvettes.

Surface modifications of AuNPs were performed using HS(PEG)5kDa-methoxy (Laysan Bio, USA) and using a previously reported procedure.[219] The successful conjugation of different PEG densities on the AuNPs was confirmed by DLS, zeta potential, and gel electrophoresis.

All SP-ICP-MS measurements were performed using the NexION 2000 B ICP-MS (PerkinElmer, USA) fitted with a commercially available High Efficiency Sample Introduction System pictured in Figure 3.2. The ICP-MS instrument was operated using the conditions summarized in Table 3.2. The SP-ICP-MS particle transport efficiency was determined using commercially available polystyrene microparticles (~3 μm in diameter) doped with Lu175 (Fluidigm, USA). A transport efficiency of 58.5 ± 3.9% was determined (Table 3.3). With the same instrument setup, Merrifield et al. demonstrated that transport efficiencies of polystyrene microparticles and standard AuNPs do not statistically differ.[231] Typical transport efficiencies for single particle/cell ICP-MS systems can range between 9-70%.[232–234] Our system's transport efficiency is on the higher end of the range reported in the literature due to the high efficiency nebulizer and spray chamber which minimize sample loss and ensure robust sample introduction to the ICP-MS. With a high transport efficiency, micro-scale dwell time, no settling time, low nebulizer gas flow, the instrument was optimized to quantify transient ion signals from nanoparticles. Next, the mass detector was set to only analyze ^{197}Au signal and the ICP-MS was calibrated with dissolved gold ion standards made from a stock solution consisting of 1,000 μg/mL (Au) ICP Single-Component Standard in 2% HCl (High Purity Standards 100021-2-100, USA) via serial dilution. With our dissolved Au calibration curve, the measured pulse intensity from an ion plume was then used to back-calculate nanoparticle mass as described by Pace et al. [235]

To accurately analyze nanoparticle mass distributions with SP-ICP-MS, nanoparticle solutions were diluted to 1.66 x 10^{-16} M in nanopure water 18.2 MΩ cm from the initial concentration determined by UV-Vis. This concentration of 1.66 x 10^{-16} M was chosen as this is approximately 1 x 10^{5} particles mL^{-1}, which can virtually eliminate the

probability of overlapping events from multiple nanoparticles during a single dwell time of 50 µs based on the Poisson distribution outlined by Pace et al. [236]

For making a 1:1 mixture of nanoparticles, 50 µL of 1.66 x 10^{-15} M of each nanoparticle size were added to 900 µL of nanopure water 18.2 MΩ cm and analyzed immediately on SP-ICP-MS. For gold nanorod analysis, 2 µL of the solution containing citrate-coated nanorods was diluted into 10 mL of nanopure water 18.2 MΩ cm. This diluted mixture of nanorods was diluted again by taking 1 µL and adding that to 999 µL of nanopure water and immediately analyzed on SP-ICP-MS. For measuring T0 of aggregation on SP-ICP-MS, the concentrated nanoparticle and salt mixture were diluted to 1.66 x 10^{-16} M and analyzed immediately after salt addition. For the later time point, the concentrated nanoparticles remained in salt and after 1 hour had elapsed, then mixture was diluted to 1.66 x 10^{-16} M and analyzed immediately. For all nanoparticle samples, the mass detector was set to analyze ^{197}Au signal.

All nanoparticle events were collected within 60 seconds. Syngistix software (PerkinElmer, USA) was used in SP-ICP-MS mode to acquire single particle elemental analysis data. Statistical analyses were performed with GraphPad Prism (GraphPad, USA)

Results and Discussion

We synthesized three different batches of quasi spherical citrate-coated colloidal gold nanoparticles (AuNPs) in house with nominal diameters of: (i) 16 nm, (ii) 30 nm, and (iii) 55 nm, and characterized these AuNPs with three commonly used analytical techniques: (i) dynamic light scattering (DLS); (ii) UV-Vis spectrophotometry (UV-Vis); and (iii) transmission electron microscopy (TEM). Two of these methods, i.e. DLS and UV-Vis, are batch methods that analyze AuNP physicochemical and photophysical

properties for an entire ensemble of nanoparticles, while TEM allows AuNP characterization at the single nanoparticle level.

The nanoparticle hydrodynamic diameters obtained by DLS measurements are summarized in Figure 3.1A. It is worth noting that hydrodynamic diameters take into account nanoparticle surface bound ions and molecules as well as the layer of hydration around a nanoparticle surface. Hence, the synthesized 16-nm, 30-nm, and 55-nm citrate-coated AuNPs exhibited average hydrodynamic diameters of 18.0 ± 1.0 nm, 37.6 ± 2.6 nm, and 54.4 ± 3.8 nm, respectively. Our DLS results demonstrate that the nanoparticle size distributions are narrow (<10% size deviation) with polydispersity indices (PDI) below 0.1 indicating colloidal stability without detectable nanoparticle aggregation.

Next, we used UV-Vis spectrophotometry to measure the nanoparticle size dependent light absorption spectra of our in-house synthesized colloidal AuNPs. Observed spectra are a result of AuNPs light absorption due to the surface plasmon resonance (SPR) effect and light scattering due to the particle nature of the AuNPs.[237] Since nanoparticles with diameters below 100 nm were used, light absorption rather than light scattering is the dominant factor accounting for the light extinction spectra seen in Figure 3.1B.[198] Compared to smaller AuNPs, larger sized AuNPs exhibited a red-shifted light absorption peak with λ_{max} 518 nm for 16-nm AuNPs, λ_{max} 526 nm for 30-nm AuNPs, and λ_{max} 532 nm for 55-nm AuNPs (Figure 3.1B). This observation can be explained by nanoparticle size-dependent changes in SPR frequencies.[238] The obtained UV-Vis spectra corroborated our DLS experiments to further confirm the colloidal stability and narrow size distribution of our synthesized AuNPs. Despite the limitations associated with ensemble light-based

techniques, DLS and UV-Vis provide rapid quantitative and qualitative information on nanoparticle size and colloidal stability.

Since DLS and UV-Vis spectrophotometry methods do not provide single particle resolution, we used TEM to measure single nanoparticles (Figure 3.1C). Quantitative image analysis of TEM micrographs revealed average sizes of AuNPs of 16.3 ± 1.2 nm (16-nm sample), 30.6 ± 5.4 nm (30-nm sample), and 52.2 ± 9.1 nm (55-nm sample). The corresponding size distribution histograms are shown in Figure 3.1D-3.1F. The TEM characterization studies confirmed our results obtained by DLS and UV-Vis methods and demonstrated that our in-house synthesized AuNPs were monodisperse without detectable nanoparticle aggregation. Although TEM provides direct images of AuNPs, it requires harsh conditions (i.e. sample drying on TEM grids, high vacuum conditions) and post-image analysis, which prevent high throughput in situ characterization.

Next, we performed SP-ICP-MS on all three citrate-coated AuNPs colloidal samples using a PerkinElmer NexION 2000 ICP-MS. The SP-ICP-MS method is an elemental analysis technique that allows mass quantification of individual nanoparticles, one nanoparticle at a time. To prepare the AuNPs samples for SP-ICP-MS analysis, we quantified the corresponding nanoparticle molar concentrations of AuNPs stock dispersions by UV-Vis spectrophotometry using the nanoparticle size dependent molar decadic extinction coefficients listed in Table 3.1. We then diluted the AuNPs to a nanoparticle concentration of 1.66×10^{-16} M (1.0×10^{5} AuNPs mL^{-1}) in nanopure water. To analyze individual AuNPs, the ICP-MS was set up and calibrated according to the parameters listed in Figure 3.2 and Table 3.2.

Individual AuNPs were introduced into the ICP-MS by a commercially available microfluidics autosampler connected to a high efficiency nebulizer and spray chamber for efficient aerosol generation of the aqueous nanoparticle dispersions (Figure 3.2). Individual AuNPs then pass through the argon plasma and become atomized and ionized, resulting in a transient gold ion plume that is analyzed by a quadrupole mass analyzer and detected with ultrafast microsecond dwell times, which enables precise quantification of nanoparticle size.[239] The intensities of the detected gold ion plumes correspond to individual AuNP masses that were then displayed as mass histograms (Figure 3.3A-3.3C).

Based on our TEM imaging results (Figure 3.1C), we approximated the shape of our in-house synthesized AuNPs to be spherical. This approximation allowed us to estimate the diameter of an individual AuNP by converting the reported SP-ICP-MS AuNP mass according to Equation 3.1:

Equation 3.1

$$d\ [nm] = \sqrt[3]{\frac{6 \cdot MassNP}{\pi \cdot \rho}}$$

with MassNP as the reported SP-ICP-MS mass in [g] unit of a single individual AuNP, and ρ is the density of gold (19.3 g/cm3). The obtained SP-ICP-MS based AuNP size distribution histograms are shown in Figure 3.3D-3.3F.

The SP-ICP-MS method accurately determined the size distributions of the three different colloidal AuNP batches that we synthesized in house at a rate of ≥ 200 particles/minute. Interestingly, with the SP-ICP-MS technique, we were able to quantify AuNPs with masses as small as 20 ag (corresponding to spherical nanoparticles with ~13 nm in diameter) which closely resembles the limits of detection mentioned in other SP-

ICP-MS reports.[240] When compared with conventional nanoparticle characterization techniques, such as DLS, UV-Vis, and TEM (Figure 3.3), SP-ICP-MS yielded overall comparable results. Table 3.4 provides a succinct head-to-head comparison of the results obtained from DLS, TEM and SP-ICP-MS. All three methods provide similar nanoparticle mean diameters and standard deviations of analyzed AuNPs batches (Table 3.4). These results validated SP-ICP-MS as a high throughput, accurate, in situ quantitative analytical method to determine the size distribution of individual AuNPs.

After successfully determining the mass and size distributions of AuNPs with different sizes, we used SP-ICP-MS to differentiate between nanoparticles of different sizes in mixtures. We prepared a 1:1 mixture of in-house synthesized spherical citrate-coated 30-nm and 55-nm AuNPs. We analyzed this 1:1 nanoparticle mixture with SP-ICP-MS and observed two clearly separated nanoparticle populations in the SP-ICP-MS mass distribution histogram as well as the corresponding calculated size distribution histogram (Figure 3.4). From the SP-ICP-MS analysis results of the 1:1 AuNPs mixture, the 30-nm and 55-nm AuNPs mean diameters were calculated to be 30.8 nm and 57.9 nm, respectively. In addition, SP-ICP-MS also accurately determined that the AuNPs mixture was indeed made from a 1:1 mixture of 30-nm and 55-nm AuNPs with 268 particles determined as 30-nm AuNPs and 234 particles determined as 55-nm AuNPs. This result indicated AuNPs recovery of ~90% from the original 1:1 mixture. We also confirmed that the mean diameters and standard deviations of the AuNPs measured in the mixture were not different from the AuNPs measurement results reported in Table 3.4 for pure, unmixed AuNPs samples. As shown in Figure 3.5, the nanoparticle diameters calculated from the SP-ICP-MS analysis of the 1:1 AuNPs mixture were not statistically significant different

($p<0.01$) compared to the pure, unmixed AuNPs. Our results confirmed that SP-ICP-MS can simultaneously and precisely measure AuNPs mass distributions of multiple nanoparticle sub-populations for a given nanoparticle mixture and points to the possibility of analyzing complex nanoparticle mixtures with single particle resolution.

Next, we wondered whether SP-ICP-MS could be used for the quantitative analysis of non-spherical nanoparticles that exhibit an aspect ratio. As a model nanoparticle system, we synthesized citrate-capped gold nanorods in house. We analyzed the size distribution of the synthesized gold nanorods with TEM and quantified length and width of individual gold nanorods from corresponding micrographs with ImageJ. The average lengths and widths of the gold nanorods were 63.5 nm and 9.0 nm, respectively (Figure 3.6). Based on the TEM micrographs, we assumed a cylindrical geometry of the gold nanorods and estimated the average nanoparticle mass to be ~313 ag. We then used SP-ICP-MS to characterize individual gold nanorods from diluted aqueous dispersions. Our SP-ICP-MS analysis revealed an average nanoparticle mass of ~319 ag (Figure 3.6), which is in close agreement with the estimated mass after TEM analysis (Figure 3.6). Our results corroborate previous reports that SP-ICP-MS is not limited to nanoparticles with spherical shape, but can additionally be used to accurately determine mass, and hence size distributions, of non-spherical and anisotropic nanoparticles.[241,242]

Since SP-ICP-MS was able to determine nanoparticle mass in mixtures and of different sizes, we determined whether we could quantify aggregation of our colloidal nanoparticles with single particle (i.e. single aggregate) resolution using SP-ICP-MS. We defined aggregation as an irreversible process that results in nanoparticle clusters of two or more individual nanoparticles. To generate aggregates of AuNPs, we exposed citrate-

coated 16-nm AuNPs model nanoparticles with narrow size distribution to physiologically relevant saline concentrations (~150 mM NaCl). Upon exposure to high ionic strength conditions, electrostatically stabilized citrate-coated AuNPs experience substantial screening of their overall negative surface charges.[243] The process of ionic strength mediated surface charge screening causes colloidal citrate coated AuNPs to irreversibly aggregate.[244] Aggregation of AuNPs results in a visible color change from red to blue. Using UV-Vis spectrophotometry, we monitored aggregation kinetics of citrate-coated 16-nm AuNPs exposed to 150-mM NaCl over a time period of 60 minutes (Figure 3.8). The observed increase in AuNP light absorption around 600 nm over time (~110% change after 60 minutes, Figure 3.8) is due to surface plasmon resonance (SPR) frequency changes as a result of AuNP aggregation. Additional DLS measurements confirmed the observed nanoparticle aggregation behavior with increases in hydrodynamic diameter and PDI and verified our UV-Vis spectrophotometry results (Table 3.5). We further performed TEM to visualize the aggregation of citrate coated 16-nm AuNPs upon addition of 150-mM NaCl (Figure 3.9).

After establishing the aggregation characteristics and kinetics of citrate-coated 16-nm AuNPs with UV-Vis spectrophotometry and DLS batch methods, we quantified the corresponding aggregation states with SP-ICP-MS at the individual aggregate level. First, AuNP aggregates were formed under the same conditions used for UV-Vis and DLS analysis. Immediately prior to SP-ICP-MS analysis, AuNPs in the NaCl solution were diluted with nanopure water to obtain an AuNP concentration 1.66×10^{-16} M which mitigated potential matrix effects from NaCl and maintained the integrity of AuNP aggregates. It is unlikely that the attractive van der Waals forces that bind the nanoparticles

in an aggregated state would be compromised to make nanoparticle aggregates fall apart.[245] Given that the mean mass of our monodisperse 16-nm AuNPs was determined to be 50 ag (Figure 3.3), we assumed that 100 ag corresponded to an aggregate consisting of 2 AuNPs, 150 ag corresponded to an aggregate consisting of 3 nanoparticles, and so forth, according to Equation 3.2. It is important to note that in Figure 3.3, few particles had a mass above 100 ag. In our study, the probability of detecting an individual nanoparticle with a true mass above 100 ag rather than an aggregate was only ~2% due to the narrow size distribution of our engineered nanoparticles.

Equation 3.2 $$N_{NPs\ per\ Aggregate} = \frac{m_{Aggregate}}{m_{NP}}$$

With $N_{NPs\ per\ Aggregate}$ as number of nanoparticles (NPs) per aggregate, $m_{Aggregate}$ as the detected mass for an event, i.e. aggregate, ≥100 ag, and m_{NP} as the mean mass of an individual 16-nm AuNP (i.e. 50 ag).

As shown in the mass histogram in Figure 3.7A, citrate-coated 16-nm AuNPs exhibited a slight increase in mass upon exposure to saline solution in as little as 5 minutes. (Note: 5 minutes after salt exposure was the earliest time point that we could physically acquire due to the time required for AuNPs sample dilution and introduction into the ICP-MS). However, after 60 minutes, multiple events with masses ≥200 ag were detected. These higher masses indicated the generation and presence of AuNPs aggregates. From the mass histograms, we quantified the number of nanoparticles per aggregate at the two time points (Figure 3.7B). Interestingly, the number of aggregates consisting of 2 and 3 nanoparticles were the most frequent aggregates after 60 minutes. It appeared that the generation of AuNPs aggregates occurred within 5 minutes, as the number of single

individual particles slightly decreased by ~ 6% while the masses corresponding to 2 and 3 nanoparticles per aggregate slightly increased by ~6% (Figure 3.7C). This increase in number of aggregates was clearly seen after 60 minutes where the number of detected individual single AuNPs decreased by 70% when compared to AuNPs in the initial measurement without saline. The number of events with masses ≥100 ag was calculated to be ~73% out of the total events detected (Figure 3.7C). Within this group, more than half (52%) were comprised of 2-5 AuNPs per aggregate while only ~21% of the detected aggregates consisted of 5 or more AuNPs (Figure 3.7D). This result indicated that the formation of larger aggregates could depend on the initial generation kinetics and frequency of smaller AuNPs aggregates. Our data also suggest that salt induced AuNP aggregation is irreversible since the frequency of individual nanoparticle masses decreased over time.

Our SP-ICP-MS experiments confirmed the findings from DLS and UV-Vis spectrophotometry and showed the rapid progression of salt-induced AuNPs aggregation. However, in stark contrast to ensemble methods and other single particle techniques, we could determine individual masses of AuNP aggregates in situ without the need for harsh sample preparation conditions as is required for electron microscopy. When compared to light scattering techniques, SP-ICP-MS results were not skewed by larger nanoparticles and did not account for the extra layer of hydration, as we only measured the gold atoms/ions of the AuNPs. In summary, SP-ICP-MS allowed high throughput quantitative analysis (200+ aggregates per minute) making it an attractive tool to monitor and study nanoparticle aggregation characteristics.

To mitigate nanoparticle aggregation, we hypothesized that the PEGylation of colloidal AuNPs, i.e. the decoration of nanoparticle surfaces with polyethylene glycol (PEG) polymers, could be adopted for our study as a robust and efficient nanoparticle surface engineering technique to control and reduce AuNPs aggregation upon exposure to physiological saline concentrations. PEG polymers are typically used to provide steric stabilization of nanoparticles to physically reduce nanoparticle aggregation.[246–248] Nanoparticles can be engineered to exhibit different PEG surface densities that affect nanoparticle colloidal stability and functionality upon environmental and biological exposure.[249,250] We prepared 16-nm AuNPs modified with various surface densities of thiol-PEG5kDa-methoxy and summarized our AuNPs physicochemical characterization results (Figure 3.10). Increasing PEG densities led to increases in hydrodynamic diameter, zeta potential, and decreases in nanoparticle mobility in gel electrophoresis. Our results demonstrated that the AuNPs with varying degrees of PEG were monodisperse without any detectable aggregation (i.e. PDI <0.1, Figure 3.10). We then tested if the amount of PEG added on the AuNPs surface played a role in colloidal stability and aggregation. We want to emphasize that the amount of PEG added to AuNPs does not necessarily represent the amount of PEG attached to AuNPs.

We exposed the PEGylated AuNPs to 150-mM NaCl and measured the corresponding UV-Vis absorption spectra over the course of 60 minutes. In stark contrast to citrate coated 16-nm AuNPs (Figure 3.8C), we observed only a small increase (~10%) in light absorption at 600 nm over a time period of 60 minutes for PEGylated AuNPs (0.010 PEG per nm^2 of nanoparticle surface area corresponding to ~6 PEG polymers per AuNP) upon exposure to 150-mM NaCl (Figure 3.8B, 3.8C). This observation was confirmed by

DLS measurements that showed a small increase in hydrodynamic diameter of ~3 nm and a more pronounced 4-fold increase in PDI indicative of slight nanoparticle aggregation (Table 3.5). It is worth noting that under the same experimental conditions, AuNPs with higher PEG surface densities (i.e. 0.025 PEG/nm^2 and 0.050 PEG/nm^2) were less affected by aggregation as demonstrated by UV-Vis spectrophotometry (data not shown) and DLS measurements (Table 3.5). Based on our collective UV-Vis spectrophotometry and DLS results, we concluded that PEGylation of 16-nm AuNPs, even at PEG surface densities of only 6-30 PEG molecules per AuNP, effectively reduced nanoparticle aggregation upon exposure to physiologically relevant NaCl concentrations (Table 3.5, Figure 3.8).

To obtain a deeper understanding of the reduced aggregation behavior seen with DLS and UV-Vis spectrophotometry, we used SP-ICP-MS to obtain mass distributions of the PEGylated AuNPs exposed to saline solution (Figure 3.11). The masses of the PEGylated AuNPs after 5 minutes primarily exhibited ^{197}Au masses below 100 ag (Figure 3.11A). Interestingly, AuNPs with the lowest PEG surface density (0.010 PEG/nm^2) exhibited a small (~10%) decrease in the number of single nanoparticles similar to the AuNPs with 0 PEG/nm^2 (Figure 3.11C). On the other hand, AuNPs with higher densities of PEG, such as 0.025PEG/nm^2, only experienced a ~5% decrease in observed single particles. Meanwhile, AuNPs with the highest density of PEG (0.050 PEG/nm^2) had only ~ 2% of all detected events above 100 ag similar to what was observed for AuNPs in Figure 3.3 without exposure to salt. These findings corroborated our observations that the onset nanoparticle aggregation occurred within 5 minutes after saline exposure. In addition, surface modifications like PEG can be used to physically hinder the rapid onset of salt-induced aggregation in a PEG surface density-dependent fashion. For a more concise

comparison, the mean masses and standard deviations of the PEGylated AuNPs in saline solutions are shown in Figure 3.12.

As the effects of aggregation were time dependent as shown in Figures 3.7, 3.10, and Table 3.5, we analyzed the PEGylated AuNPs in saline solution, after 60 minutes via SP-ICP-MS. Upon analysis, we observed that 98% of all detected events for the PEGylated AuNPs had masses below 150 ag (Figure 3.11B). Remarkably, AuNPs modified with 0.050 PEG/nm^2 had 2-fold less events above 150 ag when compared to the AuNPs with 0.010 and 0.025 PEG/nm^2. This finding indicated that the formation of larger aggregates (3 or more nanoparticles) was virtually completely inhibited by PEG. After 60 minutes in saline, more than 90% of all detected events were detected as individual nanoparticles for each PEG surface density compared to the 27% of individual nanoparticles observed for citrate-coated AuNPs. AuNPs modified with 0.010 and 0.025 PEG/nm^2 had similar amounts of masses >100 ag (~6% out of all detected events). On the other hand, for AuNPs modified with 0.050 PEG/nm^2, 97% of detected events were below a mass of 100 ag indicating negligible (if any) aggregation in the saline solution after 60 minutes. For AuNPs with 0.050 PEG/nm^2, the number of events with masses > 100 ag were nearly identical to the baseline of observed events with true masses > 100 ag at both t5min and t60min indicating that high PEG surface densities preserved the monodisperse character and colloidal stability of AuNPs in saline conditions over time. Our SP-ICP-MS results for the PEGylated AuNPs were corroborated by DLS measurements in Table 3.5 that showed lower PEG surface (0.010 and 0.025 PEG/nm^2) had PDI >0.1, while only the AuNPs with 0.050 PEG/nm^2 had a PDI <0.1 after 60 minutes in saline solution. Our SP-ICP-MS findings confirmed that, based on our testing conditions, the addition of as little as 0.010

PEG/nm^2 was sufficient for reducing the time dependent effects of aggregation for monodisperse 16-nm model AuNPs. Moreover, our results indicated that higher PEG surface densities better passivate AuNPs to reduce nanoparticle aggregation likely due to improved steric stabilization by neutral PEG polymers.

Conclusion

We established and validated SP-ICP-MS as a viable quantitative high throughput analytical technique that enables the rapid and precise measurement of engineered nanomaterials with single particle resolution. Our SP-ICP-MS results were corroborated by both conventional ensemble nanoparticle characterization methods, such as UV-Vis spectrophotometry and DLS, as well as the single particle data from TEM. With our SP-ICP-MS approach, we were able to precisely detect and quantify the heterogeneity of AuNPs with high throughput (200+ nanoparticles/minute) and recovery (>90%). Additionally, we used SP-ICP-MS to accurately quantify AuNPs with various shapes and different nanoparticle size populations from nanoparticle mixtures. Furthermore, we applied SP-ICP-MS as an *in situ* technique to quantify the colloidal stability of AuNPs in physiologically relevant saline conditions and showed the mass distributions of AuNP aggregates with single aggregate resolution. Through rational surface engineering strategies, we demonstrated that increasing nanoparticle PEG surface densities could efficiently attenuate irreversible nanoparticle aggregation through steric stabilization. The work presented in this study has potential far reaching implications for researchers who seek to understand how engineered nanoparticles aggregate over time in biologically relevant environments and how surface modifications affect nanoparticle colloidal stability.

Acknowledgements

Authors acknowledge assistance and fruitful discussions by Drs. S. Foster, R. Merrifield, C. Stephan, A. Madden P. Larson, R. Forester, H. Kirit, and PerkinElmer. This work was supported in part by an NSF MRI grant (Award # 1828234), the IBEST/OUHSC Seed Grant for Interdisciplinary Research, and the Oklahoma Tobacco Settlement Endowment Trust awarded to the University of Oklahoma - Stephenson Cancer Center. The content is solely the responsibility of the authors and does not necessarily represent the official views of the Oklahoma Tobacco Settlement Endowment Trust.

Chapter 4: Quantifying Chemical Composition and Reaction Kinetics of Individual Colloidally Dispersed Nanoparticles[3]

Abstract

To control a nanoparticle's chemical composition and thus function, researchers require readily-accessible and economical characterization methods that provide quantitative in situ analysis of individual nanoparticles with high throughput. Here, we established dual analyte single particle inductively coupled plasma quadrupole mass spectrometry to quantify the chemical composition and reaction kinetics of individual colloidally dispersed nanoparticles. We determined individual bimetallic nanoparticle mass and chemical composition changes during two different chemical reactions: (i) nanoparticle etching, and (ii) element deposition on nanoparticles at a rate of 300+ nanoparticles/minute. Our results revealed the heterogeneity of chemical reactions at the single nanoparticle level. This proof-of-concept study serves as a framework to quantitatively understand the dynamic changes of physicochemical properties that individual nanoparticles undergo during chemical reactions using a commonly-available mass spectrometer. Such methods will broadly empower and inform the synthesis and development of safer, more effective, and more efficient nanotechnologies that use nanoparticles with defined functions.

[3]Under review: Donahue ND, Kanapilly S, Stephan C, Marlin MC, Francek ER, Haddad M, Guthridge J, Wilhelm S. *Quantifying Chemical Composition and Reaction Kinetics of Individual Colloidally Dispersed Nanoparticles*

Introduction

Chemical composition governs nanoparticles' optical, magnetic, catalytic, and toxicological characteristics.[202,251–253] For effective nanotechnology applications, cost-effective techniques that provide quantitative chemical composition data with single nanoparticle resolution at a fast rate *in stiu* are essential. To that end, single particle inductively coupled plasma mass spectrometry (SP-ICP-MS) offers high throughput *in situ* mass quantification of intact colloidally dispersed individual nanoparticles.[124,216,254] Due to their affordability and cost-efficiency, a majority of ICP-MS instruments rely on quadrupole mass analyzers.[255] However, in single particle mode, these quadrupole systems permit the analysis of only one analyte (or isotope) per nanoparticle.[256] While quadrupole SP-ICP-MS systems have obtained qualitative detection of multielement nanoparticle solutions, these approaches have not been efficient in simultaneously detecting two isotopes thus lacking data on individual nanoparticle mass, chemical composition, and chemical kinetics.[257–259] Other ICPMS systems, like ICP-time-of-flight MS (ICP-TOF-MS) are unparralled in their abilities to efficiently analyze in a multielement fashion both engineered and naturally occuring nanoparticles.[260–262] Unfortunately, ICP-TOF-MS instruments can be cost-prohibitive and are less accessible compared to quadrupole ICPMS.

Other elemental analysis techniques like energy-dispersive X-ray spectroscopy (EDS) combined with scanning transmission electron microscopy (STEM) provides valuable elemental mapping of individual nanoparticles.[263] However, EDS/STEM analyses require dried samples and are limited by the number of nanoparticles within a field of view,

which restricts sample size.[264] Although gaining traction, *in situ* electron microscopy analysis of nanoparticle composition remains technically challenging and may expose nanoparticle samples to free radicals from the high energy electron beam, which may complicate monitoring chemical reactions at the single nanoparticle level.[265,266]

Consequently, we established *in situ* dual analyte quadrupole SP-ICP-MS as a readily-accessible analytical tool for quantifying the chemical composition and reaction kinetics of individual colloidally dispersed nanoparticles. For this study, we used a commonly-available quadrupole-based ICP-MS instrument to simultaneously quantify the mass of two different isotopes in individual nanoparticles. We validated the quadrupole mass analyzer's capabilities with ICP-MS-TOF and EDS/STEM. We show the feasibility of dual analyte quadrupole SP-ICP-MS to quantify chemical transformations and reaction kinetics at the individual nanoparticle level *in situ* for hundreds of bimetallic nanoparticles within seconds.

Methods and Materials

All SP-ICP-MS measurements were performed using the NexION 2000 B ICP-MS (PerkinElmer, USA) fitted with a high-efficiency sample introduction system using the conditions outlined in Table 4.1. Syngistix(V.2.5) and PerkinElmer's Nano application (V.3.0) were used to conduct all SP-ICP-MS measurements. To perform dual analyte SP-ICP-MS we systematically changed three instrument parameters: 1) collision cell parameters 2) quadrupole mass analyzer settling time, and 3) detector dwell time.

First, we sought to increase the overall duration time of the transient nanoparticle ion cloud by using collision cell technology fitted with ammonia (NH_3(g)) gas (Figure 4.1). Previous reports showed that NH_3(g) molecules in an ICP-MS collision cell could interact

with transient nanoparticle ion clouds, extending their overall duration.[267] To ensure that the transient nanoparticle ion cloud remained intact and continuous during the interaction with NH_3(g), we applied an axial field technology voltage to generate a supplementary electric potential that shortened the ion passage time through the collision cell.[268] Changing the NH_3(g) gas flow rates and the axial field technology voltages stretched the corresponding transient nanoparticle ion cloud up to several milliseconds. (Figures 4.2 and 4.3) Peak shapes were acquired in the Nano application based on a minimum of 150 nanoparticles within 30 second scan time. The use of the collision cell did not impact the transport efficiency of our SP-ICP-MS measurements (Table 4.2). Without the use of the collision cell, transient ion clouds cannot be paired; however, when the collision cell is used transient ion clouds are stretched and efficiently paired (Figure 4.4).

Our next step was to optimize the quadrupole mass analyzer to enable efficient m/z switching between two analytes of interest within a single transient nanoparticle ion cloud for isotope quantification. To accomplish this goal, we manually adjusted the quadrupole mass analyzer settling time for a given pair of isotopes. The settling time is a specific amount of time that a quadrupole mass analyzer needs to equilibrate after switching from one m/z value to another m/z value for optimal isotope filtering.[217] By systematically changing the quadrupole settling time, we ensured that two different isotopes from an individual transient nanoparticle ion cloud reached the detector for accurate quantification.

To select a quadrupole mass analyzer settling time, in-house synthesized gold and silver nanoparticles of known diameters and concentrations were used as calibration standards (see Table 4.5 & Figure 4.14, Figures 4.6 and 4.8 for characterization). These particle standards were introduced into the ICP-MS with optimized collision reaction cell

conditions while the quadrupole settling time was manually changed in the Nano application. A quadrupole settling time was used to analyze unknown samples once the known diameters for the gold and silver nanoparticle standards were simultaneously obtained. For example, a quadrupole settling time of 300 μs was used since that settling time accurately provided the mass and size distributions of previously characterized citrate-coated 65 nm gold nanoparticles and citrate-coated 70 nm silver nanoparticles. Meanwhile, a quadrupole settling time of 400 μs was found to accurately provide the correct mass and size for known citrate-coated 100 nm gold and silver nanoparticles.

As the third instrument parameter, we selected 50μs as the detector dwell times to accurately quantify two isotopes concurrently from a single transient nanoparticle ion cloud. Microsecond detector dwell times enable accurate and precise quantification of nanoparticle mass.[269] Moreover, based on Poisson statistics, microsecond detector dwell times minimize the probability of incorrectly measuring overlapping nanoparticle ion clouds for a given molar concentration of colloidal nanoparticles.[270]

Optimized dual analyte quadrupole SP-ICP-MS conditions are listed in Table 4.3. Before SP-ICP-MS analysis, all nanoparticle samples were diluted in nanopure water 18.2 MΩ cm from the initial stock solution and analyzed immediately. Given our transport efficiency (40%), flow rate (0.01 mL min-1), detector dwell time (50 μs), and low particle concentrations, we ensured that both analyte signals obtained were from discrete individual nanoparticles as opposed to multiple overlapping nanoparticles based on the Poisson distribution outlined by Pace et al.[236] To obtain nanoparticle mass distributions, the Nano application automatically converted measured signal intensities from nanoparticle samples

to mass based on the known intensities and masses from our in-house synthesized nanoparticle standards. The percent paired events were quantified using Equation 4.1:

Equation 4.1:

$$\%\ Paired\ events = \left(\frac{((\#\ of\ Isotope\ 1\ events + \#\ of\ Isotope\ 2\ events) \div 2)}{Total\ \#\ of\ Paired\ Events}\right) * 100\%$$

Further data and statistical analyses were performed with GraphPad Prism (GraphPad, USA) and OriginPro (OriginLab, USA).

For all synthesis steps, glass Erlenmeyer flasks and magnetic stir bars were cleaned before synthesis with Aqua Regia, i.e., 3:1 (v/v) mixture of hydrochloric acid (Sigma-Aldrich, ACS reagent, 37%, St. Louis, MO) and nitric acid (Sigma-Aldrich, ACS reagent, 70%) to remove potential contaminants. The following reagents were used for all nanoparticle experiments: sodium citrate tribasic dihydrate (SigmaAldrich S4641), gold(III)chloride trihydrate (SigmaAldrich 520918), silver(I)nitrate (SigmaAldrich S209139), potassium iodide (SigmaAldrich 22194), iodine (SigmaAldrich 207772).

According to a previously published protocol, citrate-capped 65-nm and 100-nm gold nanoparticles (AuNPs) were synthesized using a seed-mediated approach.[156] AuNPs were characterized by DLS (Table 4.5), TEM (Figure 4.8), and UV-VIS (Figure 4.6).

30-nm, 50-nm, 70-nm, and 100-nm citrate-capped silver nanoparticles (AgNPs) were synthesized using a modified one-pot method based on two previously published protocols.[271,272] To synthesize 50-nm citrate AgNPs, 5 mM of tannic acid and 5 mM of sodium citrate tribasic dihydrate were brought to a boil in 100 mL of nanopure water and allowed to stir for 15 minutes vigorously. Then, 0.1 mL of 250 mM $AgNO_3$ was injected immediately and allowed to react for another 15 minutes while the solution boiled.

To make 30-nm citrate-capped AgNPs, 12.2 mM sodium citrate tribasic dihydrate and 47 μM were prepared in 10 mL of nanopure water. This solution was heated in a water bath to 60°C for 10 minutes. A separate solution of 1.33 mM $AgNO_3$ was prepared in 40 mL of nanopure water and heated in a 60°C water bath for 10 minutes. Next, the solutions were mixed in an Erlenmeyer flask and kept at 60°C under vigorous stirring for 5 minutes, then brought to a rolling boil for 20 minutes. The same procedure with different concentrations of tannic acid and sodium citrate was used (while 1.33 mM of $AgNO_3$ was used for all three sizes) to make 70-nm and 100-nm citrate-capped AgNPs. To make 70-nm citrate capped AgNPs, 1.7 mM of sodium citrate tribasic dihydrate and 1.11 mM of tannic acid were prepared in 10 mL of nanopure water. To synthesize 100-nm AgNPs, we used 680 μM of citrate and 1.76 mM of tannic acid. The solutions were then combined respectively in Erlenmeyer flasks and stirred vigorously for 5 minutes at 60°C then brought to a rolling boil for 20 minutes.

Citrate-capped gold-silver alloy nanoparticles of various compositions were synthesized according to the seed-mediated protocols detailed by Rioux et al.[273] Briefly, a series of specified volumes containing 30-mM $HAuCl_4$, 30-mM $AgNO_3$, and 170-mM sodium citrate were added simultaneously with vigorous stirring to a boiling solution containing 14-nm citrate capped AuNPs over the course of several steps resulting in gold-silver alloy nanoparticles of various diameters and compositions.

An Agilent Cary 5000 UV-Vis-NIR spectrophotometer (Agilent, USA) was used to measure the visible spectrum of nanoparticles in 1.5-mL PMMA cuvettes. Transmission electron micrographs (TEM) were taken by a 200-kV field emission JEOL2010F microscope (JEOL, USA) equipped with a Direct Electron DE-12 camera (Direct Electron,

USA) and an Oxford X-ray Detector (Oxford Instruments, USA) for energy-dispersive X-ray spectroscopy (EDS). ImageJ (NIH) software was used for measuring nanoparticle size and all post imaging analyses.

Results and Discussion

Figure 4.1 depicts the critical steps of our dual analyte SP-ICP-MS method. Briefly, a dispersion of individual intact particles is introduced into an inductively coupled argon plasma where particles are atomized and ionized, resulting in a discrete ion cluster for each particle termed the transient ion cloud. Depending on particle size, transient ion clouds last only hundreds of microseconds.[274] For quadrupole ICP-MS, microsecond duration times of transient ion clouds impede efficient quantification of more than one isotope (or analyte) per nanoparticle. To enable simultaneous dual isotope quantification on single nanoparticles using quadrupole ICP-MS, we therefore optimized three ICP-MS parameters: 1) collision cell parameters, 2) quadrupole mass analyzer settling time, and 3) detector dwell time.

To validate our established quadrupole ICP-MS's dual analyte capabilities at the single particle level, we used ICP-MS-TOF, i.e., CyTOF (Helios, Fluidigm) and commercially available polymer beads doped with various lanthanide isotopes. We compared the simultaneous detection of two isotopes per bead for three different isotope pairs: (i) ^{175}Lu and ^{140}Ce; (ii) ^{175}Lu and ^{153}Eu; and (iii) ^{175}Lu and ^{165}Ho. Using optimized dual analyte SP-ICP-MS conditions, ~97% of detected beads were positive for each isotope for all three pairs of isotopes (Figure 4.5, Table 4.4). Similarly, CyTOF determined ~99% of detected beads were positive for each isotope for the same three isotope pairs (Figure 4.6). Notably, both techniques provided nearly equivalent results, validating our newly

established and economical SP-ICP-MS approach for the simultaneous detection of two different isotopes with single particle resolution.

Upon validating the dual analyte quadrupole SP-ICP-MS approach with CyTOF, we then quantified paired isotope events originating from single nanoparticles consisting of two different isotopes (Figure 4.10A). As model nanoparticles, we used in-house synthesized 100-nm silver nanoparticles (AgNPs) that naturally contain both ^{107}Ag and ^{109}Ag in nearly equal amounts.[275] Table 4.5 and Figure 4.7 provide the physicochemical characterization of AgNPs. We observed that >95% of detected events were positive for both silver isotopes at a nanoparticle concentration of $1x10^5$ AgNPs per mL (Figure 4.10C). Figure 4.8 shows the real-time signal overlap of both silver isotopes for the corresponding transient AgNP ion clouds. At high nanoparticle concentrations (>$3x10^5$ nanoparticles per mL), paired ^{107}Ag and ^{109}Ag events were lower than 90% of the total events (Figure 1C). At these high nanoparticle concentrations based on the Poisson model, multiple overlapping nanoparticles are more likely to be reaching the detector.[276] The large amount of overlapping ion signals coming from both isotopes of multiple nanoparticles would prevent the Syngistix software from distinguishing discrete paired isotope events from the same nanoparticle. In order to be a paired event, 3 pulse signals for each isotope are required to be 3σ above background. At these high nanoparticle concentrations, it is more likely that the two different isotope ions "spill over" from one event to the next, causing an increase in event length and an increase in the background signal leading to a decrease in detected paired events. Therefore, these limitations indicate that nanoparticle concentrations of ~$1x10^5$ nanoparticles per mL are optimal for simultaneously detecting two isotopes per nanoparticle.

To further establish optimal sample parameters, we then quantified the number of paired events from a 1:1 mixture of gold nanoparticles (AuNPs) and AgNPs, i.e., events positive for ^{197}Au and ^{107}Ag. We hypothesized that since these isotopes originated from different nanoparticles the detected events would remain unpaired (Figure 4.10B). In Table 4.5, Figures 4.7 and 4.9, we provide characterization of the AuNPs. The real-time SP-ICP-MS signals in Figure 4.11 show non-overlapping transient ion clouds for both AuNPs and AgNPs. Our dual analyte SP-ICP-MS results confirmed that the nanoparticle mixture was indeed 1:1 for all nanoparticle concentrations used in this experiment (Figure 4.10D). However, we observed an increase in detected paired isotope events with increasing nanoparticle concentrations indicating false-positive paired isotope events (Figure 4.10E). These results indicate that ions from multiple AgNPs and AuNPs were sufficiently above the background signal to be automatically paired which is related to the observed the decrease in paired events with pure AgNPs. These values represent the linear range in particle concentration attainable with dual analyte SP-ICP-MS. Overall, our AgNP and AuNP mixture results and AgNPs only data suggested that $\leq 1 \times 10^5$ nanoparticles per mL minimized false-positive paired isotope events, which enabled the accurate measurement of ~300 individual nanoparticles per minute.

After establishing optimal instrument and sample parameters, we then applied our dual analyte SP-ICP-MS method to quantify AgNP mass and size. We first synthesized and characterized four differently sized AgNPs (30-, 50-, 70-, and 100-nm AgNPs) (Figure 4.7 and Table 4.5). We observed increased transient nanoparticle ion cloud duration times and intensities for both silver isotopes as AgNP size increased (Figure 4.12). Interestingly, 30-nm AgNPs had 75% paired events for both ^{107}Ag and ^{109}Ag (Figure 4.13). This indicates

a size limit of nanoparticles ≤ 30 nm in dual analyte mode. As a nanoparticle event is only registered when a pulse signal is 3σ above the background signal, 25% of the signals for the 30-nm AuNPs were not above the threshold determined by the software. The observed loss in these nanoparticle events could be due to the microsecond detector dwell time that reduces the intensity within a sampling event causing ≤ 30nm nanoparticle signal to be lost to the background signal.[256] Our results indicate that particle mass is the main parameter affecting particle detection in dual analyte mode. In single analyte mode, however, we and others have found that nanoparticles of ~15 nm can be efficiently quantified with minimal effects from the background signal.[277,278]

However, for 50-, 70-, and 100-nm AgNPs, our dual analyte SP-ICP-MS results in Figure 4.14 show that the ratio of ^{107}Ag and ^{109}Ag positive events was approximately 1:1 and that 95% of the detected events were positive for both ^{107}Ag and ^{109}Ag. Median masses for all differently sized AgNPs are reported in Table 4.6. To obtain the nanoparticle size distributions based on the measured masses, we assumed AgNPs exhibited a spherical geometry and used Equation 4.2 to calculate the corresponding diameters:

Equation 4.2 $$d[nm] = \sqrt[3]{\frac{6 \cdot NPmass}{\pi \cdot \rho}}$$

Where NPmass is the reported SP-ICP-MS mass in [g] unit of a single AgNP for one isotope, and ρ is the density of silver (10.49 g/cm^3).

By applying Equation 4.2 to the mass distributions in Figures 4.14A-C, we obtained size distributions for the three differently sized AgNPs (Figures 4.14D-F). To confirm these results, we analyzed the same nanoparticles using transmission electron microscopy (TEM) (Figures 4.14G-I). and found that the nanoparticle size distributions obtained with TEM corresponded well to the dual analyte SP-ICP-MS findings. We also determined that

surface modifications such as the addition of polyethylene glycol on the surfaces of AgNPs did not affect dual analyte SP-ICP-MS measurements (Figure 4.15). In summary, our dual analyte SP-ICP-MS method accurately quantified two isotopes per nanoparticle in situ at a rate of over 300 particles per minute, which was corroborated by TEM image analysis.

After simultaneously quantifying two different isotopes of the same element within single nanoparticles, we used dual analyte SP-ICP-MS to quantify masses of different elements within the same nanoparticle. To accomplish this, we used in-house synthesized bimetallic gold-silver alloy nanoparticles. EDS/STEM confirmed that synthesized alloy nanoparticles were composed of both gold and silver (Figures 4.17A-D) with a composition of ~60 % atomic gold and ~40% atomic silver (Table 4.7). TEM size analysis of the alloy nanoparticles revealed the average nanoparticle diameter to be 77.1±10.2 nm (Figure 4.17E). Conventional ensemble measurements (i.e., dynamic light scattering and UV-Vis) were in line with previous reports and confirmed the successful synthesis of monodisperse gold-silver alloy nanoparticles (Table 4.5) (Figure 4.7).[279,280]

We then performed dual analyte SP-ICP-MS on these gold-silver alloy nanoparticles (Figure 4.17F). Real-time SP-ICP-MS signals of the transient ion clouds (Figure 4.16) and the high positivity rate (> 95%) for both 197Au and 107Ag in individual events confirmed the bimetallic nature of these alloy nanoparticles in line with our EDS results (Figures 4.17A-D). The mass distribution results in Figure 3F represent ~300 individual gold-silver alloy nanoparticles with absolute amounts of ^{197}Au and ^{107}Ag indicating a heterogeneous composition for individual gold-silver alloy nanoparticles.

We determined the median ^{197}Au and ^{107}Ag masses to be 3,261 ag and 1,925 ag, respectively. Based on these single nanoparticle mass distributions, we quantified the

elemental distribution of ^{197}Au and ^{107}Ag isotopes for each gold-silver alloy nanoparticle as shown in Figure 4.17G using Equations 4.3 and 4.4:

Equation 4.3 $$\%Isotope\ 1 = \left(\frac{Mass\ of\ Isotope\ 1}{Mass\ of\ Isotope\ 1 + Mass\ of\ Isotope\ 2}\right) \times 100\%$$

Equation 4.4 $$\%Isotope\ 2 = \left(\frac{Mass\ of\ Isotope\ 2}{Mass\ of\ Isotope\ 1 + Mass\ of\ Isotope\ 2}\right) \times 100\%$$

At the single nanoparticle level, the average gold and silver element composition was 60% and 40%, respectively (Figure 4.17G), which was previously confirmed by our quantitative EDS/STEM results.

To further explore the capabilities of our dual analyte SP-ICP-MS method, we analyzed nanoparticles of similar size made with two different compositions: (i) 70% Au / 30% Ag, and (ii) 30% Au / 70% Ag (Figure 4.18). Our dual analyte SP-ICP-MS measurements revealed that these alloy nanoparticles had average compositions of 69% Au / 31% Ag and 25% Au / 75% Ag, respectively, which was also corroborated with quantitative EDS/STEM analysis (Table 4.7). Dual analyte SP-ICP-MS provided accurate and robust mass and elemental distribution data for hundreds of individual bimetallic nanoparticles with varying compositions in situ within seconds.

Inspired by our dual analyte SP-ICP-MS results, we sought to quantify compositional transformations in individual nanoparticles. As a model system, we exposed 80-nm gold-silver alloy nanoparticles to KI/I_2 solution, which efficiently dissolves AuNPs. We started by evaluating the gold-silver alloy nanoparticle composition upon exposure to different KI/I_2 etchant concentrations with EDS/STEM (Figures 4.19A-D). EDS/STEM

results showed a gradual decrease in gold signal (red) and a more pronounced silver signal (cyan) on the outer edges of the nanoparticles with increasing KI/I_2 etchant concentrations (Figure 4.20). Quantitative analysis of the EDS/STEM images revealed that the atomic percentage of gold decreased by ~3%, ~15%, and ~33% when we exposed the gold-silver alloy nanoparticles to 68-μM, 102-μM, and 136-μM KI/I_2 etchant, respectively (Figures 4.19A-D, Table 4.7). These results demonstrated the concentration-dependent KI/I_2 etching of gold from the gold-silver alloy nanoparticles.

We then used dual analyte SP-ICP-MS to obtain the mass distributions for ^{197}Au and ^{107}Ag isotopes from hundreds of individual gold-silver alloy nanoparticles exposed to different KI/I_2 etchant concentrations within one minute *in situ* (Figures 4.19E-H). Figure 4.19I provides the average masses of ^{107}Ag and ^{197}Au from five independent dual analyte SP-ICP-MS measurements. On average, approximately 353 ag of silver was removed from individual gold-silver alloy nanoparticles at the highest concentration of KI/I_2 etchant, while approximately 2,305 ag of gold was etched away per nanoparticle (Figure 4.19I). At 68- and 102-μM KI/I_2 etchant concentrations, the average mass of silver removed was ~51 ag and ~331 ag per gold-silver alloy nanoparticle, respectively. In comparison, the same KI/I_2 etchant concentrations resulted in an average decrease of gold mass of ~1,400 ag and ~1,600 ag per gold-silver alloy nanoparticle, respectively (Figure 4.19I). Interestingly, gold was not completely removed from gold-silver alloy nanoparticles upon KI/I_2 etchant which could indicate surface passivation.[281] However, at the highest etchant concentration used, Ag^+ and Au^+ events decreased to ~ 68% of total detected events (Figure 4H). These findings may indicate that ~30% of alloy nanoparticles were etched below our dual analyte limit of detection. This could be due to the potential effects of an increased Au background

with increasing etchant concentration. As both ^{107}Ag and ^{197}Au signals need to have consecutive pulses that are 3σ above the background to be automatically paired by the Syngistix software, an increased Au background would likely impede the pairing process. On the other hand, the increase in Au background did not appear to affect the detection of single ^{197}Au events at the etchant concentrations used. These results indicate that although the higher Au background prevented pairing, this dissolved background was not high enough to prevent the detection of individual ^{197}Au events. Control experiments with a 1:1 mixture of similarly sized AuNPs and AgNPs exposed to etchant solution demonstrated the near-complete dissolution of AuNPs and a slight decrease in AgNPs mass upon etchant exposure (Figure 4.21).

To compare our dual analyte SP-ICP-MS and EDS/STEM results, we used Equations 4.2 and 4.3 to calculate the elemental composition of individual gold-silver alloy nanoparticles based on the obtained isotope mass distributions shown in Figures 4.19E-H. The average ^{197}Au isotope mass decreases were 3%, 10%, and 26% for gold-silver alloy nanoparticles exposed 68-μM, 102-μM, and 136-μM etchant, respectively, which we corroborated by EDS/STEM analysis. Figure 4.19J summarizes the obtained ^{197}Au mass distributions for hundreds of individual gold-silver alloy nanoparticles upon exposure to different KI/I_2 etchant concentrations. As shown by our dual analyte SP-ICP-MS data in Figure 4.19, individual gold-silver alloy nanoparticles underwent chemical etching reactions with various levels of efficiency.

We then sought to quantify the kinetics of metal deposition on individual colloidally dispersed nanoparticles with dual analyte SP-ICP-MS in situ. As a model nanoparticle system, we selected gold-silver alloy nanoparticles and quantified the

simultaneous deposition of gold and silver on these nanoparticles over time. Figure 4.24A, shows the process of adding Au(III) and Ag(I) ions to gold-silver alloy nanoparticles resulting in growth and thus a mass increase of individual nanoparticles over time.

We used 55-nm gold-silver alloy nanoparticles as the starting material for the seed-mediated nanoparticle growth (Figure 4.24A-B). TEM analysis confirmed that these gold-silver alloy nanoparticle seeds exhibited an average diameter of 56.3±5.2 nm (Figures 4.24B and 4.22). Dual analyte SP-ICP-MS reported that the average masses of ^{197}Au and ^{107}Ag in individual 55-nm gold-silver alloy nanoparticles were 1,882 ag and 1,070 ag, respectively, with an initial composition of 61% and 39%, respectively (Figures 4.23 and 4.25).

To increase the size of gold-silver alloy nanoparticles from 55 nm to 70 nm, we simultaneously added equal molar amounts of Au(III) and Ag(I) ions to a boiling aqueous dispersion containing colloidal 55-nm gold-silver alloy nanoparticles in the presence of the reducing agent sodium citrate (Figure 4.24A).[273] At specified time points during the chemical reaction, we analyzed the nanoparticle reaction mixture with dual analyte SP-ICP-MS to quantify the deposition of gold and silver onto the 55-nm alloy nanoparticle seeds. We show in Figure 4.25 the mass distribution dot plots for ^{197}Au and ^{107}Ag. In Figures 4.24C-D, we summarized our dual analyte SP-ICP-MS results by showing ^{197}Au (Figure 4.24C) and ^{107}Ag (Figure 4.24D) isotope mass distributions for individual nanoparticles over time. Figures 4.24C and 4.24D show a decreased frequency in lower masses and a gradual increase in events with higher masses as the reaction proceeded. These data demonstrate the heterogeneity of gold and silver deposition at the single particle level.

Based on the isotope mass distributions, we obtained the average alloy nanoparticle elemental composition at specified time points. One minute after adding Au(III) and Ag(I) ions, the nanoparticle composition changed by 5% resulting in an average composition consisting of 66% gold and 34% silver (Figure 4.24E). We corroborated the relatively fast deposition of gold by UV-Vis spectrophotometry of the colloidal nanoparticle dispersion where the absorption maximum from 480 nm at tzero red-shifted to 512 nm one minute after the addition of Au(III) and Au(I) ions to the nanoparticle seeds, indicating gold deposition (Figure 4.26).

At t_{2min}, the average alloy nanoparticle composition decreased to ~30% for silver, whereas the average nanoparticle composition for gold increased to ~70% (Figure 4.24E). Five minutes into the reaction, an increase in silver deposition was observed leading to an average elemental composition of 65% gold and 35% silver (Figure 4.24E). The element compositions obtained from the isotope mass distributions show that after 10 minutes the average gold composition remained ~64%, whereas the average silver composition remained at ~36% (Figure 4.24E). These results were corroborated by the UV-Vis absorbance measurements which stabilized at a wavelength of 500 nm after 15 minutes (Figure 4.26). These results suggest that this reaction was completed within 15 minutes.

To obtain a better understanding of the deposition reaction, using the nanoparticle mass distributions in Figures 4.24C and 4.24D, we plotted the total detected mass of ^{197}Au and ^{107}Ag of the analyzed alloy nanoparticles as a function of time (Figure 4.24F). With this data, we calculated the rate constants for gold and silver depositing onto alloy

nanoparticles using Equation 4.5, which accounts for an exponential growth phase followed by a plateau in mass.

Equation 4.5 $$Mass_{Tn} = Mass_{T60} - (Mass_{T60} - Mass_{T0}) * e^{-k*T_n}$$

Where $Mass_{Tn}$ is the total isotope mass of all detected nanoparticles at a specific time point; $Mass_{T60}$ is the total isotope mass of all detected nanoparticles at 60 minutes; $Mass_{T0}$ is the total isotope mass of all detected nanoparticles before the reaction; K is the rate constant for a specific isotope; T_n is time in units of minutes.

The rate constant K based on Equation 4.5 determined that gold deposition was ~2 times faster than the deposition of silver with rate constants of 0.08 and 0.13 min^{-1}, respectively. The faster deposition of gold onto the alloy nanoparticles is likely due to the differences in reduction potential of Au^{3+}/Au and Ag^{+}/Ag.[282] Our single particle analysis also suggests that gold deposition was 50% complete within 5 minutes, whereas silver deposition was 50% complete within 9 minutes which indicates the total reaction was virtually complete near the 15 minute mark as previously observed with spectrophotometry. Taken together, these results showcase the feasibility for simultaneously quantifying chemical reaction kinetics of two different metals on individual nanoparticles in a high-throughput manner with easily accessible quadrupole ICP-MS technology.

Conclusions

In summary, we established dual analyte SP-ICP-MS as a quantitative high-throughput analytical technique that enables the simultaneous quantification of two analytes (or isotopes) per nanoparticle in situ. Our dual analyte SP-ICP-MS results were obtained using a commonly available quadrupole-based ICP-MS system which was

corroborated by time-of-flight mass spectrometry and EDS/STEM. With our SP-ICP-MS approach, we quantified AgNP size, and the heterogeneity of bimetallic gold-silver alloy nanoparticles undergoing chemical reactions with high throughput (300+ nanoparticles/minute) in situ. Our economical elemental analysis method has the potential to transform the understanding of nanoparticle transformations in environmental and biological milieus to inform the design of safer, more effective, and more efficient nanotechnologies that use nanoparticles with defined compositions.

Acknowledgements

The authors acknowledge the assistance and fruitful discussions by Drs. S. Foster, R. Merrifield, R. Forester, J. Sabisch, and S. Liang. This work was supported in part by an NSF MRI grant (1828234), NSF CAREER award (2048130), an IBEST/OUHSC seed grant for interdisciplinary research, the OU VPRP Strategic Equipment Investment grant, the OU Faculty Investment Program, an OCAST Health Research grant (HR20-106), and the Oklahoma Tobacco Settlement Endowment Trust awarded to the University of Oklahoma - Stephenson Cancer Center. The content is solely the responsibility of the authors and does not necessarily represent the official views of the Oklahoma Tobacco Settlement Endowment Trust. This work was additionally supported by the National Institute of Arthritis and Musculoskeletal and Skin Diseases (P30AR073750) and the National Institute of General Medical Sciences (U54GM104938) through the National Institutes of Health. The Presbyterian Health Foundation and the Oklahoma Center for Adult Stem Cell Research provided funding for the CyTOF equipment.

Chapter 5: Single cell elemental analysis for quantification of nanoparticle interactions with individual B cells[4]

Abstract

Detailing nanoparticle interactions with single cells has the potential to enhance clinical translation of nano-based therapies and diagnostics. To that end, we visualized and quantified nanoparticle uptake using model gold nanoparticles (AuNPs) with single cell resolution using human B cells. First, we demonstrated efficient elemental detection of individual B cells with single cell quadrupole inductively coupled plasma mass spectrometry (SC-ICP-MS). We then determined that colloidally stable positively charged AuNPs associate 100-fold more with B cells compared to neutral charged AuNPs. We further applied SC-ICP-MS and light scattering confocal microscopy to assess AuNP uptake by B cells. With these two techniques, we simultaneously measured a pan surface marker for B cells and AuNPs to determine that >80% of single B cells had internalized AuNPs. Our study highlights the application of accessible single cell techniques to reveal nanoparticle-B cell interactions with broad applicability for biomedical applications.

[4]In preparation as: Donahue ND, Sheth V, Frickenstein AF, Holden A, Wilhelm S. Single cell elemental analysis for quantification of nanoparticle interactions with individual B cells

Introduction

Currently, single cell analysis of nanoparticle can be performed with few techniques such as flow cytometry, microscopy, or mass spectrometry. To determine nanoparticle-cell interactions using flow cytometry nanoparticles oftentimes require fluorophore labels that may alter a nanoparticle's surface chemistry therefore affecting cellular uptake and association.[283,284] Fluorophore-free measurements with flow cytometry using side scattering analysis of cells exposed to nanoparticles has been successfully demonstrated, but have yet to be used for quantifying nanoparticles within single cells and rely on nanoparticles with sizes > 20 nm.[285–287] Like flow cytometry, microscopy-based analysis of nanoparticle-cell interactions encounters similar obstacles and suffers from low-throughput.[288,289] On the other hand, mass spectrometry (*e.g.,* CyTOF) has been widely applied to quantify nanoparticle-cell interactions at the single cell level with the multi-element capabilities used for phenotyping different cell populations.[290–292] As an auxiliary and economical tool to these existing techniques, single cell inductively coupled plasma quadrupole mass spectrometry (SC-ICP-MS) is a promising analytical tool for quantifying single cell nanoparticle interactions. Previous reports have successfully used SC-ICP-MS to probe nanoparticle interactions with algae, yeast, and bacteria.[231,293,294] Other studies using SC-ICP-MS have investigated intrinsic biological metals and metallodrugs within various types of human cell lines.[218,295] In this report, we extend the versatility of SC-ICP-MS to quantify the interactions between in-house surface engineered gold nanoparticle (AuNPs) and human B cells. We chose B cells as a model cell line due to their importance in the context of nano-based vaccines.[296–298] In addition to playing a key role in long-lasting immunity, B cells can also directly interact with nanoparticles within the liver, spleen, and

lymph nodes *in vivo*.[63,299,300] Therefore, quantifying nanoparticle interactions at the single B cell level may provide novel insights on nanoparticle cellular uptake, intracellular trafficking, and nanoparticle physicochemical properties that safely favor B cell association. Such findings could be applied to inform the rational design of novel nanomaterials for enhancing B cell-nanoparticle interactions.

Here we demonstrated that quadrupole SC-ICP-MS efficiently detected individual B cells by using a routine intracellular stain used in mass cytometry and a pan B cell surface marker labeled with quantum dots. Our results indicate that the quantum dot labeling of B cells enhanced signal intensity 3-fold compared to the ionic iridium staining. We also demonstrated that B cells efficiently entered the ICP-MS as single cells with a transport efficiency of ~50% and can be detected at a rate of 30 cells per second. Having confirmed the detection of two different metals associated with B cells, we then used in-house synthesized AuNPs as a model nanoparticle to quantify nanoparticle-B cell interactions at the single cell level. We prepared model 13-nm AuNPs with different surface charges and demonstrated with SC-ICP-MS and confocal laser scanning microscopy that positively charged AuNPs efficiently enter B cells through an energy dependent endocytic pathway. Lastly, we demonstrated our quantum dot labeling of B cells facilitated the simultaneous detection of individual B cells and internalized AuNPs using confocal microscopy and SC-ICP-MS. These findings indicate that > 80% of B cells internalized positively charged AuNPs. Ultimately, this study provides a framework for utilizing cost-effective quadrupole mass spectrometry and label-free confocal laser scanning microscopy technology to measure single B cell-nanoparticle interactions. We envision that this approach far-

reaching implications for researchers interested in single cell elemental analysis, nanotoxicology, and nanoparticle delivery to immune cells.

Materials and Methods

All SC-ICP-MS measurements were performed with the NexION 2000 equipped with a commercially available single cell introduction system and single cell software (PerkinElmer, USA) using the conditions outlined in Table 5.1. AuNPs of known sizes were used as calibration standards and used to acquire ^{197}Au mass distributions. Mass histograms of cell suspensions were collected and analyzed using PerkinElmer's single cell software. Dual analyte data on B cells was collected using PerkinElmer's dual analyte Nano application using the conditions in Table 5.1 along with the collision cell and quadrupole mass filter settings Table 5.4. For ^{114}Cd and ^{193}Ir analysis in Figures 5.1 and 5.4 thresholds were applied to cell samples based on the background counts per Laborda et al.[301] For ^{197}Au analysis in Figures 5.12 and 5.15 thresholds were not applied and the acquisition included all gold events. In Figure 5.17, thresholds were applied to ^{197}Au to exclude single nanoparticles based on the peak intensities of single 13-nm gold nanoparticles. Scan times were 30 seconds for Figures 5.1 and 5.17. For Figures 5.12 and 5.15 scan times were adjusted to collect a minimum of 500 ^{197}Au events. Further data analysis was performed in GraphPad Prism.

The B cell lymphoma line (Raji ATCC #CCL-86) were kindly given by Drs. Darrell Irvine and Mariane B. Melo at MIT. B cells were cultured in RPMI 1640 containing (2 mM L-Glu, 10 mM HEPES, 1 mM sodium pyruvate, 4500 mg/L glucose, and 1500 mg/L sodium bicarbonate) supplemented with 10% FBS and 1% penicillin and streptomycin. B cells (a suspension cell line) were maintained in T-75cm^2 tissue culture flasks at 37°C in a

humidified incubator with 5% CO_2 and passaged every other day. Prior to nanoparticle exposure, cells were spun down at 500 xg for 5 minutes, counted and placed in 6 well plates at a density of 1 million cells per well in a volume of 1.5mL of RPMI media. Cells were exposed to a final concentration of 0.56 nM (determined by UV-Vis) of 13-nm AuNPs for all experiments. We prepared our B cells for SC-ICP-MS based on protocols routinely used in mass cytometry.[302,303] Following nanoparticle exposure, cells were pipetted from 6 well plates and spun down at 500 xg for 5 minutes, resuspended in 4% paraformaldehyde and allowed to fix overnight at 4 °C. The next day, cells were spun down at 800 xg for 5 minutes then resuspended in 1 mL of 1x PBS and counted. These cells were stained with 125 μM Cell-ID^{TM} Intercalator Ir (Fluidigm) using 3 μL staining solution per 1 million cells for 1 hour at room temperature. Following iridium staining, cells were spun down at 800 xg for 5 minutes, resuspended in 0.5 mL of nanopure water, counted on a hemocytometer, and analyzed on ICP-MS immediately. For etching experiments, 4 μL of gold etchant solution (Sigma Aldrich 651842) was added to the cell media after nanoparticle exposure. The etchant solution was well-mixed with cells and then immediately spun down at 500 xg for 5 minutes and resuspended in 4% paraformaldehyde to fix overnight. Following overnight fixation, AuNP-exposed B cells were spun down at 800 xg for 5 minutes, resuspended in 1mL of nanopure water and washed once more before being resuspended in 0.5 mL of nanopure water. This solution was diluted two-fold, and analyzed on ICP-MS. Scan times for analyzing ^{197}Au were adjusted to collect a minimum of 500 ^{197}Au events.

Following nanoparticle exposure, B cells were spun down at 500 g for 5 minutes. A master mix of 2% FBS in 1x PBS containing biotinylated anti-human CD-19 antibody (Clone: HIB19 BioLegend) was prepared using a 100-fold dilution of biotinylated

antibody. After the initial centrifugation, the media containing nanoparticles was aspirated and B cells were resuspended in 100μL of the biotinylated antibody solution and incubated on ice for 15 minutes. After the incubation, 1mL of 2% FBS in 1x PBS was added to the cells then the cells were centrifuged at 600 g for 6 minutes. A master mix solution of streptavidin quantum dots (ThermoFisher Scientific Q10123MP) was prepared using a 100-fold dilution of quantum dots in 1X PBS with 2% FBS. Next B cells were resuspended in 100μL of the quantum dot solution and incubated on ice for 1 hour. After the incubation, 1 mL of 2% FBS in 1x PBS was added to the cells and then followed by another round of centrifugation at 600 g for 6 minutes. The quantum dot-labeled B cells were then resuspended in 1 mL of 4% PFA and allowed to fix overnight at 4°C. Prior to ICP-MS analysis, fixed quantum dot-labeled B cells were spun down at 800 g for 6 minutes and resuspended in 1 mL nanopure water. Cells were spun once more at 800 g for 6 minutes, resuspended in 0.5 mL nanopure water, counted, and immediately analyzed by ICP-MS.

To PEGylate gold nanoparticles with OPSS-(PEG)5kDa-MAL (MW 5 kDa, Laysan Bio), a constant nanoparticle surface-area-to-volume ratio was maintained, i.e., 10 cm^2 in 500 μL of total volume. Figure 5.10 is a schematic representation of the PEGylation strategy. The following example is described for PEGylating 13-nm gold nanoparticles (nanoparticle concentration of 20 nM) with a desired surface density of 0.5 OPSS-(PEG)5kDa-MAL/nm^2. Briefly, 13-nm citrate AuNPs were reacted with orthopyridyl-polyethylene glycol-maleimide (OPSS-(PEG)5kDa-Mal) (Laysan Bio Al, USA) at a coating density of 0.5 PEG/nm^2 for 30 minutes. Next, these nanoparticles were reacted with OPSS-(PEG)2kDa-OCH_3 (Laysan Bio Al, USA) at a density of 5 PEG/nm^2 for 30 minutes to enhance colloidal stability through backfilling.[304] Following this, the nanoparticles were

spun down at 15,000 g for 30 minutes and resuspended in nanopure water with either (KKKKKKKC) or SH-(PEG)1kDA-OCH_3 at a ratio of 5 SH-Ligand/nm^2. The following day, the AuNPs were spun down at 15,000 g for 30 minutes to remove unreacted thiolated ligands, resuspended in nanopure water, and analyzed on UV-VIS to determine nanoparticle concentration.

Fixed B cells were simultaneously stained with CF633 (WGA, cat# 29024, Biotium) and NucBlue DAPI (cat# R37606, Thermo Fisher) in 1x HBSS for 15 minutes at 37°C to label the cell surface or the nuclei, respectively. To label endocytic vesicles, live B cells were incubated with Dextran-TRITC for 8 hours during the nanoparticle exposure experiments. (Sigma-Aldrich 42874). Confocal images were taken with a 40X (NA 1.3), 63X (1.4), and 100X (NA 1.4). oil immersion objective on a ZEISS LSM 880 inverted confocal microscope using photomultiplier tube detectors with a 405nm diode laser and a 633 nm helium-neon laser for fluorescent channels through a main beam splitter 488/561/633 filter. Cell nuclei were imaged using an excitation and emission wavelength of 405 and 445 nm, respectively. Cell membranes were imaged using an excitation and emission wavelength of 488 and 528 nm, respectively. AuNPs were imaged using light scattering with a 561 nm diode-pumped solid-state laser and an MBS T80/R20 filter. Endocytic vesicles were imaged using an excitation and emission wavelength of 561 and 633 nm, respectively. Quantum dots were imaged using an excitation and emission wavelength of 405 and 690 nm, respectively. Further processing was performed using ImageJ.

Results and Discussion

To quantify nanoparticle interactions with B cells at the single cell level, we used two different strategies (i. iridium staining and ii. quantum dot labeling) for the detection of intact and individual B cells using SC-ICP-MS. We hypothesized that labeling B cells with quantum dots would generate more ions per cell thus improving the detection signal of single B cells using quadrupole SC-ICP-MS. To test this hypothesis, we first stained B cells with an intracellular iridium DNA intercalator as a marker for nucleated single cells as is common practice in mass cytometry (Figure 5.1A).[305] For labeling B cells with quantum dots, we leveraged the ubiquitous pan expression of the clinically relevant target CD-19.[306,307] To detect single B cells using SC-ICP-MS *via* CD-19, we first incubated B cells with a biotinylated anti-CD-19 antibody and then used commercially-available streptavidin-coated quantum dots to selectively bind to the biotinylated B cells (Figure 5.1B).[308,309] The streptavidin-coated quantum dots consisted of a nanocrystal core made of CdSe and a shell of ZnS and were ~15 nm in size (Figure 5.2). We observed strong time resolved ^{114}Cd signals on ICP-MS only when streptavidin quantum dots were clustered with biotinylated antibodies (Figure 5.3). Additionally, due to the fluorescent nature of quantum dots, this labeling procedure permitted the fluorescent detection of B cells using confocal microscopy which confirmed efficient surface labeling of B cells with quantum dots (Figure 5.4).

To compare the two different metal stains on quadrupole SC-ICP-MS, we obtained the transient ion peak shapes of the labeled B cells. We observed that iridium-stained B cells produced discrete transient iridium ion signals of ~15 counts for ^{193}Ir (Figure 5.1C). In contrast to the iridium-stained B cells, quantum dot labeled B cells produced transient

ion signals of ~42 counts for ^{114}Cd. (Figure 5.1D). These transient ion signals and corresponding intensities indicate that quantum-dot labeling of B cells enhanced B cell intensities by 3-fold on quadrupole ICP-MS due to the larger number of ions per cell from 15 nm quantum dots attached to B cells compared to iridium staining.

After confirming two different metal cellular stains produce discrete transient ion signals, we then confirmed that intact and individual metal-stained B cells enter the ICP-MS. To do this, we sequentially measured ^{114}Cd and ^{193}Ir events as a function of B cell concentration. Figure 5.5 shows a representative hemocytometer image of the single cell stock solutions containing fixed and metal-labeled B cells. We observed that both isotopes provided the same number of detected events at the same cell concentrations and had strong linear relationships (r^2 = 0.99) with cell concentration (Figure 5.1E). We confirmed that these detected events corresponded to single intact cells by showing that B cells remain intact upon entry into the ICP-MS with epifluorescence microscopy (Figure 5.6). Quantitative analysis of epifluorescent microscope images showed that the B cell membrane and nucleus had strong correlation pre- and post- nebulization with Pearson correlation values of 0.9. Taken together, these results indicate that intact B cells containing intracellular metal ions and surface-bound quantum dots are introduced intact into the ICP-MS and are accurately detected using quadrupole ICP-MS at the single cell level. Our data also show that for quadrupole SC-ICP-MS, quantum dot labeling is preferred due to the 3-fold higher ion signal intensity compared to iridium staining.

Based on the detected ^{114}Cd and ^{193}Ir events in Figure 1E, we then used Equation 1 to calculate the transport efficiency of B cells (Figure 5.1F). Calculating the cellular transport efficiency enabled us to accurately determine how many cells would be detected

upon entry into the mass spectrometer and was later applied for the mass quantification of analytes in individual B cells.[310] Using equation 5.1, we found that the transport efficiency for B cells was ~50% for both iridium staining and quantum dot labeling at all concentrations used.

Equation 5.1 $$\left(\frac{Events\ detected}{Number\ of\ cells\ in\ 6.5\ \mu L}\right) * 100\%$$

Where events detected are the detected events within a 30 second scan time, divided by the theoretical number of cells in 6.5 µL which is based on a scan time of 30 seconds and a flow rate of 13 µL per minute.

To date, this high cellular transport efficiency using human cells that are ~15µm with an analysis rate of 30 single B cells per second has yet to be achieved using quadrupole ICP-MS in single cell mode.[311] These single B cell results were further validated by detecting events from commercially available micron-sized lanthanide doped polymer beads. At similar concentrations, the lanthanide-doped beads had a maximum analysis rate of ~40 beads per second with an average transport efficiency of ~60% (Figure 5.7). We emphasize that with microsecond detector dwell times, a sample flow rate of 13.0 µL/minute, B cell concentrations ≤ 3 x 10^5 cells/mL, a transport efficiency of 50%, and visible single B cell suspensions (Figures 5.5 and 5.6), the probability of measuring overlapping/multiple cell events was reliably minimized which can be further confirmed using Poisson statistics.[270] Collectively, these results ensured consistent detection of intracellular and surface bound metals on single B cells. With these parameters, we next wondered whether we could quantify nanoparticle interactions at the single B cell level.

To model nanoparticle B cell interactions, we used in-house synthesized 13-nm AuNPs due to the facile aqueous synthesis that produces biocompatible narrowly distributed AuNPs that have tunable surface chemistry.[228] Single particle ICP-MS revealed that our in-house synthesized 13-nm AuNPs had a narrow mass distribution where ~93% of ^{197}Au events had a mass of 24 ag corresponding to a diameter of 13 nm and produced transient ^{197}Au signals with intensities of ~4 counts (Figure 5.8). Transmission electron microscopy, dynamic light scattering, and UV-Vis spectrophotometry corroborated the single particle ICP-MS findings indicating that these particles were 13-nm with a narrow size distribution (Figures 5.8, 5.9 and Table 5.2). To probe how surface charge impacts nanoparticle association with B cells, we surface engineered 13-nm AuNPs with either i. Positively charged peptide (K7C); or ii. Neutral polyethylene glycol ((PEG)1kDA-mPEG) following a previous protocol (Figure 5.10).[156] These surface modifications produced 13-nm AuNPs with equivalent hydrodynamic diameters but with different electrokinetic potentials of ~18 mV (Table 5.3). To ensure that these surface modifications resulted in colloidally stable nanoparticles, we measured the mass of the surface-modified 13-nm AuNPs under cell culture conditions without B cells. Our mass distribution data show that the most frequent and average mass for both surface-modified AuNPs was still 24 ag indicating that surface modifications do not cause aggregation and that these AuNPs remain as single colloidally stable 13-nm nanoparticles in cell culture media at 37 °C (Figure 5.11).[124]

Having confirmed that our surface modified AuNPs remain as individual nanoparticles under cell culture conditions, we investigated how two different surface modifications (i. 7 lysine residue modified AuNPs and ii. methoxy terminated PEGylated

AuNPs) may associate with B cells. We first assessed nanoparticle association with B cells using SC-ICP-MS to quantify the average amount of ^{197}Au associated per B cell upon exposure to the differently charged 13-nm AuNPs under the same AuNP exposure conditions (Figure 5.12A). For B cells exposed to mPEG-modified AuNPs, the average ^{197}Au mass per cell was 315 ag which corresponds to ~13 AuNPs per cell. Conversely, B cells treated with the same concentration of K7C-modified 13-nm AuNPs had an average ^{197}Au mass of 30117 ag per cell which corresponds to ~1250 AuNPs per cell. These results indicate that the positively charged peptide induced nearly two orders of magnitude more association with B cells than the neutral PEGylated AuNPs.

To obtain a better understanding of how surface charge affects B cell interactions with nanoparticles, we obtained the single cell ^{197}Au mass distribution of B cells exposed to either 13-nm K7C AuNPs or 13-nm mPEG AuNPs (Figure 5.12B). Interestingly, the most frequent mass observed for B cells exposed to mPEG-modified AuNPs was 24 ag, which is the same mass of a single 13-nm AuNP (Figures 5.8 and 5.11). Only 4% of the total ^{197}Au events were above 24 ag for B cells exposed to 13-nm mPEG AuNPs with a maximum detected mass of 13000 ag per cell. On the other hand, ~95% of ^{197}Au events were above 24 ag for B cells exposed to 13-nm K7C AuNPs. We measured a maximum ^{197}Au mass of 50000 ag per cell, which was the maximum mass our software could detect. Taken together, our quantitative SC-ICP-MS results indicate that K7C-AuNPs enhanced B cell nanoparticle association ~100-fold compared to mPEG-AuNPs.

We then qualitatively assessed nanoparticle association with B cells with confocal laser scanning microscopy utilizing a label-free light scattering approach to visualize AuNPs associated with B cells.[312] Due to the ability of metallic nanoparticles to scatter

light, additional surface modifications (*e.g.,* fluorophores) were not required which can alter the nanoparticles' surface chemistry. Interestingly, only B cells exposed to K7C-modified AuNPs had detectable scattering signal within B cells (Figure 5.12C). On the other hand, B cells exposed to mPEG-modified AuNPs (Figure 5.12D) lacked scattering signal similar to B cells not exposed to AuNPs (Figures 5.12E). These qualitative label-free microscopy results corroborate the SP-ICP-MS results and demonstrate how nanoparticle surface charge governs nanoparticle- B cell interactions. To ensure biocompatibility of the K7C AuNPs, we evaluated the viability of B cells exposed to several concentrations of K7C AuNPs (Figure 5.13). The viability assay confirms that the 13-nm K7C AuNPs were non-toxic to B cells demonstrating that our model cationic nanoparticles are a safe model to further investigate nanoparticle-B cell interactions. Given that positively charged AuNPs safely associate with B cells, we then determined to examine the internalization of K7C-AuNPs to better understand nanoparticle cellular uptake at the single B cell level.

Previous groups have used KI/I_2 etching to remove free uninternalized AuNPs in *in vitro* cell culture experiments.[313] We wondered whether this approach could be applied for quantifying internalized AuNPs at the single B cell level. We confirmed that upon exposure to etchant solution, 13-nm AuNPs were undetectable using DLS and no longer had surface plasmon resonance indicating dissolution of the AuNPs (Table 5.3 and Figure 5.14). To ensure that this process was conducive with B cells, we first examined B cells exposed to AuNPs with and without KI/I_2 using confocal laser scanning microscopy. To help identify internalized AuNPs, we fluorescently labeled endocytic vesicles and acquired Z stacks on confocal microscopy of B cells exposed to 13-nm K7C-modified AuNPs (Figure 5.15). The representative Z projection in Figure 3A shows colocalization between

the AuNP scattering signal and fluorescent endocytic vesicles. Upon exposing B cells to etchant, nanoparticles were still localized within endocytic vesicles (Figures 5.15B). Our confocal results indicate that B cells internalize nanoparticles within endocytic vesicles and are not affected upon etchant solution exposure.

Upon qualitatively confirming that K7C-modified AuNPs enter endocytic vesicles within B cells, we then used SC-ICP-MS to quantify internalized AuNPs per B cell. We first obtained the average ^{197}Au mass of B cells exposed to 13-nm K7C-modified AuNPs with and without iodine etchant (Figure 5.15D). The average ^{197}Au mass decreased by ~3000 ag after B cells were exposed to etchant indicating majority of AuNPs were internalized and that up to ~125 AuNPs had been etched away. These results validated by confocal laser scanning microscopy suggest that K7C-modified AuNPs are internalized within cells as opposed to remaining on the cell membrane. To confirm the etchant's ability to remove uninternalized AuNPs, we exposed B cells to K7C-modified AuNPs at 4 °C. This temperature reduces a cell's membrane fluidity and activity to inhibit endocytosis.[207] We observed that B cells kept at 4 °C had ~10000 ag of associated ^{197}Au, however after cells were exposed to etchant, the number of ^{197}Au events decreased and over 9000 ag of ^{197}Au was removed. Similarly, B cells that were fixed prior to AuNP exposure had ~10000 ag of associated ^{197}Au. Upon etchant exposure, these fixed B cells also experienced a decrease in ^{197}Au events and lost over 9000 ag of ^{197}Au. Our single cell data show that although K7C-modified AuNPs efficiently associate with B cells ~95% of uninternalized AuNPs can be removed upon chemical etching without affecting internalized AuNPs. These results were further corroborated by the mass distribution of B cells before and after etching (Figure 5.15E). Our etching results reveal that K7C-modified AuNPs accumulate

inside B cells through an energy dependent mechanism and can be quantified at the single cell level.

However, since quadrupole SC-ICP-MS is limited to detecting one element per cell event, cells without AuNPs are not detected. To overcome this limitation, we sought to simultaneously measure B cell events (*e.g.,* ^{114}Cd or ^{193}Ir) and ^{197}Au events using quadrupole SC-ICP-MS. First, we compared the transient ion signals of iridium-stained B cells and quantum dot labeled B cells under optimized conditions that enable the simultaneous detection of two isotopes per event on quadrupole ICP-MS (Table 5.4). Figure 4A shows that the transient ion cloud for quantum dot labeled B cells extends up to 5 milliseconds with a maximum intensity of ~35 counts, whereas the iridium-stained B cells have 5-fold less counts and barely last 2 milliseconds (Figure 5.17A). We also showed that B cells exposed to K7C AuNPs had transient ^{197}Au signal durations > 5 milliseconds with intensities over 100 counts under optimized dual analyte conditions (Figure 5.16). These millisecond transient ion signals point to the possibility of efficient quadrupole switching between a metal B cell stain and internalized AuNPs thus enabling the simultaneous detection of B cells that are positive for AuNPs using quadrupole ICP-MS. We found that only quantum dot labeled B cells enabled accurate simultaneous determination of individual B cells that had internalized AuNPs in dual analyte mode (Figure 5.17B). When ^{114}Cd and ^{197}Au were measured sequentially (*i.e.,* one isotope then the next) 81.1 ± 8.9% of B cells were $AuNP^+$. Similarly, when ^{114}Cd and ^{197}Au were measured simultaneously (both isotopes detected at the same time under optimized dual analyte conditions) 79.6 ± 11.1% of B cells were $AuNP^+$. We only found similar results when ^{193}Ir and ^{197}Au were measured sequentially (83.2 ± 6.1%, Figure 5.17C). However,

when ^{193}Ir and ^{197}Au were measured simultaneously, the number of ^{193}Ir events decreased by ~50% which prohibited the accurate simultaneous detection of individual B cells and internalized AuNPs (Figure 5.17C). These results indicate that although iridium staining works well in mass cytometry and in single analyte mode on quadrupole SC-ICP-MS, high intensity and millisecond transient ion signals (*e.g.,* quantum dots and AuNPs) are needed for the accurate simultaneous measurement of two different analytes in cells.

We corroborated our dual analyte SC-ICP-MS results with confocal laser scanning microscopy and showed that B cells labeled with quantum dots and exposed to K7C AuNPs could be visualized using confocal laser scanning microscopy (Figure 5.17D). To provide a better understanding of how many B cells had AuNPs, we counted 96 quantum dot-labeled B cells from multiple fields of view and determined that 83 of those B cells had AuNP scattering intensity indicating that ~87% of B cells had internalized AuNPs (Figure 5.17E).

Conclusion

In conclusion, we show that B cells labeled with either an intracellular metal stain (iridium) or a surface bound label (quantum dots) enable the efficient detection of individual B cells on quadrupole ICP-MS with an average transport efficiency of ~50%. We demonstrated that these labeling procedures enable the accurate detection of B cells at a maximum rate of 30 cells per second and validated this acquisition rate with micron-sized beads doped with lanthanides. Having established that B cells can be detected either with intracellular or surface bound metals, we then quantified AuNP association with B cells and observed that positively charged AuNPs enhance B cell association 100-fold compared to neutral AuNPs without cytotoxicity. Our SC-ICP-MS results were corroborated by label-free light scattering confocal microscopy. We further demonstrated the ability to quantify

internalized positively charged AuNPs and showed that these nanoparticles enter B cells through an active endocytic pathway and localize within endocytic vesicles with a maximum detectable mass of 50000 ag. Lastly, we determined that >80% of B cells had internalized AuNPs by using our quantum dot labeling approach which was also confirmed with confocal microscopy and single analyte SC-ICP-MS. Our single B cell results using conventional quadrupole mass spectrometry and label free confocal laser scanning microscopy provide a framework for researchers who seek to utilize commonly available methods to quantify and visualize nanoparticle-cell interactions.

Acknowledgements

The authors acknowledge the assistance of Dr. S. Foster and Mr. S. Liang. The authors thank Drs. Darrell Irvine and Mariane B. Melo for kindly providing the Raji cell line. This work was supported in part by an NSF MRI grant (1828234), NSF CAREER award (2048130), an IBEST/OUHSC seed grant for interdisciplinary research, the OU VPRP Strategic Equipment Investment grant, the OU Faculty Investment Program, an OCAST Health Research grant (HR20-106), and the Oklahoma Tobacco Settlement Endowment Trust awarded to the University of Oklahoma - Stephenson Cancer Center. The content is solely the responsibility of the authors and does not necessarily represent the official views of the Oklahoma Tobacco Settlement Endowment Trust.

Chapter 6: Conclusion

Successful clinical translation of nanoparticles requires thorough characterization of nanoparticle physicochemical properties, fluctuations in such properties, and corresponding nanoparticle-cell interactions. Although batch-based measurements of these phenomena have been widespread and utilitarian, these approaches loose valuable information that could be used to inform the rational design of next generation nanomaterials. Due to the inherent diversities that exist among single nanoparticles and single cells, there exists a need for methods to capture both of these heterogenous phenomena. To that end, single nanoparticle and single cell techniques have the potential to further augment the development of novel nanotechnologies for controlling nanoparticle properties and subsequent cellular interactions. However, current methods to accomplish this type of analysis are either cost prohibitive, semi-quantitative, low throughput, *ex situ* and or require labor-intensive data deconvolution processes. Unfortunately, an economical analytical technique capable of simultaneously quantifying both individual nanoparticle transformations and single cell-nanoparticle interactions has yet to make headway in the nanomedicine community. To meet this need, in the current work, single particle and single cell quadrupole inductively coupled plasma mass spectrometry was established to quantify individual nanoparticle transformations and single cell nanoparticle interactions. Using the same mass spectrometer and instrument settings, nanoparticle colloidal stability and chemical reactions were quantified with single nanoparticle resolution. These elemental analysis methods were then used to guide the measurements of nanoparticle-interactions with single B cells.

In aim 1, SP-ICP-MS was established as a high throughput *in situ* method to determine the mass and size of model engineered gold nanoparticles (AuNPs). These data facilitated the quantification of nanoparticle colloidal stability as a function of surface chemistry. First, SP-ICP-MS was investigated as a technique for quantifying the size of 3 different batches of quasi-spherical AuNPs with nominal diameters of 16-, 30-, and 55-nm. Based on the mass distributions, the size distributions were calculated and validated by transmission electron microscopy, dynamic light scattering, and UV-Vis spectrophotometry. These findings established that SP-ICP-MS is a high-throughput single particle technique capable of efficiently quantifying the heterogenous mass of engineered nanoparticle at a rate of ~300 particles per minute. Next, 30- and 55-nm AuNPs were mixed in a 1:1 ratio and analyzed on SP-ICP-MS. The results show that SP-ICP-MS could simultaneously analyze both differently sized AuNPs and accurately determined that the mixture was in a 1:1 ratio. Additionally, SP-ICP-MS was demonstrated to quantify anisotropic gold nanorods and was validated by the image analysis of TEM micrographs of gold nanorods.

Given that SP-ICP-MS could reliably quantify the mass of different sizes of AuNPs with varying geometry, the aggregation behavior of 16-nm citrate coated AuNPs was measured upon exposure to 150-mM NaCl. SP-ICP-MS and the other conventional techniques confirmed an increase in average nanoparticle size. However, only SP-ICP-MS was able to quantify the number of nanoparticles per aggregate. SP-ICP-MS of AuNPs exposed to 150-Mm NaCl show that this aggregation behavior was time-dependent and led to aggregates consisting of a diverse number of nanoparticles. To passivate aggregation upon exposure to saline conditions, thiolated 5kDA PEG polymers with terminal methoxy

groups were added at varying densities to the 16-nm AuNPs. Zeta potential, gel electrophoresis, and DLS confirmed that the AuNPs had different densities of PEG. When immersed into saline solution, the PEGylated AuNPs experienced significantly less aggregation when compared to the citrate coated AuNPs. The highest density of PEG successfully inhibited aggregation altogether whereas lower densities of PEG had marginal increases in nanoparticle size as confirmed by DLS and SP-ICP-MS after 1 hour in saline solution. These results demonstrate that with varying densities of PEG we can tune the kinetics of nanoparticle stability and quantify aggregation behavior *in situ* at the single particle level with high throughput. Ultimately, this novel platform approach of quantifying individual nanoparticle transformations as a function of surface chemistry can be applied to improve our understanding of how single nanoparticle physicochemical properties change under physiological conditions.

As aim 1 was a proof-of-concept study for demonstrating the ability of SP-ICP-MS to quantify nanoparticle transformations, future studies should include later time points to determine when nanoparticle aggregation equilibrium is reached. Another potential avenue using aim 1's approach could investigate the aggregation kinetics of AuNPs with different sizes and or geometries in saline solution. Moreover, different salt solutions that are better approximation for physiological conditions should be explored, as well as the effects of temperature. To further model nanoparticle transformations in simulated biological conditions, the addition of serum proteins would also be valuable. For example, SP-ICP-MS could be used to study how adsorbed proteins on nanoparticle surfaces impact the colloidal stability of AuNPs. In terms of surface modifications, PEG polymers with different chain lengths or terminal functional groups could also be investigated using the

methodology described in aim 1. However, due to the potential immunogenicity of PEG, there exists a need to investigate alternative polymers that offer the same stabilizing and anti-fouling benefits as PEG.

In addition to detailing fundamental nanoparticle transformations, recent studies have leveraged AuNP aggregation for sensing antibodies and enzymatic activity.[314,315] Using SP-ICP-MS to quantify AuNP aggregation as a readout for a diagnostic assay could dramatically increase resolution and enable the precise detection of biomolecules (*i.e.,* antibodies, nucleic acids, etc). Although SP-ICP-MS could reliably provide diagnostic information based on AuNP aggregation, such a high-resolution technique may be excessive for clinical settings, along with its high operating costs and limited accessibility when compared to current standardized diagnostics. Another limitation in aim 1 was that only one isotope per nanoparticle could be analyzed in single particle mode therefore limiting the types of nanoparticles and physicochemical properties that could be analyzed. To address this limitation, aim 2 details the method development of simultaneous quantification of two isotopes per nanoparticle.

Building upon the quantification of AuNPs using SP-ICP-MS, in aim 2 silver nanoparticles (AgNPs) and bimetallic alloy nanoparticles were chosen as model nanoparticles to establish dual analyte quadrupole SP-ICP-MS. Due to the nature of quadrupole mass filters, the simultaneous analysis of two isotopes per nanoparticle has not been possible. To overcome this limitation, three major parameters were refined. First, the transient ion clouds of nanoparticles were elongated using the reaction cell fitted with $NH_{3(g)}$ and equipped with axial field technology voltage. Here nanoparticle transient ion clouds were elongated to last milliseconds as opposed to microseconds. Next, the

quadrupole mass analyzer was adjusted to efficiently switch between to different isotopes per nanoparticle event. Lastly, microsecond detector dwell times were selected to ensure single nanoparticle events were efficiently detected. To confirm the multielement detection of individual particles, dual analyte SP-ICP-MS was compared against ICP-TOF-MS using polymer beads doped with various lanthanide isotopes. Both instruments provided similar dual isotope detection results of 3 different pairs of isotopes from the lanthanide doped beads. Having confirmed the efficient detection of two isotopes per polymeric bead with similar results to the gold standard ICP-TOF-MS, in-house synthesized AgNPs that naturally contain only two isotopes ^{107}Ag and ^{109}Ag were then used to probe the quantitative capabilities of dual analyte SP-ICP-MS. Dual analyte SP-ICP-MS accurately obtained the masses of ^{107}Ag and ^{109}Ag for 3 different sizes of in-house synthesized AgNPs which was confirmed by TEM. Having quantified two different isotopes of the same element, model alloy nanoparticles containing two different elements (*i.e.,* ^{107}Ag and ^{197}Au) were then quantified using dual analyte SP-ICP-MS. SP-ICP-MS simultaneously quantified the mass of ^{107}Ag and ^{197}Au in alloy nanoparticles consisting of various Ag/Au compositions. Interestingly, dual analyte SP-ICP-MS revealed that the alloy nanoparticles had heterogenous elemental compositions. These mass spectrometry results were confirmed using EDS/STEM. However, ICP-MS directly quantified the elemental composition of hundreds alloy nanoparticles within seconds *in situ.* Upon validating dual analyte SP-ICP-MS as a new way to quantify two different isotopes in individual nanoparticles, the feasibility of quantifying nanoparticle transformations was assessed. First alloy nanoparticles were exposed to an iodine-based etchant that selectively removed gold from the bimetallic Ag/Au nanoparticles. Dual analyte SP-ICP-MS successfully

monitored the specific yet heterogenous removal of gold from these bimetallic nanoparticles which was corroborated by EDS/STEM. These results demonstrate the ability of dual analyte SP-ICP-MS to detect and quantify individual nanoparticles undergoing selective chemical etching *in situ* and with high throughput. Lastly, the simultaneous deposition of silver and gold onto alloy nanoparticles was then quantified as a function of time. Dual analyte SP-ICP-MS revealed that this reaction was heterogenous at the single particle level and that gold deposited onto nanoparticles 5x faster than silver. In summary, this aim established a new single particle elemental analysis method using a commonly available mass spectrometer for the quantification of chemical transformations *in situ* at a rate of over 300 particles per minute. With this high throughput platform, researchers can elucidate how key nanoparticle physicochemical properties such as mass, size, and chemical composition evolve in response to chemical or potentially biological stimuli.

With dual analyte quadrupole ICP-MS having been developed, several limitations and new avenues should be addressed. One of the limitations for dual analyte SP-ICP-MS was that nanoparticles $\leq$ 30 nm were not efficiently detected. Unfortunately, multielement nanoparticles such as quantum dots and upconversion nanoparticles are often smaller than 30 nm. Therefore, for analyzing these types of nanoparticles, one would need to further optimize reaction gases, quadrupole settling time, and detector dwell time. In addition to the size limitation, only two elements with similar masses and ionization efficiencies can be analyzed simultaneously. This limitation prevents the simultaneous analysis of lighter elements such as magnesium or phosphorus with heavier elements like gold or platinum. A potential solution to this limitation could involve using different reactive gasses such as

oxygen in lieu of ammonia. For example, oxygen could be used to react with lighter elements like phosphorous to form $^{31}P^{16}O+$ that would then be detected at a *m/z* of 47 which may facilitate the simultaneous analysis of heavier elements found in metallic nanoparticles. Another potential avenue for dual analyte SP-ICP-MS could be to explore how nanoparticle surface modifications (*i.e.,* PEGylation or protein corona formation) affect the efficiency of chemical etching or metal deposition. In addition to gold and silver nanoparticles, other metallic alloy nanoparticles consisting of different transition metals with varying compositions could be explored with dual analyte SP-ICP-MS for novel theranostic applications. Dual analyte SP-ICP-MS could be used to quantify the time-dependent deposition or leeching of metallic payloads at the single particle level. Like the aggregation-based diagnostic assay suggested for aim 1, dual analyte SP-ICP-MS also has the potential to be used for multiplexed high throughput diagnostic assays that could contain multiple multielement nanoparticles that would be "paired" in the presence of a biomolecule such as a nucleic acid or an antibody. In summary, this aim established dual analyte SP-ICP-MS as a new readily accessible tool for quantifying chemical transformations on individual nanoparticles. As the first two aims solely analyzed single nanoparticle transformations, the last aim investigated how single nanoparticles interact with single B cells.

In aim 3, the methodology detailed in aims 1 and 2 were combined to quantify nanoparticle-cell interactions with single cell resolution. To do this Raji cells which are suspension human B cell line were used as a model cell line. To determine optimal B cell sample parameters and cellular transport efficiency, B cells were labeled with either an iridium-based DNA intercalator or quantum dots. Quantum dot labeling of B cells was

accomplished by using a biotinylated anti-CD19 antibody that binds to the pan surface marker CD19. Following this, streptavidin quantum dots were then incubated with the biotinylated B cells leading to quantum dot labeled B cells. Quantum dot-labeled B cells had higher signal intensity compared when compared to the iridium-stained B cells due to the higher number of ions per quantum dot compared to the ionic iridium stain. With these two metal labels, a cellular transport efficiency of ~50% along with an analysis rate of 30 single cells per second was achieved which has not been achieved using human cells on a quadrupole ICP-MS operating in single cell mode. Next two different surface modified 13-nm AuNPs (i. K7C peptide modified AuNPs or ii. methoxy PEG modified AuNPs) were administered to B cells. ICP-MS of the individual B cells revealed that the positively charged peptide-modified AuNPs associated 100-fold more with the B cells than the neutral PEGylated AuNPs. In line with aim 1, SP-ICP-MS revealed that these surface-modified AuNPs were colloidally stable under cell culture conditions. The quantitative single B cell ICP-MS results were further corroborated with confocal scanning laser microscopy which employed label free light scattering to visually confirm enhanced AuNP-cellular association with the positively charged AuNPs. Moreover, single B cell elemental analysis also revealed that these positively charged AuNPs were internalized through an energy-dependent pathway while confocal microscopy revealed the AuNPs localized within endocytic vesicles. Lastly using the dual analyte SP-ICP-MS approach as described in aim 2, the percent of B cells that had internalized AuNPs was determined. This was accomplished by simultaneously monitoring the ^{114}Cd events (from quantum dot labeled B cells) and ^{197}Au events (from AuNPs associated with B cells). It was found that >80% of B cells analyzed were positive for AuNPs. Confocal microscopy corroborated the

ICP-MS results by analyzing B cells in multiple fields of view that had been exposed to AuNPs and labeled with quantum dots. These data showcase new capabilities for quadrupole ICP-MS to quantify nanoparticle-cell interactions at the single B cell level.

In this aim, the simultaneous detection of two isotopes per cell event using a quadrupole-based mass spectrometer was performed at a rate of 30 cells per second with a transport efficiency of ~50%. Conversely, TOF instruments (*e.g.*, CyTOF) are designed to effortlessly detect 40+ isotopes simultaneously per cell at a rate of ~250-500 cells per second. Moreover, CyTOF has been utilized to quantify nanoparticle cell interactions *in vitro* and *in vivo*.[195,291,316] As TOF technology continues to improve its dynamic linear range to accommodate events with a high number of ions (*i.e.,* nanoparticles), multiparametric high dimensional studies on nanoparticle-cell interactions utilizing TOF instrumentation will become even more feasible. However, quadrupole ICP-MS systems will remain as a readily accessible and economical tool for measuring single cell nanoparticle interactions. Ultimately, aim 3 establishes quadrupole ICP-MS as a facile approach that provides straightforward quantitative single cell results without the need for complex data processing approaches or expensive metal-tagged antibodies as required in CyTOF.

For demonstrating SC-ICP-MS as an accessible method for quantifying nanoparticle-cell interactions, B cells were exclusively investigated due to their non-adherent and single cell nature. In addition to looking at how other B cell lines (*i.e.,* Ramos cells) associate with model nanoparticles, other immune cells such as T cells, dendritic cells, or macrophages would be worthwhile to investigate in future studies. Further quantification of nanoparticles and their interactions with immune cells at the single cell level could

augment the development of immunotherapy treatments. For example, clinically relevant B cell surface receptors like CD-19 or CD-20 could be quantified on a cell-by-cell basis with SC-ICP-MS using the biotinylated antibody and streptavidin quantum dots protocol. Currently techniques such as RNA sequencing or flow cytometry are unable to quantify the actual number of expressed surface markers on individual B cells. The quantum dot labeling approach with SC-ICP-MS could be used to meet this need. Such an approach could be potentially applied to monitor genetic drift of surface markers or be used in patient samples to quantify if clinically relevant surface markers are overexpressed. Moreover, this approach could determine how heterogenous the expression of surface markers is on a single cell level which may help guide clinicians treat cancers such as leukemia. This approach could be accomplished with different compositions of streptavidin quantum dots consisting of indium gallium nitride or streptavidin silver nanoparticles as opposed to cadmium selenide. These nanomaterials have elements with more abundant isotopes (^{115}In ~96% abundance or ^{107}Ag ~51% abundance) that would enhance the signal intensities on single cells compared to the eight isotopes of cadmium that have a maximum abundance of ~30%. In short, single cell ICP-MS offers researchers a simple quantitative method for analyzing nanoparticle-cell interactions that can facilitate the clinical translation of more nano-based therapies and diagnostics.

In this dissertation, unique elemental analysis protocols were developed to quantify alterations in the physicochemical properties of engineered nanoparticles. SP-ICP-MS was employed to quantify a diverse array of individual nanoparticle sizes, masses, aggregation states, and chemical compositions. To date, changes to these critical physicochemical nanoparticle properties in response to chemical stimuli had yet to be quantified *in situ* with

high throughput. These novel findings detailed the heterogeneity of engineered nanoparticles and the diversity of their corresponding transformations. In addition to measuring single nanoparticle physicochemical properties, the cellular uptake of engineered nanoparticles was quantified with single cell resolution. In conclusion, the data from these newly established elemental analysis procedures can be used to fine tune single nanoparticle properties and their subsequent cellular interactions which can enhance the clinical translation of future nanomaterials.

References

(1) Kim, B. Y. S.; Rutka, J. T.; Chan, W. C. W. Nanomedicine. *N. Engl. J. Med.* **2010**, *365* (25), 2434–2442. https://doi.org/10.1016/j.lab.2005.11.011.

(2) Pelaz, B.; Alexiou, C.; Alvarez-Puebla, R. A.; Alves, F.; Andrews, A. M.; Ashraf, S.; Balogh, L. P.; Ballerini, L.; Bestetti, A.; Brendel, C.; Bosi, S.; Carril, M.; Chan, W. C. W.; Chen, C.; Chen, X.; Chen, X.; Cheng, Z.; Cui, D.; Du, J.; Dullin, C.; Escudero, A.; Feliu, N.; Gao, M.; George, M.; Gogotsi, Y.; Grünweller, A.; Gu, Z.; Halas, N. J.; Hampp, N.; Hartmann, R. K.; Hersam, M. C.; Hunziker, P.; Jian, J.; Jiang, X.; Jungebluth, P.; Kadhiresan, P.; Kataoka, K.; Khademhosseini, A.; Kopeček, J.; Kotov, N. A.; Krug, H. F.; Lee, D. S.; Lehr, C. M.; Leong, K. W.; Liang, X. J.; Lim, M. L.; Liz-Marzán, L. M.; Ma, X.; Macchiarini, P.; Meng, H.; Möhwald, H.; Mulvaney, P.; Nel, A. E.; Nie, S.; Nordlander, P.; Okano, T.; Oliveira, J.; Park, T. H.; Penner, R. M.; Prato, M.; Puntes, V.; Rotello, V. M.; Samarakoon, A.; Schaak, R. E.; Shen, Y.; Sjöqvist, S.; Skirtach, A. G.; Soliman, M. G.; Stevens, M. M.; Sung, H. W.; Tang, B. Z.; Tietze, R.; Udugama, B. N.; Scott VanEpps, J.; Weil, T.; Weiss, P. S.; Willner, I.; Wu, Y.; Yang, L.; Yue, Z.; Zhang, Q.; Zhang, Q.; Zhang, X. E.; Zhao, Y.; Zhou, X.; Parak, W. J. Diverse Applications of Nanomedicine. *ACS Nano* **2017**, *11* (3), 2313–2381. https://doi.org/10.1021/acsnano.6b06040.

(3) Björnmalm, M.; Thurecht, K. J.; Michael, M.; Scott, A. M.; Caruso, F. Bridging Bio-Nano Science and Cancer Nanomedicine. *ACS Nano* **2017**, *11* (10), 9594–9613. https://doi.org/10.1021/acsnano.7b04855.

(4) Wilhelm, S.; Tavares, A. J.; Dai, Q.; Ohta, S.; Audet, J.; Dvorak, H. F.; Chan, W. C. W. Analysis of Nanoparticle Delivery to Tumours. *Nat. Rev. Mater.* **2016**, *1* (5), 16014. https://doi.org/10.1038/natrevmats.2016.14.

(5) Rosenblum, D.; Joshi, N.; Tao, W.; Karp, J. M.; Peer, D. Progress and Challenges towards Targeted Delivery of Cancer Therapeutics. *Nat. Commun.* **2018**, *9* (1). https://doi.org/10.1038/s41467-018-03705-y.

(6) von Roemeling, C.; Jiang, W.; Chan, C. K.; Weissman, I. L.; Kim, B. Y. S. Breaking Down the Barriers to Precision Cancer Nanomedicine. *Trends Biotechnol.* **2017**, *35* (2), 159–171. https://doi.org/10.1016/j.tibtech.2016.07.006.

(7) Nel, A. E.; Mädler, L.; Velegol, D.; Xia, T.; Hoek, E. M. V.; Somasundaran, P.; Klaessig, F.; Castranova, V.; Thompson, M. Understanding Biophysicochemical Interactions at the Nano-Bio Interface. *Nat. Mater.* **2009**, *8* (7), 543–557. https://doi.org/10.1038/nmat2442.

(8) Ke, P. C.; Lin, S.; Parak, W. J.; Davis, T. P.; Caruso, F. A Decade of the Protein Corona. *ACS Nano* **2017**, *11* (12), 11773–11776. https://doi.org/10.1021/acsnano.7b08008.

(9) Hühn, J.; Carrillo-Carrion, C.; Soliman, M. G.; Pfeiffer, C.; Valdeperez, D.; Masood, A.; Chakraborty, I.; Zhu, L.; Gallego, M.; Yue, Z.; Carril, M.; Feliu, N.; Escudero, A.; Alkilany, A. M.; Pelaz, B.; Pino, P. Del; Parak, W. J. Selected Standard Protocols for the Synthesis, Phase Transfer, and Characterization of Inorganic Colloidal Nanoparticles. *Chem. Mater.* **2017**, *29* (1), 399–461. https://doi.org/10.1021/acs.chemmater.6b04738.

(10) Mahmoudi, M.; Bertrand, N.; Zope, H.; Farokhzad, O. C. Emerging Understanding of the Protein Corona at the Nano-Bio Interfaces. *Nano Today* **2016**, *11* (6), 817–

832. https://doi.org/10.1016/j.nantod.2016.10.005.
(11) Walkey, C. D.; Chan, W. C. W. Understanding and Controlling the Interaction of Nanomaterials with Proteins in a Physiological Environment. *Chem. Soc. Rev.* **2012**, *41* (7), 2780–2799. https://doi.org/10.1039/c1cs15233e.
(12) Albanese, A.; Tang, P. S.; Chan, W. C. W. The Effect of Nanoparticle Size, Shape, and Surface Chemistry on Biological Systems. *Annu. Rev. Biomed. Eng.* **2012**, *14* (1), 1–16. https://doi.org/10.1146/annurev-bioeng-071811-150124.
(13) Monopoli, M. P.; Åberg, C.; Salvati, A.; Dawson, K. A. Biomolecular Coronas Provide the Biological Identity of Nanosized Materials. *Nat. Nanotechnol.* **2012**, *7* (12), 779–786. https://doi.org/10.1038/nnano.2012.207.
(14) Fleischer, C. C.; Payne, C. K. Nanoparticle-Cell Interactions: Molecular Structure of the Protein Corona and Cellular Outcomes. *Acc. Chem. Res.* **2014**, *47* (8), 2651–2659. https://doi.org/10.1021/ar500190q.
(15) Ritz, S.; Schöttler, S.; Kotman, N.; Baier, G.; Musyanovych, A.; Kuharev, J.; Landfester, K.; Schild, H.; Jahn, O.; Tenzer, S.; Mailänder, V. Protein Corona of Nanoparticles: Distinct Proteins Regulate the Cellular Uptake. *Biomacromolecules* **2015**, *16* (4), 1311–1321. https://doi.org/10.1021/acs.biomac.5b00108.
(16) Walkey, C. D.; Olsen, J. B.; Song, F.; Liu, R.; Guo, H.; Olsen, D. W. H.; Cohen, Y.; Emili, A.; Chan, W. C. W. Protein Corona Fingerprinting Predicts the Cellular Interaction of Gold and Silver Nanoparticles. *ACS Nano* **2014**, *8* (3), 2439–2455. https://doi.org/10.1021/nn406018q.
(17) Walkey, C. D.; Olsen, J. B.; Guo, H.; Emili, A.; Chan, W. C. W. Nanoparticle Size and Surface Chemistry Determine Serum Protein Adsorption and Macrophage Uptake. *J. Am. Chem. Soc.* **2012**, *134* (4), 2139–2147. https://doi.org/10.1021/ja2084338.
(18) Dai, Q.; Wilhelm, S.; Ding, D.; Syed, A. M.; Sindhwani, S.; Zhang, Y.; Chen, Y. Y.; Macmillan, P.; Chan, W. C. W. Quantifying the Ligand-Coated Nanoparticle Delivery to Cancer Cells in Solid Tumors. *ACS Nano* **2018**, *12* (8), 8423–8435. https://doi.org/10.1021/acsnano.8b03900.
(19) Blanco, E.; Shen, H.; Ferrari, M. Principles of Nanoparticle Design for Overcoming Biological Barriers to Drug Delivery. *Nat. Biotechnol.* **2015**, *33* (9), 941–951. https://doi.org/10.1038/nbt.3330.
(20) Chauhan, V. P.; Jain, R. K. Strategies for Advancing Cancer Nanomedicine. *Nat. Mater.* **2013**, *12* (11), 958–962. https://doi.org/10.1038/nmat3792.
(21) Xu, X.; Ho, W.; Zhang, X.; Bertrand, N.; Farokhzad, O. Cancer Nanomedicine: From Targeted Delivery to Combination Therapy. *Trends Mol. Med.* **2015**, *21* (4), 223–232. https://doi.org/10.1016/j.molmed.2015.01.001.
(22) Kirpotin, D. B.; Drummond, D. C.; Shao, Y.; Shalaby, M. R.; Hong, K.; Nielsen, U. B.; Marks, J. D.; Benz, C. C.; Park, J. W. Antibody Targeting of Long-Circulating Lipidic Nanoparticles Does Not Increase Tumor Localization but Does Increase Internalization in Animal Models. *Cancer Res.* **2006**, *66* (13), 6732–6740. https://doi.org/10.1158/0008-5472.CAN-05-4199.
(23) Davis, M. E.; Zuckerman, J. E.; Choi, C. H. J.; Seligson, D.; Tolcher, A.; Alabi, C. A.; Yen, Y.; Heidel, J. D.; Ribas, A. Evidence of RNAi in Humans from Systemically Administered SiRNA via Targeted Nanoparticles. *Nature* **2010**, *464* (7291), 1067–1070. https://doi.org/10.1038/nature08956.

(24) Pecot, C. V.; Calin, G. A.; Coleman, R. L.; Lopez-Berestein, G.; Sood, A. K. RNA Interference in the Clinic: Challenges and Future Directions. *Nat. Rev. Cancer* **2011**, *11* (1), 59–67. https://doi.org/10.1038/nrc2966.

(25) Lee, K.; Conboy, M.; Park, H. M.; Jiang, F.; Kim, H. J.; Dewitt, M. A.; Mackley, V. A.; Chang, K.; Rao, A.; Skinner, C.; Shobha, T.; Mehdipour, M.; Liu, H.; Huang, W. C.; Lan, F.; Bray, N. L.; Li, S.; Corn, J. E.; Kataoka, K.; Doudna, J. A.; Conboy, I.; Murthy, N. Nanoparticle Delivery of Cas9 Ribonucleoprotein and Donor DNA in Vivo Induces Homology-Directed DNA Repair. *Nat. Biomed. Eng.* **2017**, *1* (11), 889–901. https://doi.org/10.1038/s41551-017-0137-2.

(26) Kodiha, M.; Wang, Y. M.; Hutter, E.; Maysinger, D.; Stochaj, U. Off to the Organelles - Killing Cancer Cells with Targeted Gold Nanoparticles. *Theranostics* **2015**, *5* (4), 357–370. https://doi.org/10.7150/thno.10657.

(27) Ali, M. R. K.; Wu, Y.; Ghosh, D.; Do, B. H.; Chen, K.; Dawson, M. R.; Fang, N.; Sulchek, T. A.; El-Sayed, M. A. Nuclear Membrane-Targeted Gold Nanoparticles Inhibit Cancer Cell Migration and Invasion. *ACS Nano* **2017**, *11* (4), 3716–3726. https://doi.org/10.1021/acsnano.6b08345.

(28) Panariti, A.; Miserocchi, G.; Rivolta, I. The Effect of Nanoparticle Uptake on Cellular Behavior: Disrupting or Enabling Functions? *Nanotechnol. Sci. Appl.* **2012**, *5*, 87–100. https://doi.org/10.2147/NSA.S25515.

(29) Clift, M. J. D.; Brandenberger, C.; Rothen-Rutishauser, B.; Brown, D. M.; Stone, V. The Uptake and Intracellular Fate of a Series of Different Surface Coated Quantum Dots in Vitro. *Toxicology* **2011**, *286* (1–3), 58–68. https://doi.org/10.1016/j.tox.2011.05.006.

(30) Chen, J.; Yu, Z.; Chen, H.; Gao, J.; Liang, W. Transfection Efficiency and Intracellular Fate of Polycation Liposomes Combined with Protamine. *Biomaterials* **2011**, *32* (5), 1412–1418. https://doi.org/10.1016/j.biomaterials.2010.09.074.

(31) Irvine, D. J.; Hanson, M. C.; Rakhra, K.; Tokatlian, T. Synthetic Nanoparticles for Vaccines and Immunotherapy. *Chem. Rev.* **2015**, *115* (19), 11109–11146. https://doi.org/10.1021/acs.chemrev.5b00109.

(32) Gleeson, P. A. The Role of Endosomes in Innate and Adaptive Immunity. *Semin. Cell Dev. Biol.* **2014**, *31*, 64–72. https://doi.org/10.1016/j.semcdb.2014.03.002.

(33) McMahon, H. T.; Boucrot, E. Molecular Mechanism and Physiological Functions of Clathrin-Mediated Endocytosis. *Nat. Rev. Mol. Cell Biol.* **2011**, *12* (8), 517–533. https://doi.org/10.1038/nrm3151.

(34) Muñoz, A.; Costa, M. Elucidating the Mechanisms of Nickel Compound Uptake: A Review of Particulate and Nano-Nickel Endocytosis and Toxicity. *Toxicol. Appl. Pharmacol.* **2012**, *260* (1), 1–16. https://doi.org/10.1016/j.taap.2011.12.014.

(35) Kaksonen, M.; Roux, A. Mechanisms of Clathrin-Mediated Endocytosis. *Nat. Rev. Mol. Cell Biol.* **2018**, *19* (5), 313–326. https://doi.org/10.1038/nrm.2017.132.

(36) Mattila, J. P.; Shnyrova, A. V.; Sundborger, A. C.; Hortelano, E. R.; Fuhrmans, M.; Neumann, S.; Müller, M.; Hinshaw, J. E.; Schmid, S. L.; Frolov, V. A. A Hemi-Fission Intermediate Links Two Mechanistically Distinct Stages of Membrane Fission. *Nature* **2015**, *524* (7563), 109–113. https://doi.org/10.1038/nature14509.

(37) Decuzzi, P.; Ferrari, M. The Receptor-Mediated Endocytosis of Nonspherical Particles. *Biophys. J.* **2008**, *94* (10), 3790–3797. https://doi.org/10.1529/biophysj.107.120238.

(38) Robertson, A. S.; Smythe, E.; Ayscough, K. R. Functions of Actin in Endocytosis. *Cell. Mol. Life Sci.* **2009**, *66* (13), 2049–2065. https://doi.org/10.1007/s00018-009-0001-y.
(39) Benyettou, F.; Rezgui, R.; Ravaux, F.; Jaber, T.; Blumer, K.; Jouiad, M.; Motte, L.; Olsen, J. C.; Platas-Iglesias, C.; Magzoub, M.; Trabolsi, A. Synthesis of Silver Nanoparticles for the Dual Delivery of Doxorubicin and Alendronate to Cancer Cells. *J. Mater. Chem. B* **2015**, *3* (36), 7237–7245. https://doi.org/10.1039/c5tb00994d.
(40) Anderson, R. G. W. The Caveolae Membrane System. *Annu. Rev. Biochem.* **1998**, *67* (1), 199–225. https://doi.org/10.1146/annurev.biochem.67.1.199.
(41) Carver, L. A.; Schnitzer, J. E. Caveolae: Mining Little Caves for New Cancer Targets. *Nat. Rev. Cancer* **2003**, *3* (8), 571–581. https://doi.org/10.1038/nrc1146.
(42) Conner, S. D.; Schmid, S. L. Regulated Portals of Entry into the Cell. *Nature* **2003**, *422* (6927), 37–44. https://doi.org/10.1038/nature01451.
(43) Yameen, B.; Choi, W. Il; Vilos, C.; Swami, A.; Shi, J.; Farokhzad, O. C. Insight into Nanoparticle Cellular Uptake and Intracellular Targeting. *J. Control. Release* **2014**, *190*, 485–499. https://doi.org/10.1016/j.jconrel.2014.06.038.
(44) Xin, X.; Pei, X.; Yang, X.; Lv, Y.; Zhang, L.; He, W.; Yin, L. Rod-Shaped Active Drug Particles Enable Efficient and Safe Gene Delivery. *Adv. Sci.* **2017**, *4* (11). https://doi.org/10.1002/advs.201700324.
(45) Wang, Z.; Tiruppathi, C.; Minshall, R. D.; Malik, A. B. Size and Dynamics of Caveolae Studied Using Nanoparticles in Living Endothelial Cells. *ACS Nano* **2009**, *3* (12), 4110–4116. https://doi.org/10.1021/nn9012274.
(46) Oh, P.; Testa, J. E.; Borgstrom, P.; Witkiewicz, H.; Li, Y.; Schnitzer, J. E. In Vivo Proteomic Imaging Analysis of Caveolae Reveals Pumping System to Penetrate Solid Tumors. *Nat. Med.* **2014**, *20* (9), 1062–1068. https://doi.org/10.1038/nm.3623.
(47) Wang, Z.; Tiruppathi, C.; Cho, J.; Minshall, R. D.; Malik, A. B. Delivery of Nanoparticle-Complexed Drugs across the Vascular Endothelial Barrier via Caveolae. *IUBMB Life* **2011**, *63* (8), 659–667. https://doi.org/10.1002/iub.485.
(48) Frank, P. G.; Pavlides, S.; Lisanti, M. P. Caveolae and Transcytosis in Endothelial Cells: Role in Atherosclerosis. *Cell Tissue Res.* **2009**, *335* (1), 41–47. https://doi.org/10.1007/s00441-008-0659-8.
(49) Sheth, V.; Wang, L.; Bhattacharya, R.; Mukherjee, P.; Wilhelm, S. Strategies for Delivering Nanoparticles across Tumor Blood Vessels. *Adv. Funct. Mater.* **2021**, *31* (8), 2007363. https://doi.org/10.1002/ADFM.202007363.
(50) Kingston, B. R.; Lin, Z. P.; Ouyang, B.; MacMillan, P.; Ngai, J.; Syed, A. M.; Sindhwani, S.; Chan, W. C. W. Specific Endothelial Cells Govern Nanoparticle Entry into Solid Tumors. *ACS Nano* **2021**. https://doi.org/10.1021/ACSNANO.1C04510.
(51) Lajoie, P.; Nabi, I. R. Regulation of Raft-Dependent Endocytosis. *J. Cell. Mol. Med.* **2007**, *11* (4), 644–653. https://doi.org/10.1111/j.1582-4934.2007.00083.x.
(52) Chinnapen, D. J. F.; Chinnapen, H.; Saslowsky, D.; Lencer, W. I. Rafting with Cholera Toxin: Endocytosis and Trafficking from Plasma Membrane to ER. *FEMS Microbiol. Lett.* **2007**, *266* (2), 129–137. https://doi.org/10.1111/j.1574-6968.2006.00545.x.
(53) Foerg, C.; Ziegler, U.; Fernandez-Carneado, J.; Giralt, E.; Rennert, R.; Beck-

Sickinger, A. G.; Merkle, H. P. Decoding the Entry of Two Novel Cell-Penetrating Peptides in HeLa Cells: Lipid Raft-Mediated Endocytosis and Endosomal Escape. *Biochemistry* **2005**, *44* (1), 72–81. https://doi.org/10.1021/bi048330+.

(54) Chen, X.; Shank, S.; Davis, P. B.; Ziady, A. G. Nucleolin-Mediated Cellular Trafficking of DNA Nanoparticle Is Lipid Raft and Microtubule Dependent and Can Be Modulated by Glucocorticoid. *Mol. Ther.* **2011**, *19* (1), 93–102. https://doi.org/10.1038/mt.2010.214.

(55) Jiang, Y.; Yan, B.; Tang, R.; Duncan, B.; Jiang, Z.; Rotello, V. M.; Mout, R. Direct Cytosolic Delivery of SiRNA Using Nanoparticle-Stabilized Nanocapsules. *Angew. Chemie Int. Ed.* **2014**, 506–510. https://doi.org/10.1002/anie.201409161.

(56) Martínez-Riaño, A.; Bovolenta, E. R.; Mendoza, P.; Oeste, C. L.; Martín-Bermejo, M. J.; Bovolenta, P.; Turner, M.; Martínez-Martín, N.; Alarcón, B. Antigen Phagocytosis by B Cells Is Required for a Potent Humoral Response. *EMBO Rep.* **2018**, e46016. https://doi.org/10.15252/embr.201846016.

(57) Chen, F.; Wang, G.; Grif, J. I.; Brenneman, B.; Banda, N. K.; Holers, V. M.; Backos, D. S.; Wu, L.; Moghimi, S. M.; Simberg, D. Complement Proteins Bind to Nanoparticle Protein Corona and Undergo Dynamic Exchange in Vivo Fangfang. *Nat. Nanotechnol.* **2017**, *12* (April). https://doi.org/10.1038/nnano.2016.269.

(58) Tavano, R.; Gabrielli, L.; Lubian, E.; Fedeli, C.; Visentin, S.; Laureto, P. P. De; Arrigoni, G.; Ge, A.; Chen, F.; Simberg, D.; Morgese, G.; Benetti, E. M.; Wu, L.; Moghimi, S. M.; Mancin, F.; Papini, E. C1q-Mediated Complement Activation and C3 Opsonization Trigger Recognition of Stealth Poly(2-Methyl-2-Oxazoline)-Coated Silica Nanoparticles by Human Phagocytes. *ACS Nano* **2018**, *12*, 5834–5847. https://doi.org/10.1021/acsnano.8b01806.

(59) Stuart, L. M.; Ezekowitz, R. A. B. Phagocytosis: Elegant Complexity. *Immunity* **2005**, *22*, 539–550. https://doi.org/10.1016/j.immuni.2005.05.002.

(60) Sahay, G.; Alakhova, D. Y.; Kabanov, A. V. Endocytosis of Nanomedicines. *J. Control. Release* **2010**, *145* (3), 182–195. https://doi.org/10.1016/j.jconrel.2010.01.036.

(61) Zhang, Y. N.; Poon, W.; Tavares, A. J.; McGilvray, I. D.; Chan, W. C. W. Nanoparticle–Liver Interactions: Cellular Uptake and Hepatobiliary Elimination. *J. Control. Release* **2016**, *240*, 332–348. https://doi.org/10.1016/j.jconrel.2016.01.020.

(62) Lazarovits, J.; Chen, Y. Y.; Sykes, E. A.; Chan, W. C. W. Nanoparticle-Blood Interactions: The Implications on Solid Tumour Targeting. *Chem. Commun.* **2015**, *51* (14), 2756–2767. https://doi.org/10.1039/c4cc07644c.

(63) Tsoi, K. M.; Macparland, S. A.; Ma, X. Z.; Spetzler, V. N.; Echeverri, J.; Ouyang, B.; Fadel, S. M.; Sykes, E. A.; Goldaracena, N.; Kaths, J. M.; Conneely, J. B.; Alman, B. A.; Selzner, M.; Ostrowski, M. A.; Adeyi, O. A.; Zilman, A.; McGilvray, I. D.; Chan, W. C. W. Mechanism of Hard-Nanomaterial Clearance by the Liver. *Nat. Mater.* **2016**, *15* (11), 1212–1221. https://doi.org/10.1038/nmat4718.

(64) Dai, Q.; Walkey, C.; Chan, W. C. W. Polyethylene Glycol Backfilling Mitigates the Negative Impact of the Protein Corona on Nanoparticle Cell Targeting. *Angew. Chemie - Int. Ed.* **2014**, *53* (20), 5093–5096. https://doi.org/10.1002/anie.201309464.

(65) Li, Y.; Kröger, M.; Liu, W. K. Endocytosis of PEGylated Nanoparticles

Accompanied by Structural and Free Energy Changes of the Grafted Polyethylene Glycol. *Biomaterials* **2014**, *35* (30), 8467–8478. https://doi.org/10.1016/J.BIOMATERIALS.2014.06.032.

(66) Ichihara, M.; Shimizu, T.; Imoto, A.; Hashiguchi, Y.; Uehara, Y.; Ishida, T.; Kiwada, H. Anti-PEG IgM Response against PEGylated Liposomes in Mice and Rats. *Pharmaceutics* **2011**, *3* (1), 1–11. https://doi.org/10.3390/pharmaceutics3010001.

(67) Shah, S.; Prematta, T.; Adkinson, N. F.; Ishmael, F. T. Hypersensitivity to Polyethylene Glycols. *J. Clin. Pharmacol.* **2013**, *53* (3), 352–355. https://doi.org/10.1177/0091270012447122.

(68) Rodriguez, P. L.; Harada, T.; Christian, D. A.; Pantano, D. A.; Tsai, R. K.; Discher, D. E. Minimal " Self " Peptides That Inhibit Delivery of Nanoparticles. *Science (80-.).* **2013**, *339* (6122), 971–976. https://doi.org/10.1126/science.1229568.

(69) Sosale, N. G.; Ivanovska, I. I.; Tsai, R. K.; Swift, J.; Hsu, J. W.; Alvey, C. M.; Zoltick, P. W.; Discher, D. E. "Marker of Self" CD47 on Lentiviral Vectors Decreases Macrophage-Mediated Clearance and Increases Delivery to SIRPA-Expressing Lung Carcinoma Tumors. *Mol. Ther. - Methods Clin. Dev.* **2016**, *3* (May), 16080. https://doi.org/10.1038/mtm.2016.80.

(70) Kerr, M. C.; Teasdale, R. D. Defining Macropinocytosis. *Traffic* **2009**, *10* (4), 364–371. https://doi.org/10.1111/j.1600-0854.2009.00878.x.

(71) Mercer, J.; Helenius, A. Virus Entry by Macropinocytosis. *Nat. Cell Biol.* **2009**, *11* (5), 510–520. https://doi.org/10.1038/ncb0509-510.

(72) Falcone, S.; Cocucci, E.; Podini, P.; Kirchhausen, T.; Clementi, E.; Meldolesi, J. Macropinocytosis: Regulated Coordination of Endocytic and Exocytic Membrane Traffic Events. *J. Cell Sci.* **2006**, *119* (22), 4758–4769. https://doi.org/10.1242/jcs.03238.

(73) Wadia, J. S.; Stan, R. V.; Dowdy, S. F. Transducible TAT-HA Fusogenic Peptide Enhances Escape of TAT-Fusion Proteins after Lipid Raft Macropinocytosis. *Nat. Med.* **2004**, *10* (3), 310–315. https://doi.org/10.1038/nm996.

(74) Love, K. T.; Mahon, K. P.; Christopher, G.; Whitehead, K. A.; Querbes, W.; Robert, J.; Qin, J.; Cantley, W.; Qin, L. L.; Frank-kamenetsky, M.; Yip, K. N.; Alvarez, R.; Sah, D. W. Y.; Fougerolles, A. De; Fitzgerald, K.; Koteliansky, V.; Akinc, A.; Langer, R.; Daniel, G.; Love, K. T.; Mahon, K. P.; Levins, C. G.; Whitehead, K. A.; Querbes, W.; Robert, J. Correction for Love et Al., Lipid-like Materials for Low-Dose, in Vivo Gene Silencing. *Proc. Natl. Acad. Sci.* **2010**, *107* (21), 9915–9915. https://doi.org/10.1073/pnas.1005136107.

(75) Diken, M.; Kreiter, S.; Selmi, A.; Britten, C. M.; Huber, C.; Türeci, Ö.; Sahin, U. Selective Uptake of Naked Vaccine RNA by Dendritic Cells Is Driven by Macropinocytosis and Abrogated upon DC Maturation. *Gene Ther.* **2011**, *18* (7), 702–708. https://doi.org/10.1038/gt.2011.17.

(76) Hirosue, S.; Kourtis, I. C.; van der Vlies, A. J.; Hubbell, J. A.; Swartz, M. A. Antigen Delivery to Dendritic Cells by Poly(Propylene Sulfide) Nanoparticles with Disulfide Conjugated Peptides: Cross-Presentation and T Cell Activation. *Vaccine* **2010**, *28* (50), 7897–7906. https://doi.org/10.1016/j.vaccine.2010.09.077.

(77) Cullis, J.; Siolas, D.; Avanzi, A.; Barui, S.; Maitra, A.; Bar-Sagi, D. Macropinocytosis of Nab-Paclitaxel Drives Macrophage Activation in Pancreatic

Cancer. *Cancer Immunol. Res.* **2017**, *5* (3), 182–190. https://doi.org/10.1158/2326-6066.CIR-16-0125.

(78) Van Lehn, R. C.; Atukorale, P. U.; Carney, R. P.; Yang, Y. S.; Stellacci, F.; Irvine, D. J.; Alexander-Katz, A. Effect of Particle Diameter and Surface Composition on the Spontaneous Fusion of Monolayer-Protected Gold Nanoparticles with Lipid Bilayers. *Nano Lett.* **2013**, *13* (9), 4060–4067. https://doi.org/10.1021/nl401365n.

(79) Yang, K.; Ma, Y. Q. Computer Simulation of the Translocation of Nanoparticles with Different Shapes across a Lipid Bilayer. *Nat. Nanotechnol.* **2010**, *5* (8), 579–583. https://doi.org/10.1038/nnano.2010.141.

(80) Heikkilä, E.; Martinez-Seara, H.; Gurtovenko, A. A.; Javanainen, M.; Häkkinen, H.; Vattulainen, I.; Akola, J. Cationic Au Nanoparticle Binding with Plasma Membrane-like Lipid Bilayers: Potential Mechanism for Spontaneous Permeation to Cells Revealed by Atomistic Simulations. *J. Phys. Chem. C* **2014**, *118* (20), 11131–11141. https://doi.org/10.1021/jp5024026.

(81) Song, B.; Yuan, H.; Pham, S. V.; Jameson, C. J.; Murad, S. Nanoparticle Permeation Induces Water Penetration, Ion Transport, and Lipid Flip-Flop. *Langmuir* **2012**, *28* (49), 16989–17000. https://doi.org/10.1021/la302879r.

(82) Pogodin, S.; Werner, M.; Sommer, J. U.; Baulin, V. A. Nanoparticle-Induced Permeability of Lipid Membranes. *ACS Nano* **2012**, *6* (12), 10555–10561. https://doi.org/10.1021/nn3028858.

(83) Hinde, E.; Thammasiraphop, K.; Duong, H. T. T.; Yeow, J.; Karagoz, B.; Boyer, C.; Gooding, J. J.; Gaus, K. Pair Correlation Microscopy Reveals the Role of Nanoparticle Shape in Intracellular Transport and Site of Drug Release. *Nat. Nanotechnol.* **2017**, *12* (1), 81–89. https://doi.org/10.1038/nnano.2016.160.

(84) Wang, T.; Bai, J.; Jiang, X.; Nienhaus, G. U. Cellular Uptake of Nanoparticles by Membrane Penetration: A Study Combining Confocal Microscopy with FTIR Spectroelectrochemistry. *ACS Nano* **2012**, *6* (2), 1251–1259. https://doi.org/10.1021/nn203892h.

(85) Jiang, Y.; Huo, S.; Mizuhara, T.; Das, R.; Lee, Y. W.; Hou, S.; Moyano, D. F.; Duncan, B.; Liang, X. J.; Rotello, V. M. The Interplay of Size and Surface Functionality on the Cellular Uptake of Sub-10 Nm Gold Nanoparticles. *ACS Nano* **2015**, *9* (10), 9986–9993. https://doi.org/10.1021/acsnano.5b03521.

(86) Jewell, C. M.; Jung, J. M.; Atukorale, P. U.; Carney, R. P.; Stellacci, F.; Irvine, D. J. Oligonucleotide Delivery by Cell-Penetrating "Striped" Nanoparticles. *Angew. Chemie - Int. Ed.* **2011**, *50* (51), 12312–12315. https://doi.org/10.1002/anie.201104514.

(87) Verma, A.; Uzun, O.; Hu, Y.; Hu, Y.; Han, H.; Watson, N.; Chen, S.; Irvine, D. J.; Stellacci, F. Surface-Structure-Regulated Cell-Membrane Penetration by Monolayer-Protected Nanoparticles. **2008**, *7* (July). https://doi.org/10.1038/nmat2202.

(88) Copolovici, D. M.; Langel, K.; Eriste, E. Cell-Penetrating Peptides: Design, Synthesis, and Applications ¨. *ACS Nano* **2014**, No. 3, 1972–1994. https://doi.org/10.1021/nn4057269.

(89) Rydströ M, A.; Deshayes, S.; Konate, K.; Crombez, L.; Padari, K. Direct Translocation as Major Cellular Uptake for CADY Self-Assembling Peptide-Based Nanoparticles. *PLoS One* **2011**, *6* (10), 25924.

https://doi.org/10.1371/journal.pone.0025924.
(90) Guterstam, P.; Madani, F.; Hirose, H.; Takeuchi, T.; Futaki, S.; El, S.; Gräslund, A.; Langel, Ü. Elucidating Cell-Penetrating Peptide Mechanisms of Action for Membrane Interaction , Cellular Uptake , and Translocation Utilizing the Hydrophobic Counter-Anion Pyrenebutyrate. *BBA - Biomembr.* **2009**, *1788* (12), 2509–2517. https://doi.org/10.1016/j.bbamem.2009.09.014.
(91) Kauffman, W. B.; Fuselier, T.; He, J.; Wimley, W. C. Mechanism Matters: A Taxonomy of Cell Penetrating Peptides. *Trends Biochem. Sci.* **2015**, *40* (12), 749–764. https://doi.org/10.1016/j.tibs.2015.10.004.
(92) Sawant, R. R.; Patel, N. R.; Torchilin, V. P. Therapeutic Delivery Using Cell-Penetrating Peptides. *Eur. J. Nanomedicine* **2013**, *5* (3), 141–158. https://doi.org/10.1515/ejnm-2013-0005.
(93) Deshayes, S.; Morris, M. C.; Divita, G.; Heitz, F. Cell-Penetrating Pep Tides: Tools for Intracellular Delivery of Therapeutics. *Cell. Mol. Life Sci.* **2005**, *62* (16), 1839–1849. https://doi.org/10.1007/s00018-005-5109-0.
(94) Lin, Q.; Jin, H.; Yang, M.; Chen, J.; Zheng, G.; Lovell, J. F.; Zhang, Z.; Ding, L.; Ng, K. K. Efficient Cytosolic Delivery of SiRNA Using HDL-Mimicking Nanoparticles. *Small* **2011**, *7* (5), 568–573. https://doi.org/10.1002/smll.201001589.
(95) Steinbach, J. M.; Seo, Y.; Saltzman, W. M. Cell Penetrating Peptide-Modified Poly (Lactic-Co-Glycolic Acid) Nanoparticles with Enhanced Cell Internalization. *Acta Biomater.* **2016**, *30*, 49–61. https://doi.org/10.1016/j.actbio.2015.11.029.
(96) Qian, Z.; Martyna, A.; Hard, R. L.; Wang, J.; Appiah-kubi, G.; Coss, C.; Phelps, M. A.; Rossman, J. S.; Pei, D. Discovery and Mechanism of Highly Efficient Cyclic Cell-Penetrating Peptides. *Biochemistry* **2016**, *55*, 2601–2612. https://doi.org/10.1021/acs.biochem.6b00226.
(97) Kleusch, C.; Hersch, N.; Hoffmann, B.; Merkel, R.; Csiszár, A. Fluorescent Lipids: Functional Parts of Fusogenic Liposomes and Tools for Cell Membrane Labeling and Visualization. *Molecules* **2012**, *17* (1), 1055–1073. https://doi.org/10.3390/molecules17011055.
(98) Kube, S.; Hersch, N.; Naumovska, E.; Gensch, T.; Hendriks, J.; Franzen, A.; Landvogt, L.; Siebrasse, J. P.; Kubitscheck, U.; Hoffmann, B.; Merkel, R.; Csiszár, A. Fusogenic Liposomes as Nanocarriers for the Delivery of Intracellular Proteins. *Langmuir* **2017**, *33* (4), 1051–1059. https://doi.org/10.1021/acs.langmuir.6b04304.
(99) He, S.; Fan, W.; Wu, N.; Zhu, J.; Miao, Y.; Miao, X.; Li, F.; Zhang, X.; Gan, Y. Lipid-Based Liquid Crystalline Nanoparticles Facilitate Cytosolic Delivery of SiRNA via Structural Transformation. *Nano Lett.* **2018**, *18* (4), 2411–2419. https://doi.org/10.1021/acs.nanolett.7b05430.
(100) Kim, B.; Pang, H. B.; Kang, J.; Park, J. H.; Ruoslahti, E.; Sailor, M. J. Immunogene Therapy with Fusogenic Nanoparticles Modulates Macrophage Response to Staphylococcus Aureus. *Nat. Commun.* **2018**, *9* (1). https://doi.org/10.1038/s41467-018-04390-7.
(101) Atukorale, P. U.; Guven, Z. P.; Bekdemir, A.; Carney, R. P.; Van Lehn, R. C.; Yun, D. S.; Jacob Silva, P. H.; Demurtas, D.; Yang, Y. S.; Alexander-Katz, A.; Stellacci, F.; Irvine, D. J. Structure-Property Relationships of Amphiphilic Nanoparticles That Penetrate or Fuse Lipid Membranes. *Bioconjug. Chem.* **2018**, *29* (4), 1131–1140. https://doi.org/10.1021/acs.bioconjchem.7b00777.

(102) Yuba, E.; Kanda, Y.; Yoshizaki, Y.; Teranishi, R.; Harada, A.; Sugiura, K.; Izawa, T.; Yamate, J.; Sakaguchi, N.; Koiwai, K.; Kono, K. PH-Sensitive Polymer-Liposome-Based Antigen Delivery Systems Potentiated with Interferon-γ Gene Lipoplex for Efficient Cancer Immunotherapy. *Biomaterials* **2015**, *67*, 214–224. https://doi.org/10.1016/j.biomaterials.2015.07.031.
(103) Liang, S. Designing Self-Amplifying Replicons for Transient Gene Expression of Interleukin-18. *Harvard Univ. ProQuest Diss. Publ.* **2021**.
(104) Saulis, G.; Saule, R. Size of the Pores Created by an Electric Pulse: Microsecond vs Millisecond Pulses. *Biochim. Biophys. Acta - Biomembr.* **2012**, *1818* (12), 3032–3039. https://doi.org/10.1016/j.bbamem.2012.06.018.
(105) Kim, T.; Momin, E.; Choi, J.; Yuan, K.; Zaidi, H.; Kim, J.; Park, M.; Lee, N.; McMahon, M. T.; Quinones-Hinojosa, A.; Bulte, J. W. M.; Hyeon, T.; Gilad, A. A. Mesoporous Silica-Coated Hollow Manganese Oxide Nanoparticles as Positive T1contrast Agents for Labeling and MRI Tracking of Adipose-Derived Mesenchymal Stem Cells. *J. Am. Chem. Soc.* **2011**, *133* (9), 2955–2961. https://doi.org/10.1021/ja1084095.
(106) Hobo, W.; Novobrantseva, T. I.; Fredrix, H.; Wong, J.; Milstein, S.; Epstein-Barash, H.; Liu, J.; Schaap, N.; Van Der Voort, R.; Dolstra, H. Improving Dendritic Cell Vaccine Immunogenicity by Silencing PD-1 Ligands Using SiRNA-Lipid Nanoparticles Combined with Antigen MRNA Electroporation. *Cancer Immunol. Immunother.* **2013**, *62* (2), 285–297. https://doi.org/10.1007/s00262-012-1334-1.
(107) Boukany, P. E.; Morss, A.; Liao, W. C.; Henslee, B.; Jung, H.; Zhang, X.; Yu, B.; Wang, X.; Wu, Y.; Li, L.; Gao, K.; Hu, X.; Zhao, X.; Hemminger, O.; Lu, W.; Lafyatis, G. P.; Lee, L. J. Nanochannel Electroporation Delivers Precise Amounts of Biomolecules into Living Cells. *Nat. Nanotechnol.* **2011**, *6* (11), 747–754. https://doi.org/10.1038/nnano.2011.164.
(108) Chang, L.; Bertani, P.; Gallego-Perez, D.; Yang, Z.; Chen, F.; Chiang, C.; Malkoc, V.; Kuang, T.; Gao, K.; Lee, L. J.; Lu, W. 3D Nanochannel Electroporation for High-Throughput Cell Transfection with High Uniformity and Dosage Control. *Nanoscale* **2016**, *8* (1), 243–252. https://doi.org/10.1039/c5nr03187g.
(109) Damalakiene, L.; Karabanovas, V.; Bagdonas, S.; Valius, M.; Rotomskis, R. Intracellular Distribution of Nontargeted Quantum Dots after Natural Uptake and Microinjection. *Int. J. Nanomedicine* **2013**, No. 8, 555–568.
(110) Candeloro, P.; Tirinato, L.; Malara, N.; Fregola, A.; Casals, E.; Puntes, V.; Perozziello, G.; Gentile, F.; Coluccio, L.; Das, G.; Liberale, C.; De, F. Nanoparticle Microinjection and Raman Spectroscopy as Tools for Nanotoxicology Studies. *Analyst* **2011**, 4402–4408. https://doi.org/10.1039/c1an15313g.
(111) Tang, P. S.; Sathiamoorthy, S.; Lustig, L. C.; Ponzielli, R.; Inamoto, I.; Penn, L. Z.; Shin, J. A.; Chan, W. C. W. The Role of Ligand Density and Size in Mediating Quantum Dot Nuclear Transport. *Small* **2014**, *10* (20), 4182–4192. https://doi.org/10.1002/smll.201401056.
(112) Martens, T. F.; Remaut, K.; Demeester, J.; De Smedt, S. C.; Braeckmans, K. Intracellular Delivery of Nanomaterials: How to Catch Endosomal Escape in the Act. *Nano Today* **2014**, *9* (3), 344–364. https://doi.org/10.1016/j.nantod.2014.04.011.
(113) Saha, K.; Kim, S. T.; Yan, B.; Miranda, O. R.; Alfonso, F. S.; Shlosman, D.; Rotello,

V. M. Surface Functionality of Nanoparticles Determines Cellular Uptake Mechanisms in Mammalian Cells. **2013**, No. 2, 300–305. https://doi.org/10.1002/smll.201201129.

(114) Serpooshan, V.; Sheibani, S.; Pushparaj, P.; Wojcik, M.; Jang, A. Y.; Santoso, M. R.; Jang, J. H.; Huang, H.; Safavi-Sohi, R.; Haghjoo, N.; Nejadnik, H.; Aghaverdi, H.; Vali, H.; Kinsella, J. M.; Presley, J.; Xu, K.; Yang, P. C. M.; Mahmoudi, M. Effect of Cell Sex on Uptake of Nanoparticles: The Overlooked Factor at the Nanobio Interface. *ACS Nano* **2018**, *12* (3), 2253–2266. https://doi.org/10.1021/acsnano.7b06212.

(115) Bohmer, N.; Jordan, A. Caveolin-1 and CDC42 Mediated Endocytosis of Silica-Coated Iron Oxide Nanoparticles in HeLa Cells. *Beilstein J. Nanotechnol.* **2015**, *6* (1), 167–176. https://doi.org/10.3762/bjnano.6.16.

(116) Agarwal, R.; Singh, V.; Jurney, P.; Shi, L.; Sreenivasan, S. V.; Roy, K. Mammalian Cells Preferentially Internalize Hydrogel Nanodiscs over Nanorods and Use Shape-Specific Uptake Mechanisms. *Proc. Natl. Acad. Sci.* **2013**, *110* (43), 17247–17252. https://doi.org/10.1073/pnas.1305000110.

(117) Chithrani, B. D.; Ghazani, A. A.; Chan, W. C. W. Determining the Size and Shape Dependence of Gold Nanoparticle Uptake into Mammalian Cells. *Nano Lett.* **2006**, *6* (4), 662–668. https://doi.org/10.1021/nl052396o.

(118) Jiang, W.; Kim, B. Y. S.; Rutka, J. T.; Chan, W. C. W. Nanoparticle-Mediated Cellular Response Is Size-Dependent. *Nat. Nanotechnol.* **2008**, *3* (3), 145–150. https://doi.org/10.1038/nnano.2008.30.

(119) Cho, E. C.; Zhang, Q.; Xia, Y. The Effect of Sedimentation and Diffusion on Cellular Uptake of Gold Nanoparticles. *Nat. Nanotechnol.* **2011**, *6* (6), 385–391. https://doi.org/10.1038/nnano.2011.58.

(120) MacParland, S. A.; Tsoi, K. M.; Ouyang, B.; Ma, X. Z.; Manuel, J.; Fawaz, A.; Ostrowski, M. A.; Alman, B. A.; Zilman, A.; Chan, W. C. W.; McGilvray, I. D. Phenotype Determines Nanoparticle Uptake by Human Macrophages from Liver and Blood. *ACS Nano* **2017**, *11* (3), 2428–2443. https://doi.org/10.1021/acsnano.6b06245.

(121) Dos Santos, T.; Varela, J.; Lynch, I.; Salvati, A.; Dawson, K. A. Quantitative Assessment of the Comparative Nanoparticle-Uptake Efficiency of a Range of Cell Lines. *Small* **2011**, *7* (23), 3341–3349. https://doi.org/10.1002/smll.201101076.

(122) Cheng, X.; Tian, X.; Wu, A.; Li, J.; Tian, J.; Chong, Y.; Chai, Z.; Zhao, Y.; Chen, C.; Ge, C. Protein Corona Influences Cellular Uptake of Gold Nanoparticles by Phagocytic and Nonphagocytic Cells in a Size-Dependent Manner. *ACS Appl. Mater. Interfaces* **2015**, *7* (37), 20568–20575. https://doi.org/10.1021/acsami.5b04290.

(123) Albanese, A.; Chan, W. C. W. Effect of Gold Nanoparticle Aggregation on Cell Uptake and Toxicity. *ACS Nano* **2011**, *5* (7), 5478–5489. https://doi.org/10.1021/nn2007496.

(124) Donahue, N. D.; Francek, E. R.; Kiyotake, E.; Thomas, E. E.; Yang, W.; Wang, L.; Detamore, M. S.; Wilhelm, S.; Wilhelm, S. Assessing Nanoparticle Colloidal Stability with Single-Particle Inductively Coupled Plasma Mass Spectrometry (SP-ICP-MS). *Anal. Bioanal. Chem.* **2020**.

(125) Suen, W. L. L.; Chau, Y. Size-Dependent Internalisation of Folate-Decorated

Nanoparticles via the Pathways of Clathrin and Caveolae-Mediated Endocytosis in ARPE-19 Cells. *J. Pharm. Pharmacol.* **2014**, *66* (4), 564–573. https://doi.org/10.1111/jphp.12134.

(126) Chang, T.; Lord, M. S.; Bergmann, B.; MacMillan, A.; Stenzel, M. H. Size Effects of Self-Assembled Block Copolymer Spherical Micelles and Vesicles on Cellular Uptake in Human Colon Carcinoma Cells. *J. Mater. Chem. B* **2014**, *2* (19), 2883–2891. https://doi.org/10.1039/c3tb21751e.

(127) Dasgupta, S.; Auth, T.; Gompper, G. Shape and Orientation Matter for the Cellular Uptake of Nonspherical Particles. *Nano Lett.* **2014**, *14* (2), 687–693. https://doi.org/10.1021/nl403949h.

(128) Arnida; Malugin, A.; Ghandehari, H. Cellular Uptake and Toxicity of Gold Nanoparticles in Prostate Cancer Cells: A Comparative Study of Rods and Spheres. *J. Appl. Toxicol.* **2010**, *30* (3), 212–217. https://doi.org/10.1002/jat.1486.

(129) Meng, H.; Yang, S.; Li, Z.; Xia, T.; Chen, J.; Ji, Z.; Zhang, H.; Wang, X.; Lin, S.; Huang, C.; Zhou, Z. H.; Zink, J. I.; Nel, A. E. Aspect Ratio Determines the Quantity of Mesoporous Silica Nanoparticle Uptake by a Small Gtpase-Dependent Macropinocytosis Mechanism. *ACS Nano* **2011**, *5* (6), 4434–4447. https://doi.org/10.1021/nn103344k.

(130) Bartneck, M.; Keul, H. A.; Singh, S.; Czaja, K.; Bockstaller, M.; Moeller, M.; Zwadlo-klarwasser, G.; Bornemann, J.; Groll, J. Rapid Uptake of Gold Nanorods by Primary Human Blood Phagocytes and Chemistry. *ACS Nano* **2010**, *4* (6), 3073–3086. https://doi.org/10.1021/nn100262h.

(131) Li, Z.; Sun, L.; Zhang, Y.; Dove, A. P.; O'Reilly, R. K.; Chen, G. Shape Effect of Glyco-Nanoparticles on Macrophage Cellular Uptake and Immune Response. *ACS Macro Lett.* **2016**, *5* (9), 1059–1064. https://doi.org/10.1021/acsmacrolett.6b00419.

(132) Doshi, N.; Mitragotri, S. Macrophages Recognize Size and Shape of Their Targets. *PLoS One* **2010**, *5* (4), 1–6. https://doi.org/10.1371/journal.pone.0010051.

(133) Wang, J.; Chen, H. J.; Hang, T.; Yu, Y.; Liu, G.; He, G.; Xiao, S.; Yang, B. ru; Yang, C.; Liu, F.; Tao, J.; Wu, M. X.; Xie, X. Physical Activation of Innate Immunity by Spiky Particles. *Nat. Nanotechnol.* **2018**, *13* (11), 1078–1086. https://doi.org/10.1038/s41565-018-0274-0.

(134) Hunter, R. J. *Zeta Potential in Colloid Science : Principles and Applications*; 1988.

(135) Doorley, G. W.; Payne, C. K. Cellular Binding of Nanoparticles in the Presence of Serum Proteinswz COMMUNICATION Www.Rsc.Org/Chemcomm | ChemComm. *Chem. Commun* **2011**, *47*, 466–468. https://doi.org/10.1039/c0cc02618b.

(136) Dobrovolskaia, M. A.; Patri, A. K.; Zheng, J.; Clogston, J. D.; Ayub, N.; Aggarwal, P.; Neun, B. W.; Hall, J. B.; Mcneil, S. E. Interaction of Colloidal Gold Nanoparticles with Human Blood: Effects on Particle Size and Analysis of Plasma Protein Binding Profiles. *Nanomedicine* **2009**, *5*, 106–117. https://doi.org/10.1016/j.nano.2008.08.001.

(137) Tenzer, S.; Docter, D.; Kuharev, J.; Musyanovych, A.; Fetz, V.; Hecht, R.; Schlenk, F.; Fischer, D.; Kiouptsi, K.; Reinhardt, C.; Landfester, K.; Schild, H.; Maskos, M.; Knauer, S. K.; Stauber, R. H. Rapid Formation of Plasma Protein Corona Critically Affects Nanoparticle Pathophysiology. *Nat. Nanotechnol.* **2013**, *8*, 772–781. https://doi.org/10.1038/NNANO.2013.181.

(138) Lynch, I.; Dawson, K. A. *Protein-Nanoparticle Interactions*; 2008; Vol. 3.
(139) Bhattacharya, S.; Ahir, M.; Patra, P.; Mukherjee, S.; Ghosh, S.; Mazumdar, M.; Chattopadhyay, S.; Das, T.; Chattopadhyay, D.; Adhikary, A. PEGylated-Thymoquinone-Nanoparticle Mediated Retardation of Breast Cancer Cell Migration by Deregulation of Cytoskeletal Actin Polymerization through MiR-34a. *Biomaterials* **2015**, *51*, 91–107. https://doi.org/10.1016/j.biomaterials.2015.01.007.
(140) Schäffler, M.; Semmler-Behnke, M.; Sarioglu, H.; Takenaka, S.; Wenk, A.; Schleh, C.; Hauck, S. M.; Johnston, B. D.; Kreyling, W. G. Serum Protein Identification and Quantification of the Corona of 5, 15 and 80 Nm Gold Nanoparticles. *Nanotechnology* **2013**, *24* (26). https://doi.org/10.1088/0957-4484/24/26/265103.
(141) Deng, Z. J.; Mortimer, G.; Schiller, T.; Musumeci, A.; Martin, D.; Minchin, R. F. Differential Plasma Protein Binding to Metal Oxide Nanoparticles. *Nanotechnology* **2009**, *20* (45). https://doi.org/10.1088/0957-4484/20/45/455101.
(142) Chertok, B.; David, A. E.; Yang, V. C. Polyethyleneimine-Modified Iron Oxide Nanoparticles for Brain Tumor Drug Delivery Using Magnetic Targeting and Intra-Carotid Administration. *Biomaterials* **2010**, *31* (24), 6317–6324. https://doi.org/10.1016/j.biomaterials.2010.04.043.
(143) Li, X.; Chen, Y.; Wang, M.; Ma, Y.; Xia, W.; Gu, H. A Mesoporous Silica Nanoparticle - PEI - Fusogenic Peptide System for SiRNA Delivery in Cancer Therapy. *Biomaterials* **2013**, *34* (4), 1391–1401. https://doi.org/10.1016/j.biomaterials.2012.10.072.
(144) Ngamcherdtrakul, W.; Morry, J.; Gu, S.; Castro, D. J.; Goodyear, S. M.; Sangvanich, T.; Reda, M. M.; Lee, R.; Mihelic, S. A.; Beckman, B. L.; Hu, Z.; Gray, J. W.; Yantasee, W. Cationic Polymer Modified Mesoporous Silica Nanoparticles for Targeted SiRNA Delivery to $HER2^{+}$ Breast Cancer. *Adv. Funct. Mater.* **2015**, *25* (18), 2646–2659. https://doi.org/10.1002/adfm.201404629.
(145) Vigderman, L.; Manna, P.; Zubarev, E. R. Quantitative Replacement of Cetyl Trimethylammonium Bromide by Cationic Thiol Ligands on the Surface of Gold Nanorods and Their Extremely Large Uptake by Cancer Cells. *Angew. Chemie - Int. Ed.* **2012**, *51* (3), 636–641. https://doi.org/10.1002/anie.201107304.
(146) Ayala, V.; Herrera, A. P.; Latorre-Esteves, M.; Torres-Lugo, M. L. M.; Rinaldi, C. Effect of Surface Charge on the Colloidal Stability and in Vitro Uptake of Carboxymethyl Dextran-Coated Iron Oxide Nanoparticles. *J. Nanopart. Res.* **2013**, *15* (8), 1874. https://doi.org/10.1007/s11051-013-1874-0.
(147) Zhou, Y.; Shi, L.; Li, Q.; Jiang, H.; Lv, G.; Zhao, J.; Wu, C.; Selke, M.; Wang, X. Imaging and Inhibition of Multi-Drug Resistance in Cancer Cells via Specific Association with Negatively Charged CdTe Quantum Dots. *Biomaterials* **2010**, *31* (18), 4958–4963. https://doi.org/10.1016/j.biomaterials.2010.02.053.
(148) Lee, J. S.; Ankone, M.; Pieters, E.; Schiffelers, R. M.; Hennink, W. E.; Feijen, J. Circulation Kinetics and Biodistribution of Dual-Labeled Polymersomes with Modulated Surface Charge in Tumor-Bearing Mice: Comparison with Stealth Liposomes. *J. Control. Release* **2011**, *155* (2), 282–288. https://doi.org/10.1016/j.jconrel.2011.07.028.
(149) Xie, Y.; Qiao, H.; Su, Z.; Chen, M.; Ping, Q.; Sun, M. PEGylated Carboxymethyl Chitosan/Calcium Phosphate Hybrid Anionic Nanoparticles Mediated HTERT SiRNA Delivery for Anticancer Therapy. *Biomaterials* **2014**, *35* (27), 7978–7991.

https://doi.org/10.1016/j.biomaterials.2014.05.068.
(150) Secret, E.; Maynadier, M.; Gallud, A.; Gary-Bobo, M.; Chaix, A.; Belamie, E.; Maillard, P.; Sailor, M. J.; Garcia, M.; Durand, J. O.; Cunin, F. Anionic Porphyrin-Grafted Porous Silicon Nanoparticles for Photodynamic Therapy. *Chem. Commun.* **2013**, *49* (39), 4202–4204. https://doi.org/10.1039/c3cc38837a.
(151) Chithrani, B. D.; Chan, W. C. W. Elucidating the Mechanism of Cellular Uptake and Removal of Protein-Coated Gold Nanoparticles of Different Sizes and Shapes. **2007**. https://doi.org/10.1021/nl070363y.
(152) Lin, J.; Zhang, H.; Chen, Z.; Zheng, Y. Penetration of Lipid Membranes by Gold Nanoparticles: Insights into Cellular Uptake, Cytotoxicity, and Their Relationship. *ACS Nano* **2010**, *4* (9), 5421–5429. https://doi.org/10.1021/nn1010792.
(153) Arvizo, R. R.; Miranda, O. R.; Thompson, M. A.; Pabelick, C. M.; Bhattacharya, R.; David Robertson, J.; Rotello, V. M.; Prakash, Y. S.; Mukherjee, P. Effect of Nanoparticle Surface Charge at the Plasma Membrane and Beyond. *Nano Lett.* **2010**, *10* (7), 2543–2548. https://doi.org/10.1021/nl101140t.
(154) Wang, F.; Bexiga, M. G.; Anguissola, S.; Boya, P.; Simpson, J. C.; Salvati, A.; Dawson, K. A. Time Resolved Study of Cell Death Mechanisms Induced by Amine-Modified Polystyrene Nanoparticles. *Nanoscale* **2013**, *5* (22), 10868–10876. https://doi.org/10.1039/c3nr03249c.
(155) Kedmi, R.; Ben-Arie, N.; Peer, D. The Systemic Toxicity of Positively Charged Lipid Nanoparticles and the Role of Toll-like Receptor 4 in Immune Activation. *Biomaterials* **2010**, *31*, 6867–6875. https://doi.org/10.1016/j.biomaterials.2010.05.027.
(156) Lee, J. C.; Donahue, N. D.; Mao, A. S.; Karim, A.; Komarneni, M.; Thomas, E. E.; Francek, E. R.; Yang, W.; Wilhelm, S. Exploring Maleimide-Based Nanoparticle Surface Engineering to Control Cellular Interactions. *ACS Appl. Nano Mater.* **2020**. https://doi.org/10.1021/acsanm.9b02541.
(157) Elkin, S. R.; Lakoduk, A. M.; Schmid, S. L. Endocytic Pathways and Endosomal Trafficking: A Primer. *Wiener Medizinische Wochenschrift* **2016**, *166* (7–8), 196–204. https://doi.org/10.1007/s10354-016-0432-7.
(158) Moyano, D. F.; Saha, K.; Prakash, G.; Yan, B.; Kong, H.; Yazdani, M.; Rotello, V. M. Fabrication of Corona Free Nanoparticles with Tunable Hydrophobicity. *ACS Nano* **2014**, *8* (7), 6748–6755. https://doi.org/10.1002/adma.200901407.
(159) Cho, K.; Wang, X.; Nie, S.; Chen, Z.; Shin, D. M. Therapeutic Nanoparticles for Drug Delivery in Cancer. *Clin. Cancer Res.* **2008**, *14* (5), 1310–1316. https://doi.org/10.1158/1078-0432.CCR-07-1441.
(160) Bertrand, N.; Wu, J.; Xu, X.; Kamaly, N.; Farokhzad, O. C. Cancer Nanotechnology: The Impact of Passive and Active Targeting in the Era of Modern Cancer Biology ☆. *Adv. Drug Deliv. Rev.* **2013**, *66*, 2–25. https://doi.org/10.1016/j.addr.2013.11.009.
(161) Byrne, J. D.; Betancourt, T.; Brannon-Peppas, L. Active Targeting Schemes for Nanoparticle Systems in Cancer Therapeutics. *Adv. Drug Deliv. Rev.* **2008**, *60*, 1615–1626. https://doi.org/10.1016/j.addr.2008.08.005.
(162) Belfiore, L.; Saunders, D. N.; Ranson, M.; Thurecht, K. J.; Storm, G.; Vine, K. L. Towards Clinical Translation of Ligand-Functionalized Liposomes in Targeted Cancer Therapy: Challenges and Opportunities. *J. Control. Release* **2018**, *277*, 1–

13. https://doi.org/10.1016/j.jconrel.2018.02.040.
(163) Hak, S.; Helgesen, E.; Hektoen, H. H.; Huuse, E. M.; Jarzyna, P. A.; Mulder, W. J. M.; Haraldseth, O.; Davies, C. D. L. The Effect of Nanoparticle Polyethylene Glycol Surface Density on Ligand-Directed Tumor Targeting Studied in Vivo by Dual Modality Imaging. *ACS Nano* **2012**, *6* (6), 5648–5658. https://doi.org/10.1021/nn301630n.
(164) Zern, B. J.; Chacko, A. M.; Liu, J.; Greineder, C. F.; Blankemeyer, E. R.; Radhakrishnan, R.; Muzykantov, V. Reduction of Nanoparticle Avidity Enhances the Selectivity of Vascular Targeting and PET Detection of Pulmonary Inflammation. *ACS Nano* **2013**, *7* (3), 2461–2469. https://doi.org/10.1021/nn305773f.
(165) Qhattal, H. S. S.; Hye, T.; Alali, A.; Liu, X. Hyaluronan Polymer Length, Grafting Density, and Surface Poly(Ethylene Glycol) Coating Influence in Vivo Circulation and Tumor Targeting of Hyaluronan-Grafted Liposomes. *ACS Nano* **2014**, *8* (6), 5423–5440. https://doi.org/10.1021/nn405839n.
(166) Pozzi, D.; Colapicchioni, V.; Caracciolo, G.; Piovesana, S.; Capriotti, A. L.; Palchetti, S.; De Grossi, S.; Riccioli, A.; Amenitsch, H.; Laganà, A. Effect of Polyethyleneglycol (PEG) Chain Length on the Bio-Nano- Interactions between PEGylated Lipid Nanoparticles and Biological Fluids: From Nanostructure to Uptake in Cancer Cells. *Nanoscale* **2014**, *6* (5), 2782–2792. https://doi.org/10.1039/c3nr05559k.
(167) Mou, Q.; Ma, Y.; Zhu, X.; Yan, D. A Small Molecule Nanodrug Consisting of Amphiphilic Targeting Ligand-Chemotherapy Drug Conjugate for Targeted Cancer Therapy. *J. Control. Release* **2016**, *230*, 34–44. https://doi.org/10.1016/j.jconrel.2016.03.037.
(168) Ding, H. M.; Ma, Y. Q. Role of Physicochemical Properties of Coating Ligands in Receptor-Mediated Endocytosis of Nanoparticles. *Biomaterials* **2012**, *33* (23), 5798–5802. https://doi.org/10.1016/j.biomaterials.2012.04.055.
(169) Ding, H.; Tian, W.; Ma, Y. Designing Nanoparticle Translocation through Membranes by Computer Simulations. *ACS Nano* **2012**, *6* (2), 1230–1238. https://doi.org/10.1021/nn2038862.
(170) Colombo, M.; Fiandra, L.; Alessio, G.; Mazzucchelli, S.; Nebuloni, M.; De Palma, C.; Kantner, K.; Pelaz, B.; Rotem, R.; Corsi, F.; Parak, W. J.; Prosperi, D. Tumour Homing and Therapeutic Effect of Colloidal Nanoparticles Depend on the Number of Attached Antibodies. *Nat. Commun.* **2016**, *7*. https://doi.org/10.1038/ncomms13818.
(171) Narum, S. M.; Le, T.; Le, D. P.; Lee, J. C.; Donahue, N. D.; Yang, W.; Wilhelm, S. *Passive Targeting in Nanomedicine: Fundamental Concepts, Body Interactions, and Clinical Potential*; 2019. https://doi.org/10.1016/B978-0-12-816662-8.00004-7.
(172) Caracciolo, G.; Farokhzad, O. C.; Mahmoudi, M. Biological Identity of Nanoparticles In Vivo: Clinical Implications of the Protein Corona. *Trends Biotechnol.* **2017**, *35* (3), 257–264. https://doi.org/10.1016/j.tibtech.2016.08.011.
(173) Behzadi, S.; Serpooshan, V.; Tao, W.; Hamaly, M. A.; Alkawareek, M. Y.; Dreaden, E. C.; Brown, D.; Alkilany, A. M.; Farokhzad, O. C.; Mahmoudi, M. Cellular Uptake of Nanoparticles: Journey inside the Cell. *Chem. Soc. Rev.* **2017**, *46* (14), 4218–4244. https://doi.org/10.1039/C6CS00636A.

(174) Lazarovits, J.; Chen, Y. Y.; Song, F.; Ngo, W.; Tavares, A. J.; Zhang, Y. N.; Audet, J.; Tang, B.; Lin, Q.; Tleugabulova, M. C.; Wilhelm, S.; Krieger, J. R.; Mallevaey, T.; Chan, W. C. W. Synthesis of Patient-Specific Nanomaterials. *Nano Lett.* **2019**, *(1) 19*, 116–123. https://doi.org/10.1021/acs.nanolett.8b03434.
(175) Mirshafiee, V.; Kim, R.; Mahmoudi, M.; Kraft, M. L. The Importance of Selecting a Proper Biological Milieu for Protein Corona Analysis in Vitro: Human Plasma versus Human Serum. *Int. J. Biochem. Cell Biol.* **2016**, *75*, 188–195. https://doi.org/10.1016/j.biocel.2015.11.019.
(176) Salvati, A.; Pitek, A. S.; Monopoli, M. P.; Prapainop, K.; Bombelli, F. B.; Hristov, D. R.; Kelly, P. M.; Åberg, C.; Mahon, E.; Dawson, K. A. Transferrin-Functionalized Nanoparticles Lose Their Targeting Capabilities When a Biomolecule Corona Adsorbs on the Surface. *Nat. Nanotechnol.* **2013**, *8*, 137–143. https://doi.org/10.1038/NNANO.2012.237.
(177) Tonigold, M.; Simon, J. Pre-Adsorption of Antibodies Enables Targeting of Nanocarriers despite a Biomolecular Corona. *Nat. Nanotechnol.* **2018**, *13*, 862–869. https://doi.org/10.1038/s41565-018-0171-6.
(178) Miller, M. A.; Zheng, Y. R.; Gadde, S.; Pfirschke, C.; Zope, H.; Engblom, C.; Kohler, R. H.; Iwamoto, Y.; Yang, K. S.; Askevold, B.; Kolishetti, N.; Pittet, M.; Lippard, S. J.; Farokhzad, O. C.; Weissleder, R. Tumour-Associated Macrophages Act as a Slow-Release Reservoir of Nano-Therapeutic Pt(IV) pro-Drug. *Nat. Commun.* **2015**, *6*, 1–13. https://doi.org/10.1038/ncomms9692.
(179) Kim, H.-Y.; Li, R.; Ng, T. S. C.; Courties, G.; Rodell, C. B.; Prytyskach, M.; Kohler, R. H.; Pittet, M.; Nahrendorf, M.; Weissleder, R.; Miller, M. A. Quantitative Imaging of Tumor Associated Macrophages and Their Response to Therapy Using 64Cu-Labeled Macrin. *ACS Nano* **2018**, *12*, 12015–12029. https://doi.org/10.1021/acsnano.8b04338.
(180) Miller, M. A.; Gadde, S.; Pfirschke, C.; Engblom, C.; Melissa, M.; Kohler, R. H.; Yang, K. S.; Laughney, A. M.; Kamaly, N.; Bhonagiri, S.; Pittet, M.; Farokhzad, O. C.; Weissleder, R. Predicting Therapeutic Nanoparticle Efficacy Using a Companion MR Imaging Nanoparticle. *Sci. Transl. Med.* **2015**, *7* (314), 314ra183. https://doi.org/10.1126/scitranslmed.aac6522.Predicting.
(181) Kim, C. S.; Li, X.; Jiang, Y.; Yan, B.; Tonga, G. Y.; Ray, M.; Solfiell, D. J.; Rotello, V. M. Cellular Imaging of Endosome Entrapped Small Gold Nanoparticles. *MethodsX* **2015**, *2*, 306–315. https://doi.org/10.1016/j.mex.2015.06.001.
(182) Peckys, D. B.; De Jonge, N. Visualizing Gold Nanoparticle Uptake in Live Cells with Liquid Scanning Transmission Electron Microscopy. *Nano Lett.* **2011**, *11* (4), 1733–1738. https://doi.org/10.1021/nl200285r.
(183) Van Der Zwaag, D.; Vanparijs, N.; Wijnands, S.; De Rycke, R.; De Geest, B. G.; Albertazzi, L. Super Resolution Imaging of Nanoparticles Cellular Uptake and Trafficking. *ACS Appl. Mater. Interfaces* **2016**, *8* (10), 6391–6399. https://doi.org/10.1021/acsami.6b00811.
(184) Al-Hajaj, N. A.; Moquin, A.; Neibert, K. D.; Soliman, G. M.; Winnik, F. M.; Maysinger, D. Short Ligands Affect Modes of QD Uptake and Elimination in Human Cells. *ACS Nano* **2011**, *5* (6), 4909–4918. https://doi.org/10.1021/nn201009w.
(185) Nel, A.; Xia, T.; Li, N. Toxic Potential of Materials. *Science (80-.).* **2007**, *311*

(5726), 622–627. https://doi.org/10.1126/science.1114397.
(186) Liu, J.; Erogbogbo, F.; Yong, K. T.; Ye, L.; Liu, J.; Hu, R.; Chen, H.; Hu, Y.; Yang, Y.; Yang, J.; Roy, I.; Karker, N. A.; Swihart, M. T.; Prasad, P. N. Assessing Clinical Prospects of Silicon Quantum Dots: Studies in Mice and Monkeys. *ACS Nano* **2013**, *7* (8), 7303–7310. https://doi.org/10.1021/nn4029234.
(187) Hirai, T.; Yoshioka, Y.; Izumi, N.; Ichihashi, K. I.; Handa, T.; Nishijima, N.; Uemura, E.; Sagami, K. I.; Takahashi, H.; Yamaguchi, M.; Nagano, K.; Mukai, Y.; Kamada, H.; Tsunoda, S. I.; Ishii, K. J.; Higashisaka, K.; Tsutsumi, Y. Metal Nanoparticles in the Presence of Lipopolysaccharides Trigger the Onset of Metal Allergy in Mice. *Nat. Nanotechnol.* **2016**, *11* (9), 808–816. https://doi.org/10.1038/nnano.2016.88.
(188) Almeida Silva, A. C.; Silva, M. J. B.; Da Luz, F. A. C.; Silva, D. P.; De Deus, S. L. V.; Oliveira Dantas, N. Controlling the Cytotoxicity of CdSe Magic-Sized Quantum Dots as a Function of Surface Defect Density. *Nano Lett.* **2014**, *14* (9), 5452–5457. https://doi.org/10.1021/nl5028028.
(189) Stoneham, C. A.; Hollinshead, M.; Hajitou, A. Clathrin-Mediated Endocytosis and Subsequent Endo-Lysosomal Trafficking of Adeno-Associated Virus/Phage. *J. Biol. Chem.* **2012**, *287* (43), 35849–35859. https://doi.org/10.1074/jbc.M112.369389.
(190) Zheng, L. L.; Li, C. M.; Zhen, S. J.; Li, Y. F.; Huang, C. Z. A Dynamic Cell Entry Pathway of Respiratory Syncytial Virus Revealed by Tracking the Quantum Dot-Labeled Single Virus. *Nanoscale* **2017**, *9* (23), 7880–7887. https://doi.org/10.1039/c7nr02162c.
(191) Qin, C.; Li, W.; Li, Q.; Yin, W.; Zhang, X.; Zhang, Z.; Zhang, X.-E.; Cui, Z. Real-Time Dissection of Dynamic Uncoating of Individual Influenza Viruses. *Proc. Natl. Acad. Sci.* **2019**, 201812632. https://doi.org/10.1073/pnas.1812632116.
(192) Pridgen, E. M.; Alexis, F.; Kuo, T. T.; Levy-nissenbaum, E.; Karnik, R.; Blumberg, R. S.; Langer, R.; Farokhzad, O. C. Transepithelial Transport of Nanoparticles Targeted to the Neonatal Fc Receptor for Oral Delivery Applications. *Sci. Transl. Med.* **2013**, *5* (213). https://doi.org/10.1126/scitranslmed.3007049.
(193) Acar, H.; Samaeekia, R.; Schnorenberg, M. R.; Sasmal, D. K.; Huang, J.; Tirrell, M. V; Labelle, J. L. Cathepsin-Mediated Cleavage of Peptides from Peptide Amphiphiles Leads to Enhanced Intracellular Peptide Accumulation. *Bioconjugate Chem* **2017**, *28*, 38. https://doi.org/10.1021/acs.bioconjchem.7b00364.
(194) Wilhelm, S.; Bensen, R. C.; Kothapali, N. R.; Burgett, A. W. G.; Merrifield, R.; Stephan, C. Quantification of Gold Nanoparticle Uptake into Cancer Cells Using Single Cell ICP-MS. *PerkinElmer Appl. Note* **2018**, No. i.
(195) Yang, Y. S. S.; Atukorale, P. U.; Moynihan, K. D.; Bekdemir, A.; Rakhra, K.; Tang, L.; Stellacci, F.; Irvine, D. J. High-Throughput Quantitation of Inorganic Nanoparticle Biodistribution at the Single-Cell Level Using Mass Cytometry. *Nat. Commun.* **2017**, *8*, 1–9. https://doi.org/10.1038/ncomms14069.
(196) Kalyanasundaram, S.; Gradinaru, V.; Chung, K.; Mirzabekov, J. J.; Kim, S.-Y.; Wallace, J.; Zalocusky, K. A.; Mattis, J.; Denisin, A. K.; Deisseroth, K.; Grosenick, L.; Bernstein, H.; Ramakrishnan, C.; Davidson, T. J.; Pak, S.; Andalman, A. S. Structural and Molecular Interrogation of Intact Biological Systems. *Nature* **2013**, *497* (7449), 332–337. https://doi.org/10.1038/nature12107.
(197) Sindhwani, S.; Syed, A. M.; Wilhelm, S.; Glancy, D. R.; Chen, Y. Y.; Dobosz, M.;

Chan, W. C. W. Three-Dimensional Optical Mapping of Nanoparticle Distribution in Intact Tissues. *ACS Nano* **2016**, *10* (5), 5468–5478. https://doi.org/10.1021/acsnano.6b01879.

(198) Muhammad Syed, A.; Sindhwani, S.; Wilhelm, S.; R. Kingston, B.; S. W. Lee, D.; L. Gommerman, J.; C. W. Chan, W. Three-Dimensional Imaging of Transparent Tissues via Metal Nanoparticle Labeling. *J. Am. Chem. Soc.* **2017**, *139* (29), 9961–9971. https://doi.org/10.1021/jacs.7b04022.

(199) Pan, C.; Cai, R.; Quacquarelli, F. P.; Ghasemigharagoz, A.; Lourbopoulos, A.; Matryba, P.; Plesnila, N.; Dichgans, M.; Hellal, F.; Ertürk, A. Shrinkage-Mediated Imaging of Entire Organs and Organisms Using UDISCO. *Nat. Methods* **2016**, *13* (10), 859–867. https://doi.org/10.1038/nmeth.3964.

(200) Chen, F.; Tillberg, P. W.; Boyden, E. S. Expansion Microscopy. *Science (80-.).* **2015**, *37* (6221), 543–547. https://doi.org/10.1126/science.1260088.

(201) Sindhwani, S.; Syed, A. M.; Wilhelm, S.; Chan, W. C. W. Exploring Passive Clearing for 3d Optical Imaging of Nanoparticles in Intact Tissues. *Bioconjug. Chem.* **2017**, *28* (1), 253–259. https://doi.org/10.1021/acs.bioconjchem.6b00500.

(202) Wilhelm, S. Perspectives for Upconverting Nanoparticles. *ACS Nano*. American Chemical Society November 28, 2017, pp 10644–10653. https://doi.org/10.1021/acsnano.7b07120.

(203) Narum, S. M.; Le, T.; Le, D. P.; Lee, J. C.; Donahue, N. D.; Yang, W.; Wilhelm, S. Passive Targeting in Nanomedicine: Fundamental Concepts, Body Interactions, and Clinical Potential. In *Nanoparticles for Biomedical Applications*; Elsevier, 2020; pp 37–53. https://doi.org/10.1016/b978-0-12-816662-8.00004-7.

(204) Albanese, A.; Walkey, C. D.; Olsen, J. B.; Guo, H.; Emili, A.; Chan, W. C. W. Secreted Biomolecules Alter the Biological Identity and Cellular Interactions of Nanoparticles. *ACS Nano* **2014**, *8* (6), 5515–5526. https://doi.org/10.1021/nn4061012.

(205) Wilhelm, S.; Tavares, A. J.; Dai, Q.; Ohta, S.; Audet, J.; Dvorak, H. F.; Chan, W. C. W. Analysis of Nanoparticle Delivery to Tumours. *Nature Reviews Materials*. Nature Publishing Group April 26, 2016, pp 1–12. https://doi.org/10.1038/natrevmats.2016.14.

(206) Poon, W.; Zhang, Y. N.; Ouyang, B.; Kingston, B. R.; Wu, J. L. Y.; Wilhelm, S.; Chan, W. C. W. Elimination Pathways of Nanoparticles. *ACS Nano* **2019**, *13* (5), 5785–5798. https://doi.org/10.1021/acsnano.9b01383.

(207) Donahue, N. D.; Acar, H.; Wilhelm, S. Concepts of Nanoparticle Cellular Uptake, Intracellular Trafficking, and Kinetics in Nanomedicine. *Adv. Drug Deliv. Rev.* **2019**, *143*. https://doi.org/10.1016/j.addr.2019.04.008.

(208) Modena, M. M.; Rühle, B.; Burg, T. P.; Wuttke, S. Nanoparticle Characterization: What to Measure? *Adv. Mater.* **2019**, *31* (32), 1901556. https://doi.org/10.1002/adma.201901556.

(209) Marquis, B. J.; Love, S. A.; Braun, K. L.; Haynes, C. L. Analytical Methods to Assess Nanoparticle Toxicity. *Analyst*. Royal Society of Chemistry February 23, 2009, pp 425–439. https://doi.org/10.1039/b818082b.

(210) Hoo, C. M.; Starostin, N.; West, P.; Mecartney, M. L. A Comparison of Atomic Force Microscopy (AFM) and Dynamic Light Scattering (DLS) Methods to Characterize Nanoparticle Size Distributions. *J. Nanoparticle Res.* **2008**, *10*

(SUPPL. 1), 89–96. https://doi.org/10.1007/s11051-008-9435-7.
(211) Olson, J.; Dominguez-Medina, S.; Hoggard, A.; Wang, L. Y.; Chang, W. S.; Link, S. Optical Characterization of Single Plasmonic Nanoparticles. *Chemical Society Reviews*. Royal Society of Chemistry January 7, 2015, pp 40–57. https://doi.org/10.1039/c4cs00131a.
(212) Montaño, M. D.; Lowry, G. V; Blue, J. Current Status and Future Direction for Examining Engineered Nanoparticles in Natural Systems. **2010**. https://doi.org/10.1071/EN14037.
(213) Brar, S. K.; Verma, M. Measurement of Nanoparticles by Light-Scattering Techniques. *TrAC - Trends in Analytical Chemistry*. Elsevier January 1, 2011, pp 4–17. https://doi.org/10.1016/j.trac.2010.08.008.
(214) Dastanpour, R.; Boone, J. M.; Rogak, S. N. Automated Primary Particle Sizing of Nanoparticle Aggregates by TEM Image Analysis. *Powder Technol.* **2016**, *295*, 218–224. https://doi.org/10.1016/j.powtec.2016.03.027.
(215) Filipe, V.; Hawe, A.; Jiskoot, W. Critical Evaluation of Nanoparticle Tracking Analysis (NTA) by NanoSight for the Measurement of Nanoparticles and Protein Aggregates. *Pharm. Res.* **2010**, *27* (5), 796–810. https://doi.org/10.1007/s11095-010-0073-2.
(216) Montaño, M. D.; Olesik, J. W.; Barber, A. G.; Challis, K.; Ranville, J. F. Single Particle ICP-MS: Advances toward Routine Analysis of Nanomaterials. *Anal. Bioanal. Chem.* **2016**, *408* (19), 5053–5074. https://doi.org/10.1007/s00216-016-9676-8.
(217) Mozhayeva, D.; Engelhard, C. A Critical Review of Single Particle Inductively Coupled Plasma Mass Spectrometry – A Step towards an Ideal Method for Nanomaterial Characterization. *J. Anal. At. Spectrom.* **2020**. https://doi.org/10.1039/c9ja00206e.
(218) Corte Rodríguez, M.; Álvarez-Fernández García, R.; Blanco, E.; Bettmer, J.; Montes-Bayón, M. Quantitative Evaluation of Cisplatin Uptake in Sensitive and Resistant Individual Cells by Single-Cell ICP-MS (SC-ICP-MS). *Anal. Chem.* **2017**, *89* (21), 11491–11497. https://doi.org/10.1021/acs.analchem.7b02746.
(219) C. Lee, J.; D. Donahue, N.; S. Mao, A.; Karim, A.; Komarneni, M.; E. Thomas, E.; R. Francek, E.; Yang, W.; Wilhelm, S. Exploring Maleimide-Based Nanoparticle Surface Engineering to Control Cellular Interactions. *ACS Appl. Nano Mater.* **2020**, *3* (3), 2421–2429. https://doi.org/10.1021/acsanm.9b02541.
(220) Wilhelm, S.; Kaiser, M.; Würth, C.; Heiland, J.; Carrillo-Carrion, C.; Muhr, V.; Wolfbeis, O. S.; Parak, W. J.; Resch-Genger, U.; Hirsch, T. Water Dispersible Upconverting Nanoparticles: Effects of Surface Modification on Their Luminescence and Colloidal Stability. *Nanoscale* **2015**, *7* (4), 1403–1410. https://doi.org/10.1039/c4nr05954a.
(221) Muhr, V.; Wilhelm, S.; Hirsch, T.; Wolfbeis, O. S. Upconversion Nanoparticles: From Hydrophobic to Hydrophilic Surfaces. *Acc. Chem. Res.* **2014**, *47* (12), 3481–3493. https://doi.org/10.1021/ar500253g.
(222) Hassellöv, M.; Readman, J. W.; Ranville, J. F.; Tiede, K. Nanoparticle Analysis and Characterization Methodologies in Environmental Risk Assessment of Engineered Nanoparticles. *Ecotoxicology*. Springer July 16, 2008, pp 344–361. https://doi.org/10.1007/s10646-008-0225-x.

(223) Love, S. A.; Maurer-Jones, M. A.; Thompson, J. W.; Lin, Y.-S.; Haynes, C. L. Assessing Nanoparticle Toxicity. *Annu. Rev. Anal. Chem.* **2012**, *5* (1), 181–205. https://doi.org/10.1146/annurev-anchem-062011-143134.
(224) Buchman, J. T.; Hudson-Smith, N. V.; Landy, K. M.; Haynes, C. L. Understanding Nanoparticle Toxicity Mechanisms to Inform Redesign Strategies to Reduce Environmental Impact. *Acc. Chem. Res.* **2019**, *52* (6), 1632–1642. https://doi.org/10.1021/acs.accounts.9b00053.
(225) Maurer-Jones, M. A.; Lin, Y. S.; Haynes, C. L. Functional Assessment of Metal Oxide Nanoparticle Toxicity in Immune Cells. *ACS Nano* **2010**, *4* (6), 3363–3373. https://doi.org/10.1021/nn9018834.
(226) Maurer-Jones, M. A.; Gunsolus, I. L.; Murphy, C. J.; Haynes, C. L. Toxicity of Engineered Nanoparticles in the Environment. *Anal. Chem.* **2013**, *85* (6), 3036–3049. https://doi.org/10.1021/ac303636s.
(227) Kim, H. A.; Lee, B. T.; Na, S. Y.; Kim, K. W.; Ranville, J. F.; Kim, S. O.; Jo, E.; Eom, I. C. Characterization of Silver Nanoparticle Aggregates Using Single Particle-Inductively Coupled Plasma-Mass Spectrometry (SpICP-MS). *Chemosphere* **2017**, *171*, 468–475. https://doi.org/10.1016/j.chemosphere.2016.12.063.
(228) D. Perrault, S.; C. W. Chan, W. Synthesis and Surface Modification of Highly Monodispersed, Spherical Gold Nanoparticles of 50−200 Nm. *J. Am. Chem. Soc.* **2009**, *131* (47), 17042–17043. https://doi.org/10.1021/ja907069u.
(229) Vigderman, L.; R. Zubarev, E. High-Yield Synthesis of Gold Nanorods with Longitudinal SPR Peak Greater than 1200 Nm Using Hydroquinone as a Reducing Agent. *Chem. Mater.* **2013**, *25* (8), 1450–1457. https://doi.org/10.1021/cm303661d.
(230) Zhou, S.; Huo, D.; Goines, S.; Yang, T.-H.; Lyu, Z.; Zhao, M.; D. Gilroy, K.; Wu, Y.; D. Hood, Z.; Xie, M.; Xia, Y. Enabling Complete Ligand Exchange on the Surface of Gold Nanocrystals through the Deposition and Then Etching of Silver. *J. Am. Chem. Soc.* **2018**, *140* (38), 11898–11901. https://doi.org/10.1021/jacs.8b06464.
(231) Merrifield, R. C.; Stephan, C.; Lead, J. R. Quantification of Au Nanoparticle Biouptake and Distribution to Freshwater Algae Using Single Cell - ICP-MS. *Environ. Sci. Technol.* **2018**, *52* (4), 2271–2277. https://doi.org/10.1021/acs.est.7b04968.
(232) Corte-Rodríguez, M.; Blanco-González, E.; Bettmer, J.; Montes-Bayón, M. Quantitative Analysis of Transferrin Receptor 1 (TfR1) in Individual Breast Cancer Cells by Means of Labeled Antibodies and Elemental (ICP-MS) Detection. *Anal. Chem.* **2019**, *91* (24), 15532–15538. https://doi.org/10.1021/acs.analchem.9b03438.
(233) Mavrakis, E.; Mavroudakis, L.; Lydakis-Simantiris, N.; Pergantis, S. A. Investigating the Uptake of Arsenate by Chlamydomonas Reinhardtii Cells and Its Effect on Their Lipid Profile Using Single Cell ICP-MS and Easy Ambient Sonic-Spray Ionization-MS. *Anal. Chem.* **2019**, *91* (15), 9590–9598. https://doi.org/10.1021/acs.analchem.9b00917.
(234) Cuello-Nuñez, S.; Abad-Álvaro, I.; Bartczak, D.; del Castillo Busto, M. E.; Ramsay, D. A.; Pellegrino, F.; Goenaga-Infante, H. The Accurate Determination of Number Concentration of Inorganic Nanoparticles Using SpICP-MS with the Dynamic Mass Flow Approach. *J. Anal. At. Spectrom.* **2020**. https://doi.org/10.1039/c9ja00415g.

(235) Pace, H. E.; Rogers, N. J.; Jarolimek, C.; Coleman, V. A.; Higgins, C. P.; Ranville, J. F. Determining Transport Efficiency for the Purpose of Counting and Sizing Nanoparticles via Single Particle Inductively Coupled Plasma Mass Spectrometry. *Anal. Chem.* **2011**, *83* (24), 9361–9369. https://doi.org/10.1021/ac201952t.
(236) Pace, H. E.; Rogers, N. J.; Jarolimek, C.; Coleman, V. A.; Gray, E. P.; Higgins, C. P.; Ranville, J. F. Single Particle Inductively Coupled Plasma-Mass Spectrometry: A Performance Evaluation and Method Comparison in the Determination of Nanoparticle Size. *Environ. Sci. Technol.* **2012**, *46* (22), 12272–12280. https://doi.org/10.1021/es301787d.
(237) Kang, H.; Buchman, J. T.; Rodriguez, R. S.; Ring, H. L.; He, J.; Bantz, K. C.; Haynes, C. L. Stabilization of Silver and Gold Nanoparticles: Preservation and Improvement of Plasmonic Functionalities. *Chemical Reviews*. American Chemical Society January 9, 2019, pp 664–699. https://doi.org/10.1021/acs.chemrev.8b00341.
(238) Haiss, W.; Thanh, N. T. K.; Aveyard, J.; Fernig, D. G. Determination of Size and Concentration of Gold Nanoparticles from UV-Vis Spectra. *Anal. Chem.* **2007**, *79* (11), 4215–4221. https://doi.org/10.1021/ac0702084.
(239) Hineman, A.; Stephan, C. Effect of Dwell Time on Single Particle Inductively Coupled Plasma Mass Spectrometry Data Acquisition Quality. *J. Anal. At. Spectrom.* **2014**, *29* (7), 1252–1257. https://doi.org/10.1039/c4ja00097h.
(240) Lee, S.; Bi, X.; Reed, R. B.; Ranville, J. F.; Herckes, P.; Westerhoff, P. Nanoparticle Size Detection Limits by Single Particle ICP-MS for 40 Elements. *Environ. Sci. Technol.* **2014**, *48* (17), 10291–10300. https://doi.org/10.1021/es502422v.
(241) Tan, J.; Yang, Y.; El Hadri, H.; Li, M.; Hackley, V. A.; Zachariah, M. R. Fast Quantification of Nanorod Geometry by DMA-SpICP-MS. *Analyst* **2019**, *144* (7), 2275–2283. https://doi.org/10.1039/c8an02250j.
(242) Kálomista, I.; Kéri, A.; Ungor, D.; Csapó, E.; Dékány, I.; Prohaska, T.; Galbács, G. Dimensional Characterization of Gold Nanorods by Combining Millisecond and Microsecond Temporal Resolution Single Particle ICP-MS Measurements. *J. Anal. At. Spectrom.* **2017**, *32* (12), 2455–2462. https://doi.org/10.1039/c7ja00306d.
(243) Christau, S.; Moeller, T.; Genzer, J.; Koehler, R.; Von Klitzing, R. Salt-Induced Aggregation of Negatively Charged Gold Nanoparticles Confined in a Polymer Brush Matrix. *Macromolecules* **2017**, *50* (18), 7333–7343. https://doi.org/10.1021/acs.macromol.7b00866.
(244) Pamies, R.; Cifre, J. G. H.; Espín, V. F.; Collado-González, M.; Baños, F. G. D.; De La Torre, J. G. Aggregation Behaviour of Gold Nanoparticles in Saline Aqueous Media. *J. Nanoparticle Res.* **2014**, *16* (4). https://doi.org/10.1007/s11051-014-2376-4.
(245) Kim, T.; Lee, C. H.; Joo, S. W.; Lee, K. Kinetics of Gold Nanoparticle Aggregation: Experiments and Modeling. *J. Colloid Interface Sci.* **2008**, *318* (2), 238–243. https://doi.org/10.1016/j.jcis.2007.10.029.
(246) Suk, J. S.; Xu, Q.; Kim, N.; Hanes, J.; Ensign, L. M. PEGylation as a Strategy for Improving Nanoparticle-Based Drug and Gene Delivery. *Advanced Drug Delivery Reviews*. Elsevier B.V. April 1, 2016, pp 28–51. https://doi.org/10.1016/j.addr.2015.09.012.
(247) Jokerst, J. V.; Lobovkina, T.; Zare, R. N.; Gambhir, S. S. Nanoparticle PEGylation

for Imaging and Therapy. *Nanomedicine*. NIH Public Access June 2011, pp 715–728. https://doi.org/10.2217/nnm.11.19.

(248) Manson, J.; Kumar, D.; Meenan, B. J.; Dixon, D. Polyethylene Glycol Functionalized Gold Nanoparticles: The Influence of Capping Density on Stability in Various Media. *Gold Bull.* **2011**, *44* (2), 99–105. https://doi.org/10.1007/s13404-011-0015-8.

(249) Zhang, X. D.; Wu, D.; Shen, X.; Liu, P. X.; Yang, N.; Zhao, B.; Zhang, H.; Sun, Y. M.; Zhang, L. A.; Fan, F. Y. Size-Dependent in Vivo Toxicity of PEG-Coated Gold Nanoparticles. *Int. J. Nanomedicine* **2011**, *6*, 2071–2081. https://doi.org/10.2147/ijn.s21657.

(250) Walkey, C. D.; Olsen, J. B.; Guo, H.; Emili, A.; Chan, W. C. W. Nanoparticle Size and Surface Chemistry Determine Serum Protein Adsorption and Macrophage Uptake. *J. Am. Chem. Soc.* **2012**, *134* (4), 2139–2147. https://doi.org/10.1021/ja2084338.

(251) Lazarovits, J.; Chen, Y. Y.; Song, F.; Ngo, W.; Tavares, A. J.; Zhang, Y. N.; Audet, J.; Tang, B.; Lin, Q.; Cruz Tleugabulova, M.; Wilhelm, S.; Krieger, J. R.; Mallevaey, T.; Chan, W. C. W. Synthesis of Patient-Specific Nanomaterials. *Nano Lett.* **2019**, *19* (1), 116–123. https://doi.org/10.1021/acs.nanolett.8b03434.

(252) Yang, W.; Wang, L.; Mettenbrink, E. M.; Deangelis, P. L.; Wilhelm, S. Nanoparticle Toxicology. *Annu. Rev. Pharmacol. Toxicol.* **2021**, *61*, 269–289. https://doi.org/10.1146/annurev-pharmtox-032320-110338.

(253) del Barrio, M.; Cases, R.; Cebolla, V.; Hirsch, T.; de Marcos, S.; Wilhelm, S.; Galbán, J. A Reagentless Enzymatic Fluorescent Biosensor for Glucose Based on Upconverting Glasses, as Excitation Source, and Chemically Modified Glucose Oxidase. *Talanta* **2016**, *160*, 586–591. https://doi.org/10.1016/j.talanta.2016.07.062.

(254) Merrifield, R. C.; Stephan, C.; Lead, J. Determining the Concentration Dependent Transformations of Ag Nanoparticles in Complex Media: Using SP-ICP-MS and Au@Ag Core-Shell Nanoparticles as Tracers. *Environ. Sci. Technol.* **2017**, *51* (6), 3206–3213. https://doi.org/10.1021/acs.est.6b05178.

(255) Don Potter. A Commercial Perspective on the Growth and Development of the Quadrupole ICP-MS Market. *J. Anal. At. Spectrom.* **2008**, *23* (5), 690–693. https://doi.org/10.1039/B717322A.

(256) Montaño, M. D.; Badiei, H. R.; Bazargan, S.; Ranville, J. F. Improvements in the Detection and Characterization of Engineered Nanoparticles Using SpICP-MS with Microsecond Dwell Times. *Environ. Sci. Nano* **2014**, *1* (4), 338–346. https://doi.org/10.1039/c4en00058g.

(257) Zhu, Y. L.; Lian, Y. M.; Wang, J. K.; Chen, Z. P.; Yu, R. Q. Highly Sensitive and Specific Mass Spectrometric Platform for MiRNA Detection Based on the Multiple-Metal-Nanoparticle Tagging Strategy. *Anal. Chem.* **2021**, *93* (14), 5839–5848. https://doi.org/10.1021/acs.analchem.1c00065.

(258) Zhang, X. W.; Liu, M. X.; He, M. Q.; Chen, S.; Yu, Y. L.; Wang, J. H. Integral Multielement Signals by DNA-Programmed UCNP-AuNP Nanosatellite Assemblies for Ultrasensitive ICP-MS Detection of Exosomal Proteins and Cancer Identification. *Anal. Chem.* **2021**, *93* (16), 6437–6445. https://doi.org/10.1021/acs.analchem.1c00152.

(259) Naasz, S.; Weigel, S.; Borovinskaya, O.; Serva, A.; Cascio, C.; Undas, A. K.; Simeone, F. C.; Marvin, H. J. P.; Peters, R. J. B. Multi-Element Analysis of Single Nanoparticles by ICP-MS Using Quadrupole and Time-of-Flight Technologies. *J. Anal. At. Spectrom.* **2018**, *33* (5), 835–845. https://doi.org/10.1039/c7ja00399d.

(260) Hendriks, L.; Gundlach-Graham, A.; Günther, D. Analysis of Inorganic Nanoparticles by Single-Particle Inductively Coupled Plasma Time-of-Flight Mass Spectrometry. *Chimia (Aarau).* **2018**, *72* (4), 221–226. https://doi.org/10.2533/chimia.2018.221.

(261) Mehrabi, K.; Gundlach-Graham, A.; Günther, D.; Gundlach-Graham, A. Single-Particle ICP-TOFMS with Online Microdroplet Calibration for the Simultaneous Quantification of Diverse Nanoparticles in Complex Matrices. *Environ. Sci. Nano* **2019**, *6* (11), 3349–3358. https://doi.org/10.1039/c9en00620f.

(262) Praetorius, A.; Gundlach-Graham, A.; Goldberg, E.; Fabienke, W.; Navratilova, J.; Gondikas, A.; Kaegi, R.; Günther, D.; Hofmann, T.; Von Der Kammer, F. Single-Particle Multi-Element Fingerprinting (SpMEF) Using Inductively-Coupled Plasma Time-of-Flight Mass Spectrometry (ICP-TOFMS) to Identify Engineered Nanoparticles against the Elevated Natural Background in Soils. *Environ. Sci. Nano* **2017**, *4* (2), 307–314. https://doi.org/10.1039/c6en00455e.

(263) Jiang, Y.; Wang, L.; Meunier, M.; Mirsaidov, U. Formation Pathways of Porous Alloy Nanoparticles through Selective Chemical and Electrochemical Etching. *Small* **2021**, *2006953*, 6–11. https://doi.org/10.1002/smll.202006953.

(264) Al-Zubeidi, A.; Stein, F.; Flatebo, C.; Rehbock, C.; Hosseini Jebeli, S. A.; Landes, C. F.; Barcikowski, S.; Link, S. Single-Particle Hyperspectral Imaging Reveals Kinetics of Silver Ion Leaching from Alloy Nanoparticles. *ACS Nano* **2021**, *15* (5), 8363–8375. https://doi.org/10.1021/ACSNANO.0C10150/.

(265) Zheng, H.; Meng, Y. S.; Zhu, Y. Frontiers of in Situ Electron Microscopy. *MRS Bull.* **2015**, *40* (1), 12–18. https://doi.org/10.1557/mrs.2014.305.

(266) Sutter, E.; Jungjohann, K.; Bliznakov, S.; Courty, A.; Maisonhaute, E.; Tenney, S.; Sutter, P. In Situ Liquid-Cell Electron Microscopy of Silver-Palladium Galvanic Replacement Reactions on Silver Nanoparticles. *Nat. Commun.* **2014**, *5*. https://doi.org/10.1038/ncomms5946.

(267) Bolea-Fernandez, E.; Leite, D.; Rua-Ibarz, A.; Liu, T.; Woods, G.; Aramendia, M.; Resano, M.; Vanhaecke, F. On the Effect of Using Collision/Reaction Cell (CRC) Technology in Single-Particle ICP-Mass Spectrometry (SP-ICP-MS). *Anal. Chim. Acta* **2019**, *1077*, 95–106. https://doi.org/10.1016/j.aca.2019.05.077.

(268) Tanner, S. D.; Baranov, V. I.; Bandura, D. R. Reaction Cells and Collision Cells for ICP-MS: A Tutorial Review. *Spectrochim. Acta - Part B At. Spectrosc.* **2002**, *57* (9), 1361–1452. https://doi.org/10.1016/S0584-8547(02)00069-1.

(269) Hineman, A.; Stephan, C. Effect of Dwell Time on Single Particle Inductively Coupled Plasma Mass Spectrometry Data Acquisition Quality. In *Journal of Analytical Atomic Spectrometry*; Royal Society of Chemistry, 2014; Vol. 29, pp 1252–1257. https://doi.org/10.1039/c4ja00097h.

(270) Olesik, J. W.; Gray, P. J. Considerations for Measurement of Individual Nanoparticles or Microparticles by ICP-MS: Determination of the Number of Particles and the Analyte Mass in Each Particle. *J. Anal. At. Spectrom.* **2012**, *27* (7), 1143–1155. https://doi.org/10.1039/c2ja30073g.

(271) Bastús, N. G.; Merkoçi, F.; Piella, J.; Puntes, V. Synthesis of Highly Monodisperse Citrate-Stabilized Silver Nanoparticles of up to 200 Nm: Kinetic Control and Catalytic Properties. *Chem. Mater.* **2014**, *26* (9), 2836–2846. https://doi.org/10.1021/cm500316k.
(272) Rainville, L.; Dorais, M.-C.; Boudreau, D. Controlled Synthesis of Low Polydispersity Ag@SiO 2 Core-Shell Nanoparticles for Use in Plasmonic Applications. *Cite this RSC Adv.* **2013**, No. 3. https://doi.org/10.1039/c3ra41677a.
(273) Rioux, D.; Meunier, M. Seeded Growth Synthesis of Composition and Size-Controlled Gold-Silver Alloy Nanoparticles. *J. Phys. Chem. C* **2015**, *119* (23), 13160–13168. https://doi.org/10.1021/acs.jpcc.5b02728.
(274) Fuchs, J.; Aghaei, M.; Schachel, T. D.; Sperling, M.; Bogaerts, A.; Karst, U. Impact of the Particle Diameter on Ion Cloud Formation from Gold Nanoparticles in ICPMS. *Anal. Chem.* **2018**, *90* (17), 10271–10278. https://doi.org/10.1021/acs.analchem.8b02007.
(275) Lu, D.; Liu, Q.; Zhang, T.; Cai, Y.; Yin, Y.; Jiang, G. Stable Silver Isotope Fractionation in the Natural Transformation Process of Silver Nanoparticles. *Nat. Nanotechnol.* **2016**, *11* (8), 682–686. https://doi.org/10.1038/nnano.2016.93.
(276) Laborda, F.; Gimenez-Ingalaturre, A. C.; Bolea, E.; Castillo, J. R. About Detectability and Limits of Detection in Single Particle Inductively Coupled Plasma Mass Spectrometry. *Spectrochim. Acta Part B At. Spectrosc.* **2020**, *169*, 105883. https://doi.org/10.1016/J.SAB.2020.105883.
(277) Newman, K.; Metcalfe, C.; Martin, J.; Hintelmann, H.; Shaw, P.; Donard, A. Improved Single Particle ICP-MS Characterization of Silver Nanoparticles at Environmentally Relevant Concentrations. *J. Anal. At. Spectrom.* **2016**, *31* (10), 2069–2077. https://doi.org/10.1039/C6JA00221H.
(278) Donahue, N. D.; Francek, E. R.; Kiyotake, E.; Thomas, E. E.; Yang, W.; Wang, L.; Detamore, M. S.; Wilhelm, S. Assessing Nanoparticle Colloidal Stability with Single-Particle Inductively Coupled Plasma Mass Spectrometry (SP-ICP-MS). *Anal. Bioanal. Chem.* **2020**, *412* (22), 5205–5216. https://doi.org/10.1007/S00216-020-02783-6.
(279) Wang, C.; Peng, S.; Chan, R.; Sun, S. Synthesis of AuAg Alloy Nanoparticles from Core/Shell-Structured Ag/Au. *Small* **2009**, *5* (5), 567–570. https://doi.org/10.1002/smll.200801169.
(280) Wang, C.; Yin, H.; Chan, R. Alloy NPs and Their Catalysis for CO Oxidation. *Chem. Mater.* **2009**, *21* (3), 2007–2009.
(281) Li, X.; Chen, Q.; McCue, I.; Snyder, J.; Crozier, P.; Erlebacher, J.; Sieradzki, K. Dealloying of Noble-Metal Alloy Nanoparticles. *Nano Lett.* **2014**, *14* (5), 2569–2577. https://doi.org/10.1021/nl500377g.
(282) Gilroy, K. D.; Ruditskiy, A.; Peng, H. C.; Qin, D.; Xia, Y. Bimetallic Nanocrystals: Syntheses, Properties, and Applications. *Chem. Rev.* **2016**, *116* (18), 10414–10472. https://doi.org/10.1021/acs.chemrev.6b00211.
(283) Gottstein, C.; Wu, G.; Wong, B. J.; Zasadzinski, J. A. Precise Quantification of Nanoparticle Internalization. *ACS Nano* **2013**, *7* (6), 4933–4945. https://doi.org/10.1021/NN400243D.
(284) HyeRim Shin; Minjeong Kwak; Geol Lee, T.; Youn Lee, J. Quantifying the Level of Nanoparticle Uptake in Mammalian Cells Using Flow Cytometry. *Nanoscale*

2020, *12* (29), 15743–15751. https://doi.org/10.1039/D0NR01627F.
(285) Wu, Y.; Ali, M. R. K.; Dansby, K.; El-Sayed, M. A. Improving the Flow Cytometry-Based Detection of the Cellular Uptake of Gold Nanoparticles. *Anal. Chem.* **2019**. https://doi.org/10.1021/ACS.ANALCHEM.9B02248.
(286) Romeu, H. G.; Deville, S.; Salvati, A. Time- and Space-Resolved Flow-Cytometry of Cell Organelles to Quantify Nanoparticle Uptake and Intracellular Trafficking by Cells. *Small* **2021**, *17* (34), 2100887. https://doi.org/10.1002/SMLL.202100887.
(287) Zucker, R. M.; Massaro, E. J.; Sanders, K. M.; Degn, L. L.; Boyes, W. K. Detection of TiO2 Nanoparticles in Cells by Flow Cytometry. *Cytom. Part A* **2010**, *77A* (7), 677–685. https://doi.org/10.1002/CYTO.A.20927.
(288) Elsaesser, A.; Taylor, A.; Yanés, G. S. de; McKerr, G.; Kim, E.-M.; O'Hare, E.; Howard, C. V. Quantification of Nanoparticle Uptake by Cells Using Microscopical and Analytical Techniques. *https://doi.org/10.2217/nnm.10.118* **2010**, *5* (9), 1447–1457. https://doi.org/10.2217/NNM.10.118.
(289) Suutari, T.; Silen, T.; Karaman, D. S.; Saari, H.; Desai, D.; Kerkelä, E.; Laitinen, S.; Hanzlikova, M.; Rosenholm, J. M.; Yliperttula, M.; Viitala, T. Real-Time Label-Free Monitoring of Nanoparticle Cell Uptake. *Small* **2016**, *12* (45), 6289–6300. https://doi.org/10.1002/SMLL.201601815.
(290) Yang, Y. S. S.; Atukorale, P. U.; Moynihan, K. D.; Bekdemir, A.; Rakhra, K.; Tang, L.; Stellacci, F.; Irvine, D. J. High-Throughput Quantitation of Inorganic Nanoparticle Biodistribution at the Single-Cell Level Using Mass Cytometry. *Nat. Commun.* **2017**, *8* (1), 1–11. https://doi.org/10.1038/ncomms14069.
(291) Malysheva, A.; Ivask, A.; Doolette, C. L.; Voelcker, N. H.; Lombi, E. Cellular Binding, Uptake and Biotransformation of Silver Nanoparticles in Human T Lymphocytes. *Nat. Nanotechnol. 2021 168* **2021**, *16* (8), 926–932. https://doi.org/10.1038/s41565-021-00914-3.
(292) Pichaandi, J.; Tong, L.; Bouzekri, A.; Yu, Q.; Ornatsky, O.; Baranov, V.; Winnik, M. A. Liposome-Encapsulated NaLnF4 Nanoparticles for Mass Cytometry: Evaluating Nonspecific Binding to Cells. *Chemistry of Materials*. 2017, pp 4980–4990. https://doi.org/10.1021/acs.chemmater.7b01339.
(293) Gomez-Gomez, B.; Corte-Rodríguez, M.; Perez-Corona, M. T.; Bettmer, J.; Montes-Bayón, M.; Madrid, Y. Combined Single Cell and Single Particle ICP-TQ-MS Analysis to Quantitatively Evaluate the Uptake and Biotransformation of Tellurium Nanoparticles in Bacteria. *Anal. Chim. Acta* **2020**, *1128*, 116–128. https://doi.org/10.1016/j.aca.2020.06.058.
(294) Álvarez-Fernández García, R.; Corte-Rodríguez, M.; Macke, M.; Leblanc, K. L.; Mester, Z.; Montes-Bayón, M.; Bettmer, J. Addressing the Presence of Biogenic Selenium Nanoparticles in Yeast Cells: Analytical Strategies Based on ICP-TQ-MS. *Analyst* **2020**, *145* (4), 1457–1465. https://doi.org/10.1039/c9an01565e.
(295) Cao, Y.; Feng, J.; Tang, L.; Yu, C.; Mo, G.; Deng, B. A Highly Efficient Introduction System for Single Cell- ICP-MS and Its Application to Detection of Copper in Single Human Red Blood Cells. *Talanta* **2020**, *206* (July 2019), 120174. https://doi.org/10.1016/j.talanta.2019.120174.
(296) Tokatlian, T.; Kulp, D. W.; Mutafyan, A. A.; Jones, C. A.; Menis, S.; Georgeson, E.; Kubitz, M.; Zhang, M. H.; Melo, M. B.; Silva, M.; Yun, D. S.; Schief, W. R.; Irvine, D. J. Enhancing Humoral Responses Against HIV Envelope Trimers via

Nanoparticle Delivery with Stabilized Synthetic Liposomes. *Sci. Rep.* **2018**, *8* (1), 1–13. https://doi.org/10.1038/s41598-018-34853-2.

(297) Tokatlian, T.; Read, B. J.; Jones, C. A.; Kulp, D. W.; Menis, S.; Chang, J. Y. H.; Steichen, J. M.; Kumari, S.; Allen, J. D.; Dane, E. L.; Liguori, A.; Sangesland, M.; Lingwood, D.; Crispin, M.; Schief, W. R.; Irvine, D. J. Innate Immune Recognition of Glycans Targets HIV Nanoparticle Immunogens to Germinal Centers. *Science (80-.).* **2019**, *363* (6427). https://doi.org/10.1126/SCIENCE.AAT9120.

(298) Schudel, A.; Francis, D. M.; Thomas, S. N. Material Design for Lymph Node Drug Delivery. *Nat. Rev. Mater.* **2019**, *4* (6), 415. https://doi.org/10.1038/S41578-019-0110-7.

(299) JP, A.; AY, L.; RJ, L.; P, E.; AE, F.; RA, D. In Vivo Immune Cell Distribution of Gold Nanoparticles in Naïve and Tumor Bearing Mice. *Small* **2014**, *10* (4), 812–819. https://doi.org/10.1002/SMLL.201301998.

(300) Singh, A. Eliciting B Cell Immunity against Infectious Diseases Using Nanovaccines. *Nat. Nanotechnol. 2020 161* **2020**, *16* (1), 16–24. https://doi.org/10.1038/s41565-020-00790-3.

(301) Laborda, F.; Jiménez-Lamana, J.; Bolea, E.; Castillo, J. R. Critical Considerations for the Determination of Nanoparticle Number Concentrations, Size and Number Size Distributions by Single Particle ICP-MS. *J. Anal. At. Spectrom.* **2013**, *28* (8), 1220–1232. https://doi.org/10.1039/C3JA50100K.

(302) Zhang, Y.; Zabinyakov, N.; Majonis, D.; Bouzekri, A.; Ornatsky, O.; Baranov, V.; Winnik, M. A. Tantalum Oxide Nanoparticle-Based Mass Tag for Mass Cytometry. *Anal. Chem.* **2020**, *92* (8), 5741–5749. https://doi.org/10.1021/acs.analchem.9b04970.

(303) Pichaandi, J.; Zhao, G.; Bouzekri, A.; Lu, E.; Ornatsky, O.; Baranov, V.; Nitz, M.; Winnik, M. A. Lanthanide Nanoparticles for High Sensitivity Multiparameter Single Cell Analysis. *Chem. Sci.* **2019**, *10* (10), 2965–2974. https://doi.org/10.1039/c8sc04407d.

(304) Dai, Q.; Walkey, C.; Chan, W. C. W. Polyethylene Glycol Backfilling Mitigates the Negative Impact of the Protein Corona on Nanoparticle Cell Targeting. *Angewandte Chemie - International Edition*. 2014, pp 5093–5096. https://doi.org/10.1002/anie.201309464.

(305) Yin, L.; Zhang, Z.; Liu, Y.; Gao, Y.; Gu, J. Recent Advances in Single-Cell Analysis by Mass Spectrometry. *Analyst* **2019**, *144* (3), 824–845. https://doi.org/10.1039/c8an01190g.

(306) Fousek, K.; Watanabe, J.; Joseph, S. K.; George, A.; An, X.; Byrd, T. T.; Morris, J. S.; Luong, A.; Martínez-Paniagua, M. A.; Sanber, K.; Navai, S. A.; Gad, A. Z.; Salsman, V. S.; Mathew, P. R.; Kim, H. N.; Wagner, D. L.; Brunetti, L.; Jang, A.; Baker, M. L.; Varadarajan, N.; Hegde, M.; Kim, Y.-M.; Heisterkamp, N.; Abdel-Azim, H.; Ahmed, N. CAR T-Cells That Target Acute B-Lineage Leukemia Irrespective of CD19 Expression. *Leuk. 2020 351* **2020**, *35* (1), 75–89. https://doi.org/10.1038/s41375-020-0792-2.

(307) Webster, B.; Xiong, Y.; Hu, P.; Wu, D.; Alabanza, L.; Orentas, R. J.; Dropulic, B.; Schneider, D. Self-Driving Armored CAR-T Cells Overcome a Suppressive Milieu and Eradicate CD19+ Raji Lymphoma in Preclinical Models. *Mol. Ther.* **2021**, *29* (9), 2691–2706. https://doi.org/10.1016/J.YMTHE.2021.05.006.

(308) Bjornson, Z. B.; Nolan, G. P.; Fantl, W. J. Single Cell Mass Cytometry for Analysis of Immune System Functional States. *Curr. Opin. Immunol.* **2013**, *25* (4), 484–494. https://doi.org/10.1016/J.COI.2013.07.004.
(309) Ijsselsteijn, M. E.; van der Breggen, R.; Farina Sarasqueta, A.; Koning, F.; de Miranda, N. F. C. C. A 40-Marker Panel for High Dimensional Characterization of Cancer Immune Microenvironments by Imaging Mass Cytometry. *Front. Immunol.* **2019**, *0* (OCT), 2534. https://doi.org/10.3389/FIMMU.2019.02534.
(310) Corte-Rodríguez, M.; Álvarez-Fernández, R.; García-Cancela, P.; Montes-Bayón, M.; Bettmer, J. Single Cell ICP-MS Using on Line Sample Introduction Systems: Current Developments and Remaining Challenges. *TrAC Trends Anal. Chem.* **2020**, *132*, 116042. https://doi.org/10.1016/J.TRAC.2020.116042.
(311) Theiner, S.; Loehr, K.; Koellensperger, G.; Mueller, L.; Jakubowski, N. Single-Cell Analysis by Use of ICP-MS. *J. Anal. At. Spectrom.* **2020**, *35* (9), 1784–1813. https://doi.org/10.1039/d0ja00194e.
(312) Wang, F.; Chen, B.; Yan, B.; Yin, Y.; Hu, L.; Liang, Y.; Song, M.; Jiang, G. Scattered Light Imaging Enables Real-Time Monitoring of Label-Free Nanoparticles and Fluorescent Biomolecules in Live Cells. *J. Am. Chem. Soc.* **2019**, *141* (36), 14043–14047. https://doi.org/10.1021/jacs.9b05894.
(313) Cho, E. C.; Xie, J.; Wurm, P. A.; Xia, Y. Understanding the Role of Surface Charges in Cellular Adsorption versus Internalization by Selectively Removing Gold Nanoparticles on the Cell Surface with a I 2/KI Etchant. *Nano Lett.* **2009**, *9* (3), 1080–1084. https://doi.org/10.1021/nl803487r.
(314) Okyem, S.; Awotunde, O.; Ogunlusi, T.; Riley, M. B.; Driskell, J. D. Probing the Mechanism of Antibody-Triggered Aggregation of Gold Nanoparticles. *Langmuir* **2021**, *37* (9), 2993–3000. https://doi.org/10.1021/ACS.LANGMUIR.1C00100/SUPPL_FILE/LA1C00100_SI_001.PDF.
(315) Creyer, M. N.; Jin, Z.; Moore, C.; Yim, W.; Zhou, J.; Jokerst, J. V. Modulation of Gold Nanorod Growth via the Proteolysis of Dithiol Peptides for Enzymatic Biomarker Detection. *ACS Appl. Mater. Interfaces* **2021**, *13* (38), 45236–45243. https://doi.org/10.1021/ACSAMI.1C11620/SUPPL_FILE/AM1C11620_SI_001.PDF.
(316) Ivask, A.; Mitchell, A. J.; Hope, C. M.; Barry, S. C.; Lombi, E.; Voelcker, N. H. Single Cell Level Quantification of Nanoparticle-Cell Interactions Using Mass Cytometry. *Anal. Chem.* **2017**, *89* (16), 8228–8232. https://doi.org/10.1021/acs.analchem.7b01006.
(317) Hao, X.; Wu, J.; Shan, Y.; Cai, M.; Shang, X.; Jiang, J.; Wang, H. Caveolae-Mediated Endocytosis of Biocompatible Gold Nanoparticles in Living Hela Cells. *J. Phys. Condens. Matter* **2012**, *24* (16). https://doi.org/10.1088/0953-8984/24/16/164207.
(318) Wu, X. A.; Choi, C. H. J.; Zhang, C.; Hao, L.; Mirkin, C. A. Intracellular Fate of Spherical Nucleic Acid Nanoparticle Conjugates. *J. Am. Chem. Soc.* **2014**, *136* (21), 7726–7733. https://doi.org/10.1021/ja503010a.
(319) Rothen-Rutishauser, B.; Kuhn, D. A.; Ali, Z.; Gasser, M.; Amin, F.; Parak, W. J.; Vanhecke, D.; Fink, A.; Gehr, P.; Brandenberger, C. Quantification of Gold Nanoparticle Cell Uptake under Controlled Biological Conditions and Adequate

Resolution. **2014**, *9* (5), 607–621. https://doi.org/10.2217/NNM.13.24.
(320) Ng, C. T.; Tang, F. M. A.; Li, J. J. en; Ong, C.; Yung, L. L. Y.; Bay, B. H. Clathrin-Mediated Endocytosis of Gold Nanoparticles in Vitro. *Anat. Rec.* **2015**, *298* (2), 418–427. https://doi.org/10.1002/ar.23051.
(321) Klingberg, H.; Oddershede, L. B.; Loeschner, K.; Larsen, E. H. Uptake of Gold Nanoparticles in Primary Human Endothelial Cells. *Toxicol. Res. (Camb).* **2015**, No. 4, 655. https://doi.org/10.1039/c4tx00061g.
(322) Krpetić, Ž.; Porta, F.; Caneva, E.; Dal Santo, V.; Scarì, G. Phagocytosis of Biocompatible Gold Nanoparticles. *Langmuir* **2010**, *26* (18), 14799–14805. https://doi.org/10.1021/la102758f.
(323) Leduc, C.; Jung, J. M.; Carney, R. R.; Stellacci, F.; Lounis, B. Direct Investigation of Intracellular Presence of Gold Nanoparticles via Photothermal Heterodyne Imaging. *ACS Nano* **2011**, *5* (4), 2587–2592. https://doi.org/10.1021/nn1023285.
(324) Lund, T.; Callaghan, M. F.; Williams, P.; Turmaine, M.; Bachmann, C.; Rademacher, T.; Roitt, I. M.; Bayford, R. The Influence of Ligand Organization on the Rate of Uptake of Gold Nanoparticles by Colorectal Cancer Cells. *Biomaterials* **2011**, *32* (36), 9776–9784. https://doi.org/10.1016/j.biomaterials.2011.09.018.
(325) Huang, S.; Deshmukh, H.; Rajagopalan, K. K.; Wang, S. Gold Nanoparticles Electroporation Enhanced Polyplex Delivery to Mammalian Cells. *Electrophoresis* **2014**, *35* (12–13), 1837–1845. https://doi.org/10.1002/elps.201300617.
(326) Taylor, U.; Garrels, W.; Barchanski, A.; Peterson, S.; Sajti, L.; Lucas-Hahn, A.; Gamrad, L.; Baulain, U.; Klein, S.; Kues, W. A.; Barcikowski, S.; Rath, D. Injection of Ligand-Free Gold and Silver Nanoparticles into Murine Embryos Does Not Impact Pre-Implantation Development. *Beilstein J. Nanotechnol.* **2014**, *5* (1), 677–688. https://doi.org/10.3762/bjnano.5.80.
(327) Zhang, B.; Shen, S.; Liao, Z.; Shi, W.; Wang, Y.; Zhao, J.; Hu, Y.; Yang, J.; Chen, J.; Mei, H.; Hu, Y.; Pang, Z.; Jiang, X. Targeting Fibronectins of Glioma Extracellular Matrix by CLT1 Peptide-Conjugated Nanoparticles. *Biomaterials* **2014**, *35* (13), 4088–4098. https://doi.org/10.1016/j.biomaterials.2014.01.046.
(328) Chung, E. J.; Cheng, Y.; Morshed, R.; Nord, K.; Han, Y.; Wegscheid, M. L.; Auffinger, B.; Wainwright, D. A.; Lesniak, M. S.; Tirrell, M. V. Fibrin-Binding, Peptide Amphiphile Micelles for Targeting Glioblastoma. *Biomaterials* **2014**, *35* (4), 1249–1256. https://doi.org/10.1016/j.biomaterials.2013.10.064.
(329) Cieslewicz, M.; Tang, J.; Yu, J. L.; Cao, H.; Zavaljevski, M.; Motoyama, K.; Lieber, A. Targeted Delivery of Proapoptotic Peptides to Tumor-Associated Macrophages Improves Survival. *Proc. Natl. Acad. Sci.* **2013**, *110* (40), 15919–15924. https://doi.org/10.1073/pnas.1312197110.
(330) Ngambenjawong, C.; Pun, S. H. Multivalent Polymers Displaying M2 Macrophage-Targeting Peptides Improve Target Binding Avidity and Serum Stability. *ACS Biomater. Sci. Eng.* **2017**, *3* (9), 2050–2053. https://doi.org/10.1021/acsbiomaterials.7b00332.
(331) Zhang, J.; Yuan, Z. F.; Wang, Y.; Chen, W. H.; Luo, G. F.; Cheng, S. X.; Zhuo, R. X.; Zhang, X. Z. Multifunctional Envelope-Type Mesoporous Silica Nanoparticles for Tumor-Triggered Targeting Drug Delivery. *J. Am. Chem. Soc.* **2013**, *135* (13), 5068–5073. https://doi.org/10.1021/ja312004m.
(332) Zhang, M. Z.; Yu, Y.; Yu, R. N.; Wan, M.; Zhang, R. Y.; Zhao, Y. Di. Tracking the

Down-Regulation of Folate Receptor-α in Cancer Cells through Target Specific Delivery of Quantum Dots Coupled with Antisense Oligonucleotide and Targeted Peptide. *Small* **2013**, *9* (24), 4183–4193. https://doi.org/10.1002/smll.201300994.

(333) Locatelli, E.; Naddaka, M.; Uboldi, C.; Loudos, G.; Fragogeorgi, E.; Molinari, V.; Pucci, A.; Tsotakos, T.; Psimadas, D.; Ponti, J.; Franchini, M. C. Targeted Delivery of Silver Nanoparticles and Alisertib: *In Vitro* and *in Vivo* Synergistic Effect against Glioblastoma. *Nanomedicine* **2014**, *9* (6), 839–849. https://doi.org/10.2217/nnm.14.1.

(334) Lam, F. C.; Morton, S. W.; Wyckoff, J.; Vu Han, T. L.; Hwang, M. K.; Maffa, A.; Balkanska-Sinclair, E.; Yaffe, M. B.; Floyd, S. R.; Hammond, P. T. Enhanced Efficacy of Combined Temozolomide and Bromodomain Inhibitor Therapy for Gliomas Using Targeted Nanoparticles. *Nat. Commun.* **2018**, *9* (1). https://doi.org/10.1038/s41467-018-04315-4.

(335) Schmid, D.; Park, C. G.; Hartl, C. A.; Subedi, N.; Cartwright, A. N.; Puerto, R. B.; Zheng, Y.; Maiarana, J.; Freeman, G. J.; Wucherpfennig, K. W.; Irvine, D. J.; Goldberg, M. S. T Cell-Targeting Nanoparticles Focus Delivery of Immunotherapy to Improve Antitumor Immunity. *Nat. Commun.* **2017**, *8* (1), 1–11. https://doi.org/10.1038/s41467-017-01830-8.

(336) Dai, Q.; Yan, Y.; Ang, C. S.; Kempe, K.; Kamphuis, M. M. J.; Dodds, S. J.; Caruso, F. Monoclonal Antibody-Functionalized Multilayered Particles: Targeting Cancer Cells in the Presence of Protein Coronas. *ACS Nano* **2015**, *9* (3), 2876–2885. https://doi.org/10.1021/nn506929e.

(337) Song, J.; Zhou, J.; Duan, H. Self-Assembled Plasmonic Vesicles of SERS-Encoded Amphiphilic Gold Nanoparticles for Cancer Cell Targeting and Traceable Intracellular Drug Delivery. *J. Am. Chem. Soc.* **2012**, *134* (32), 13458–13469. https://doi.org/10.1021/ja305154a.

(338) Kotagiri, N.; Li, Z.; Xu, X.; Mondal, S.; Nehorai, A.; Achilefu, S. Antibody Quantum Dot Conjugates Developed via Copper-Free Click Chemistry for Rapid Analysis of Biological Samples Using a Microfluidic Microsphere Array System. *Bioconjug. Chem.* **2014**, *25* (7), 1272–1281. https://doi.org/10.1021/bc500139u.

(339) Engelberg, S.; Modrejewski, J.; Walter, J. G.; Livney, Y. D.; Assaraf, Y. G. Cancer Cell-Selective, Clathrin-Mediated Endocytosis of Aptamer-Decorated Nanoparticles. *Oncotarget* **2018**, *9* (30), 20993–21006. https://doi.org/10.18632/oncotarget.24772.

(340) Prusty, D. K.; Adam, V.; Zadegan, R. M.; Irsen, S.; Famulok, M. Supramolecular Aptamer Nano-Constructs for Receptor-Mediated Targeting and Light-Triggered Release of Chemotherapeutics into Cancer Cells. *Nat. Commun.* **2018**, *9*. https://doi.org/10.1038/s41467-018-02929-2.

(341) Wang, J.; Ma, Q.; Hu, X. X.; Liu, H.; Zheng, W.; Chen, X.; Yuan, Q.; Tan, W. Autofluorescence-Free Targeted Tumor Imaging Based on Luminous Nanoparticles with Composition-Dependent Size and Persistent Luminescence. *ACS Nano* **2017**, *11* (8), 8010–8017. https://doi.org/10.1021/acsnano.7b02643.

(342) Porta, F.; Lamers, G. E. M.; Morrhayim, J.; Chatzopoulou, A.; Schaaf, M.; den Dulk, H.; Backendorf, C.; Zink, J. I.; Kros, A. Folic Acid-Modified Mesoporous Silica Nanoparticles for Cellular and Nuclear Targeted Drug Delivery. *Adv. Healthc. Mater.* **2013**, *2* (2), 281–286. https://doi.org/10.1002/adhm.201200176.

(343) Mackey, M. A.; Saira, F.; Mahmoud, M. A.; El-Sayed, M. A. Inducing Cancer Cell Death by Targeting Its Nucleus: Solid Gold Nanospheres versus Hollow Gold Nanocages. *Bioconjug. Chem.* **2013**, *24* (6), 897–906. https://doi.org/10.1021/bc300592d.

(344) Yuan, Y.; Chen, S.; Paunesku, T.; Gleber, S. C.; Liu, W. C.; Doty, C. B.; Mak, R.; Deng, J.; Jin, Q.; Lai, B.; Brister, K.; Flachenecker, C.; Jacobsen, C.; Vogt, S.; Woloschak, G. E. Epidermal Growth Factor Receptor Targeted Nuclear Delivery and High-Resolution Whole Cell x-Ray Imaging of Fe3O4@TiO 2 Nanoparticles in Cancer Cells. *ACS Nano* **2013**, *7* (12), 10502–10517. https://doi.org/10.1021/nn4033294.

(345) Misra, R.; Sahoo, S. K. Intracellular Trafficking of Nuclear Localization Signal Conjugated Nanoparticles for Cancer Therapy. *Eur. J. Pharm. Sci.* **2010**, *39* (1–3), 152–163. https://doi.org/10.1016/j.ejps.2009.11.010.

(346) Ma, Kun Shen, Haijun Shen, Song Xie, Men Mao, Chaunbin Qui, Liyan Jin, Y. Development of a Successive Targeting Liposome with Multi-Ligand for Efficient Targeting Gene Delivery. *J. Gene Med.* **2011**, *13*, 290–301. https://doi.org/10.1002/jgm.

(347) Tammam, S. N.; Azzazy, H. M. E.; Lamprecht, A. The Effect of Nanoparticle Size and NLS Density on Nuclear Targeting in Cancer and Normal Cells; Impaired Nuclear Import and Aberrant Nanoparticle Intracellular Trafficking in Glioma. *J. Control. Release* **2017**, *253*, 30–36. https://doi.org/10.1016/j.jconrel.2017.02.029.

(348) Qu, Q.; Ma, X.; Zhao, Y. Targeted Delivery of Doxorubicin to Mitochondria Using Mesoporous Silica Nanoparticle Nanocarriers. *Nanoscale* **2015**, *7* (40), 16677–16686. https://doi.org/10.1039/c5nr05139h.

(349) Jeena, M. T.; Palanikumar, L.; Go, E. M.; Kim, I.; Kang, M. G.; Lee, S.; Park, S.; Choi, H.; Kim, C.; Jin, S. M.; Bae, S. C.; Rhee, H. W.; Lee, E.; Kwak, S. K.; Ryu, J. H. Mitochondria Localization Induced Self-Assembly of Peptide Amphiphiles for Cellular Dysfunction. *Nat. Commun.* **2017**, *8* (1), 1–9. https://doi.org/10.1038/s41467-017-00047-z.

(350) Kwon, H. J.; Cha, M. Y.; Kim, D.; Kim, D. K.; Soh, M.; Shin, K.; Hyeon, T.; Mook-Jung, I. Mitochondria-Targeting Ceria Nanoparticles as Antioxidants for Alzheimeŕs Disease. *ACS Nano* **2016**, *10* (2), 2860–2870. https://doi.org/10.1021/acsnano.5b08045.

(351) Friedmann-morvinski, D.; Kotamraju, V. R.; Roth, L.; Sugahara, K. N.; Girard, O. M.; Robert, F.; Mendoza, H. De; Perez-garcia, C. G.; Kroll, T. T.; Hoong, N. H.; Leary, D. D. M. O.; Agemy, L.; Friedmann-morvinski, D.; Ramana, V.; Roth, L.; Sugahara, K. N. Correction for Agemy et Al., Targeted Nanoparticle Enhanced Proapoptotic Peptide as Potential Therapy for Glioblastoma. *Proc. Natl. Acad. Sci.* **2014**, *111* (32), 11906–11906. https://doi.org/10.1073/pnas.1413457111.

(352) Kang, J. W.; So, P. T. C.; Dasari, R. R.; Lim, D. K. High Resolution Live Cell Raman Imaging Using Subcellular Organelle-Targeting SERS-Sensitive Gold Nanoparticles with Highly Narrow Intra-Nanogap. *Nano Lett.* **2015**, *15* (3), 1766–1772. https://doi.org/10.1021/nl504444w.

(353) Yamada, Y.; Harashima, H. Enhancement in Selective Mitochondrial Association by Direct Modification of a Mitochondrial Targeting Signal Peptide on a Liposomal Based Nanocarrier. *Mitochondrion* **2013**, *13* (5), 526–532.

https://doi.org/10.1016/j.mito.2012.09.001.
(354) Zhang, Z.; Zhou, L.; Zhou, Y.; Liu, J.; Xing, X.; Zhong, J.; Xu, G.; Kang, Z.; Liu, J. Mitophagy Induced by Nanoparticle–Peptide Conjugates Enabling an Alternative Intracellular Trafficking Route. *Biomaterials* **2015**, *65*, 56–65. https://doi.org/10.1016/J.BIOMATERIALS.2015.06.029.
(355) Fujiwara, T.; Akita, H.; Harashima, H. Intracellular Fate of Octaarginine-Modified Liposomes in Polarized MDCK Cells. *Int. J. Pharm.* **2010**, *386* (1–2), 122–130. https://doi.org/10.1016/j.ijpharm.2009.11.005.
(356) Krpetić, Ž.; Saleemi, S.; Prior, I. A.; Sée, V.; Qureshi, R.; Brust, M. Negotiation of Intracellular Membrane Barriers by TAT-Modified Gold Nanoparticles. *ACS Nano* **2011**, *5* (6), 5195–5201. https://doi.org/10.1021/nn201369k.
(357) Dalal, C.; Jana, N. R. Multivalency Effect of TAT-Peptide-Functionalized Nanoparticle in Cellular Endocytosis and Subcellular Trafficking. *J. Phys. Chem. B* **2017**, *121* (14), 2942–2951. https://doi.org/10.1021/acs.jpcb.6b12182.
(358) Li, R. S.; Gao, P. F.; Zhang, H. Z.; Zheng, L. L.; Li, C. M.; Wang, J.; Li, Y. F.; Liu, F.; Li, N.; Huang, C. Z. Chiral Nanoprobes for Targeting and Long-Term Imaging of the Golgi Apparatus. *Chem. Sci.* **2017**, *8* (10), 6829–6835. https://doi.org/10.1039/c7sc01316g.
(359) Wang, Guankui Norton, An Pokharel, Deep Song, Yuan Hill, R. KDEL Peptide Gold Nanoconstructs: Promising Nanoplatforms for Drug Delivery. *Nanomedicine* **2013**, *9* (3), 336–374. https://doi.org/10.1016/j.nano.2012.09.002.
(360) Pan, T.; Song, W.; Gao, H.; Li, T.; Cao, X.; Zhong, S.; Wang, Y. MiR-29b-Loaded Gold Nanoparticles Targeting to the Endoplasmic Reticulum for Synergistic Promotion of Osteogenic Differentiation. *ACS Appl. Mater. Interfaces* **2016**, *8* (30), 19217–19227. https://doi.org/10.1021/acsami.6b02969.

Appendix A: Figures

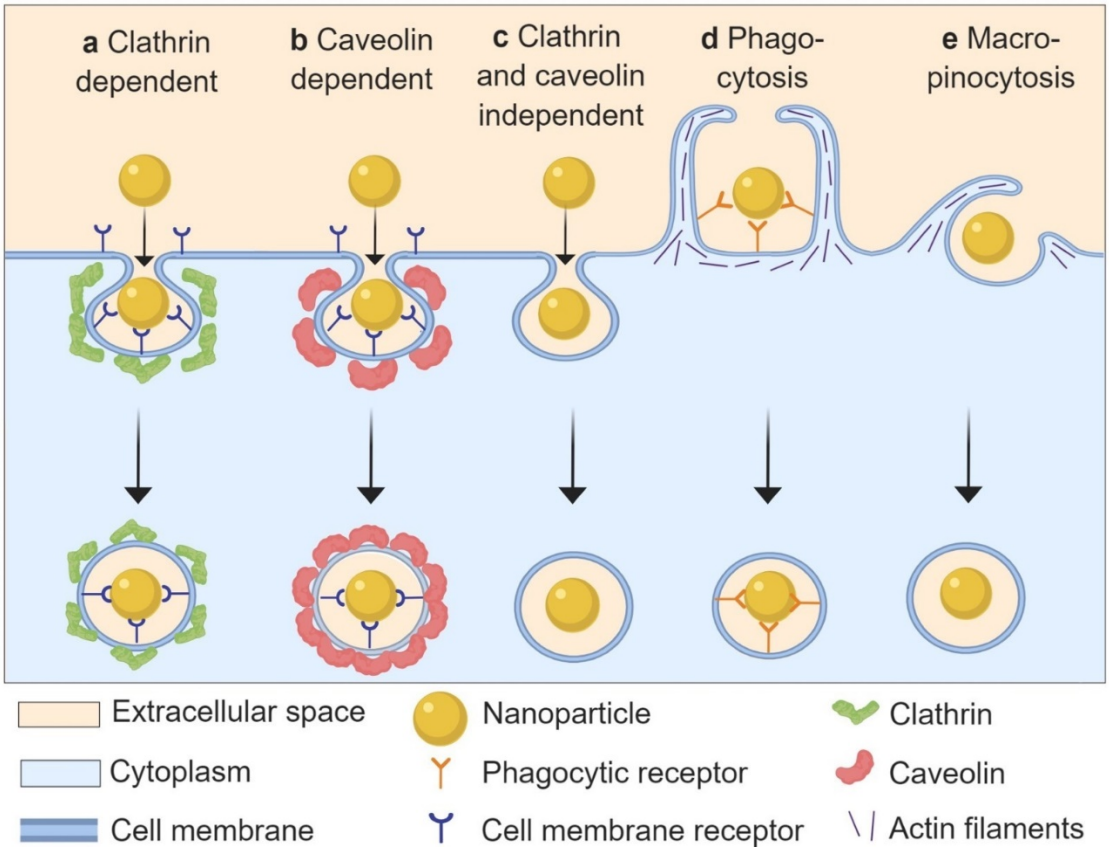


Figure 2.1. Schematic overview of nanoparticle uptake pathways *via* endocytosis. Multiple different pathways for cellular entry of nanoparticles *via* endocytosis mechanisms exist: (a) clathrin-dependent; (b) caveolin-dependent; (c) clathrin- and caveolin-independent; (d) phagocytosis; and (e) macropinocytosis pathways. These nanoparticle cell uptake pathways are mechanistically distinct and highly regulated at the biomolecular level. The pathway by which nanoparticles enter cells is important, as it determines intracellular nanoparticle transport and corresponding biological response and therapeutic effect.

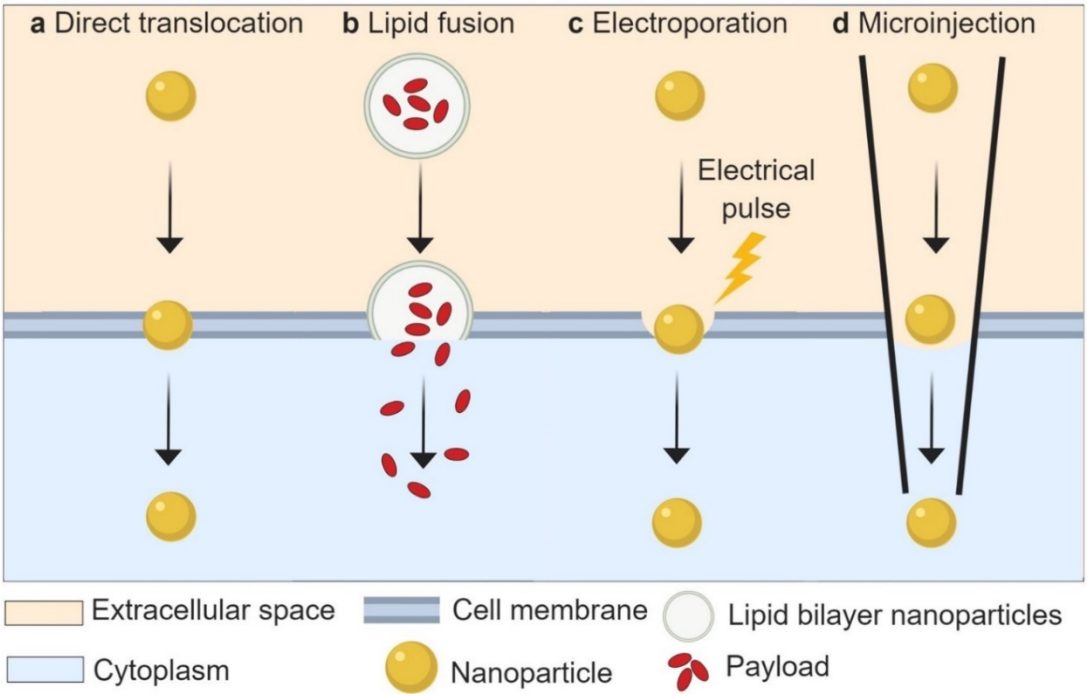


Figure 2.2. Schematic overview of nanoparticle cytoplasmic delivery pathways and strategies. Major pathways and strategies for nanoparticles to cross the cell plasma membrane for direct cytoplasmic entry include: (a) direct translocation; (b) lipid fusion; (c) electroporation; and (d) microinjection. Each of these pathways allows nanoparticles to directly enter the cell's cytoplasm. Direct translocation and lipid fusion are dependent upon physicochemical properties of the nanoparticles. Electroporation strategies use electrical pulses to disrupt the cell plasma membrane, while for microinjection strategies the plasma membrane is punctured by a microscopic needle to inject nanoparticles directly into the cytoplasm.

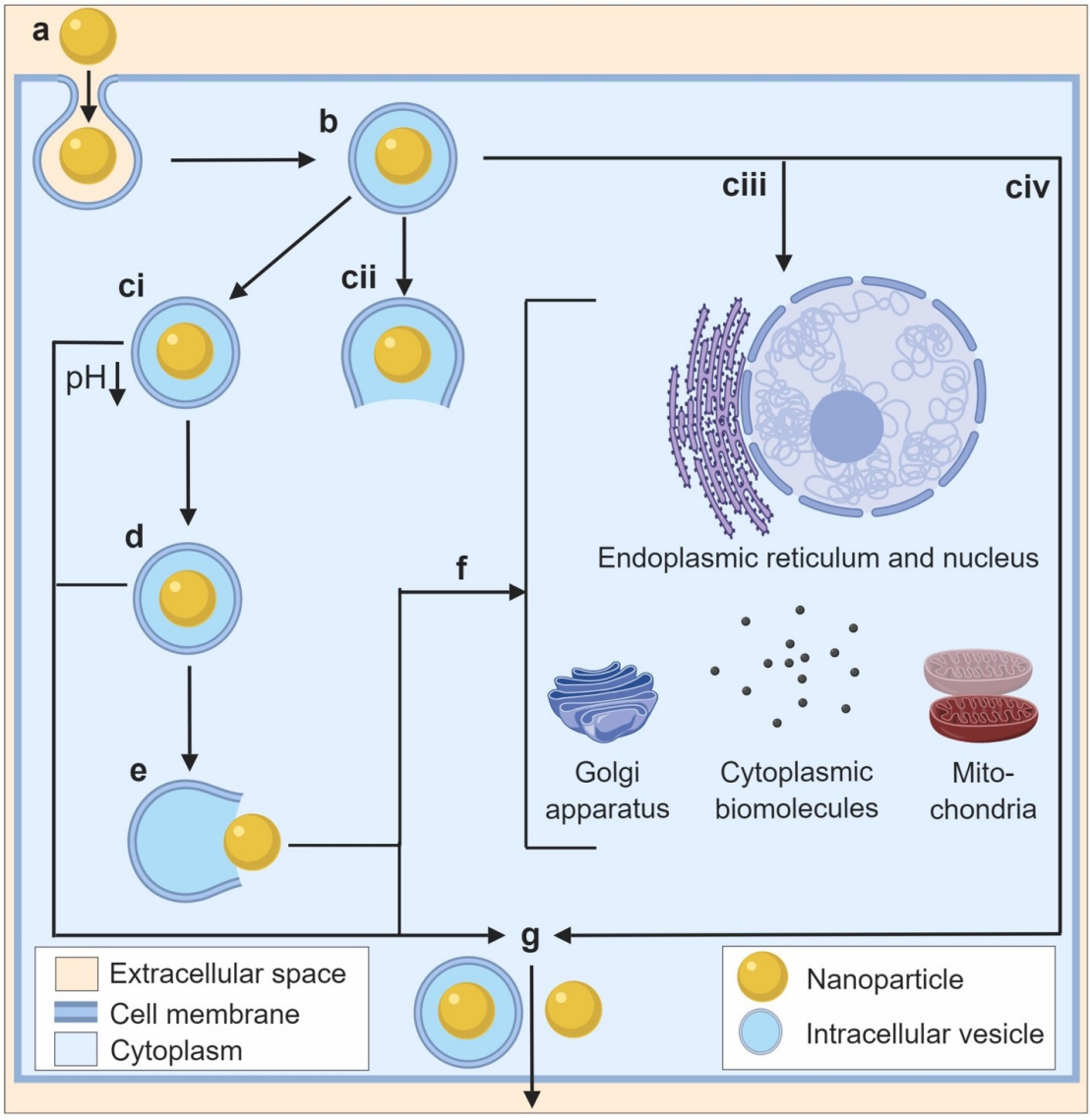


Figure 2.3. Simplified overview of main nanoparticle intracellular trafficking pathways and mechanisms. (a) Cellular entry of nanoparticles often occurs through an endocytotic pathway. (b) After internalization, nanoparticles are typically trafficked to a sorting/early endosome which can undertake several intracellular transformations. (ci) The sorting/early endosome forms a late endosome as the pH decreases that then fuses with other components to become a lysosome (d) from which nanoparticles can either escape for subsequent intracellular targeting (f) or in which nanoparticles can get degraded or exocytosed (g). An alternative to lysosome formation can either be (cii) endosomal escape and subsequent intracellular targeting (f), or (ciii) a recycling process through a recycling endosome located near the perinuclear region, or even (civ/g) rapid recycling directly to the plasma membrane.

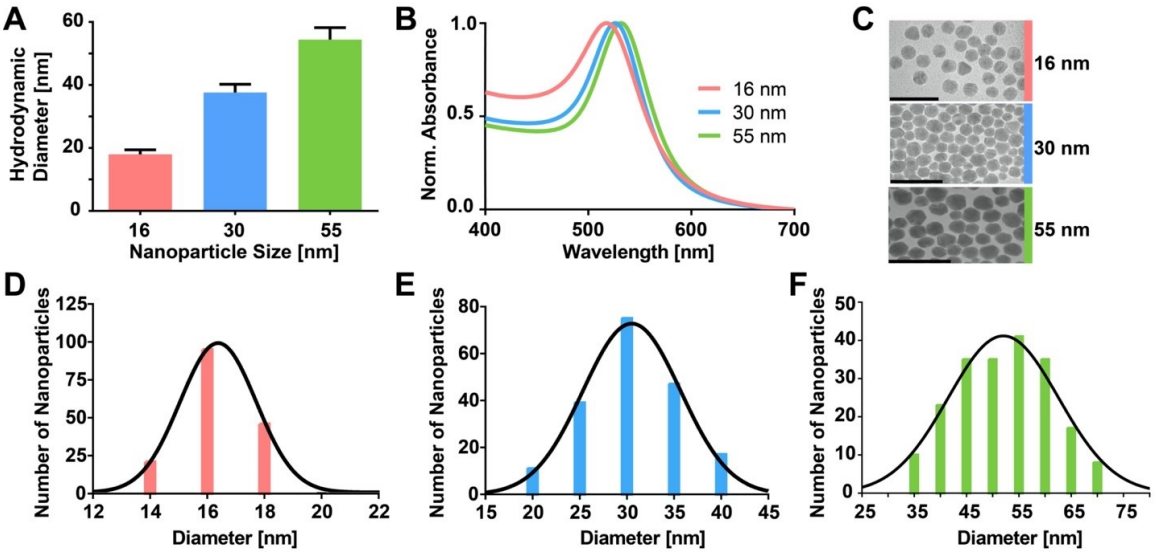


Figure 3.1: Nanoparticle characterization of three different batches of citrate coated AuNPs. (A) Hydrodynamic diameters as obtained by DLS. Bars represent mean values and standard deviation (n=3). (B) UV-Vis spectrophotometry spectra. (C) Transmission electron micrographs. Scale bars indicate 50 nm, 100 nm, and 200 nm, respectively (top to bottom). (D-F) Nanoparticle size distribution histograms based on TEM image analysis using ImageJ. The AuNP distributions (black lines) were fitted using a Gaussian distribution in GraphPad Prism.

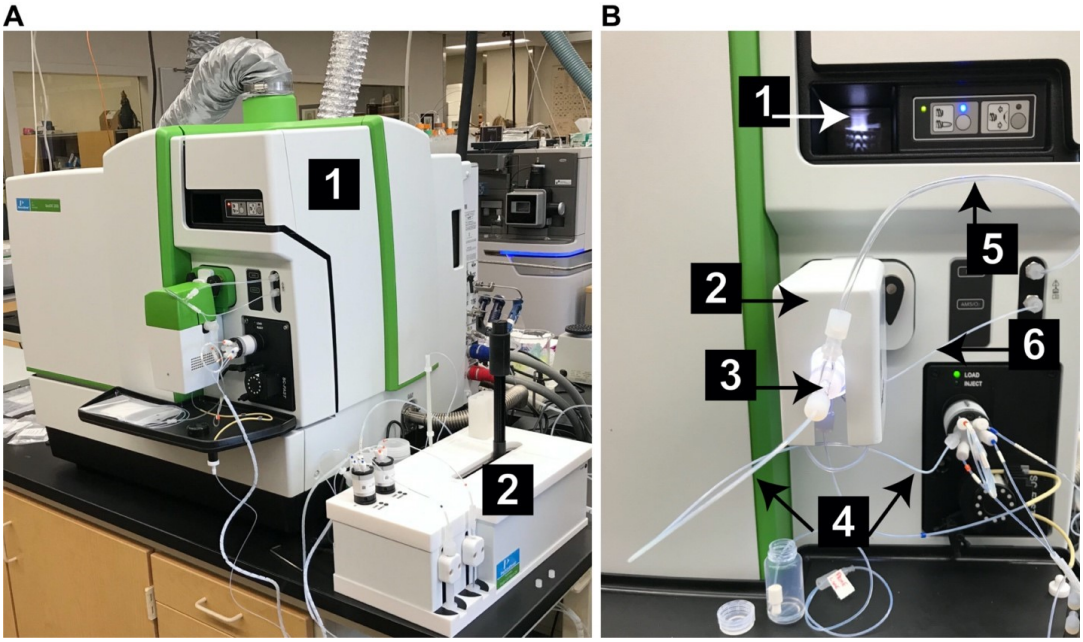


Figure 3.2: Single Particle Inductively Coupled Plasma Mass Spectrometer (SP-ICP-MS). (A) Overall instrument setup with 1: ICP-MS, and 2: autosampler. (B) ICP-MS sample introduction setup with 1: inductively coupled argon plasma, 2: spray chamber, 3: high efficiency nebulizer, 4: microfluidics sample introduction lines, 5: nebulizer gas line, 6: makeup gas flow line.

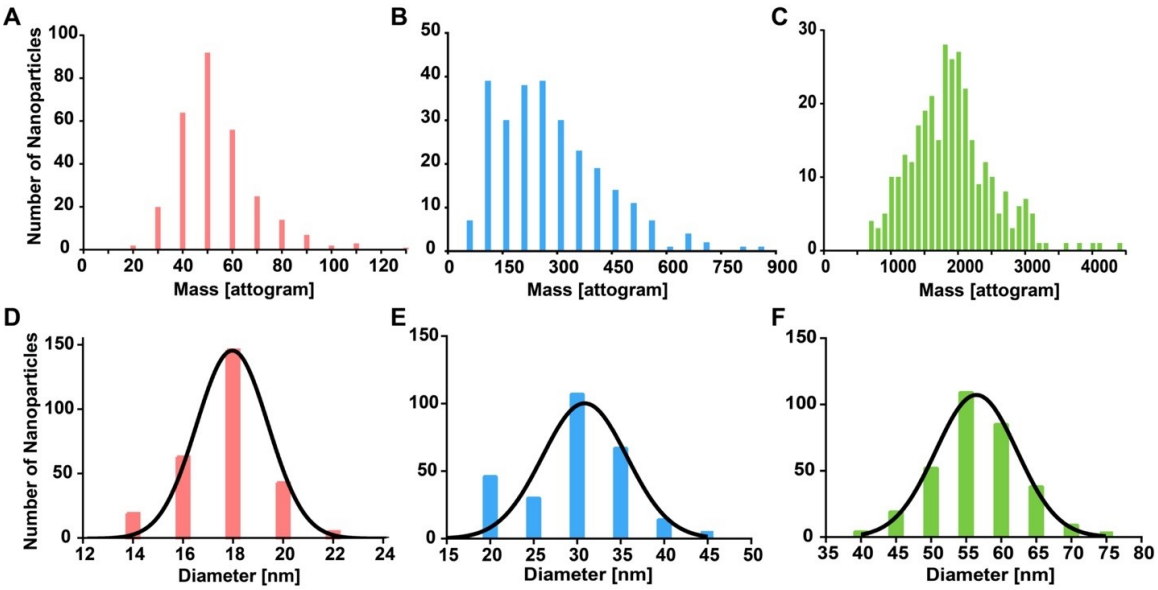


Figure 3.3: Nanoparticle size characterization based on SP-ICP-MS. Panels A-C show SP-ICP-MS mass histograms for 16-nm AuNPs (A), 30-nm AuNPs (B), and 55-nm AuNPs (C). In panels D-F, the masses of A-C histograms are converted into corresponding nanoparticle diameters. The AuNP distributions (black lines) were fitted using a Gaussian distribution in GraphPad Prism.

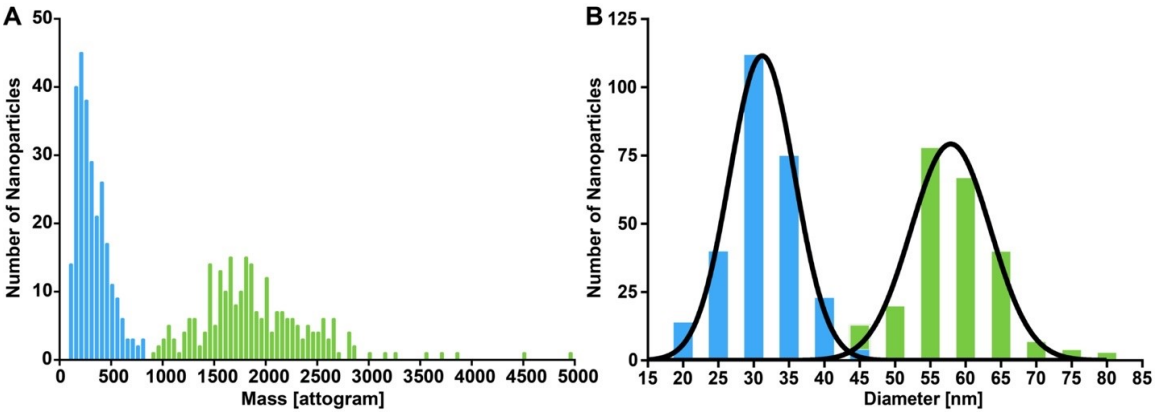


Figure 3.4: SP-ICP-MS analysis of 1:1 mixture of AuNPs. (A) Mass histogram of 1:1 mixtures of 30-nm (blue population) and 55-nm (green population) AuNPs obtained by SP-ICP-MS. (B) Mass histogram from panel A is converted into diameter histogram. The total number of AuNPs analyzed were 502, with 268 particles determined as 30-nm AuNPs (blue) and 234 particles determined as 55-nm (green) AuNPs by SP-ICP-MS. The AuNP distributions (black lines) were fitted using a Gaussian distribution in GraphPad Prism. The AuNP distributions were statistically significant different based on an unpaired T test ($t = 52.28$, $df = 500$, $p < 0.0001$).

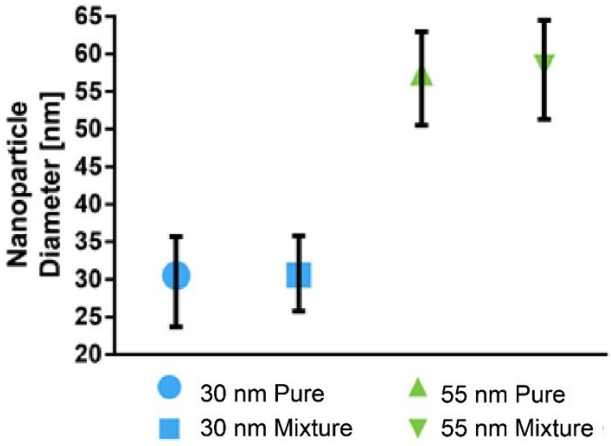
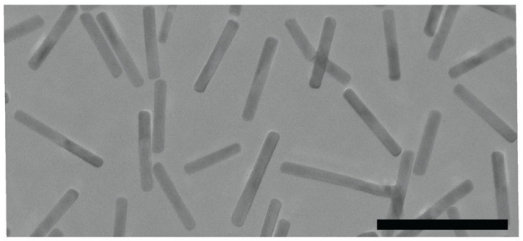
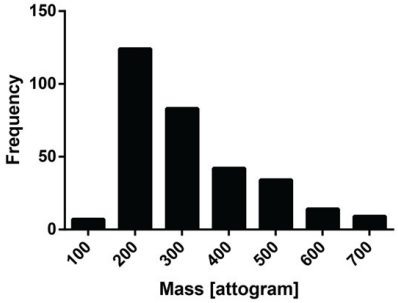


Figure 3.5: Comparison of nanoparticle mean diameters measured pure versus in a 1:1 mixture of 30-nm and 55-nm AuNPs. No statistical significance was observed ($p<0.01$) for nanoparticles measured pure versus in a mixture using an unpaired T test.

A



B



C

Nanorod Maximum Feret Diameter [nm][a]	Nanorod Minimum Feret Diameter [nm][a]	Nanorod Volume [nm^3][b]	Expected Nanorod Mass [ag][c]	SP-ICP-MS Mean Mass [ag][d]
63.5	9.0	16227	313	319

[a] Average value as obtained by TEM image analysis.
[b] As calculated by Equation S1.
[c] As calculated by Equation S2.
[d] Mean mass as obtained by SP-ICP-MS measurements.

Figure 3.6: (A) Transmission electron micrograph of citrate gold nanorods, scale bar represents 100 nm. (B) SP-ICP-MS mass histogram of gold nanorods. (C) Comparison of estimated gold nanorod masses from TEM (converted from obtained length and width measurements) and measured gold nanorod masses by SP-ICP-MS. Masses are provided as mean values +/- standard deviation.

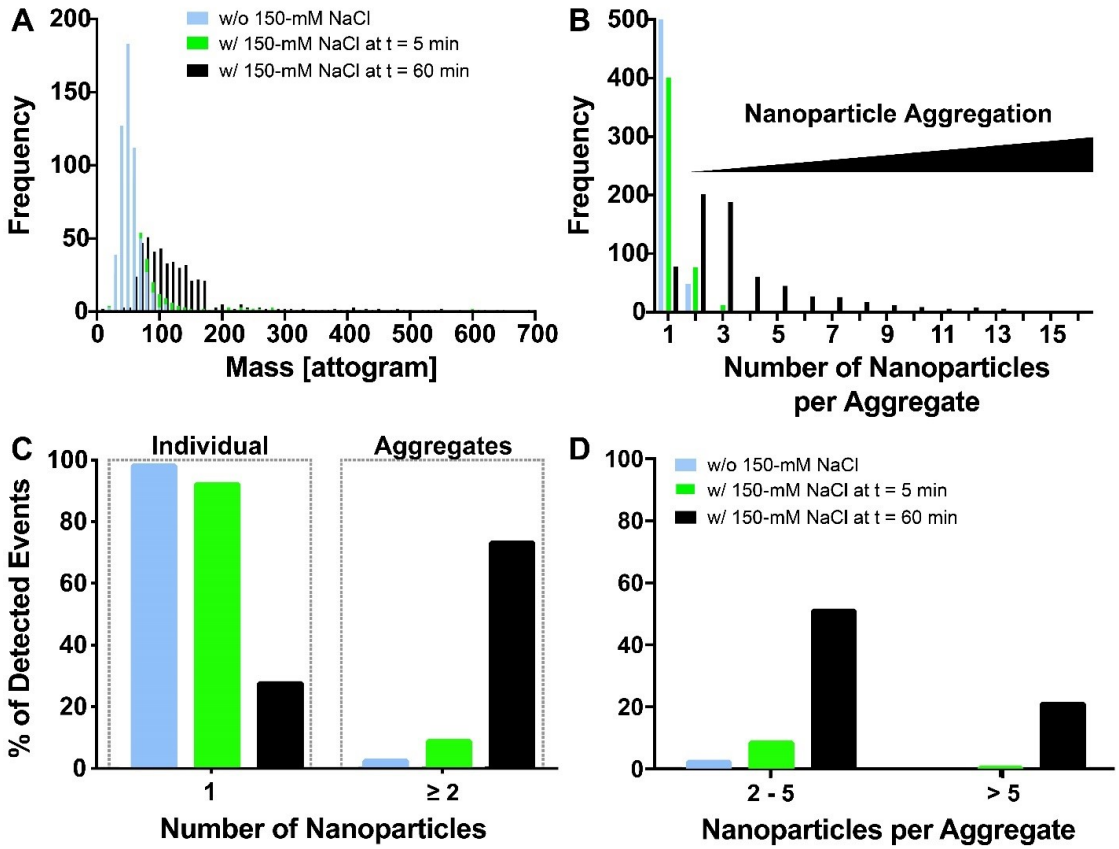


Figure 3.7: SP-ICP-MS to assess citrate coated AuNPs aggregation. (A) Mass histograms of citrate coated 16-nm colloidal AuNPs exposed to 150-mM aqueous NaCl solution over time. (B) Detected mass distribution in panel A is converted into number of nanoparticles per aggregate (Bin size = 50 ag). (C) Percentage of individual nanoparticles are compared to masses >100 ag, a mass which is equal to >2 nanoparticles per aggregate (i.e. detected event). (D) Breakdown of AuNPs aggregates into bins of 2-5 and >5 AuNPs per aggregate (i.e. detected event).

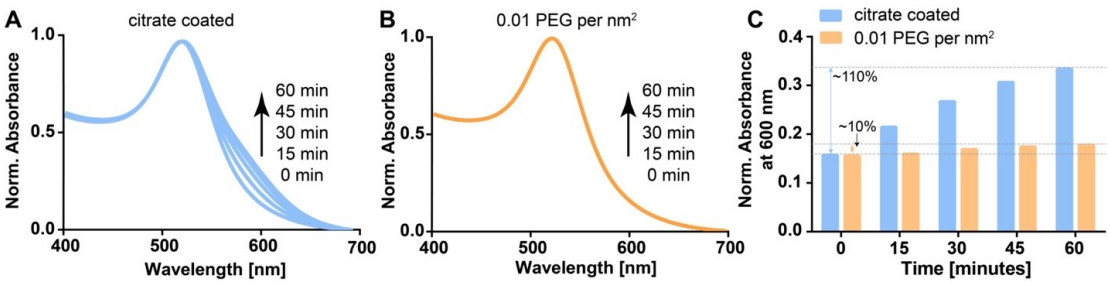


Figure 3.8: Monitoring nanoparticle aggregation kinetics via UV-Vis spectrophotometry. (A) Normalized UV-Vis absorption spectra (overlap of 6 individual spectra) of 16-nm AuNPs without PEG surface modification (0 PEG/nm^2) over time. (B) Normalized UV-Vis absorption spectra (overlap of 6 individual spectra) of 16-nm AuNPs surface modified with 0.01 PEG/nm^2 over time. (C) Quantitative comparison of normalized absorbance at 600 nm over time for both nanoparticle groups shown in panels A and B.

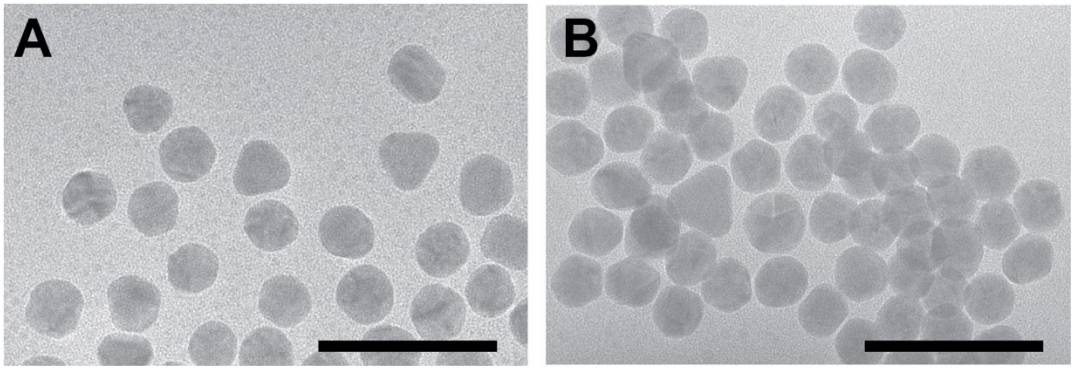
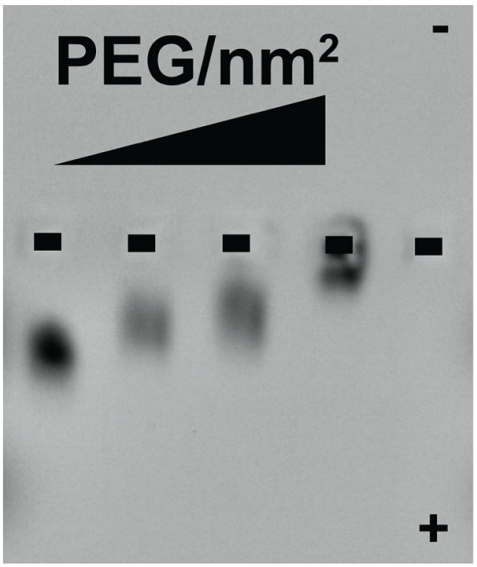


Figure 3.9: Representative transmission electron micrographs. (A) TEM micrograph of 16-nm citrate coated AuNPs without addition of saline solution. (B) TEM micrograph of aggregated 16-nm citrate coated AuNPs upon addition of 150-mM NaCl. Scale bar: 50 nm.

A



B

PEG /nm^2	Hydrodynamic Diameter [nm]	PDI
0	23.9 ± 0.4	0.04
0.010	25.4 ± 0.3	0.04
0.025	26.9 ± 0.4	0.06
0.050	28.5 ± 0.1	0.04

C

PEG /nm^2	Zeta Potential [mV]
0	-12.8 ± 0.8
0.010	-13.7 ± 1.2
0.025	-9.5 ± 0.2
0.050	-7.9 ± 0.2

Figure 3.10: (A) Gel electrophoresis of PEGylated 16 nm gold nanoparticles with increasing PEG density 0, 0.010, 0.025, 0.050 PEG/nm^2 from left to right. Dashed lines represent wells. (B) DLS measurements of 16-nm AuNPs with increasing PEG density are provided as mean values +/- standard deviation (n =3). (C) Zeta potential measurements of 16-nm AuNPs in DI water with increasing PEG density are provided as mean values +/- standard deviation (n =3).

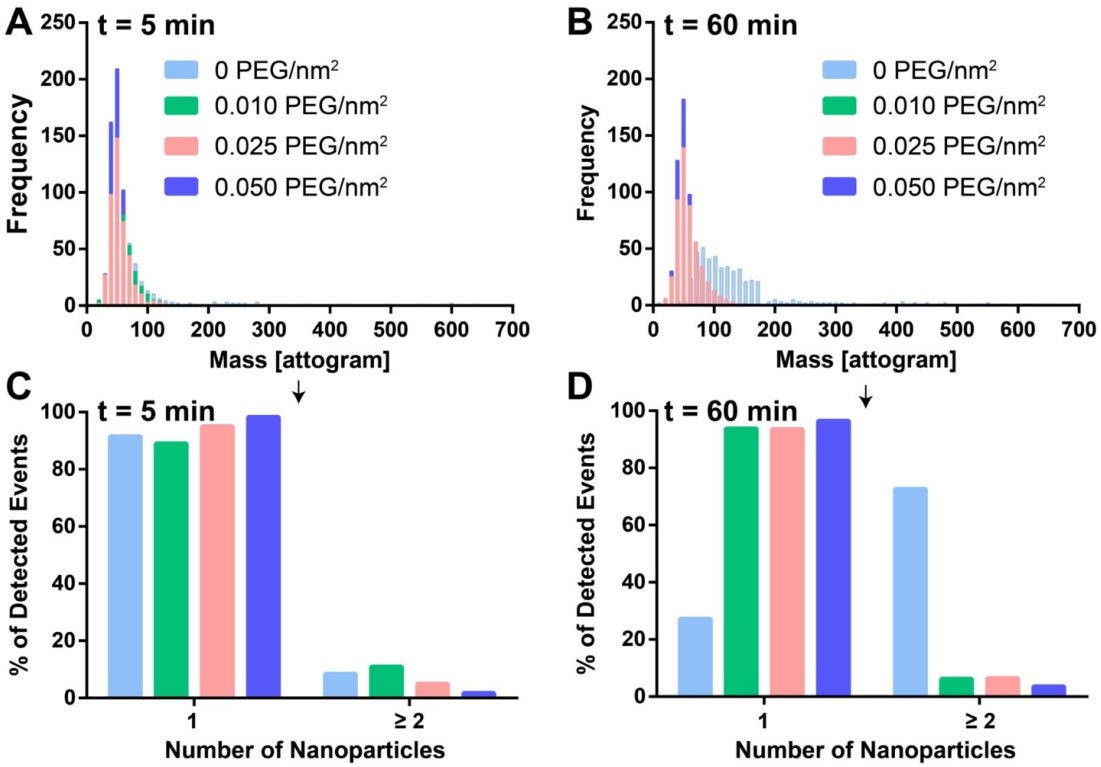


Figure 3.11: SP-ICP-MS to evaluate aggregation characteristics of PEGylated 16-nm AuNPs exposed to 150-mM NaCl. Mass histograms of PEGylated 16-nm AuNPs at t_{5min} in saline solution (A), and t_{60min} in saline solution (B). Percentages of individual nanoparticles of total detected nanoparticle events are plotted at t_{5min} (C) and t_{60min} (D) for PEGylated AuNPs in 150-mM NaCl.

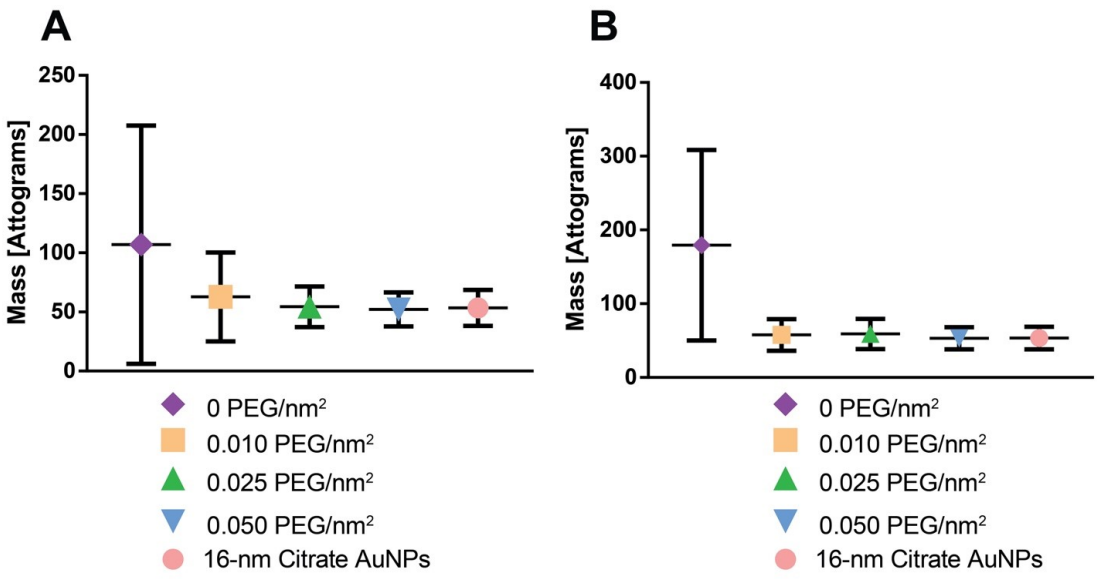


Figure 3.12: Comparison of the mean nanoparticle masses from SP-ICP-MS of PEGylated 16-nm AuNPs in 150-mM NaCl at T0min (A) and at T60min (B) after exposure. Error bars indicate standard deviation. As a control group, 16-nm citrate-coated AuNPs are represented that were not exposed to NaCl. For each group, a minimum of 400 events were collected by SP-ICP-MS.

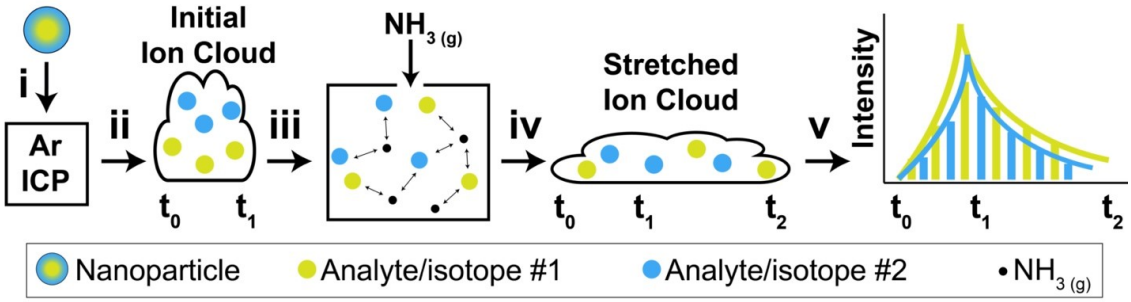


Figure 4.1: Overview of dual analyte (isotope) analysis with quadrupole ICP-MS technology in single particle mode. i. An intact, single nanoparticle containing two different isotopes, (blue and green) is introduced into an inductively coupled argon plasma, where the nanoparticle is atomized and ionized. **ii.** Initially, a short-lasting (µs range) transient nanoparticle ion cloud (t_0-t_1) is produced. **iii.** The transient nanoparticle ion cloud enters the collision cell, where it interacts with NH_3 gas. Through axial field technology (AFT) voltage application, ion passage time is increased. **iv.** The interactions between the transient nanoparticle ion cloud, the NH_3 gas, and the AFT result in an ion cloud stretching (from µs to ms; t_0-t_2). **v.** The stretched ion cloud then enters the quadrupole mass filter. Due to the long duration time of the nanoparticle ion cloud, the quadrupole mass filter can be switched between different m/z ratios to allow simultaneous quantification of two analytes (or isotopes) of interest per ion cloud, which is enabled by sufficiently short microseconds detector dwell times.

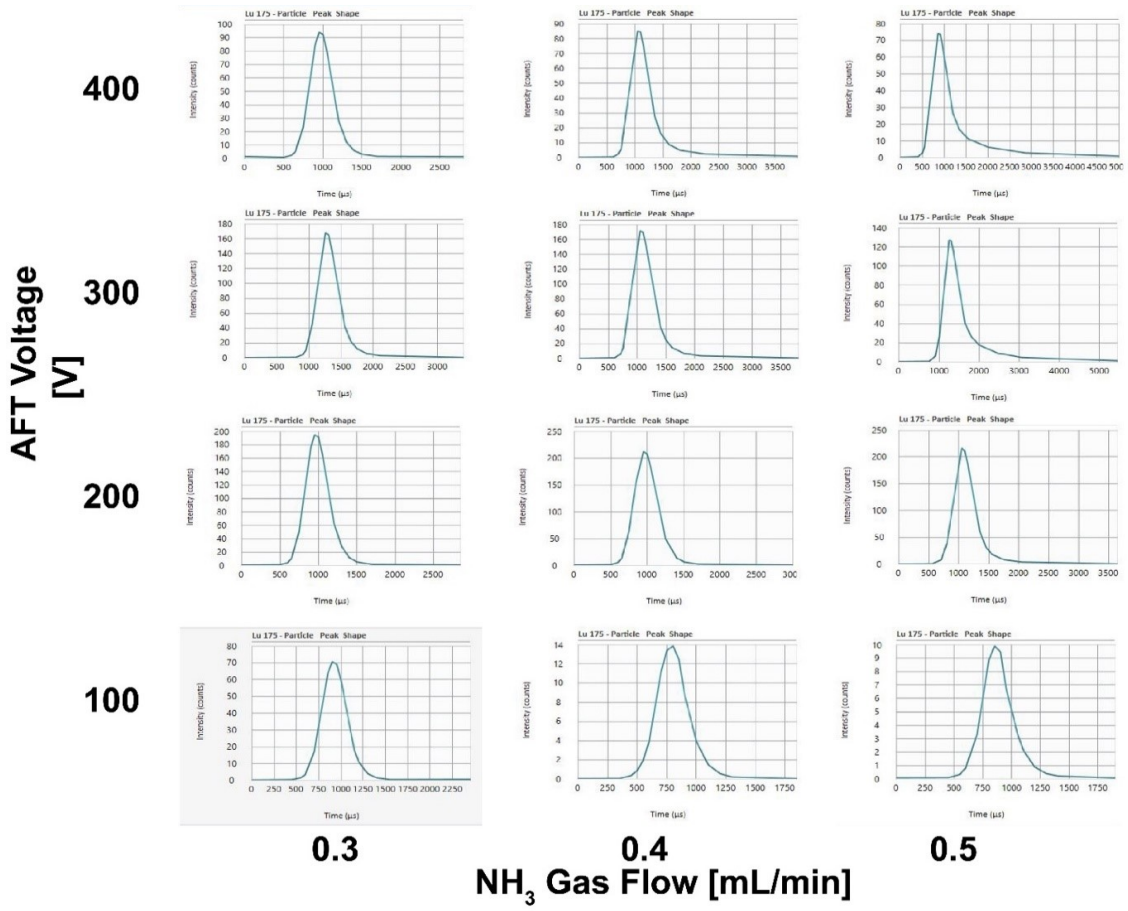


Figure 4.2: Effects of Axial Field Technology (AFT) voltage and NH_3 gas flow on duration of transient ion cloud. ^{175}Lu from the commercially available lanthanide-ion doped polymer beads was analyzed at a particle concentration of 1E5 particles per mL.

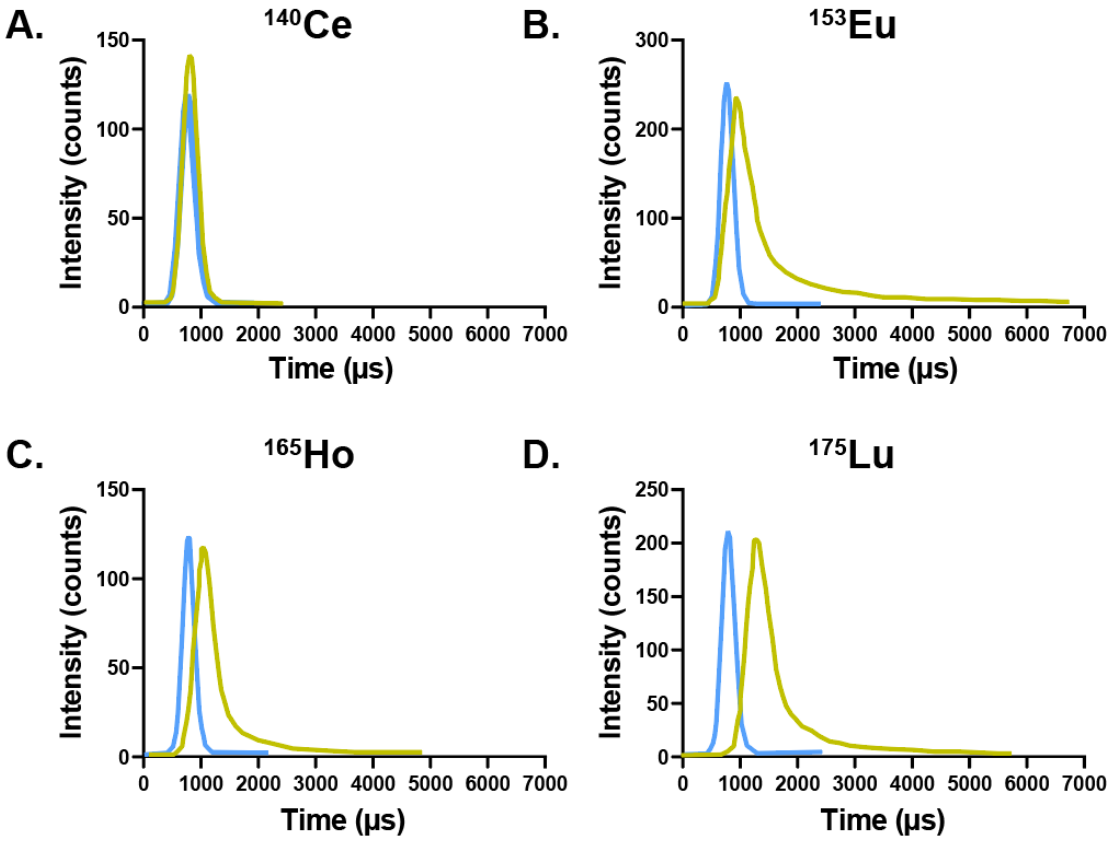


Figure 4.3: A-D Average transient particle ion cloud duration of each isotope from the commercially available lanthanide-ion doped polymer beads in standard (blue) mode, and when the collision cell is used (green) at a particle concentration of 1E5 particles per mL.

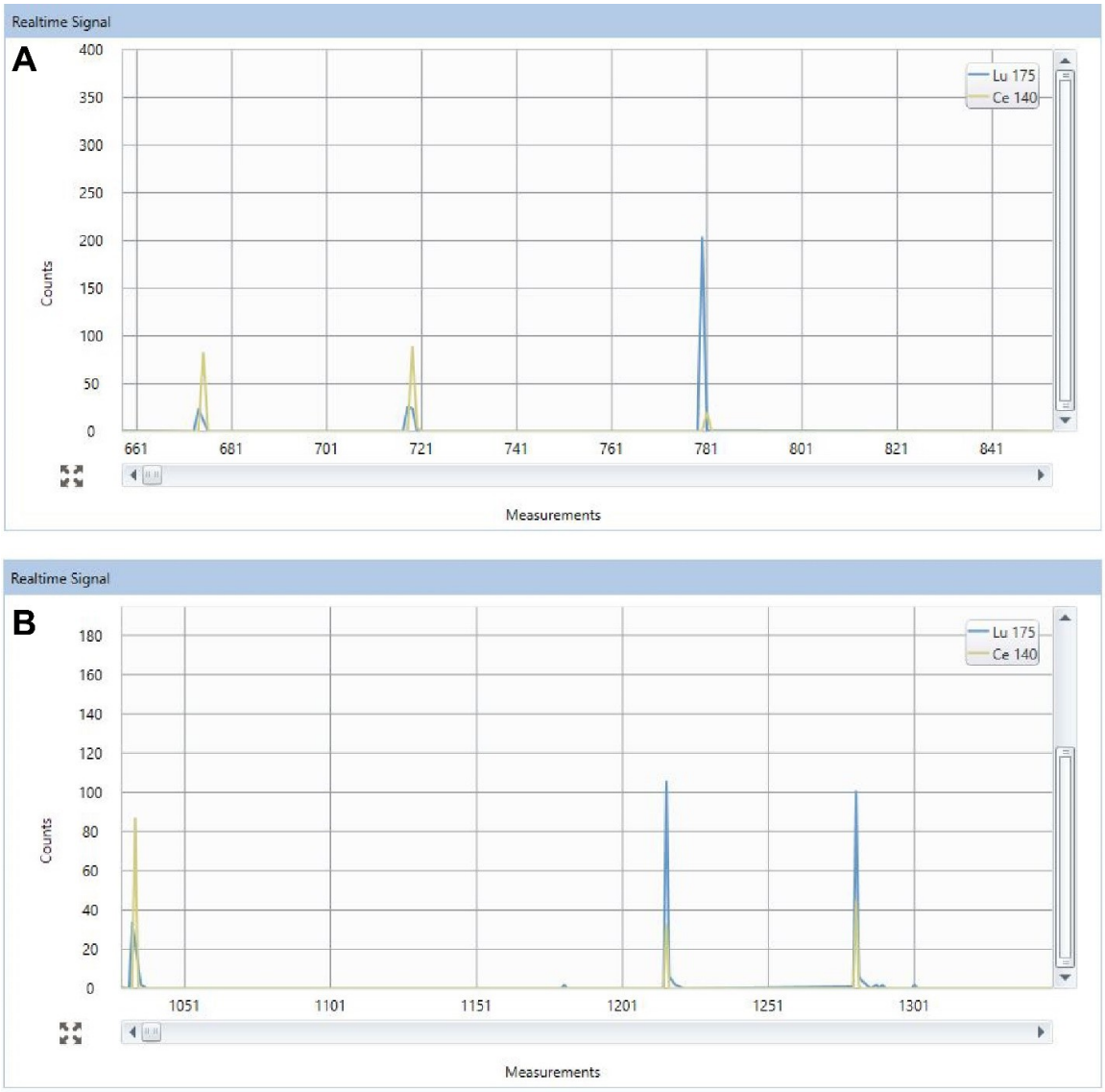


Figure 4.4: Realtime signal of commercially available lanthanide-ion doped polymer beads when: **A.** the collision cell is not operational; **B.** optimized collision cell parameters are used.

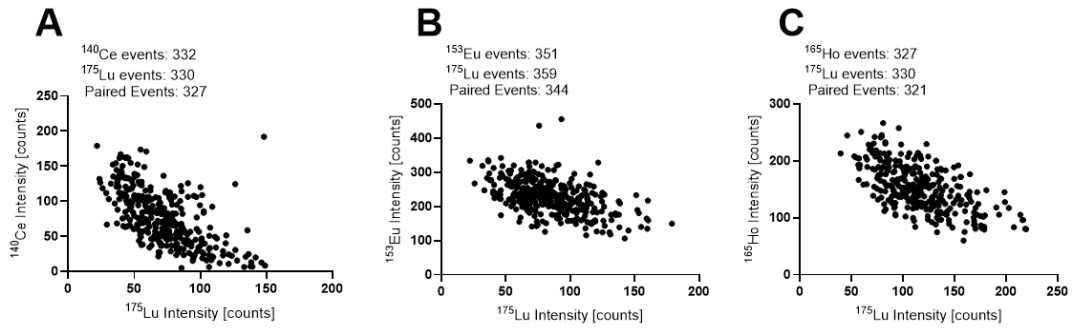


Figure 4.5: Dual analyte intensity distributions of lanthanide beads using optimized dual analyte SP ICP MS. **A.** Paired isotope events of ^{175}Lu and ^{140}Ce. **B.** Paired isotope events of ^{175}Lu and ^{153}Eu. **C.** Paired isotope events of ^{175}Lu and ^{165}Ho.

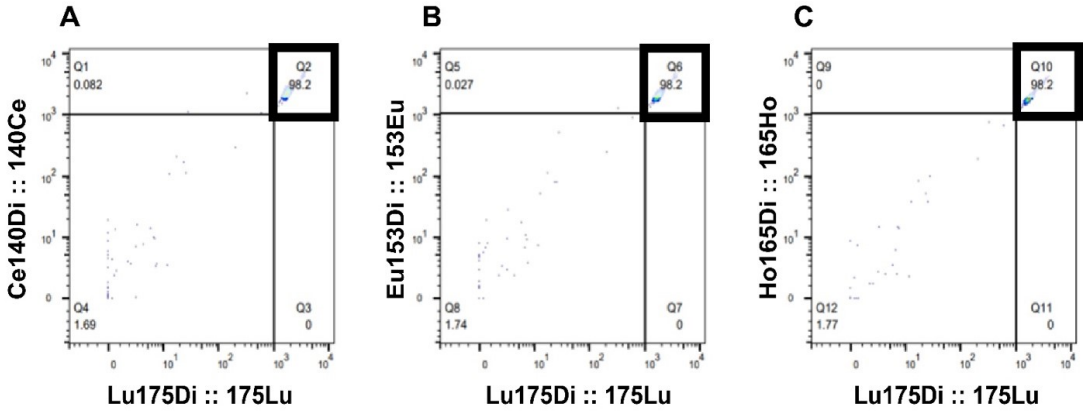


Figure 4.6: FlowJo analysis of commercially available lanthanide-ion doped polymer beads analyzed on CyTOF. **A.** Paired isotope events of ^{175}Lu and ^{140}Ce. **B.** Paired isotope events of ^{175}Lu and ^{153}Eu. **C.** Paired isotope events of ^{175}Lu and ^{165}Ho. Gates were placed on 10^3 counts for all isotopes. ~99% paired events were observed for each pair of isotopes. ~1000 events were collected for each isotope.

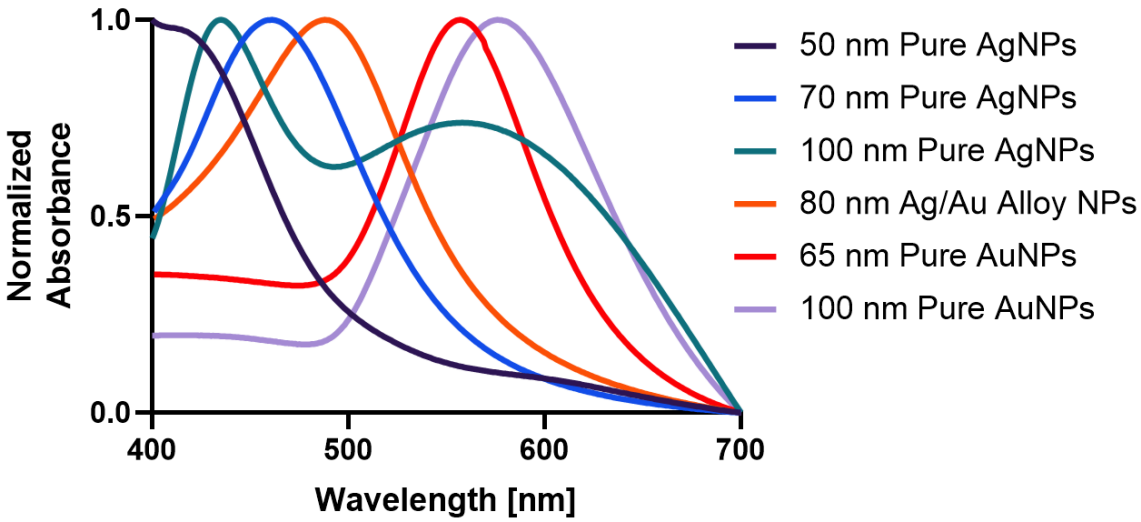


Figure 4.7: UV-Vis spectra of in-house synthesized silver, gold, and Ag/Au alloy nanoparticles.

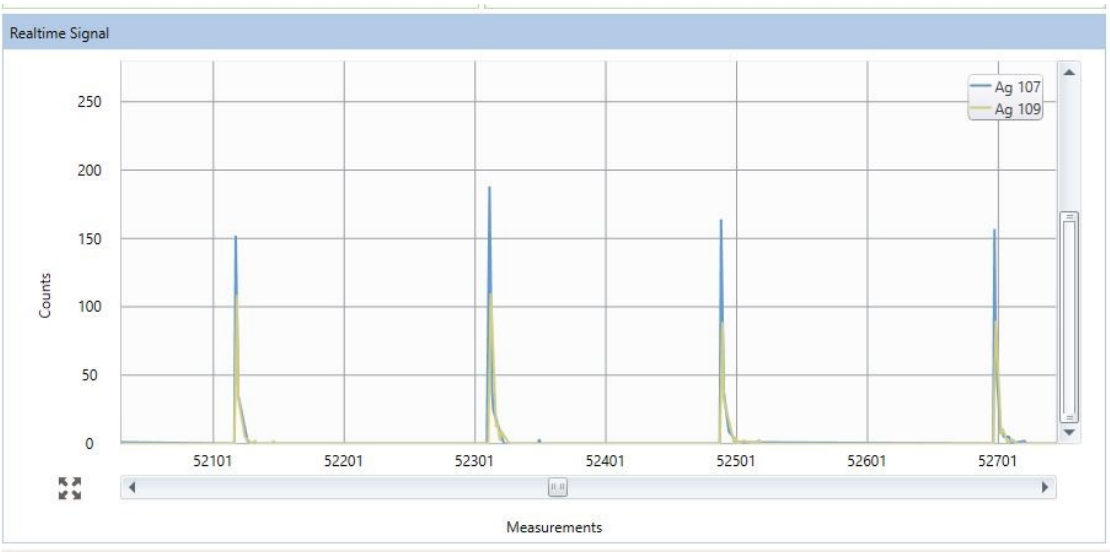


Figure 4.8: Realtime dual analyte SP-ICP-MS signals of overlapping transient nanoparticle ion clouds from 100-nm AgNPs for both silver isotopes using optimized collision reaction cell conditions.

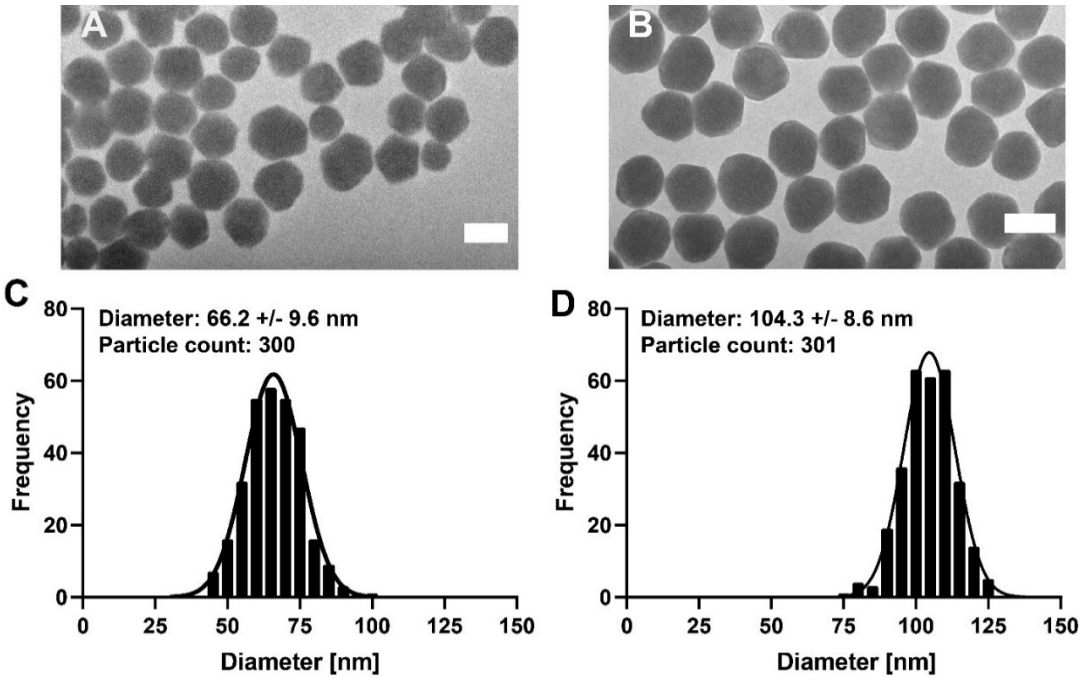


Figure 4.9: TEM micrographs of **A.** 65-nm AuNPs; **B.** 100-nm AuNPs. Scale bars represent 65 and 100 nm, respectively. **C.** Size analysis of TEM micrographs of 65-nm AuNPs. **D.** Size analysis of TEM micrographs of 100-nm AuNPs. Values represent the means values and standard deviations.

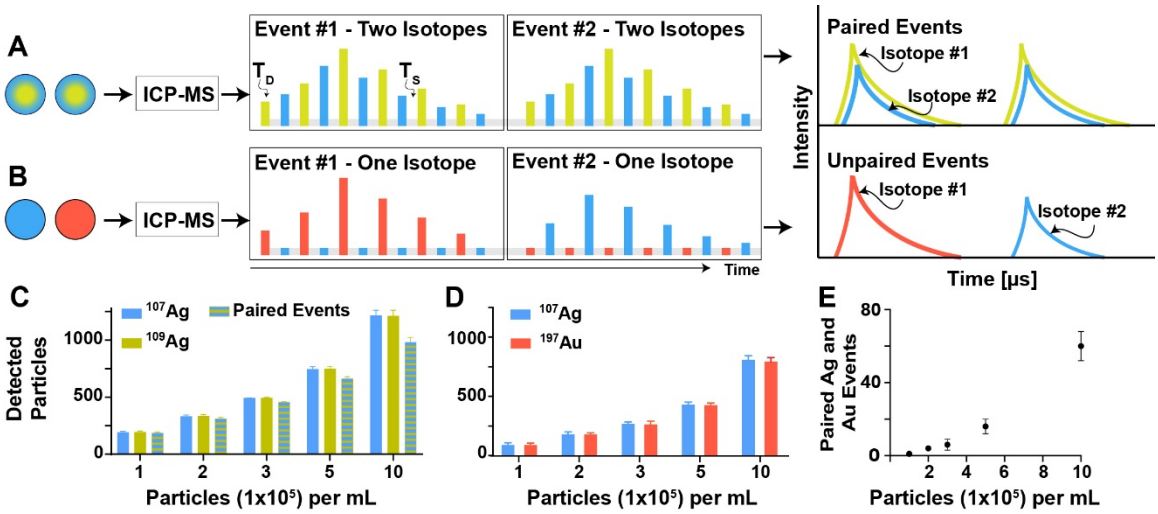


Figure 4.10: Quantifying paired and unpaired isotope events in dual analyte quadrupole SP-ICP-MS mode for individual nanoparticles. A. Schematic representation of paired events for two different isotopes (blue and green) in the same nanoparticle, where T_D is the detector dwell time and T_s is the quadrupole mass filter settling time. **B.** Schematic representation of unpaired events for two different isotopes (blue and red) in different nanoparticles (blue and red). **C.** Detection of paired isotope events (^{107}Ag and ^{109}Ag) using 100-nm silver nanoparticles (AgNPs) as a function of nanoparticle concentration; mean +/- StD, n=5. **D.** Detected particles of a 1:1 mixture of 100-nm AgNPs and 100-nm gold nanoparticles (AuNPs) as a function of nanoparticle concentration; mean +/- StD, n=5. **E.** Detected paired isotope events from the 1:1 mixture of 100-nm AgNPs and AuNPs as a function of nanoparticle concentration; mean +/- StD, n=5. For all measurements, the scan time was 30 seconds.

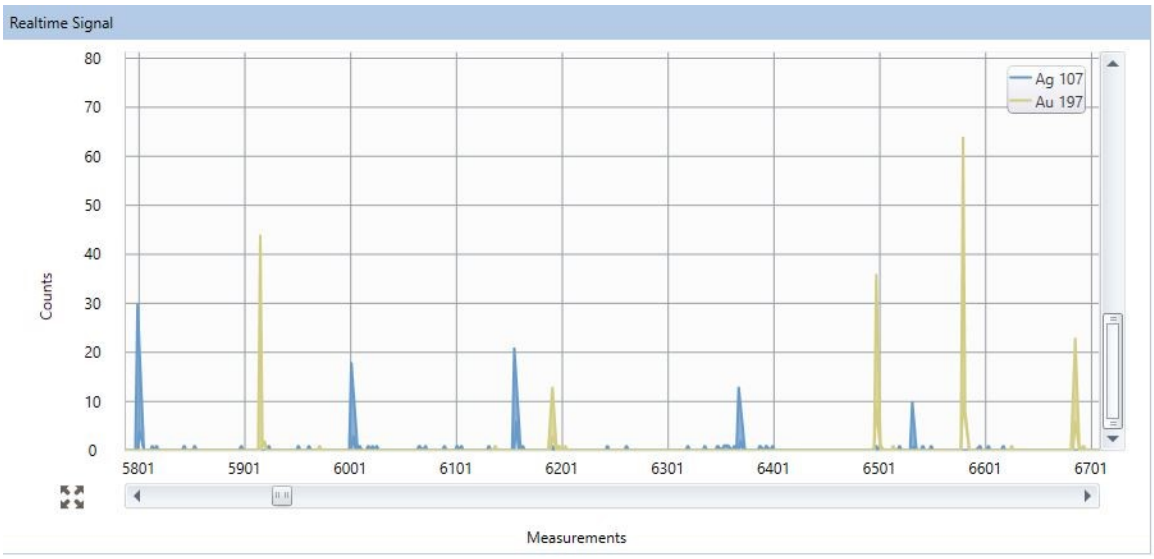


Figure 4.11: Realtime dual analyte SP-ICP-MS signals of non-overlapping transient nanoparticle ion clouds from a nanoparticle mixture containing 100-nm AgNPs (blue) and 100-nm AuNPs (green).

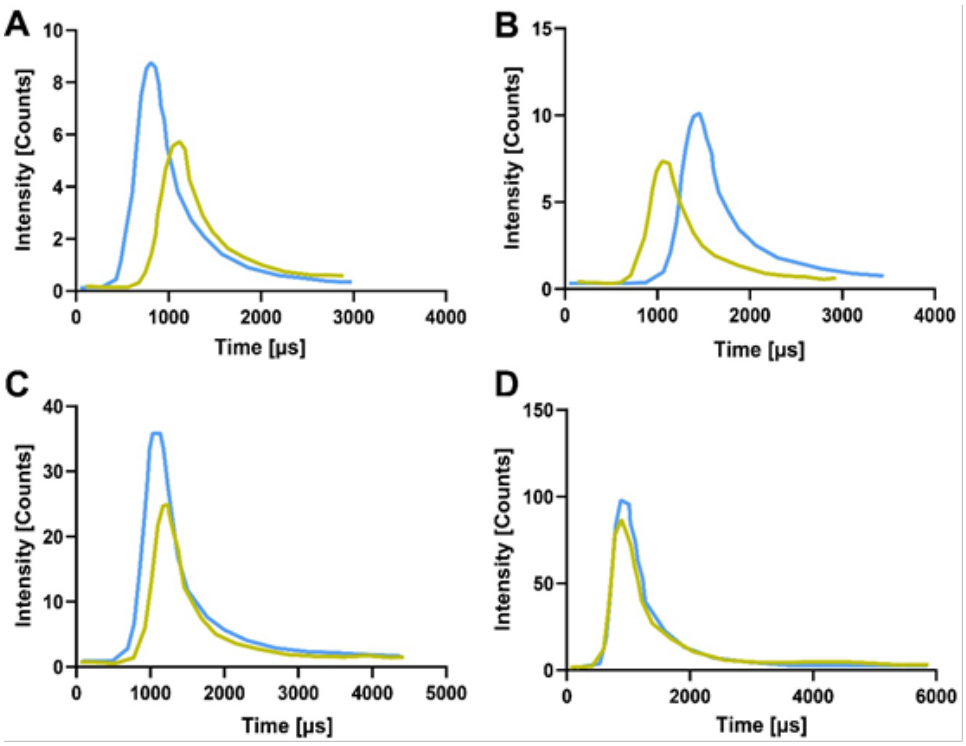


Figure 4.12: Transient ion cloud duration time of AgNPs for silver isotopes ^{107}Ag (blue) and ^{109}Ag (green) with nominal diameters of: **A.** 30 nm; **B.** 50 nm; **C.** 70 nm; **D.** 100 nm.

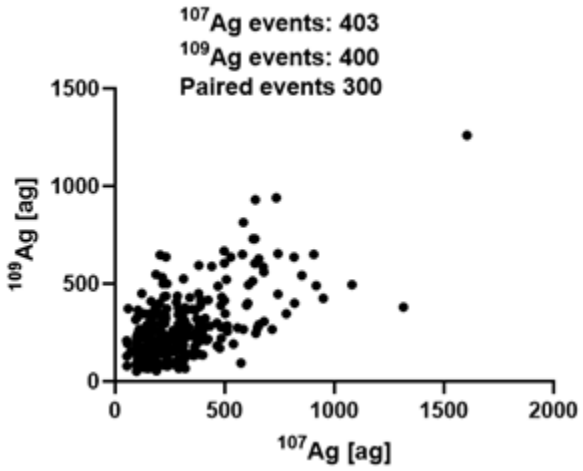


Figure 4.13: Dual isotope mass distribution of 30-nm AgNPs for ^{107}Ag and ^{109}Ag using optimized dual analyte ICP-MS conditions.

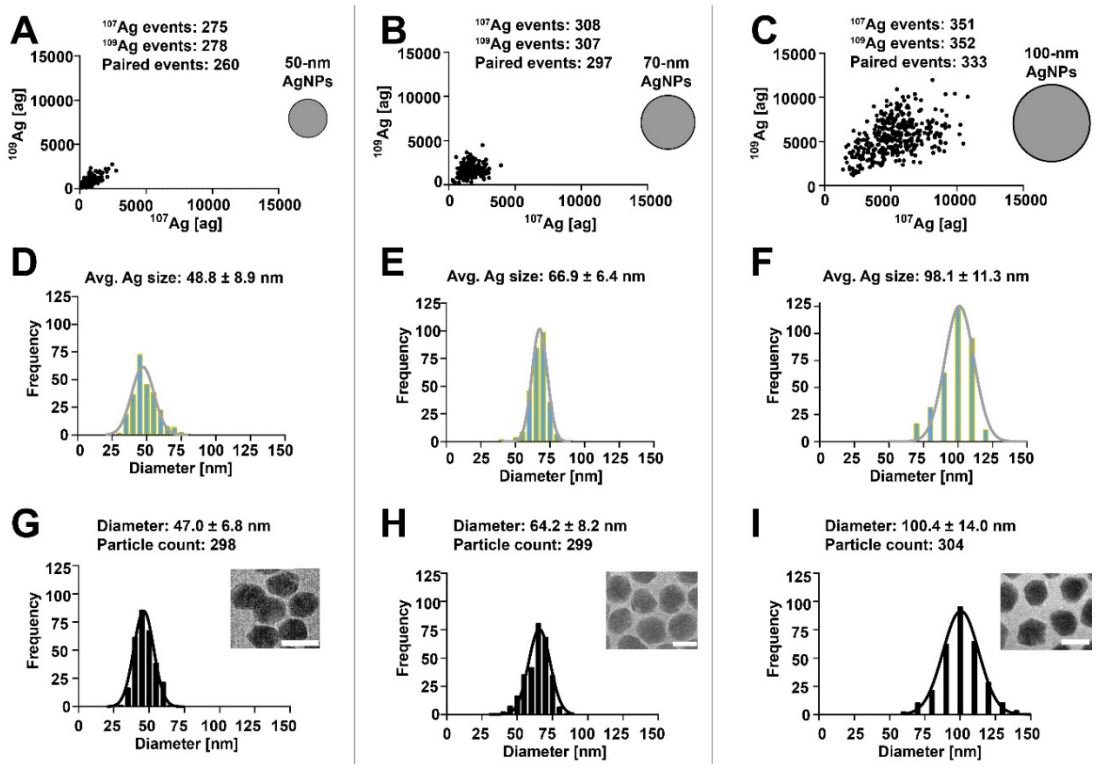


Figure 4.14: Single particle analysis of 50-nm, 70-nm, and 100-nm silver nanoparticles (AgNPs) using dual analyte SP-ICP-MS mode. A-C. Mass distributions of differently sized AgNPs based on both silver isotopes (^{107}Ag and ^{109}Ag). **D-F.** Size distribution histograms of differently sized AgNPs for both silver isotopes based on dual analyte SP-ICP-MS mass distributions values represent averages and standard deviations. **G-I.** Nanoparticle size distribution histograms based on TEM with representative micrographs values represent averages and standard deviations. Scale bars represent 50 nm, 70 nm, and 100 nm, respectively. Gaussian curves were fitted to frequency distributions in GraphPad Prism.

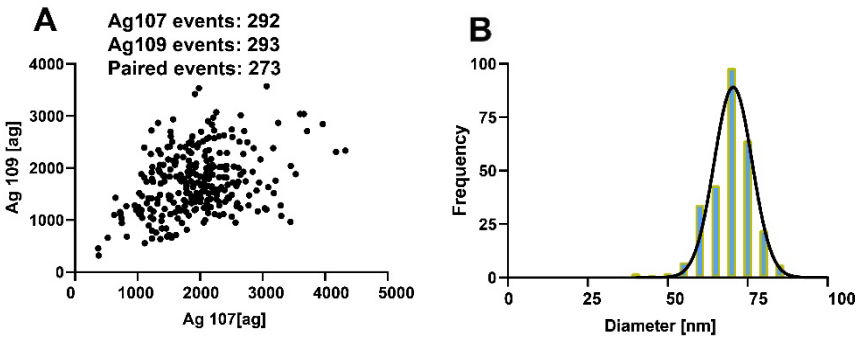


Figure 4.15: Single Particle Analysis of Surface Engineered 70-nm AgNPs. **A.** Mass distribution for both silver isotopes of PEGylated AgNPs. Median ^{107}Ag mass: 1,928 ag; Median ^{109}Ag mass: 1,700 ag. **B.** Size distribution histogram of PEGylated AgNPs by combining the sizes from both silver isotopes based on mass distributions; average size and StD: 69.3 +/- 6.8 nm.

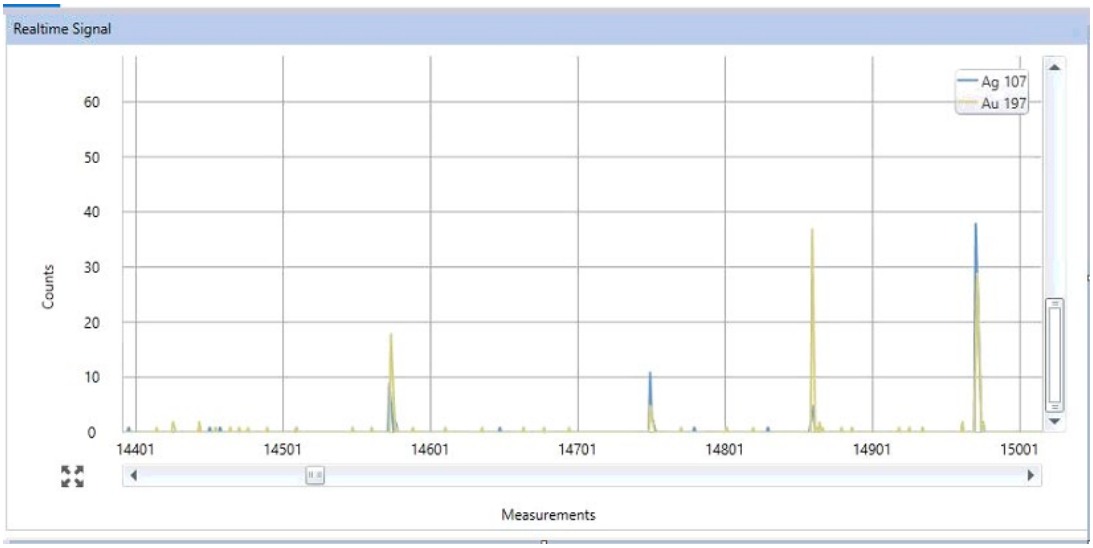


Figure 4.16: Realtime dual analyte SP-ICP-MS signals of overlapping transient nanoparticle ion clouds from 80-nm gold-silver alloy nanoparticles where silver signal ^{107}Ag is blue and gold signal ^{197}Au is green.

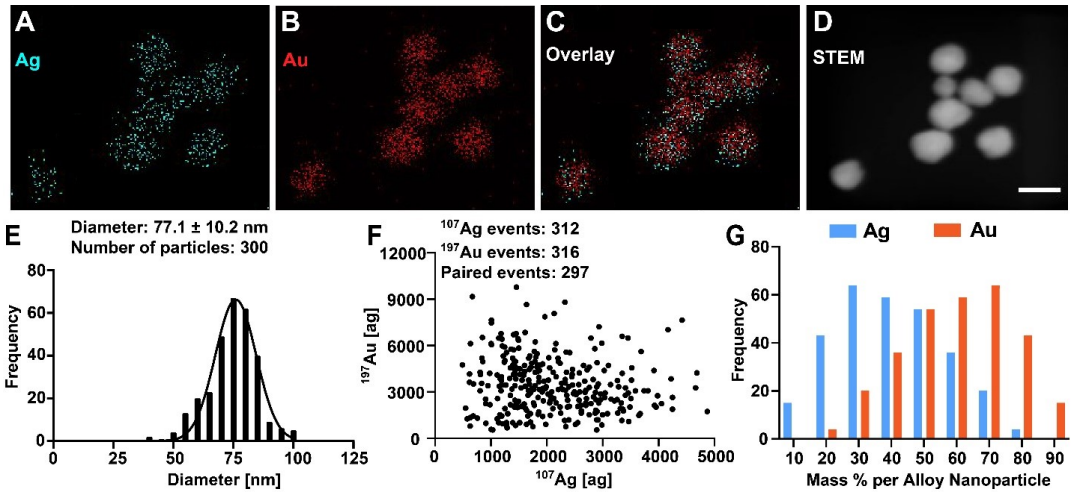


Figure 4.17: Compositional analysis of individual 80-nm gold/silver alloy nanoparticles (Au/AgNPs). A-D. EDS/STEM of 80-nm Au/AgNPs, where **A.** represents the EDS/STEM signal from silver in cyan; **B.** represents the EDS/STEM signal from gold in red; **C.** represents the overlay of gold and silver EDS/STEM signals. **D.** STEM image of 80-nm Au/AgNPs. Scale bar represents 100 nm. **E.** Size distribution histogram of 80-nm Au/AgNPs obtained from TEM imaging values represent averages and standard deviation. **F.** Mass distribution of individual 80-nm Au/AgNPs obtained with dual analyte SP-ICP-MS mode. **G.** Mass % distribution of silver and gold isotopes for individual 80-nm Au/AgNPs obtained with dual analyte SP-ICP-MS.

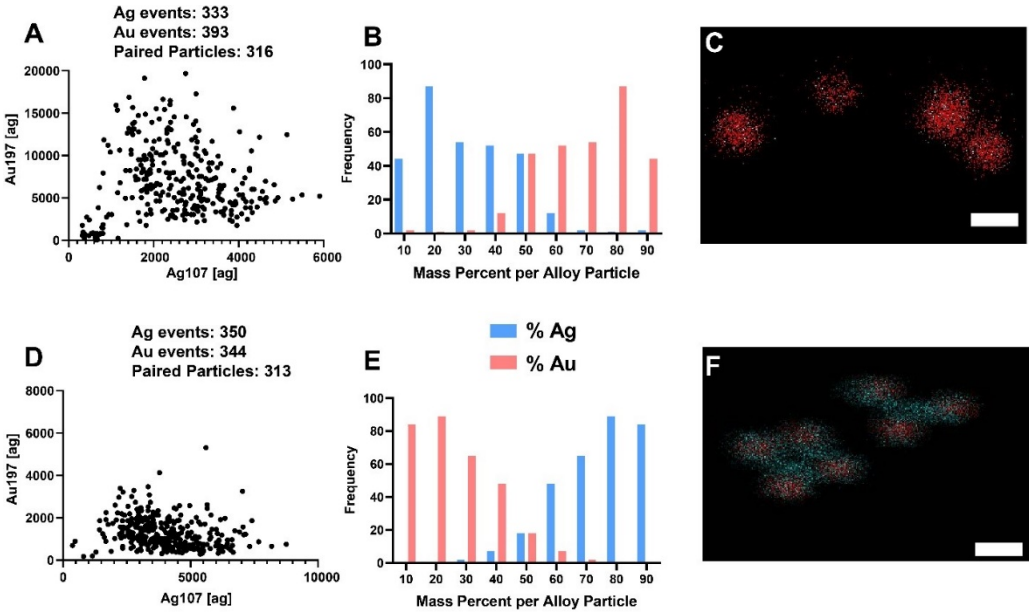


Figure 4.18: Elemental analysis of different compositions of gold-silver alloy nanoparticles. **A.** Dot plot mass distribution of 70-nm 30% silver 70% gold alloy nanoparticles with an average mass of gold and silver of 7,096 ag and 2,559 ag, respectively. **B.** Element distribution of 30% silver 70% gold alloy nanoparticles based on SP-ICP-MS mass histogram with an average silver mass% of 31% and average gold mass% of 69%. **C.** EDS/STEM image of 30% silver 70% gold alloy nanoparticles, where red signal is gold and cyan is silver. **D.** Dot plot mass distribution of 70-nm 70% silver 30% gold alloy nanoparticles with average mass of silver and gold 4,103 ag and 1,338 ag, respectively. **E.** Elemental distribution of 70% silver 30% gold alloy nanoparticles based on SP-ICP-MS mass histogram with an average silver mass% of 75% and average gold mass% of 25%. **F.** EDS/STEM image of 70% silver 30% gold alloy nanoparticles, where red signal is gold and cyan is silver.

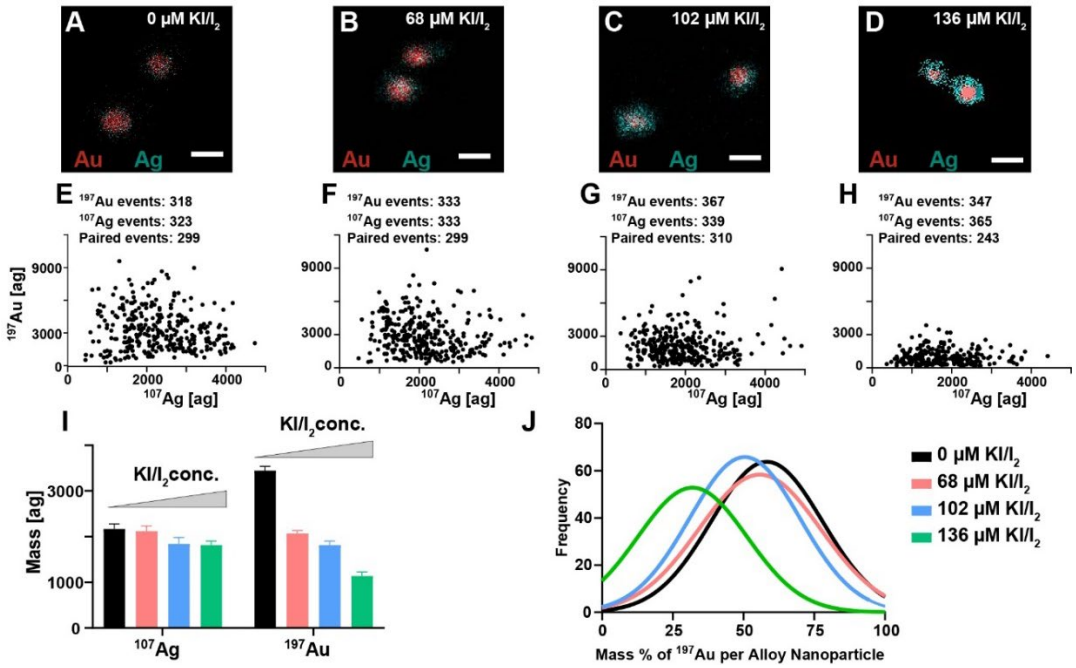


Figure 4.19: Quantifying gold etching using KI/I2 in individual gold/silver alloy nanoparticles (Au/AgNPs) *in situ*. Gold/silver alloy nanoparticles with an average diameter of 80 nm were exposed to various concentrations of KI/I2. **A-D.** STEM/EDS of Au/Ag alloy nanoparticles exposed to 0-μM, 68-μM, 102-μM, and 136-μM KI/I2, respectively. Scale bars represent 100 nm. **E-H.** Mass distributions of individual 80-nm Au/Ag alloy nanoparticles exposed to 0-μM, 68-μM, 102-μM, and 136-μM KI/I2, respectively, as obtained using dual analyte SP-ICP-MS mode. **I.** Average masses of individual Au/Ag alloy nanoparticles particles. Bars represent the mean values and standard deviations of five measurements. **J.** Mass % distribution of ^{197}Au remaining in individual Au/Ag alloy nanoparticles based on dual analyte SP-ICP-MS mass distributions from panels (E-H).

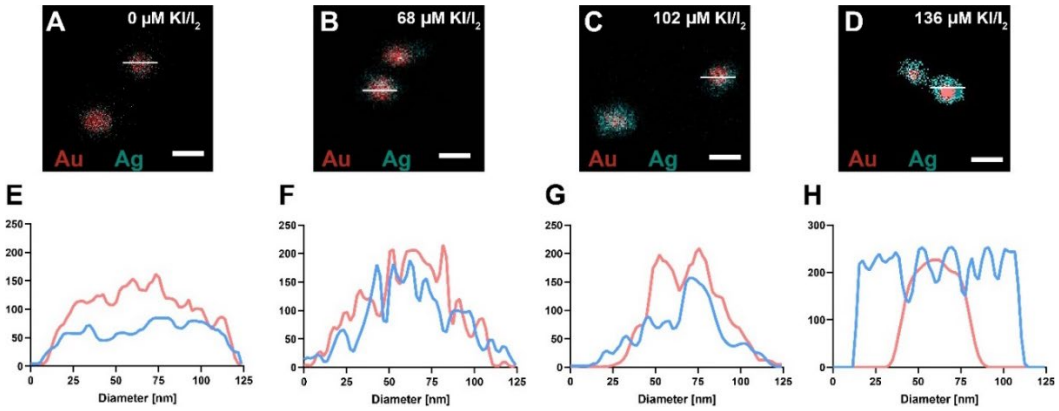


Figure 4.20: Line analysis of EDS/STEM images for gold-silver alloy nanoparticles exposed to different molar concentrations of KI/I_2 etchant. **A-D.** STEM/EDS of Au/Ag alloy nanoparticles exposed to 0-μM, 68-μM, 102-μM, and 136-μM KI/I_2, respectively. Scale bars represent 100 nm. **E-H** Pixel intensity for gold (red) and silver (blue), where white line intersects gold-silver alloy nanoparticles in EDS/STEM images.

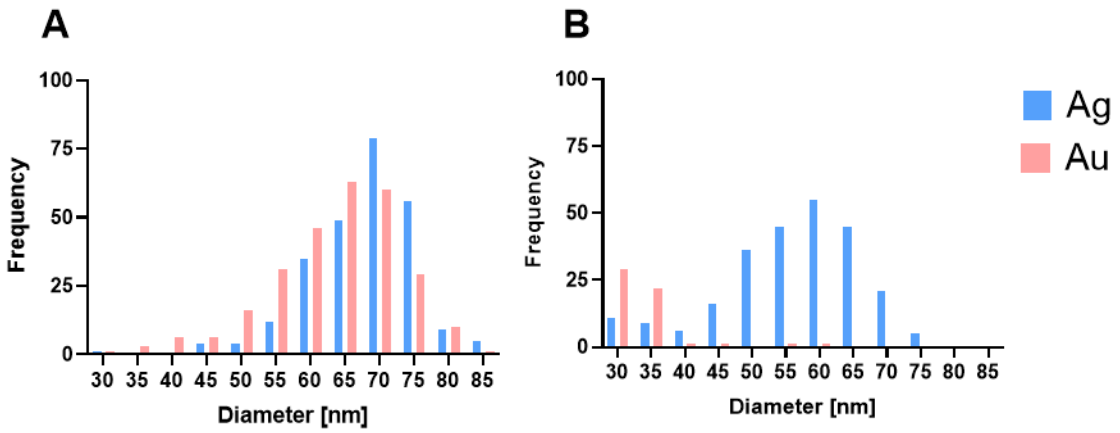


Figure 4.21: A. Nanoparticle size distribution of 65-nm AuNPs and 70-nm AuNPs mixed in a 1:1 ratio and analyzed using optimized conditions on dual analyte SP-ICP-MS in nanopure water. Mean diameter of AuNPs and AgNPs were both 67 nm. **B.** The same mixture of AuNPs and AgNPs exposed to etchant solution. In etchant solution the mean diameter of AuNPs decreased to 32 nm while the mean diameter of AgNPs was 56 nm.

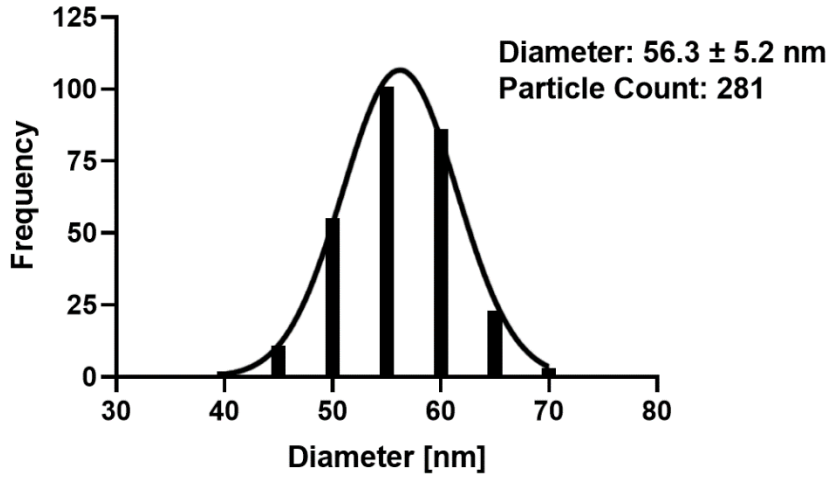


Figure 4.22: Size distribution histogram based on TEM analysis of in-house synthesized 55-nm Ag/Au alloy nanoparticles. Mean +/- StD.

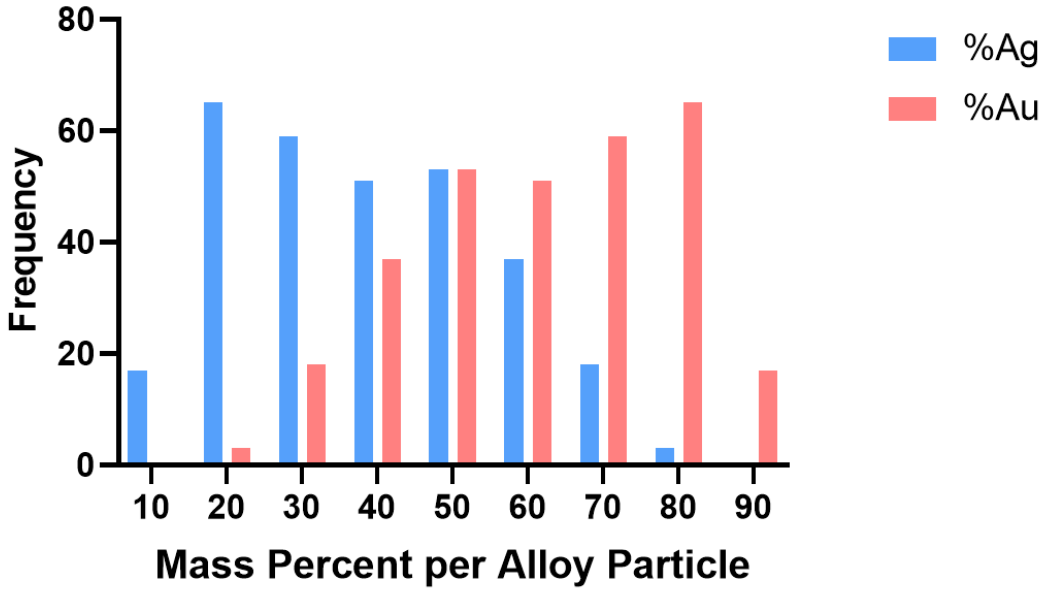


Figure 4.23: Elemental distribution based on dual analyte SP-ICP-MS mass histogram for 55-nm Au/Ag alloy seed nanoparticles.

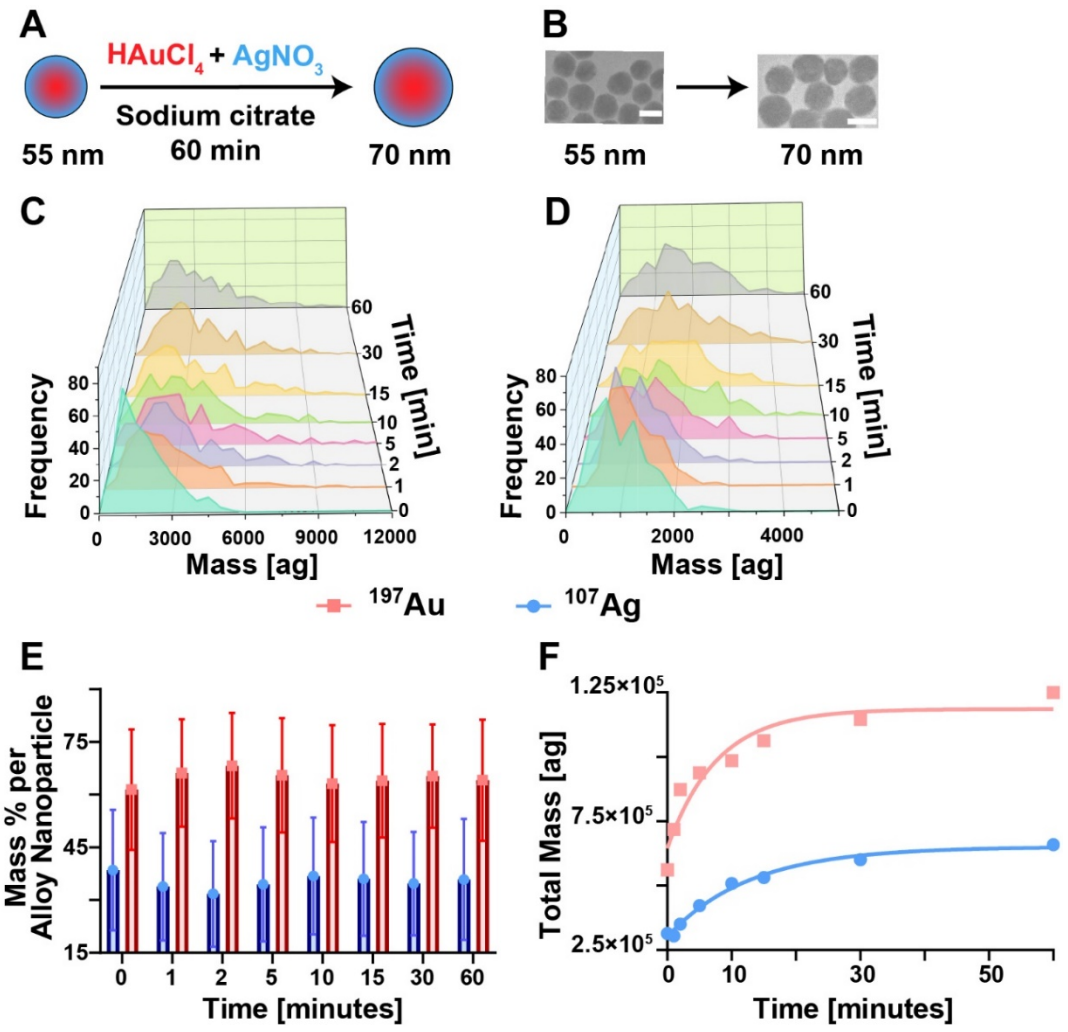


Figure 4.24: Quantifying metal deposition kinetics on individual gold/silver alloy nanoparticles *in situ*. A. Schematic representation of seed-mediated nanoparticle growth using 55-nm gold/silver alloy nanoparticles as seeds. **B.** TEM micrographs of (left) 55-nm gold/silver alloy nanoparticles (scale bar represents 55 nm), and (right) 70-nm gold/silver alloy nanoparticles (scale bar represents 70 nm). **C,D.** Mass distributions of ^{197}Au (C) and ^{107}Ag (D) deposition on individual alloy nanoparticles as a function of time obtained with SP-ICPMS. **E.** Average elemental composition of individual gold/silver alloy nanoparticles as a function of time during seed-mediated growth calculated from mass distributions in panels C and D where values represent averages and standard deviations. **F.** Summation of detected nanoparticle masses from panels C and D.^{197}Au (red; $r^2 = 0.92$) and ^{107}Ag (blue; $r^2 = 0.99$)

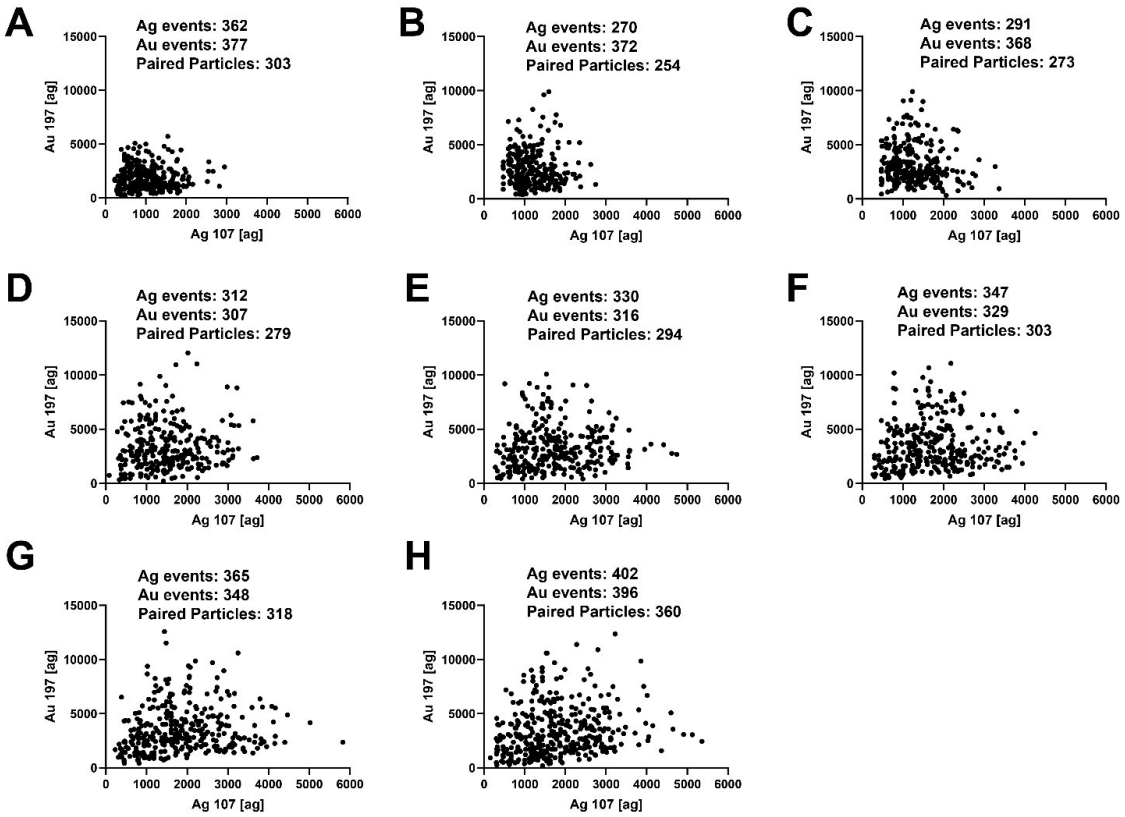


Figure 4.25: Mass dot plots obtained with dual analyte SP-ICP-MS of Au/Ag deposition onto 55-nm Au/Ag alloy nanoparticles at different time points. **A-H**: 0, 1, 2 5, 10, 15, 30, and 60 minutes, respectively.

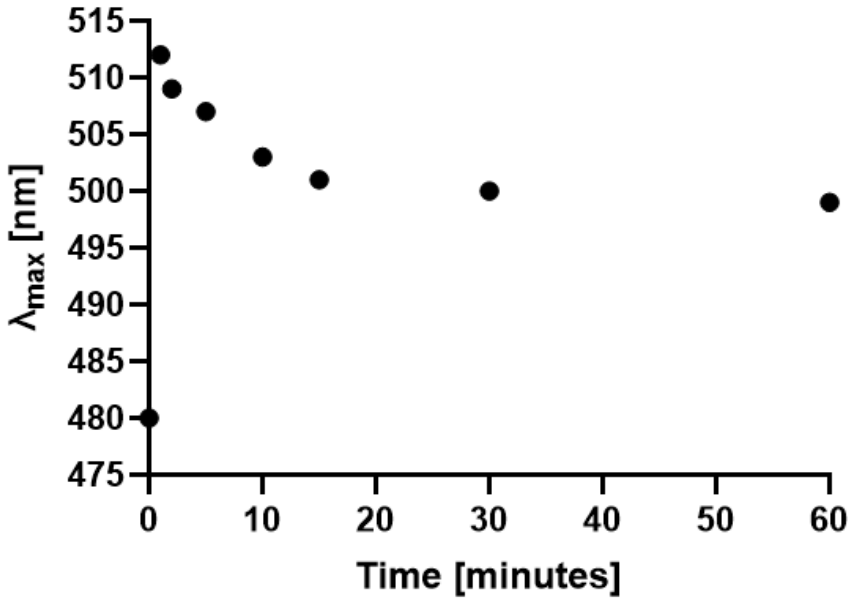


Figure 4.26: Maximum UV-Vis absorbance wavelength for seed-mediated growth of gold-silver alloy nanoparticles over time.

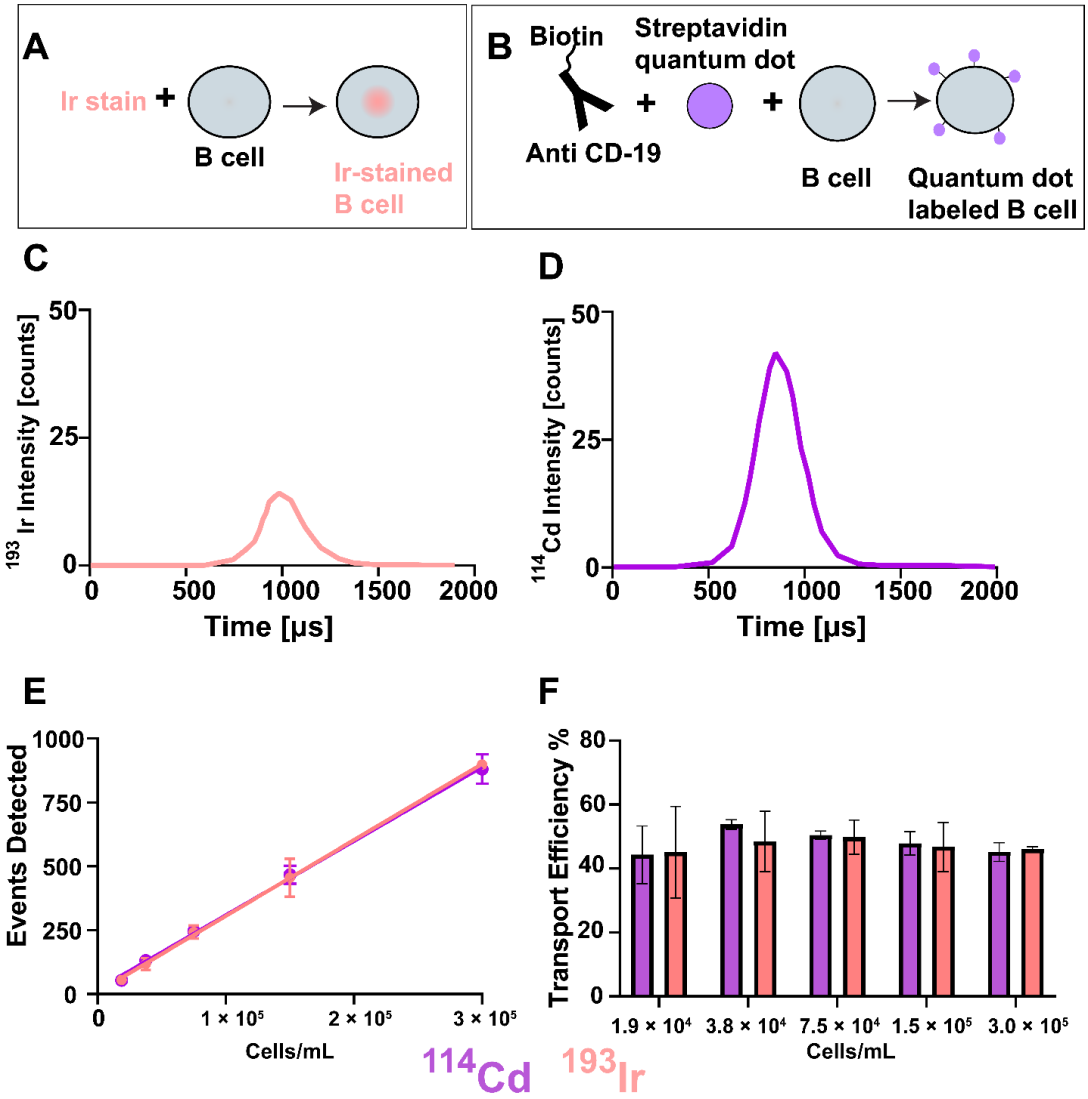


Figure 5.1: Detecting individual metal-labeled B cells. **A.** Schematic representation of iridium staining of B cells **B.** Schematic representation of labeling B cells with quantum dots. **C.** Transient ^{193}Ir ion signal of iridium-stained B cells. **D.** Transient ^{114}Cd ion signal of quantum dot labeled B cells. **E.** Detected events as a function of cell concentration for ^{114}Cd ($r^2 = 0.99$) and ^{193}Ir ($r^2 = 0.99$); Values represent averages and standard deviations of 3 independent measurements. Scan time = 30 seconds. **F.** Transport efficiency of B cells based on detected events in Panel E and equation 1.

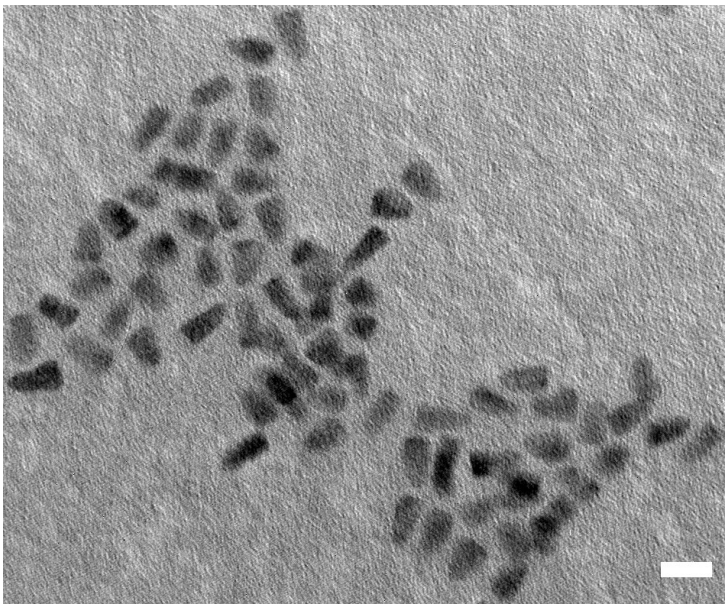


Figure 5.2 TEM micrograph of commercially available streptavidin-coated quantum dots. Scale bar represents 15 nm. Micrograph was acquired using the JEOL 2000-FX.

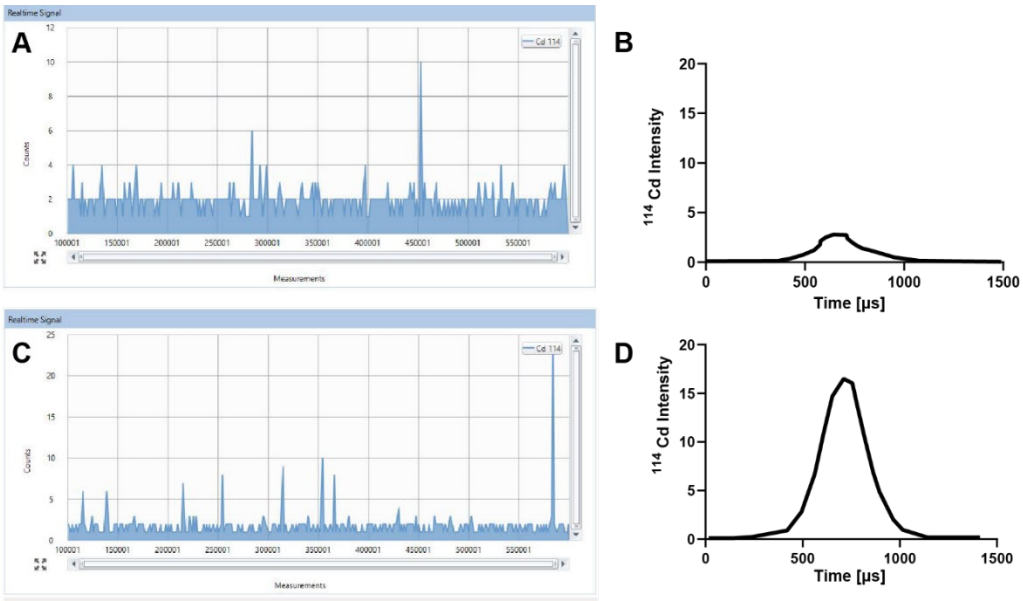


Figure 5.3 Time resolved SC-ICP-MS signal and peak shapes of streptavidin quantum dots. Scan times were 30 seconds. **A.** Time resolved ^{114}Cd signal of streptavidin quantum dots without biotinylated antibody. **B.** Transient ion signal of streptavidin quantum dots alone based on ^{114}Cd signal. **C.** Time resolved ^{114}Cd signal of streptavidin quantum dots mixed with biotinylated antibody. The same biotinylated antibody/quantum dot ratio was used as described above. **D.** Transient ion signal of streptavidin quantum dots mixed with biotinylated antibody based on ^{114}Cd signal.

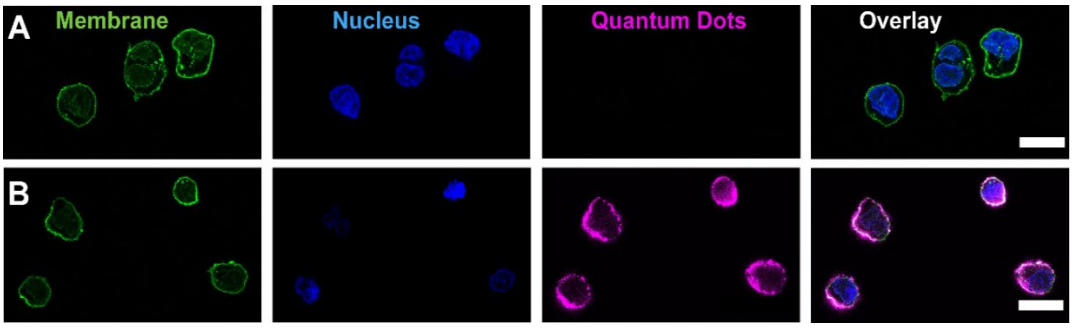


Figure 5.4 A. Representative confocal image of B cells without quantum dot labeling. **B.** Representative confocal image of B cells labeled with quantum dots. Scale bars represent 20 microns.

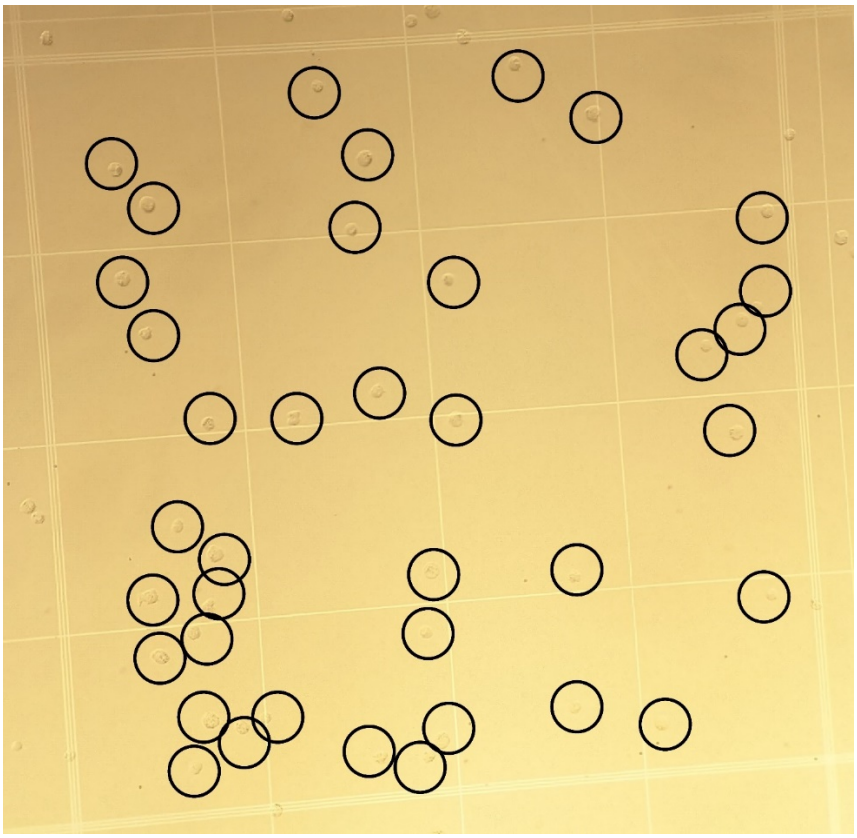


Figure 5.5 Hemocytometer image of a stock solution containing metal-stained B cells in nanopure water. Circles indicate individual Ir-stained B cells. Total number 38. Ir-stained cells were diluted to achieve a final concentration of 300,000 cells per mL

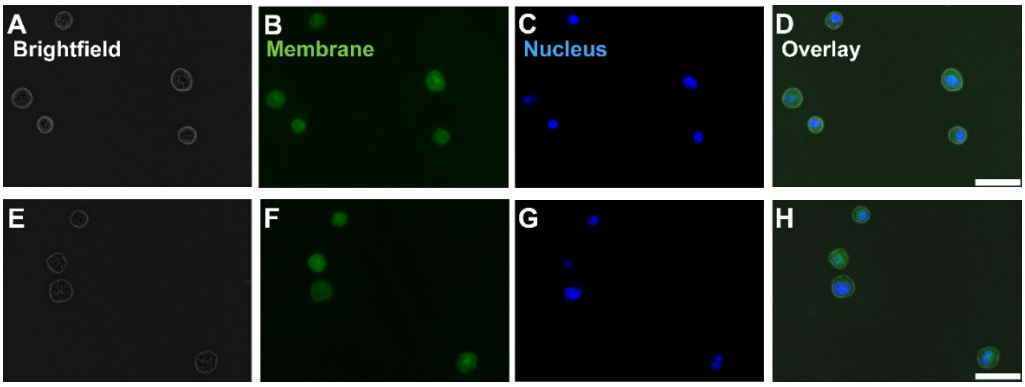


Figure 5.6 Fluorescence images of fixed B cells pre nebulization (top row: A-D) and post nebulization (bottom row: E-H). Scale bars are 20 microns.

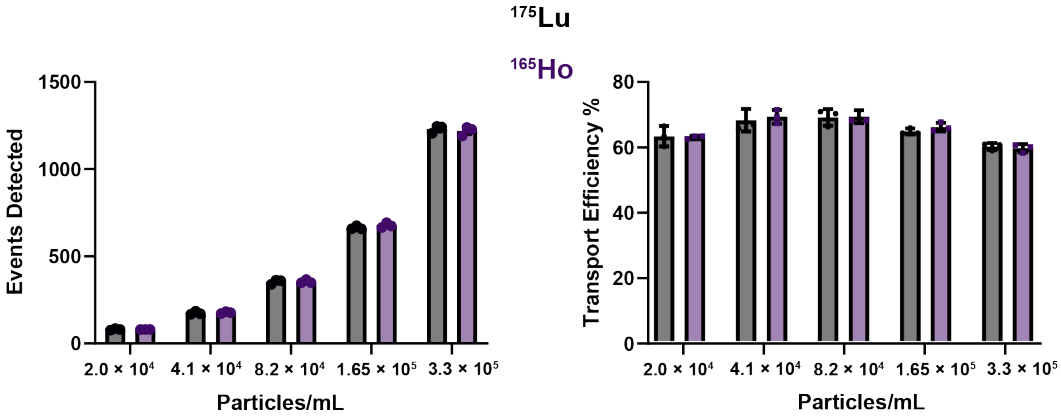


Figure 5.7 Detection of lanthanide doped micron-sized beads. **A.** Commercially available lanthanide-doped beads (Fluidigm) were serially diluted and ^{165}Ho and ^{175}Lu events were measured sequentially with a scan time of 30 seconds; $r^2 = 0.99$ for both isotopes. Values represent averages and standard deviations of 3 independent measurements. **B.** Transport efficiency of the beads was calculated for both isotopes based on detected events in Panel A and equation 1.

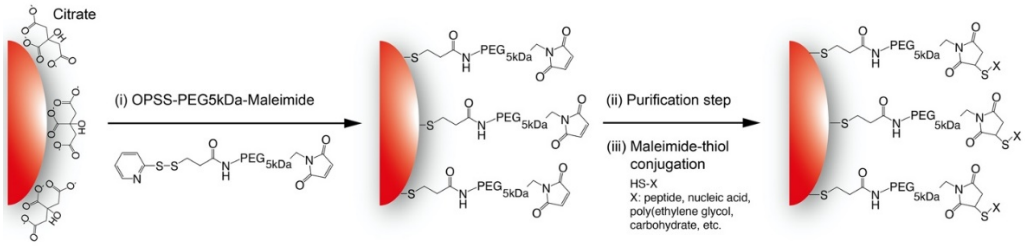


Figure 5.8: Schematic representation of maleimide-based nanoparticle surface functionalization. (i) OPSS-(PEG)5kDa-Mal is conjugated to the surface of citrate-stabilized gold nanoparticles (depicted by red surface) via a ligand exchange reaction to form maleimide-functionalized nanoparticles. (ii) Maleimide-functionalized nanoparticles are then purified by centrifugation to remove excess OPSS-(PEG)5kDa-Mal. (iii) Virtually any molecule with accessible thiol groups can then be conjugated to the nanoparticles via maleimide-thiol chemistry.

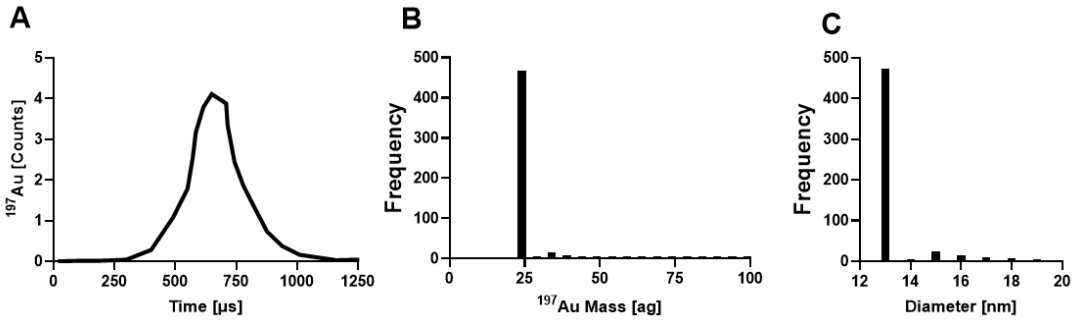


Figure 5.9 A. Transient ion peak shape of 13-nm AuNPs. **B.** Mass distribution of 13-nm AuNPs using single particle ICP-MS. **C.** Mass distributions from panel B converted to diameter assuming a spherical geometry.

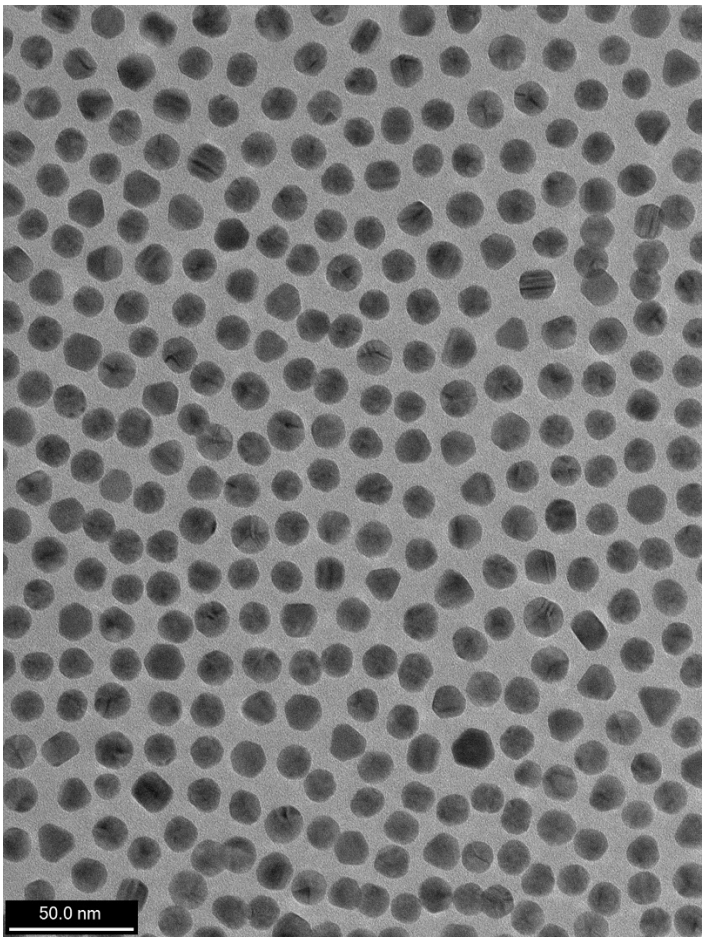


Figure 5.10 TEM micrograph of 13-nm AuNPs. Image was acquired on the JEOL 2010F. Scale bar represents 50 nm.

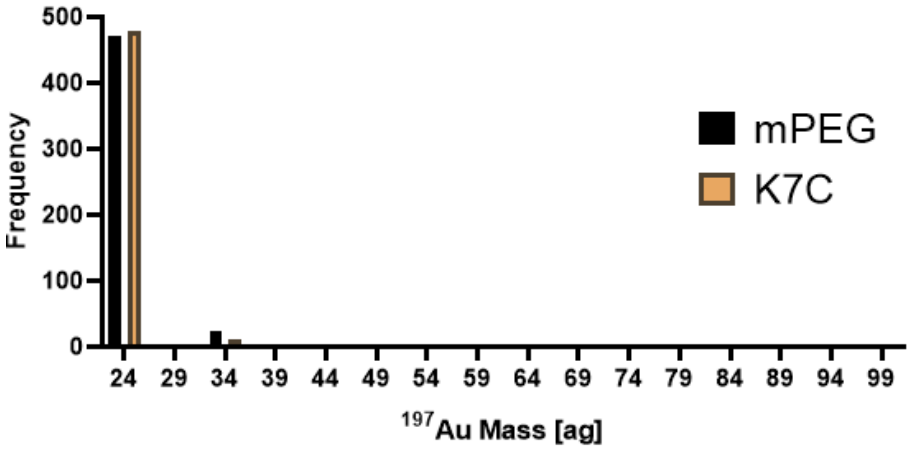


Figure 5.11 Mass distribution of K7C-modified AuNPs (orange), and m-PEG-modified AuNPs (black) in RPMI with 10% FBS at 37°C for 12 hours.

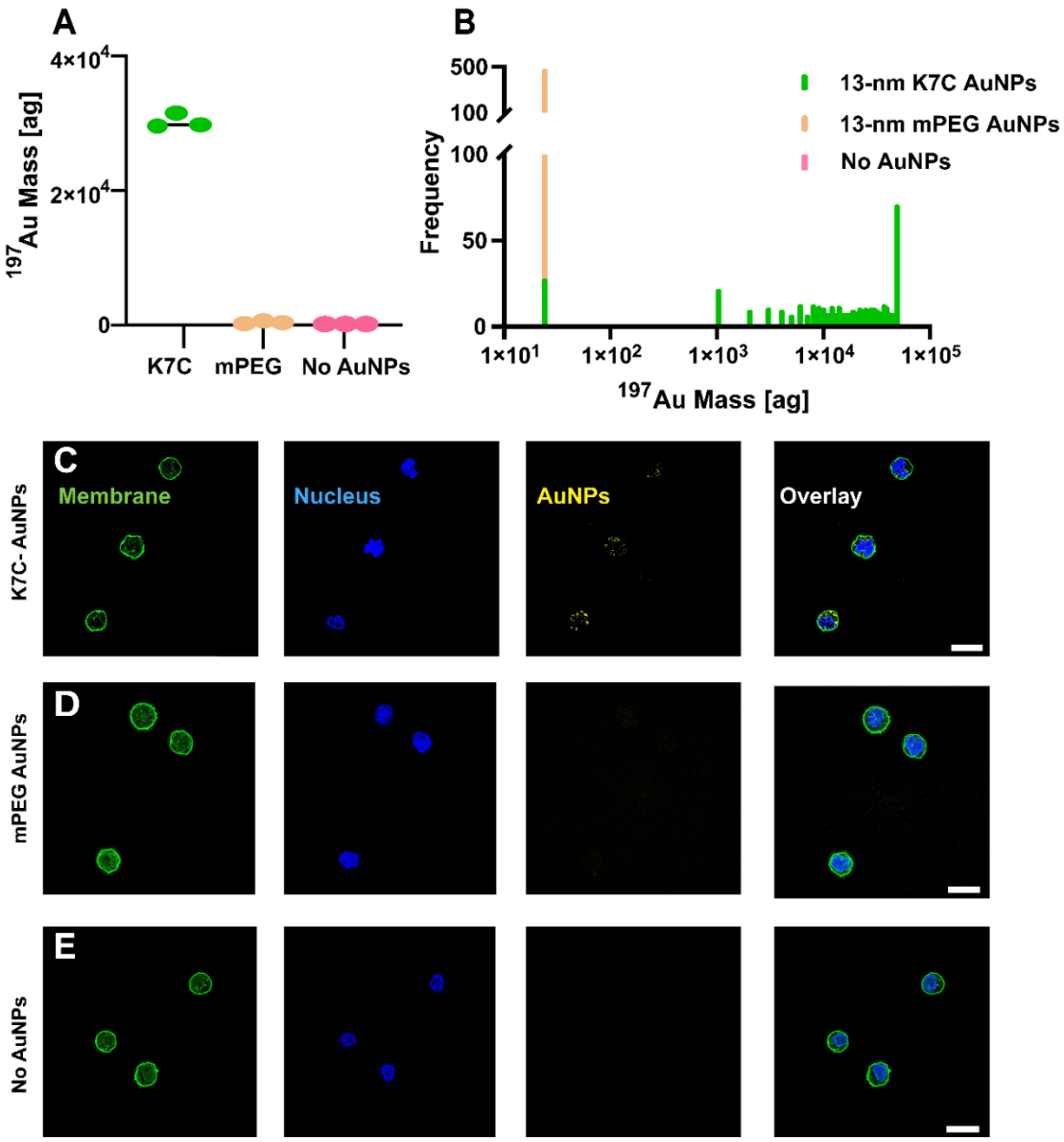


Figure 5.12: Quantifying and visualizing nanoparticle-cellular association. **A.** Average ^{197}Au masses of B cells exposed to 13-nm K7C AuNPs, 13-nm mPEG AuNPs, or no AuNPs for 12 hours. Bars represent the average of 3 independent measurements. **B.** Mass distribution of B cells exposed to either 13-nm K7C conjugated AuNPs (green), 13-nm mPEG conjugated AuNPs (orange), or no AuNPs (pink) for 12 hours. **C.** Confocal microscopy of B cells exposed to 13-nm K7C-modified AuNPs for 12 hours. **D.** Confocal microscopy of B cells exposed to 13-nm mPEG-modified AuNPs for 12 hours. **E** Confocal microscopy of B cells without AuNPs. Scale bars represent 20 microns.

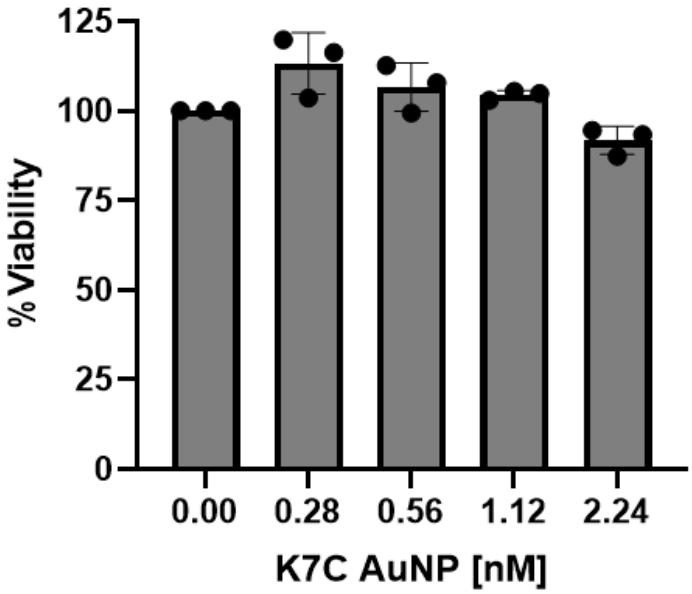


Figure 5.13 B cell viability exposed to various concentrations of K7C AuNPs for 8 hours determined by XTT assay.

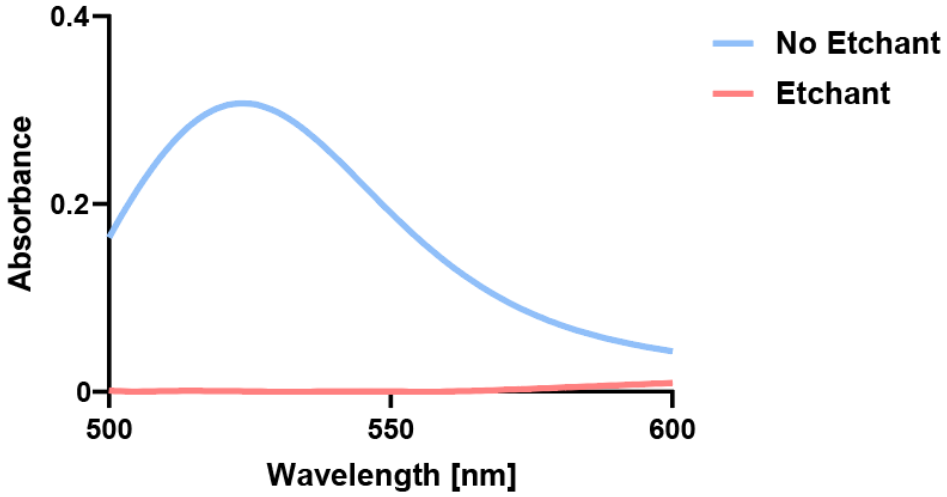


Figure 5.14 UV-Vis spectrum of 13-nM AuNPs without etchant (blue) and with etchant (red).

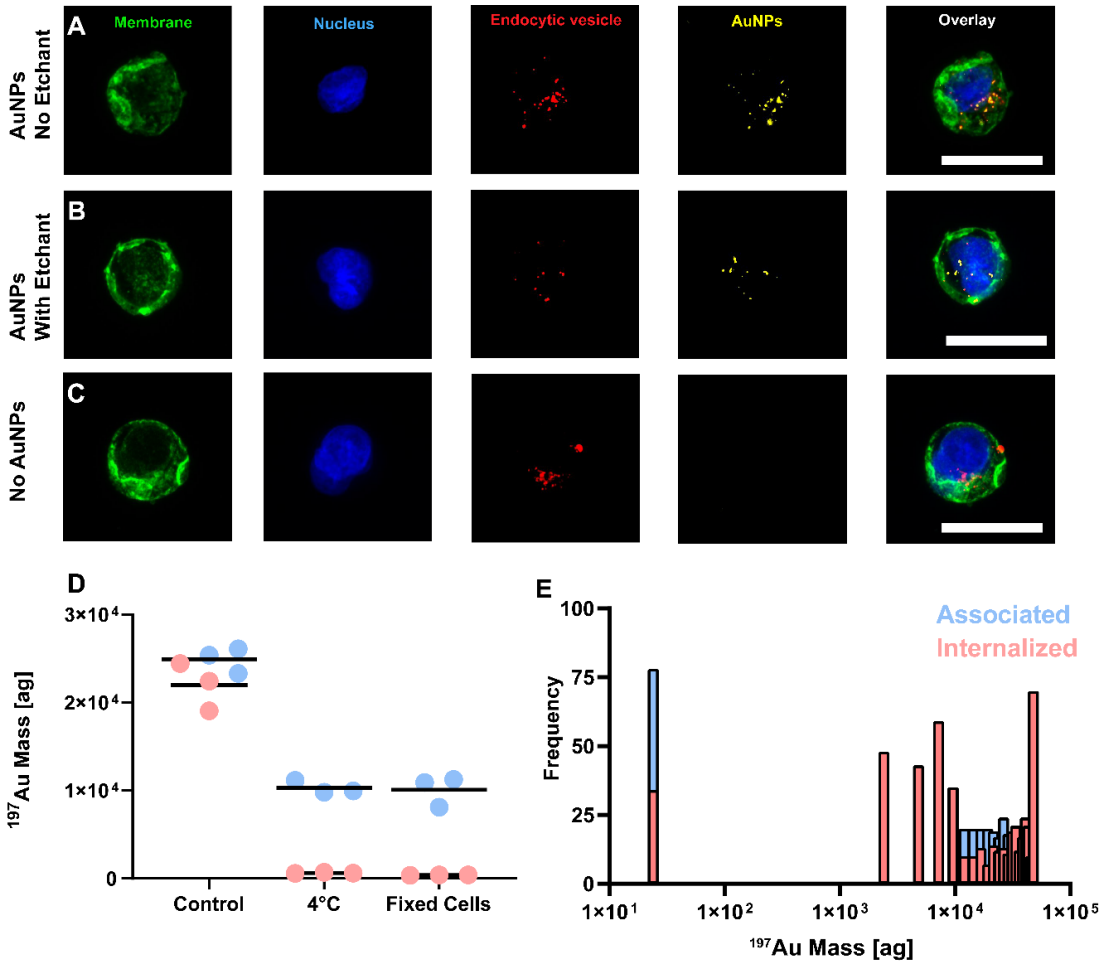


Figure 5.15: Visualizing and quantifying internalized 13-nm K7C AuNPs. **A** Z projections of B cells exposed to 13-nm K7C AuNPs for 8 hours without etchant. **B.** Z projections of B cells exposed to 13-nm K7C AuNPs for 8 hours with etchant. **C.** Z projections of B cells without AuNPs. Scale bars represent 20 microns. **D.** Average ^{197}Au masses of B cells exposed to 13-nm K7C AuNPs under different conditions for 8 hours without etchant (blue) and with etchant (red). Bars represent the average of 3 independent measurements. **E.** ^{197}Au mass distribution based on B cells exposed to 13-nm K7C AuNPs without etchant (blue) and with etchant (red).

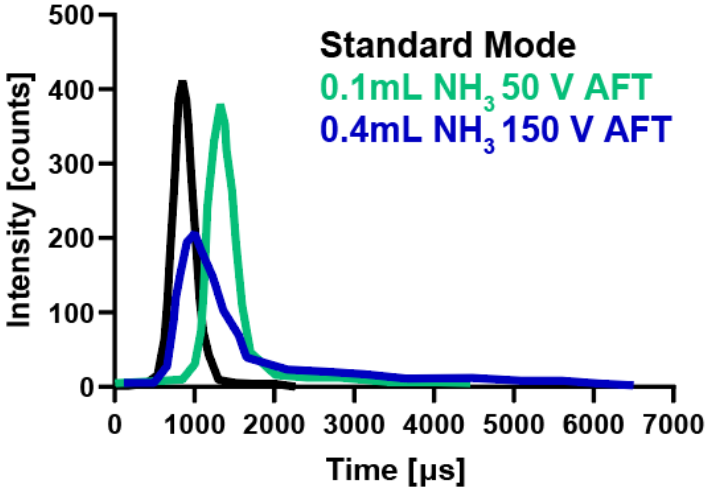


Figure 5.16 Transient ion signals of B cells exposed to K7C AuNPs under different reaction cell conditions.

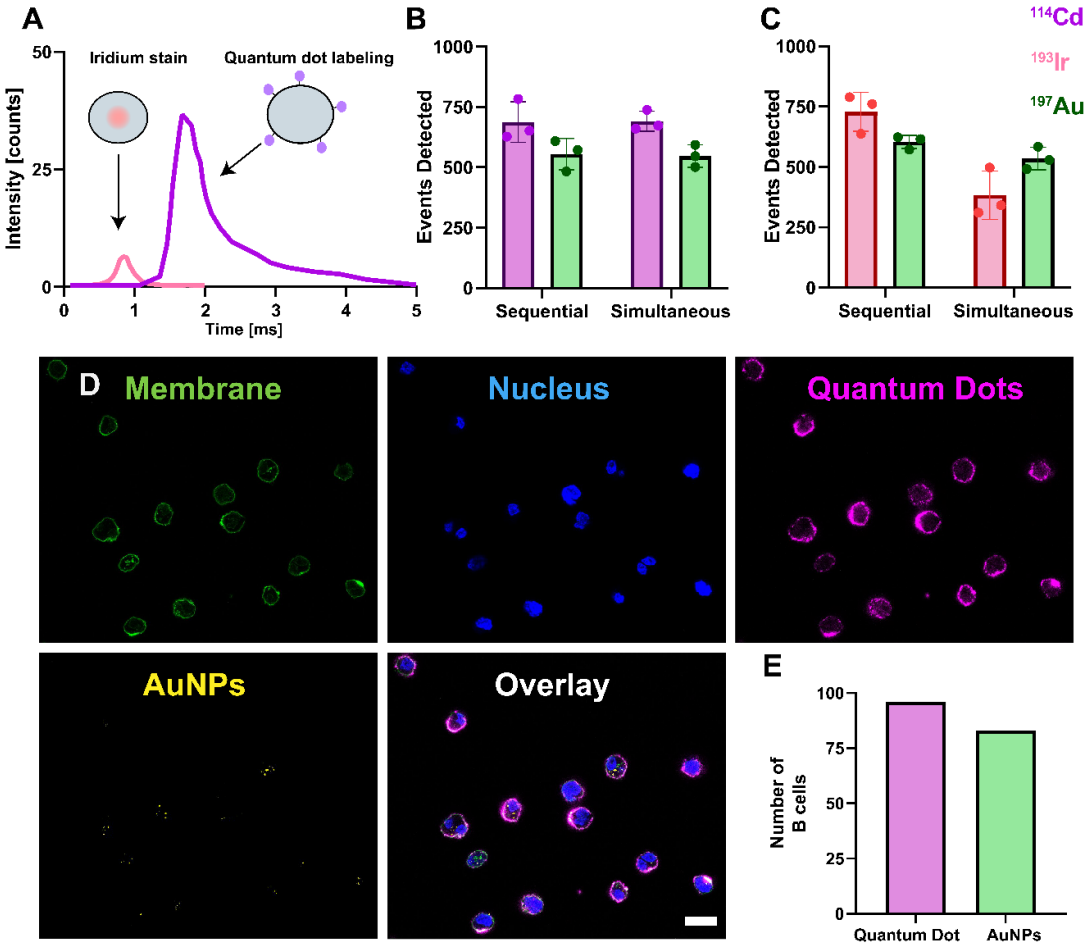


Figure 5.17: Determining $AuNP^+$ B cells. **A.** Representative confocal microscopy image of B cells exposed to 13-nm K7C AuNPs for 8 hours labeled with quantum dots. Scale bar represents 20 microns. **B.** Number of quantum dot labeled B cells and cells with AuNP scattering intensity from multiple fields of view using 40x objective. **C.** Transient ion peak shapes of cadmium and iridium labeled B cells using optimized dual analyte conditions. **D.** SC-ICP-MS determination of B cells $AuNP^+$ with sequential and simultaneous analysis of ^{114}Cd and ^{197}Au. Values represent 3 independent measurements. **E.** SC-ICP-MS determination of B cells $AuNP^+$ with sequential and simultaneous analysis of ^{193}Ir and ^{197}Au. Values represent 3 independent measurements.

Appendix B: Tables

Table 2.1. Examples of different cellular uptake pathways of gold nanoparticles in tissue culture for both cancerous and non-cancerous cells.

Major Uptake Pathways	Cell Line	Nanoparticle Surface Modification	Gold Nanoparticle Core Size [nm]	Ref.
CVE	HeLa	Cysteine-Cyan5	4.5	317
CVE	HeLa	Cationic monolayer	2	113
CVE and Lipid Rafts	C166	Nucleic acids	10	318
CVE, Macropinocytosis	A549	Poly(isobutylene-alt-maleic anhydride)	13	319
CDE	MRC-5,	Coating with fetal bovine serum (FBS)	20	320
CDE, CCIE	HUVEC	Citrate	80	321
CDE	MCF10	Cationic monolayer	2	113
CCIE	HeLa	Cationic monolayer	2	113
Phagocytosis	Murine peritoneal-isolated macrophages	5-aminovaleric acid, L-DOPA, Melatonin, Serotonin-HCl,	30-50	322
Direct Translocation	Mouse dendritic cells	MUS/OT with "striped" domains	4-5	323
Direct Translocation	HCT-116	Glutathione/Glucose	5	324
Electroporation	NIH/3T3 K562	Polyethyleneimine + DNA plasmids, siRNA	5-40	325
Microinjection	Murine 2-cell embryos	"Ligand free"; no deliberate surface modification	11	326

Abbreviations: CDE: Clathrin-dependent endocytosis, CVE: Caveolin-dependent endocytosis, CCIE: Clathrin/caveolin-independent endocytosis, HeLa: human cervical cancer cells, C166: mouse endothelial cells, A549: adenocarcinoma human alveolar basal epithelial cells, MRC-5: human lung fibroblasts, HUVEC: human umbilical vein vascular endothelium cells, HCT-116: human colorectal carcinoma, NIH/3T3: mouse embryo fibroblasts, K562 human chronic myelogenous leukemia, L-DOPA: (S)-2-amino-

3-(3,4-dihydroxyphenyl)propanoic acid, Melatonin: N-acetyl-5-methoxytryptamine, Serotonin HCl: 5-hydroxytryptamine hydrochloride, MUS/OT: 11-mercapto-1-undecanesulphonate and 1-octanethiol, siRNA: small interfering Ribonucleic Acids

Table 2.2 Examples of different types of nanoparticle targeting ligands for enhanced nanoparticle cellular interaction with targeted cell types.

Targeting Ligand	**Nanoparticle Core Material**	**Targeted Cell Types**	**Used for Cell Targeting *in vitro* or *in vivo***	**Ref.**
Peptides				
CLT1 peptide for fibronectins	PEG-PLA	C6 glioma cells	*In vitro* and *in vivo*	327
CREKA Pentapeptide sequence for fibrin	DSPE-PEG_{2000}	GL261 glioma cells	*In vivo*	328
M2-Macrophage targeting peptide	HPMA polymer	Tumor associated macrophages	*In vitro* and *in vivo*	329 330
RGD Motif for integrin binding	Mesoporous Silica	SCC-7 Mouse squamous cell carcinoma HT-29 Human colon cancer cells	*In vitro*	331
P160 targeting peptide found through phage display	Cadmium-selenide core zinc-sulfide shell Quantum dots	MCF-7 Human breast cancer cells	*In vitro*	332
Chlorotoxin peptide for MMP2	Silver	U87MG glioblastoma	*In vitro* and *in vivo*	333
Glycoproteins				
Transferrin to cross blood brain barrier	DSPC-Cholesterol-POPG	U87MG glioblastoma	*In vitro* and *in vivo*	334

		GL261 glioma cells		
Antibodies and antibody fragments				
Anti-CD8a $F(ab')_2$	PLGA-PEG	$CD8^+$ T-cells	*In vitro* and *in vivo*	335
HuA33 monoclonal antibody	Poly(methacrylic) acid	LIM1889, LIM2405+, LIM2405- human colon cancer cells	*In vitro*	336
HER2 monoclonal antibody	Gold plasmonic vesicles	SKBR-3 Human breast cancers	*In vitro*	337
Anti-epidermal growth factor receptor	Quantum dots	MDA-MB-231 mammary adenocarcinoma BxPC-3 pancreatic adenocarcinoma	*In vitro*	338
Nucleic acids				
Single-stranded oligonucleotide-based aptamers	Quantum dots	A549 lung adenocarcinoma	*In vitro*	339
Anti-cMet DNA aptamer	Lipidated aptamer-based nanocarriers loaded with doxorubicin	H1838 Non-small cell lung	*In vitro*	340
G- rich DNA aptamer	Zinc gallogermanate	4T1 mammary carcinoma	*In vivo*	341
Small molecules				
Folic acid for folate receptors	Mesoporous Silica	U20 osteosarcoma	*In vitro*	342

Abbreviations:
CTL1: fibronectin targeting peptide, CREKA: fibrin binding peptide cysteine, arginine, glutamic acid, lysine, aspartic acid, RGD: arginine, glycine aspartic acid, MMP2- Matrix metalloproteinase, PEG-PLA:

poly(ethylene glycol)-poly(lactide), DSPE-PEG2000: 1,2-distearoyl-sn-glycero-3-phosphoethanolamine-N-[amino(polyethylene glycol)-2000], HPMA: poly(N-(2-hydroxypropyl) methacrylamide), DSPC: 1,2-distearoyl-sn-glycero-3-phosphocholine, POPG: 1,2-distearoyl-sn-glycero-3-phosphocholine, PLGA-PEG: poly(lactic-co-glycolic acid) (PLGA) and polyethylene glycol

Table 2.3. Nanoparticle Surface Modifications and Surface Ligands for Intracellular Organelle Targeting**.**

Nanoparticle Surface Modification	**Organelle Destination(s)**	**Ref.**
Folic Acid	Nucleus	342
RGD + CGGGPKKKRKVGG peptide	Nucleus	343
3,4-diphenylacetic acid-MYIEALDKYAC-COOH peptide	Nucleus	344
DRQIKIWFQNRRMKWKK peptide	Nucleus	345
Triamcinolone acetonide	Nucleus	346
Nuclear Localization Sequence (NLS) peptide	Nucleus	347
Triphenoylphosphonium	Mitochondria	348–350
D[KLAKLAK]$_2$ peptide	Mitochondria	351
RGD + MLALLGWWWFFSRKKC peptide	Mitochondria	352
MVSGSSGLAAARLLSRTFLLQQNGIRH GSYC peptide	Mitochondria	353
Dmt-D-Arg-Phe-Lys-NH2 peptide	Mitochondria	354
Octaarginine peptide	Golgi apparatus, Mitochondria	43, 355
TAT peptide CALNNAGRKKRRQRRR	Golgi apparatus, Nucleus	356, 357
L-cysteine moieties	Golgi apparatus	358
KDEL peptide	Endoplasmic Reticulum	359
mi-R29b + PEI	Endoplasmic Reticulum	360

Table 3.1: Gold Nanoparticle Molar Decadic Extinction Coefficients

Gold Nanoparticle Size (nm)	**Peak Absorbance Wavelength (nm)**	**Molar Decadic Extinction Coefficient (M^{-1} cm^{-1})**
16	518	4.52E+8
30	526	3.36E+9
55	532	2.33E+10

Table 3.2: Single Particle ICP-MS Conditions

RF Power [W]	1600
Nebulizer Gas Flow [mL min^{-1}]	0.4
Make up Gas Flow [mL min^{-1}]	0.7
Sample Flow Rate [mL min^{-1}]	0.010
Sample Volume [µL]	150
Dwell Time [µs]	50
Scan time [s]	60
Transport Efficiency [%], Mean ± StD	58.5 ± 3.9

Table 3.3: Determining Transport Efficiency

Particles Detected	**Instrument Calculated Particles mL^{-1}**
193	33003
195	33516
197	33687

Table 3.4: Comparison of Nanoparticle Measurements

Sample	**Hydrodynamic Diameter [nm]**	**Nanoparticle Core Diameter [nm]**	**Mean Nanoparticle Mass [ag]**	**Calculated Nanoparticle Diameter [nm]**
16-nm AuNPs	18.0 ± 1.0	16.3 ± 1.2	53.2 ± 16.0	17.2 ± 1.7
30-nm AuNPs	37.6 ± 2.6	30.6 ± 5.4	290.7 ± 164.4	29.7 ± 5.5
55-nm AuNPs	54.4 ± 3.8	52.2 ± 9.1	1952.1 ± 643.6	57.1 ± 6.1

Diameters and masses are provided as mean values +/- standard deviation.

Table 3.5: DLS of 16-nm AuNPs in Saline Solution

Time [minutes]	**Citrate 0 mM NaCl** HDD, PDI	**Citrate 150mM NaCl** HDD, PDI	**0.010 PEG/nm^2 150mM NaCl** HDD, PDI	**0.025 PEG/nm^2 150 mM NaCl** HDD, PDI	**0.050 PEG/nm^2 150mM NaCl** HDD, PDI
0	23.9 ± 0.4 nm, 0.04	28.9 ± 0.2 nm, 0.3	25.7 ± 0.2 nm, 0.08	26.6 ± 0.5 nm, 0.06	28.1 ± 0.2 nm, 0.06
60	23.8 ± 0.2 nm, 0.04	41.2 ± 0.4 nm, 0.3	26.6 ± 0.7 nm, 0.16	26.9 ± 0.3 nm, 0.11	29.8 ± 0.5 nm, 0.05

Diameters are provided as mean values +/- standard deviation (n=3).

Table 4.1: Optimized conditions for Single Particle ICP-MS

RF Power [W]	1600
Nebulizer Gas Flow [mL min ^{1}]	0.44
Make up Gas Flow [mL min^{-1}]	0.75
Sample Flow Rate [mL min^{-1}]	0.010
Sample Volume [µL]	150
Detector Dwell Time [µs]	50

Table 4.2: Transport efficiency based on the number of events detected from a known particle concentration (100,000 particles per mL) diluted from a stock of ^{175}Lu-doped beads with an initial concentration of 330,000 particles per mL. Paired T test found no statistically significant difference between the transport efficiency when the optimized collision cell parameters were applied. Values represent averages and standard deviations of 5 measurements.

Standard Mode Transport Efficiency	Transport Efficiency using Collision Cell
39.8 ± 3.1 %	40.4 ± 2.2 %

Table 4.3: Collision cell mode conditions for dual analyte SP-ICP-MS analysis in single particle mode.

Isotopes Analyzed Simultaneously	NH_3 Gas Flow [mL min^{-1}]	Axial Field Technology [V]	RPq*	Quadrupole Settling Time [µs]
^{140}Ce & ^{175}Lu	0.5	300	0.31 & 0.25	150
^{153}Eu & ^{175}Lu	0.5	300	0.29 & 0.25	150
^{165}Ho & ^{175}Lu	0.5	300	0.27 & 0.25	150
^{107}Ag & ^{109}Ag	0.4	100	0.25 & 0.25	150
^{107}Ag & ^{197}Au *100nm mixture*	0.4	100	0.46 & 0.25	400
^{107}Ag & ^{197}Au *Alloys*	0.4	100	0.46 & 0.25	300

*RPq- rejection parameters for quadrupole mass filter

Table 4.4: Paired isotope events of 3 pairs of isotopes in standard mode, optimized collision cell conditions, quadrupole settling time 150 µs, and on CyTOF.

Lanthanide isotopes detected concurrently	% Paired isotope events detected via SP-ICP-MS without peak stretching*	% Paired isotope events detected via optimized dual analyte SP-ICP-MS**	% Paired isotope events detected via CyTOF**
^{175}Lu & ^{140}Ce	53.8 ± 0.7 %	96.5 ± 1.0%	99.6 ± 0.4%
^{175}Lu & ^{153}Eu	54.8 ± 1.8 %	96.8 ± 1.5%	99.6 ± 0.4%
^{175}Lu & ^{165}Ho	37.8 ± 1.3%	97.2 ± 0.6%	99.6 ± 0.4%

* Values represent the means and standard deviations of three independent measurements.
** Values represent the means and standard deviations of five independent measurements.

Table 4.5: Summary of Dynamic Light Scattering Results of Nanoparticles.

Sample	**Hydrodynamic Diameter [nm]**	**Polydispersity Index**
30 nm AgNPs	42.3 ± 0.5	0.11
50 nm AgNPs	63.4 ± 2.5	0.12
70 nm AgNPs	77.4 ± 2.0	0.06
PEGylated 70 nm AgNPs	110.1 ± 1.5	0.06
100 nm AgNPs	112.0 ± 2.7	0.04
100 nm AuNPs	119.4 ± 1.1	0.03
Alloy nanoparticle seeds	69.4 ± 0.5	0.05
80 nm Alloy nanoparticles	88.1 ± 0.9	0.03

* Measurements represent the averages of three measurements and standard deviations.

Table 4.6: Median masses of both silver isotopes in differently sized AgNPs

Nominal AgNP Diameter [nm]	**Median ^{107}Ag Mass [ag]**	**Median ^{109}Ag Mass [ag]**
30	246	228
50	652	720
70	1,562	1,599
100	5,186	5,352

Table 4.7: EDS/STEM quantification of gold-silver alloy nanoparticle composition.

Sample	Atomic % Ag	Atomic % Au
30% Ag 70% Au Alloys	35.1%	64.9%
80-nm Ag/Au Alloys (0-µM KI/I_2)	40.6%	59.4%
70% Ag 30% Au Alloys	75.5%	24.5%
80-nm Ag/Au Alloys + 68-µM KI/I_2	43.3%	56.7%
80-nm Ag/Au Alloys + 102-µM KI/I_2	54.7%	45.3%
80-nm Ag/Au Alloys + 136-µM KI/I_2	72.3%	27.7%

Table 5.1: Optimized conditions for Single Cell ICP-MS

RF Power [W]	1600
Nebulizer Gas Flow [mL min ^{1}]	0.44
Make up Gas Flow [mL min^{-1}]	0.75
Sample Flow Rate [mL min^{-1}]	0.013
Detector Dwell Time [µs]	50

Table 5.2: DLS and Zeta Potential of differently surface modified AuNPs

Surface Modification	Hydrodynamic Diameter [nm]*	PDI	Zeta Potential [mV]*
Citrate w/ Tween 20	25.1 ± 0.4	0.03	-26.5 ± 3.0
0.5 OPSS-PEG-MAL/nm^2	36.1 ± 0.6	0.06	-10.0 ± 3.0
OPSS-PEG-MAL-K7C	45.5 ± 0.7	0.10	17.1 ± 3.9
OPSS-PEG-MAL-SH-mPEG	45.6 ± 0.5	0.10	-1.5 ± 0.1

*Values represent averages and standard deviations of 3 independent measurements.

Table 5.3: DLS of etched 13-nm AuNPs

Sample	**Hydrodynamic diameter [nm]**	**PDI**	**Scattering [KCPS]**
13-nm AuNPs no Etchant	18.8 ± 0.4	0.03	175 ± 25
13-nm AuNPs with Etchant	1248 ± 523	0.9	30± 10

Values indicate averages and standard deviations of 3 independent measurements.

Table 5.4 Dual analyte single cell parameters

Isotopes Analyzed Simultaneously	NH_3 Gas Flow [mL min^{-1}]	Axial Field Technology [V]	RPq*	Quadrupole Settling Time [µs]
^{114}Cd & ^{197}Au	0.4	150	0.43 & 0.25	300
^{193}Ir & ^{197}Au	0.1	50	0.25 & 0.26	150

*RPq- rejection parameters for quadrupole mass filter